

University of Nottingham
UK | CHINA | MALAYSIA

Porous Carbons for CO_2 Capture

Alison Taylor

Thesis submitted to the University of Nottingham for the degree of Doctor of Philosophy

September 2019

Abstract

This thesis investigates the tailoring of activated porous carbon materials in order to improve CO_2 adsorbance capacity. The investigation is comprised of 4 studies focussing on different aspects of porous carbon synthesis, including metal doping, a novel carbonisation technique, an alternative activating agent and the use of harsh activating conditions.

The first study is an investigation into the effects of heteroatom doping of the carbon surface in order to increase the selectivity and adsorbance of CO_2. Potassium hydrogen phthalate was heated at 800 and 900 °C to create microporous, high surface area carbons. The Group 1 and 2 metals Li, K, Na and Ba were doped onto the carbons post-activation in nitrate form. Assessments of the effects of metal presence on accessibility of the pore structure, surface chemistry, selectivity and CO_2 uptake of the resulting carbons were carried out. The presence of metal ions was found to reduce the accessibility of the pore structure, with this effect generally increasing with decreasing metal ion size. This reduction of accessible porosity reduced the adsorption sites available to CO_2, but the presence of metals was shown the increase the heterogeneity and selectivity of the carbon surface in favour of CO_2 adsorption. Selectivity

calculated using the IAST method under flue gas conditions reached 45.

The second study is an investigation of a novel carbonisation method, air-carbonisation. The aim of the study was threefold. Firstly, a method of conducting air-carbonisation of biomass was established. Secondly, a comprehensive comparison of the novel carbonisation method with traditional hydrothermal carbonisation was carried out. Finally, the effects of air-carbonisation on different wood types was analysed. The carbons produced via air-carbonisation exhibited excellent surface area and pore volume of up to 3159 m^2 g^{-1} and 1.82 cm^3 g^{-1}, respectively. The carbons also showed very high CO_2 uptake at low pressures of 0.15 bar and 1 bar, of 1.1 and 4.5 mmol g^{-1} respectively at 25 °C. Air-carbonisation was found to produce a char that was more resistant to the effects of KOH activation than traditional hydrochars. Wood type was found to have some effect on the char produced by air-carbonisation, due to varying composition of lignin, cellulose and hemi-cellulose.

The third study is an investigation into the use of $Ca(OH)_2$ as an alternative activating agent to commonly used, highly corrosive KOH. A series of samples was produced though $Ca(OH)_2$ activation of biomass. The pore structures produced

were found to be mainly mesoporous, with varying degrees of both micro and macroporosity. However, overall pore development was low, with surface area and pore volume reaching a maximum of 562 m^2 g^{-1} and 1.07 cm^3 g^{-1} respectively. This resulted in low CO_2 uptake, reaching a maximum of 2.3 mmol g^{-1} at 25 °C and 1 bar.

The final study was an investigation into the effects of harsh activation conditions. Potassium hydrogen phthalate was activated at temperatures of up to 1200 °C and for durations of up to 10 hrs. To overcome the low carbon yields expected from use of such conditions, a series of samples was activated with an additional carbon source of either airchar or hydrochar.

The harsh activating conditions produced a series of high surface area carbons with pore volume comprised of a mixed proportion of both meso and microporosity. The addition of a char during the activation process was shown to produce high yielding, highly microporous carbons that exhibit good CO_2 uptake up to 3.4 mmol g^{-1} at 25 °C and 1 bar. The char type added affected the textural properties of the carbons; adding hydrochar produced less developed, mesoporous carbons when compared with the addition of airchar.

Publications and Conferences

Publications

E. Hirst, A. Taylor and R. Mokaya, 'A simple flash carbonization route for conversion of biomass to porous carbons with high CO_2 storage capacity', *J. Mater. Chem. A.*, 2018, **6**, 12393-12403

Conferences

Poster – 'Metal Doped Porous Carbons for Gas Capture', A. Taylor and R. Mokaya, A Sustainable Future through New Materials for Chemistry, University of Nottingham, January 2017

Acknowledgements

If it takes a village to raise a girl, then it takes a small cathedral city to get that girl a PhD.

Firstly, I would like to thank Professor Robert Mokaya for his guidance and supervision over the last 4 years. By allowing me to work independently, I have grown both as a scientist and as a person. I would also like to thank the extended Mokaya research group for all their help and cooperation throughout this project. Thank you in particular to Helena Matabosch Coromina, Jonathan Welsh, Edward Hirst and Rose McCarthy.

I would like to thank the staff of the NMRC and the technical staff of the School of Chemistry, especially Mark Guyler and Neil Barnes for helping to fix everything I break.

Thank you to Fiona Norten and Neelam Mughal for both their SEM expertise and their friendship and support over the years. Thank you to Katie Reynolds, who has been there for all of the high-points and low-points of the last 6+ years. Thank you also to Max, Dave, Glen, Pritesh, Jasper, Ivy and Helen. Thank you to Rowena for her spiritual mentoring.

A very special thank you to Abdul Salam Al-Jumialy. I can say with confidence that I wouldn't have made it to the end of this

PhD without his help. I am very grateful for his support and understanding, which has been imperative and endless.

My biggest thanks are for my mum and dad and Lewis. Thank you to my mum and dad for their love, encouragement, cake, proof-reading and doubtless belief. Thank you to Lewis for putting up with me, looking after me and being absolutely everything.

Acronyms

BET – Brunauer, Emmett and Teller

CCS – Carbon Capture and Storage

EDX – Energy Dispersive X-Ray

EOR – Enhanced Oil Recovery

GHG – Greenhouse Gas

IAST – Ideal Adsorbed Solution Theory

IUPAC – International Union of Pure and Applied Chemistry

MOFs – Metal Organic Frameworks

NLDFT – Non-Local Density Functional Theory

PSA – Pressure Swing Adsorption

PSD – Pore Size Distribution

PXRD – Powder X-Ray Diffraction

SE – Secondary Electron

SEM – Scanning Electron Microscopy

TGA – Thermal Gravimetric Analysis

TSA – Temperature Swing Adsorption

VSA – Vacuum Swing Adsorption

Definitions

Å = $1x10^{-10}$ m

Micropore: pore of width < 20 Å

Mesopore: pore of width 20 – 500 Å

Macropore: pore of width > 500 Å

Absorption: the process by which molecules enter the bulk volume of another material

Absorbent: the substance entering the bulk volume of another material

Absorbate: the bulk material into which another substance enters

Adsorption: the process by which molecules adhere onto a solid surface through chemical or physical bonds

Adsorbent: the material onto which a substance is adsorbs

Adsorbate: the substance being adsorbed onto a surface

Chemisorption: a contraction of the term 'chemical adsorption', refers to adsorption onto a surface that takes place through the formation of new chemical bonds. The adsorbent and the adsorbate are chemically changed during the process

Physisorption: a contraction of the term 'physical adsorption', refers to adsorption onto a surface that takes place only through electrostatic interactions. Both the adsorbent and the adsorbate remain unchanged throughout the process

Table of Contents

Chapter 1 – Introduction

1. 1. Motivation 1

1. 1. 1. Climate Change 1

1. 1. 2. Carbon Capture and Storage 5

1. 2. Current State of Carbon Capture Research 8

1. 2. 1. Current Commercial Technologies 10

1. 3. Swing Adsorption for CCS 13

1. 4. Sorption Theory 17

1. 4. 1. Physisorption 19

1. 4. 2. Pore Classifications 21

1. 4. 3. Pore Filling Mechanisms 25

1. 4. 4. Sorption Isotherms 27

1. 4. 5. Isotherm Classifications 31

1. 4. 6. Hysteresis Classifications 35

1. 4. 7. Calculating Porosity Values 38

1. 5. Porous Materials for Gas Adsorption 42

1. 5. 1. Metal Organic Frameworks 42

1. 5. 2. Zeolites 44

1. 5. 3. Porous Carbons 45

1. 6. References 55

Chapter 2 – Characterisation Techniques

2. 1. CHN Elemental Microanalysis 73

2. 2. Thermal Gravimetric Analysis 74

2. 3. Scanning Electron Microscopy 75

2. 4. Powder X-Ray Diffraction 77

2. 5. Gas Sorption Analysis 79

2. 6. CO_2 Uptake 80

2. 7. Gas Selectivity Calculations 82

2. 8. References 84

Chapter 3 – The Effects of Metal Doping on the Properties of Organic-salt-derived Porous Carbons

3. 1. Abstract 87

3. 2. Introduction 89

3. 3. Materials Synthesis 99

3. 4. Results and Discussion 102

3. 4. 1. Elemental Analysis 102

3. 4. 2. Scanning Electron Microscopy and Energy Dispersive X-Ray Spectroscopy Analysis 104

3. 4. 3. Thermal Gravimetric Analysis 112

3. 4. 4. Powder X-Ray Diffraction Patterns 116

3. 4. 5. Nitrogen Sorption Isotherms 123

3. 4. 6. Textual Properties; Surface Area and Pore Volume 126

3. 4. 7. Textural Properties; Pore Size Distributions 130

3. 4. 8. CO_2 Uptake Analysis 134

3. 4. 9. Selectivity Measurements 140

3. 5. Conclusions 144

3. 6. Future Work 147

3. 7. References 148

3. 8. Appendix 152

Chapter 4 – Pre-Activation Treatment of Biomass Derived Porous Carbons

4. 1. Abstract 155

4. 2. Introduction 156

4. 3. Materials Synthesis 167

4. 4. Results and Discussion 172

4. 4. 1. Elemental Analysis and Yield 172

4. 4. 2. Scanning Electron Microscopy 179

4. 4. 3. Thermal Gravimetric Analysis 182

4. 4. 4. Powder X-Ray Diffraction Patterns 192

4. 4. 5. Nitrogen Sorption Isotherms 200

4. 4. 6. Textural Properties; Surface Area and Pore Volume 209

4. 4. 7. Textural Properties; Pore Size Distributions 223

4. 4. 8. CO_2 Uptake Analysis 234

4. 5. Conclusions 251

4. 6. Future Work 254

4. 7. References 255

4. 8. Appendix 261

Chapter 5 – An Alternative Activating Agent in the Synthesis of Activated Carbons

5. 1. Abstract 263

5. 2. Introduction 264

5. 3. Materials Synthesis 271

5. 4. Results and Discussion 274

5. 4. 1. Elemental Analysis and Carbon Yield 274

5. 4. 2. Scanning Electron Microscopy 278

5. 4. 3. Thermal Gravimetric Analysis 280

5. 4. 4. Powder X-Ray Diffraction Patterns 284

5. 4. 5. Nitrogen Sorption Isotherms 289

5. 4. 6. Textual Properties; Surface Area and Pore Volume 293

5. 4. 7. Textural Properties; Pore Size Distributions 298

5. 4. 8. CO_2 Uptake Analysis 305

5. 4. 9. Selectivity Measurements 313

5. 5. Conclusions 316

5. 6. Future Work 319

5. 7. References 320

5. 8. Appendix 325

Chapter 6 – Investigating the Effects of Harsh Activation Conditions

6. 1. Abstract 329

6. 2. Introduction 331

6. 3. Materials Synthesis 337

6. 4. Results and Discussion 341

6. 4. 1. Elemental Analysis and Carbon Yield 341

6. 4. 2. Scanning Electron Microscopy 348

6. 4. 3. Thermal Gravimetric Analysis 351

6. 4. 4. Powder X-Ray Diffraction Patterns 357

6. 4. 5. Nitrogen Sorption Isotherms 363

6. 4. 6. Textual Properties; Surface Area and Pore Volume 369

6. 4. 7. Textural Properties; Pore Size Distributions 375

6. 4. 8. CO_2 Uptake Analysis 382

6. 5. Conclusions 397

6. 6. Future Work 402

6. 7. References 403

Chapter 7 – Overall Conclusions 407

Chapter 1 - Introduction

1. 1. Motivation

1. 1. 1. Climate Change

Climate change is one of the biggest challenges currently facing our planet. It is a worldwide problem that affects populations and ecosystems; threatening habitats, food supply and ultimately, lives. The link between global atmospheric warming, and the increase in so-called 'greenhouse gases' present in the lower atmosphere is well established, and has been accepted by the majority of researchers for more than 4 decades.[1–4] Greenhouse gases (GHGs) are defined as gases which absorb and emit thermal energy within the infrared range, notably H_2O, CO_2, N_2O and CH_4.[5] The increased presence of such gases in recent decades is changing the natural climate through the process of radiative forcing, as a greater amount of thermal energy is re-radiated back to the earth's surface.[4,6] This is known as the 'enhanced greenhouse effect'. The overall effect of this is a gradual rise in global surface temperatures.[4]

CO_2 is a major contributor to the enhanced greenhouse effect. The relative effect of an individual GHG on atmospheric change is assessed using its Global Warming Potentials (GWP), based on the amount of thermal energy a molecule can absorb within

its average atmospheric lifetime and the abundance of that gas within the atmosphere.[7,8] Despite having a considerably lower GWP value than other GHGs, such as CH_4 and N_2O, CO_2 is substantially more abundant in the atmosphere, reaching 390,500 ppb in 2011, compared with 1,803 and 324 ppb for CH_4 and N_2O respectively.[9] Atmospheric CO_2 has increased to this level since the beginning of the industrial revolution in the 18th century when it was 278,000 ppb.[9]

It is well accepted that this unprecedented rise in atmospheric CO_2 concentrations within such a short timescale can be attributed to the increase in anthropogenic CO_2 sources resulting from the advances in science and technology since the industrial revolution.[2–4,10] Today, the main contributors of anthropogenic CO_2 emissions are fossil-fuel based power generation, transport, industrial processes and chemical production.[11] CO_2 emissions from the energy sector reached an historic high of 32.5 Gt in 2017, with emissions from the burning of fossil fuels and industrial processes accounting for 65% of global anthropogenic CO_2 emissions, and approximately 78% of global GHG emissions.[12,13] To address climate change, there needs to be a drastic reduction in the amount of anthropogenic CO_2 being released into the atmosphere, particularly from the burning of fossil fuels.

Despite some individuals branding anthropogenically enhanced climate change as a 'myth', the majority of nations are tackling the problem through a series of landmark agreements; from the 1992 United Nations Framework Convention on Climate Change, the 1997 Kyoto Protocol, and more recently the 2015 Paris Agreement, drafted at the 21st Conference of the Parties (COP21). Currently, 195 countries have signed the agreement, committing to working to keep the global average increase in temperatures to well below 2 °C, compared with pre-industrial times.

A necessary part of the solution to climate change is to become entirely reliant on renewable sources of energy production; primarily solar, wind, hydro and biomass-based processes. However, although imperative, it is likely that this hugely significant step towards the stabilisation of atmospheric CO_2 levels will take decades to achieve. The most optimistic studies estimate that complete reliance on renewable energy could be achieved by 2050[14,15]; however, the Intergovernmental Panel on Climate Change (IPCC) issued a special report in October 2018, stating that in order to avoid highly damaging changes to the climate, drastic action to reduce CO_2 emissions must be taken within the next 12 years.[16]

Unfortunately, there are numerous barriers to overcome in order to achieve complete reliance on renewable energy. Currently, there are many industrial processes which have no viable 'green' alternatives; the chemical and cement industries currently account for over 5.5% and 5% of global anthropogenic CO_2 emissions respectively.[17–19] The scale of new infrastructure and capital investment needed to build a network of renewable energy sources is currently unfeasible for the majority of nations; therefore simply 'turning off' fossil fuel-based power supplies is not an option. In addition, several world leaders and global corporations are still supporting the burning of fossil fuels; in June 2017, the President of the USA announced he would withdraw the U.S.A. from the Paris Agreement, while oil companies such ExxonMobil have historically misled the public about the science of climate change.[20] In short, a future completely reliant on renewable energy, alongside a reduction in industrial CO_2 emissions is a long-term ambition. Therefore, a short-term solution must be implemented.

1. 1. 2. Carbon Capture and Storage

Carbon capture and storage (CCS) is a more closely attainable solution to climate change, as it allows for fossil fuels to be burned and industrial processes to continue, without the release of CO_2 emissions into the atmosphere.

CCS is the process of using various technologies to capture CO_2 emissions from, for example, power generation and industrial processes, and its transportation and storage, commonly in underground geological formations.

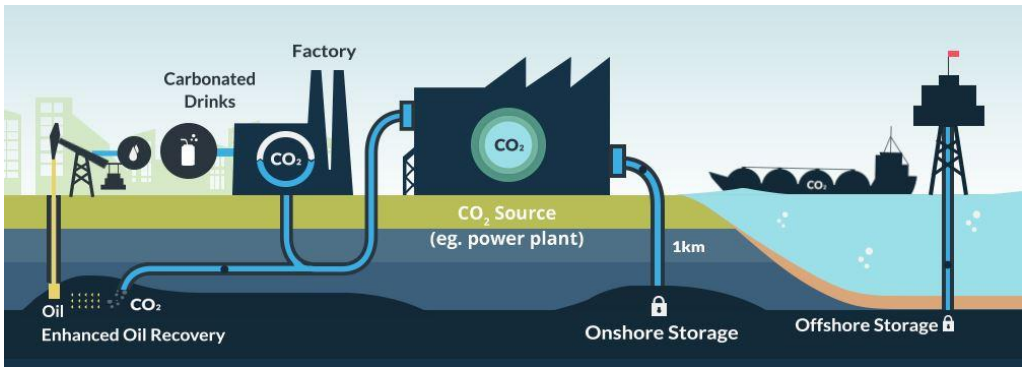

Figure 1.1. Representation of the CCs process[21]

As well as preventing CO_2 from entering the atmosphere, CCS is a 'carbon-negative' solution when used with biomass-based processes, facilitating the removal of CO_2 from the atmosphere. Crucially, CCS offers a way of limiting climate change while keeping up with a growing global energy demand. With widespread utilisation, it has been predicted that CCS

technology could account for up to 12% of CO_2 emissions reduction by 2050, compared with a 'do nothing' approach.[22] In many cases, CCS technology can be retro-fitted to existing plants; a lower and easier investment than constructing new networks of renewable sources.

Worldwide, there are many different carbon capture technologies being researched and developed, with a few making it into the trialling and commercial stages. The Global CCS Institute currently identifies 18 'large-scale' CCS facilities across the globe, where CO_2 is being captured in various ways across a range of industries, as well as many projects in planning and development.[23] Currently, the largest operating post-combustion CCS system is the Petra Nova Carbon Capture facility, at WA Parish power station in Texas, U.S.A.[23,24] An amine scrubbing process is used to capture 90% of the plant's CO_2 emissions (5000 t per day), which is then pumped through an 80 mile pipeline to be used for CO_2-enhanced oil recovery (CO_2-EOR). CO_2-EOR is the process whereby CO_2 is injected into and stored in oil reservoirs, simultaneously increasing the amount of oil that is extracted from the reservoir, and providing a long-term storage solution for captured CO_2.[25,26] The Petra Nova Carbon Capture system's contribution to CO_2-EOR

increased local oil recovery by 1300%, providing both environmental and economic benefits.[27]

In 2014, the Boundary Dam Carbon Capture project in Saskatchewan, Canada was the first power station in the world to successfully implement retro-fitted CCS technology.[28] An amine scrubbing process is used to capture 90% of CO_2 emissions from the coal power station, which is then pumped to the Weyburn Oil unit for CO_2-EOR; one of the largest geological CO_2 storage projects in the world.[29,30] Despite several functional and financial problems, the project acts as one of the first and largest demonstrations of commercial CCS technology.

The UK is trailing behind many other developed countries in terms of CCS, with no current operating carbon capture projects. In 2015, the UK government withdrew a £1 billion fund for investment in a new CCS project, arguing that the money was better invested elsewhere.[31,32] It is clear that, although it has been agreed that implementing wide-scale CCS is a necessary step towards tackling climate change, extensive research and development is required to make the technology more efficient and financially viable, and thereby, a more appealing investment for private companies and governments alike.

1. 2. Current State of Carbon Capture Research

Research into carbon capture spans a wide range of different technologies. There is not a 'one size fits all' solution to carbon capture; a variety of approaches to suit individual industries is required. The various existing technologies can be broadly categorised into three different groups, with some crossover: oxy-fuel combustion, pre-combustion and post-combustion processes.[33–37] Using the example of a fossil-fuel based power station, oxy-fuel combustion systems involve burning the fuel in pure oxygen to produce a flue stream rich in CO_2 (80-98%) and absent of nitrous compounds. This removes the need for any sort of separation technology, but the cost of purifying oxygen is high, both financially and environmentally.[33,36] A pre-combustion process involves gasification of the fuel with steam and oxygen, creating a mixture of H_2 and CO known as 'syngas'. A further reaction with steam converts CO into CO_2, which is then separated from the gas mixture.[33–35,38] Post-combustion capture is based on separating CO_2 from a flue gas stream, after combustion of the fuel.[33–36] Pre- and post-combustion capture both utilise technologies that separate and capture CO_2 from a mixed gas stream. However, post-combustion capture is the only one of these three methods which can be applied to both fossil-fuel based power stations, and a range of industrial

processes such as cement or chemical production, due to its position as the final step in the processing chain.

Post-combustion capture methods are often preferred, as they can usually be retro-fitted to existing plants.[37] Such technologies are commonly in the form of liquid absorbents, solid adsorbents and membranes, with each solution in different stages of the research and development process.

1. 2. 1. Current Commercial Technologies

Two CO_2 capture technologies that are commercially available are liquid amine solvents and separation membranes. Absorbing CO_2 emissions using liquid amine solvents is perhaps the most popular and most established choice of capture technology, with large industrial trials and commercial demonstrations at plants worldwide.[23] The absorption with aqueous amines, also known as 'amine scrubbing' commonly uses alkanolamines to absorb CO_2 from a flue stream. The 'rich' amine solution is then heated to strip it of absorbed CO_2, which is in turn condensed.[39] Chemical absorbents have been shown to have a higher absorption capacity at low CO_2 partial pressure than solid absorbents, with amine scrubbers showing up to 99% CO_2 capture efficiency.[39–41] The common choice of amine solvent is monoethanolamine (MEA), due to its high reactivity with CO_2 and relatively low cost and easy regenerability.[40,42,43]

Despite its leading role in the development of CCS, amine scrubbing has many disadvantages. The amines used succumb easily to both oxidative and thermal degradation, whereby the amines are fragmented into smaller amides, or form amine chains respectively. This, combined with emission loss due to their high volatility, results in a short working lifetime.[43,44] The corrosive nature of the amines used reduces the lifetime of

plant equipment, further adding to costs.[45] Current research focuses on developing alternative, more advantageous amine solvents, with lower corrosivity and degradation rates, as well as lower regeneration costs. Diethanolamine (DEA) is a well-researched alternative, as is methyldiethanolamine (MDEA) and 2-amino-2-methyl-1-propanol (AMP). However, each alternative comes with its own associated disadvantages, and more research is needed to develop the 'ideal' amine solvent.[40,43] The largest obstacle to widespread utilisation of amine solvents for carbon capture is the energy cost of solvent regeneration. The heat needed to strip CO_2 from the rich amine stream can reduce a fossil fuel-based power station's efficiency from 40% to 30%, dramatically raising the cost of employing carbon capture.[41,45–47]

The use of separation membranes for post-combustion CO_2 capture has become a competitive substitute for chemical absorption.[48] The technology is based on the differing rates of permeation of individual gas components through a thin membrane.[49,50] Materials for gas separation membranes can be broadly split into two categories: inorganic (ceramic) and organic (polymer) membranes. Inorganic membranes tend to show higher selectivity but low permeability. Additionally, poor mechanical strength means large membrane sheets are difficult

to produce. Organic membranes generally exhibit higher permeability and mechanical strength, however they can offer lower selectivity rates.[49] The main focus of membrane research is to address the compromise of selectivity versus permeability.[49–52]

Although the use of separation membranes is relatively cheap, and has a much lower environmental impact than amine absorbers, there are several other practical drawbacks.[48,51] The low concentration of CO_2 in most flue streams means that high power is needed to create a pressure gradient across the membrane. The resulting CO_2 stream is of low purity and therefore not suitable for commercial resale. Typically, membrane materials cannot withstand the high temperatures and chemical impurities often found in flue streams.[53]

Neither of these two post-combustion CO_2 capture technologies offer any distinct advantages in terms of efficiency, cost or energy consumption over the other.[48] Research must focus on developing technologies that surpass the current options; the use of swing adsorption combined with solid sorbents for post-combustion CO_2 uptake is proving to be a very promising field of research.

1. 3. Swing Adsorption for CCS

Swing Adsorption is a post-combustion CO_2 capture technology that has sparked much interest in recent years. It covers a variety of processes, primarily pressure/vacuum swing adsorption (PSA/VSA), and temperature swing adsorption (TSA). Swing adsorption is used in combination with various solid sorbent materials, which selectively adsorb CO_2 onto the material surface from a mixed gas flue stream. Adsorption takes place under certain pressure or temperature conditions; desorption, and so sorbent regeneration occurs when these conditions are changed.[47,54–59]

In a PSA process, adsorption takes place above atmospheric pressure. Desorption, and so regeneration, then occurs when the pressure is lowered. In a VSA process, adsorption generally takes place at atmospheric pressure, and regeneration occurs when the pressure is lowered to vacuum. In a TSA process, sorption takes place at atmospheric pressure; elevated temperature is used for sorbent regeneration.[47,57–59] Pressure dependent swing adsorption processes are considered more desirable than TSA, as they offer a simpler process and work over a wide range of pressures and temperatures. Crucially, this process can be used at the high temperatures typical of flue gases, and a cooling stage of the gas stream is not required. Of

the two processes, PSA and VSA, the latter is considered less energy intensive, as less energy is required to take a system to vacuum than to compress the large quantities of gasses being processed.[47,57,58]

The use of swing adsorption combined with solid sorbents has many benefits. As opposed to popular liquid amines, which capture CO_2 through chemisorption, adsorption of CO_2 on to a solid material surface generally takes places through physisorption. Whereas chemisorption involves the creation of new strong chemical bonds, physisorption only occurs through weak electrostatic interactions. This results in fast CO_2 adsorption/desorption kinetics. Additionally, release of the captured CO_2 and so the regeneration of the sorbent requires much lower energy input than conventional chemical absorption techniques. Solid sorbents should remain unchanged throughout the swing adsorption process, extending their industrial lifetime compared to alternative technologies. Overall, using solid sorbents for CO_2 capture is significantly cheaper than current chemical absorbents.[54,57,60]

Solid sorbents for CCS are materials that selectively adsorb CO_2 from a mixed gas flue stream onto the material surface, offering the advantage of being able to absorb and store CO_2 at a higher concentration than capturing the gas at standard temperature

and pressure (STP). Adsorption onto solid sorbents is generally more environmentally friendly than chemical absorption techniques; as capture takes place through physisorption, no chemical reactions take place on the material surface which could lead to hazardous by-products. Solid sorbents can be cheap and simple to produce, and covers a broad range of materials with many different applications. Solid sorbent materials exhibit optimum performance under different swing adsorption processes, therefore the choice between PSA, VSA, or TSA should be made based on the material used.[57]

Swing adsorption with solid sorbent carbon capture has the benefit of being easily retro-fitted to existing plants.[47] Maintenance is often also more straightforward as it does not require halting of the plant operation.[57] Compared to current commercial carbon capture technologies, swing adsorption with solid sorbents is simpler and has lower energy requirements.

Research into the use of solid sorbents for CCS covers a variety of different materials, each with potential advantages over the current commercial options. Promising and well-developed solid sorbent materials include metal organic frameworks (MOFs), zeolites, zeolitic imidazolate frameworks (ZIFs), porous silicas and carbon materials.

A solid sorbent for the use of swing adsorption CO_2 capture in an industrial setting, such as a coal-fired power station, should meet particular criteria. The material should have a strong selectivity for CO_2, particularly over N_2, which is the main constituent of most flue streams. It should have a reasonable CO_2 affinity and a high loading capacity. The sorbent needs to be thermally and chemically stable, in order to withstand the high temperatures and moisture levels often found in flue streams, as well as the presence of chemical contaminants such as acids and heavy metals.[55,56] It should exhibit fast sorption kinetics and readily release CO_2 after adsorption for easy sorbent regeneration. The material needs to maintain its high performance over many cycles, to give high recyclability and a long industrial lifetime. Finally, the material should be cheap and simple to produce, in order to be commercially viable.[55,56]

The biggest challenge facing the development of new solid sorbents for CO_2 capture, is overcoming the low selectivity exhibited by many solid materials. Chemical absorption, achieves high selectivity as a chemical reaction is taking place. Physisorption has the benefit of easy regeneration, but tends to lead to lower selectivity for CO_2.[57] In order to overcome these challenges and develop more effective and efficient materials

for solid sorbent CO_2 capture, the process of physisorption of CO_2 onto a material surface must be understood.

1. 4. Sorption Theory

In the case of a gas/solid system, adsorption is defined as the enrichment of molecules, atoms or ions which takes place in the vicinity of the solid surface and outside the solid structure.[61] The adsorption of gases onto solid materials is a concept that has been investigated for many centuries, but comprehensive understanding of the adsorption process has only developed over last few decades. During this time, adsorption of gases onto a solid surface has been utilised not only in the field of carbon capture, but also for uses such as heterogeneous catalysis,[62] adsorption chillers,[63] air purification,[64] gas separation[65] and hydrogen storage.[66–68]

References to the investigation of adsorbance can be found as early as ~1500 BC in the medical text of the Ebers Papyrus and adsorption experiments recorded in the Bible.[69–72] However, the first recorded systematic investigation into the phenomenon of adsorption was conducted by Scheele in 1773. He observed the desorption and adsorption of gases during heating and cooling of a charcoal sample. [69,70,72,73] Berzelius stated in 1836 that highly porous materials were the best adsorbents.[73] Chappuis

and Kayser in 1881 discovered that increasing the surface area of a sorbent material, increased its adsorption capacity.[73] Kayser introduced the term 'adsorption' and concluded that it was a surface phenomenon. He indicated that there should be a distinction between *ad*sorption and *ab*sorption. Chappuis and Kayser were also among the first researchers to measure adsorption isotherms.[69,70,72,73]

Langmuir built on previous work and in 1918 devised a model for monolayer adsorption that became the basis for modern day adsorption theory.[74] The Langmuir theory relies on a series of assumptions; the adsorbent has a fixed number of energetically equivalent adsorption sites, and localised adsorption takes place either chemically or physically. The adsorptive behaves as a perfect gas, therefore interactions between gas molecules are not considered.[72,74] During the 1930's, Brunauer, Emmett and Teller (BET) developed Langmuir's ideal localised monolayer model to include multilayer adsorption.[75] BET theory assumes that the Langmuir model applies to each adsorption layer on an energetically homogenous surface.[72,75] Later, Brunauer, along with Demming, Demming and Teller further extended BET theory to include capillary condensation, the phenomenon of a gas adsorptive condensing to a liquid-like phase within a pore structure, at a pressure lower than the bulk liquid saturation

pressure.[61,76] Classifications of 5 different types of adsorption isotherm were laid out, which were later adapted into the classifications defined by the IUPAC today.[61]

BET theory provides an explanation for the monolayer, multilayer and capillary condensation sections of the adsorption isotherm. However, it cannot adequately describe capillary condensation in a material with various capillary widths, and cannot account for adsorption taking place above the critical temperature of the adsorptive.[72,75] Despite these limitations, BET theory is still regarded as the accepted method of measuring the surface area and volume of powders and porous materials.[61]

1. 4. 1. Physisorption

Adsorption is defined as the enrichment of molecules in the vicinity of an interface. In a gas/solid system, adhesion takes place in the vicinity of the solid surface and on the outside of the solid surface.[61] In a solid porous material, adsorbance takes place within the internal pore structure and on the outer particle surface. Adsorption differs from absorption; adsorption describes the interaction when a molecule comes into contact with a surface, whereas absorption defines an absorptive

infiltrating the material surface and entering the bulk material.[61]

Adsorption can occur either chemically (chemisorption) or physically (physisorption). Chemisorption refers to adsorption onto a surface that takes place through the formation of new chemical bonds. Both the adsorptive and the adsorbent are chemically changed through the process. Physisorption refers to adsorption onto a surface that takes place through intermolecular forces. Both the adsorptive and the adsorbent remain unchanged, and the process is readily reversible.[61]

The types of intermolecular forces involved in physisorption depend on the polarity of both the adsorbent and adsorbate, but include short-range repulsive forces and long-range attractive forces, including dispersion forces, hydrogen bonding, dipole-dipole and dipole-induced dipole interactions. The strength of the interaction between adsorbent and physisorbed adsorbate depends on the materials and molecules involved.[77]

1. 4. 2. Pore Classifications

A porous material is defined as a material containing an interconnected pore system, whereby the pores are deeper than they are wide.[78] Pores are voids within the matrix of the material that can contain a fluid. Pores are categorised by size, shape and type. The IUPAC defines pore size classifications according to:[61]

Micropores: pores of width < 20 Å

Mesopores: pores of width 20 – 500 Å

Macropores: pores of width > 500 Å

The category of micropores can be further divided into:[61]

Supermicropores: micropores > 7 Å

Ultramicropores: micropores < 7 Å

These classifications are based on the differences in adsorption behaviour of a fluid in pores of different sizes. The maximum width of an ultramicropore is defined by the width of a double layer of nitrogen molecules adsorbed onto a micropore surface

(2 x 3.54 Å).[79] Pores can also be classified by their shape. In reality, few materials show uniform porosity where all pores are of the same size and shape. Therefore, adsorption calculations are based on four 'ideal pore shapes' defined by Kaneko and adapted by the IUPAC (Fig. 1.1); cylindrical, funnel, slit-shaped and ink-bottle.[78,80–82]

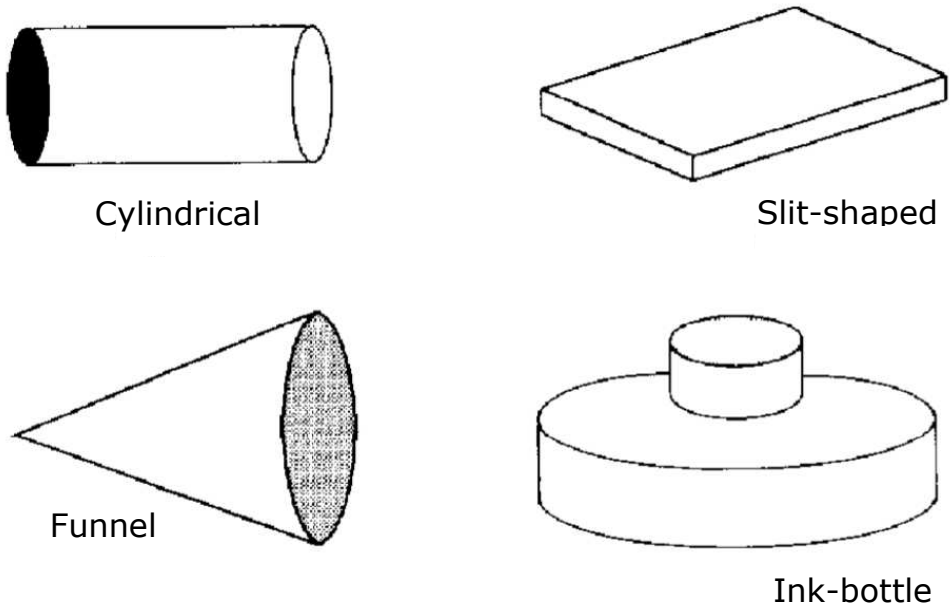

Figure 1.2. Pore shape classifications[78,81]

Some materials characteristically show certain pore shapes. Alumina oxides often show cylindrical pores, while activated carbons typically have slit-shaped pore structures.[82]

Pores can also be classified by their accessibility. Pores accessible from the external particle surface are 'open' pores. An 'open' pore that is open at both ends is labelled a 'through' pore, while an 'open' pore that is closed at one end is known as a 'blind' pore. Pores that are not accessible from the external

particle surface are ‘closed’ pores. Closed pores can form when insufficient heating causes a pore’s opening to collapse, blocking access. A pore can also be designated ‘chemically closed’; the pore is open to the external surface, but has an opening of width smaller than that of the adsorbing molecule used for analysis. Therefore, although the pore is open, it cannot be analysed and does not contribute to overall surface area and porosity.

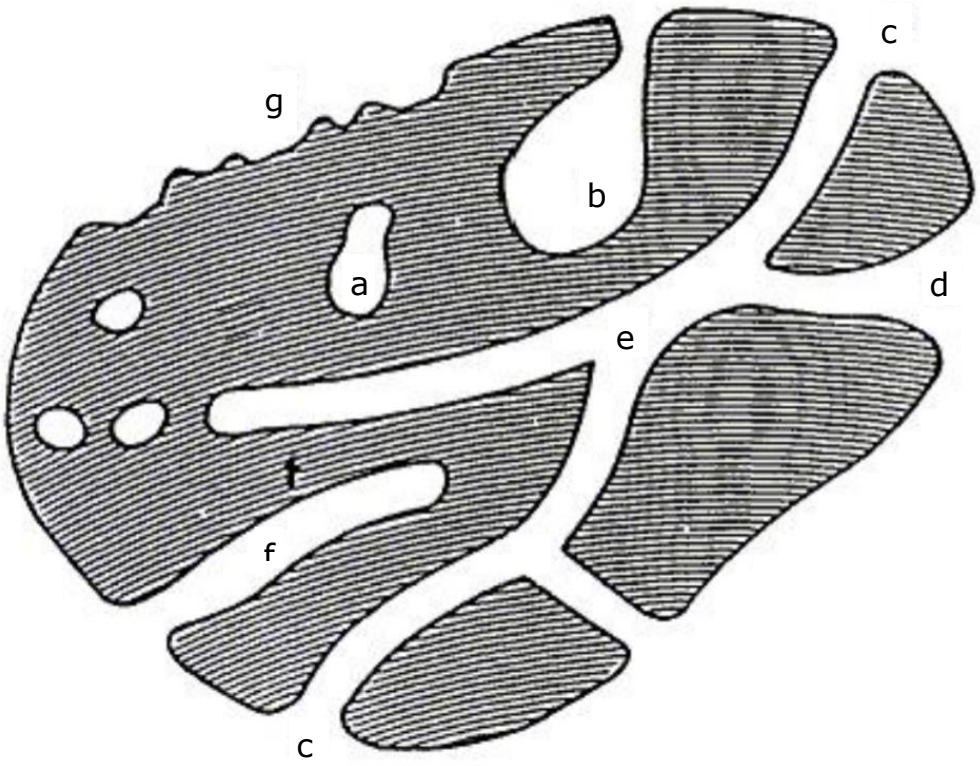

Figure 1.3. Pore Type Classifications. (a) closed (b) blind, ink-bottle (c) through, cylindrical (d) through, funnel (e) blind, cylindrical (f) blind, cylindrical (g) external pores[78,82]

However, 'closed' pores still contribute to the material's macroscopic properties such as bulk density and mechanical strength. The rough external surface of a particle is considered porous if its irregularities are deeper than they are wide.[78,82,83] Figure 1.2 shows examples of pores of differing shapes and accessibility.

Porous materials show either 'uniform porosity', whereby all the pores of the material are of the same shape and dimension, or 'hierarchical porosity'. A hierarchically porous material contains a pore structure comprising pores of differing dimensions. Different materials characteristically show particular porous structures, which can be altered depending on the synthesis conditions used. MOFs and zeolites can show uniform porosity, where pore size and shape is mostly controlled by the structure of the material.[84–86] Activated carbons typically display a non-uniform, hierarchical pore structure, which can be controlled by the synthesis conditions and materials used.[87–92]

The wide variety of porous materials available, each with their own unique porous properties and structures, results in porous materials playing an important role not only in adsorption, but also in fields such as purification, electrode synthesis, catalysis, medicine and superconductors.[84,88,93–98]

1. 4. 3. Pore Filling Mechanisms

Understanding the mechanism of how porous structures fill with an adsorbing gas is important when analysing and developing porous materials. The process of pore filling can be described by four main phenomena: micropore filling, monolayer adsorption, multilayer adsorption and capillary condensation.

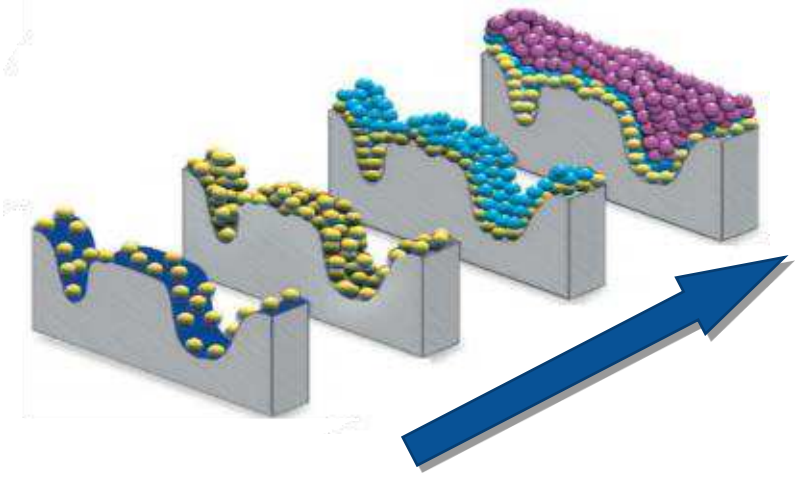

Figure 1.4. Representation of the pore filling process[99]

In a system at vacuum, micropore filling takes place initially as an adsorptive is introduced. Adsorbent-adsorbate interaction is strongest in micropores, as adsorbing molecules are surrounded by stabilising intermolecular forces from all pore walls. In narrower pores, the adsorption potentials of opposite walls may overlap. As a result, isosteric heat of adsorption is generally highest in micropores and micropore filling completes at very low pressure.[61,100–102]

As pressure in the system increases, mesopores begin to fill. Monolayer adsorption occurs first. All adsorbed molecules are in contact with the adsorbent surface. Once monolayer adsorption is complete, all accessible micropores are full. With a further increase in pressure of the system, multilayer adsorption begins to occur in the mesopores. Here, the adsorption layer contains more than one layer of adsorbed molecules, and not all adsorbed molecules are in contact with the adsorbent surface. Adsorption interaction energies for the additional layers are low as adsorbing molecules are increasingly further away from the adsorbent surface; therefore, multilayer adsorption only occurs at higher relative pressure.[61,100] Co-operative adsorption aids multilayer adsorption: monolayer adsorption reduces the remaining space in small mesopores, causing them to behave as smaller micropores. This provides a more stabilising environment for incoming molecules, therefore encouraging further adsorption.[103]

Capillary condensation occurs at higher relative pressure (P/P_0 > ~ 0.2) and is the phenomenon of gas condensing into a 'liquid-like' phase within the mesopores, at a pressure (P) below the saturation pressure of the bulk liquid (P_0). The condensed fluid fills residual space within the mesopores once multilayer

adsorption has completed as a result of increased van der Waals forces in the confined pore.[61]

Generally, when studying gas adsorption in a hierarchical pore structure, isosteric heat of adsorption decreases as gas uptake increases. Adsorption sites with strong binding energies (small micropores) fill at very low pressures, with less favourable sites not filling until the system is at higher relative pressure.[100–102]

Gas adsorption occurs efficiently in hierarchical pore structures. The presence of micropores encourages high uptake at low pressures, while mesopores provide good channel connectivity, allowing for quick diffusion of gas through the pore structure. Macropores enable quick diffusion of adsorptive molecules from outside the particle into the internal pore structure.[103]

1. 4. 4. Sorption Isotherms

The analysis of gas adsorption onto a material is conducted by measuring a sorption isotherm. A sorption isotherm plots adsorption and desorption measurements over varying pressure at a constant temperature and describes the relationship between the amount of gas adsorbed onto the material, and the equilibrium pressure of the gas. The shape of both the adsorption and the desorption curve provide information about a material's porous structure. Data points

from the isotherm can be analysed with various equations to calculate information such as surface area, pore volume and pore size distribution of the material.

Physisorption can be measured either gravimetrically or volumetrically. Gravimetric analysis measures weight changes of an adsorbent sample as an adsorbing gas is introduced. Volumetric analysis measures pressure changes of an adsorbing gas as it is introduced to an adsorbent sample within a known volume.[61] Physisorption for the purpose of measuring textural properties of a porous structure is usually done volumetrically.

The sorption isotherm is presented as quantity of gas adsorbed (standardly reported in $cm^3\ g^{-1}$ or $mol\ g^{-1}$) vs pressure. When the measurement is carried out at a temperature below the critical temperature of the adsorbing gas, pressure is reported as relative pressure (P/P_0). This describes the relationship between the equilibrium pressure of each data point (P) and the saturation vapour pressure of the adsorbing gas (P_0) at the analysis temperature.[61]

The simplest sorption isotherm is the Langmuir isotherm, originally developed to describe the adsorption of a gas onto activated carbon. The Langmuir isotherm is based on the Langmuir equation (eqn. 1.1):[74,104]

$$\theta_A = \frac{N_s}{N_{tot}} = \frac{K_{eq}P_A}{1+K_{eq}P_A} \qquad \textbf{Eqn. 1.1}$$

where θ_A is the fractional occupancy of adsorption sites, N_s is the areal density of adsorbed molecules, N_{tot} is the total number of available adsorption sites, K_{eq} is an equilibrium constant representing the distribution of adsorbate between the surface and the gas phase and P_A is the partial pressure of the adsorptive gas.[104]

The Langmuir equation only works at low pressures; at low pressure:

$$1+K_{eq}P_A \approx 1$$

Therefore:

$$\theta_A = K_{eq}P_A$$

However, at high pressure:

$$1+K_{eq}P_A \approx K_{eq}P_A$$

Therefore:

$$\theta_A = 1$$

As previously mentioned, the Langmuir isotherm is based on the assumptions that: the adsorption only takes place on a finite

number of fixed, energetically equivalent sites across the adsorbent surface; the adsorptive acts as an ideal gas, with no lateral interactions or steric hindrance between adsorbed molecules; and that the adsorption layer is only one molecule thick, so only a monolayer forms.[72,74,105]

The resulting isotherm depicts adsorption occurring linearly with increasing pressure up to equilibrium saturation point, after which the isotherm plateaus. At the equilibrium saturation point, every adsorption site is full and the monolayer is assumed to be complete. According to the Langmuir assumptions, no further adsorption can take place beyond this point.[105]

The BET equation allows for multilayer adsorption, by applying the Langmuir equation to each adsorption layer after the monolayer. Therefore, the BET equation can account for the monolayer, multilayer and capillary condensation sections of the adsorption process. BET theory uses the equilibrium saturation point described by Langmuir, defined as 'point-b', to calculate the surface area of a sample from the monolayer coverage.[72,75,76]

1. 4. 5. Isotherm Classifications

The development of BET theory led to the IUPAC defining 6 classifications of sorption isotherms in 1985.[106] Over the following 30 years, further research into pore structures led to the IUPAC redefining the classifications into 8 isotherm types (Fig. 1.3).[61]

The shape and classification of an isotherm can be used to determine the characteristics of a porous material and the process by which it adsorbs a fluid.

Type I isotherms indicate a microporous solid with relatively small external surface area. The curve of the isotherm is concave to the P/P_0 axis. Uptake is limited by the accessibility of the microporous volume, rather than the internal surface area. High uptake at very low P/P_0 in both type I isotherms indicate enhanced favourable adsorbate-adsorbent interactions in small micropores. However, the sharp knee of type I(a) isotherms indicates the presence of micropores < 10 Å, whereas the broader knee of type I(b) isotherms indicates a broader pore size distribution, and the presence of larger micropores and small mesopores < ~ 25 Å.

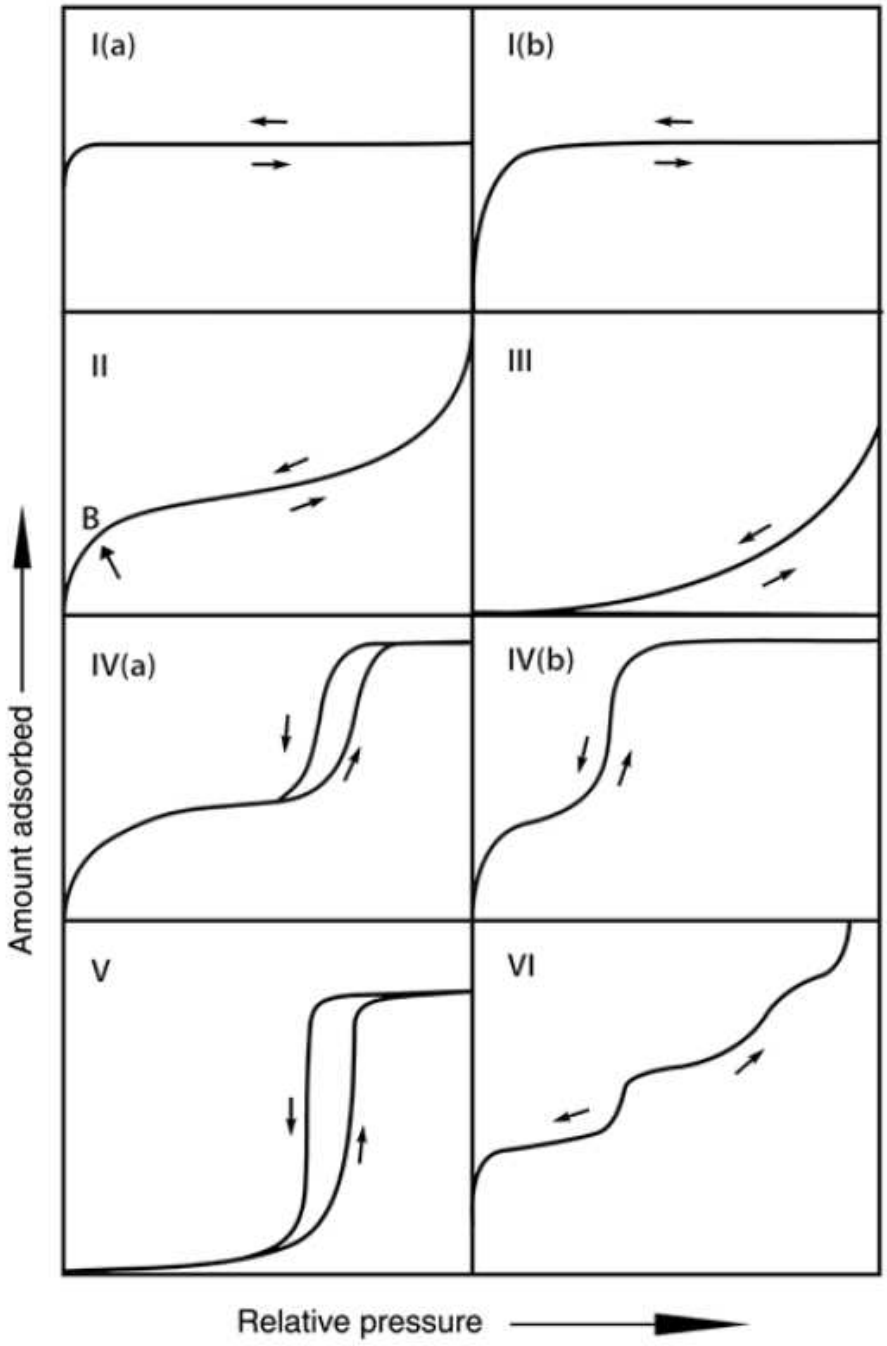

Figure 1.5. IUPAC classifications of sorption isotherms[61]

Type II isotherms correspond to adsorption of gases onto a non-porous or macroporous material. The first knee, 'point-b', indicates the point at which monolayer adsorption is complete and multilayer adsorption begins. A broader knee indicates more overlap between the completion of the monolayer and the onset of multilayer adsorption. The second knee, convex to the P/P_0 axis indicates continuing multilayer adsorption onto the particle surface at increasing pressure, not reaching saturation at $P/P_0 = 1$.

Type III isotherms also correspond to a non-porous or macroporous material. The convex curve and absence of a 'point-b' knee indicate weak adsorbate-adsorbent interactions with no definable monolayer.

Type IV isotherms indicate a mesoporous material. Initial uptake mirrors that of a type II isotherm, as monolayer-multilayer adsorption takes place on the mesopore walls. Type IV isotherms then account for capillary condensation, followed by a plateau indicating saturation. Type IV(a) isotherms show a hysteresis due to capillary condensation taking place in mesopores above a certain width. For analysis systems using nitrogen at 77 K, hysteresis occurs when capillary condensation takes place in pores > ~ 40 Å. Type IV(b) isotherms are completely reversible and correspond to structures with

narrower mesopores. In general, type IV(b) isotherms are produced by blind cylindrical or funnel shaped pores.

Type V isotherms are caused by weak adsorbate-adsorbent interactions, with pore filling only taking place at higher relative pressures.

Type VI isotherms indicate stepwise adsorption of individual layers onto a uniform, non-porous solid. The step height indicates the layer capacity.[61]

1. 4. 6. Hysteresis Classifications

Capillary condensation often results in the sorption isotherm containing a hysteresis loop. A hysteresis loop occurs when sections of the adsorption and desorption curve do not take place at the same relative pressure. As with isotherms, hysteresis loops can provide information about the structure of a pore network, by analysing its size, shape and position.

Pore shape can be an important factor in hysteresis formation; capillary condensation, and so hysteresis, occurs due to the presence of a metastable state of adsorption in mesoporous multilayer adsorption. A wide mesopore with only narrow access to the external surface (i.e. an ink-bottle shaped pore) will fill as expected as relative pressure increases. Adsorbate can diffuse through the narrow pore opening and multilayer adsorption, and capillary condensation, can occur in the wide mesopore. During desorption, the narrow pore opening will not empty until lower relative pressure, trapping the condensate within the pore structure and so forming a hysteresis loop in the multilayer section of the isotherm.[106,107]

Adsorption layer thickness is also a factor in capillary condensation, and therefore hysteresis formation. During mesoporous multilayer adsorption, if the film thickness is thin,

then adsorption potential dominates and has a stabilising effect. As the adsorption film layer gets thicker as relative pressure increases, the effect of the adsorption potential lessens, and surface tension effects become more significant. Once a critical temperature is reached, the adsorption film can no longer be stabilised and pore condensation occurs. Critical thickness, and therefore hysteresis formation, depends on pore shape, size and relative pressure.[61,106–108]

The IUPAC defines 6 classifications of hysteresis loop (Fig. 1.4), each indicative of certain features or characteristics of a porous structure and adsorption.[61]

Type H1 hysteresis loops are given by mesoporous structures with a narrow pore size distribution (PSD) of uniformly shaped pores. The narrow loop present at high relative pressure indicates that capillary condensation occurs late during adsorption.

Type H2 hysteresis loops are given by complex structures. Here pore network effects are significant. H2(a) loops show a steep desorption branch compared to the adsorption curve, due to blocking in pore necks of narrow size distribution. H2(b) loops have a gentler desorption curve due to pore blocking occurring in pore necks of a broader size distribution.

A type H3 hysteresis loop closely resembles a type II isotherm, and can be due to the presence of macropores which are not entirely filled with condensed adsorbate.

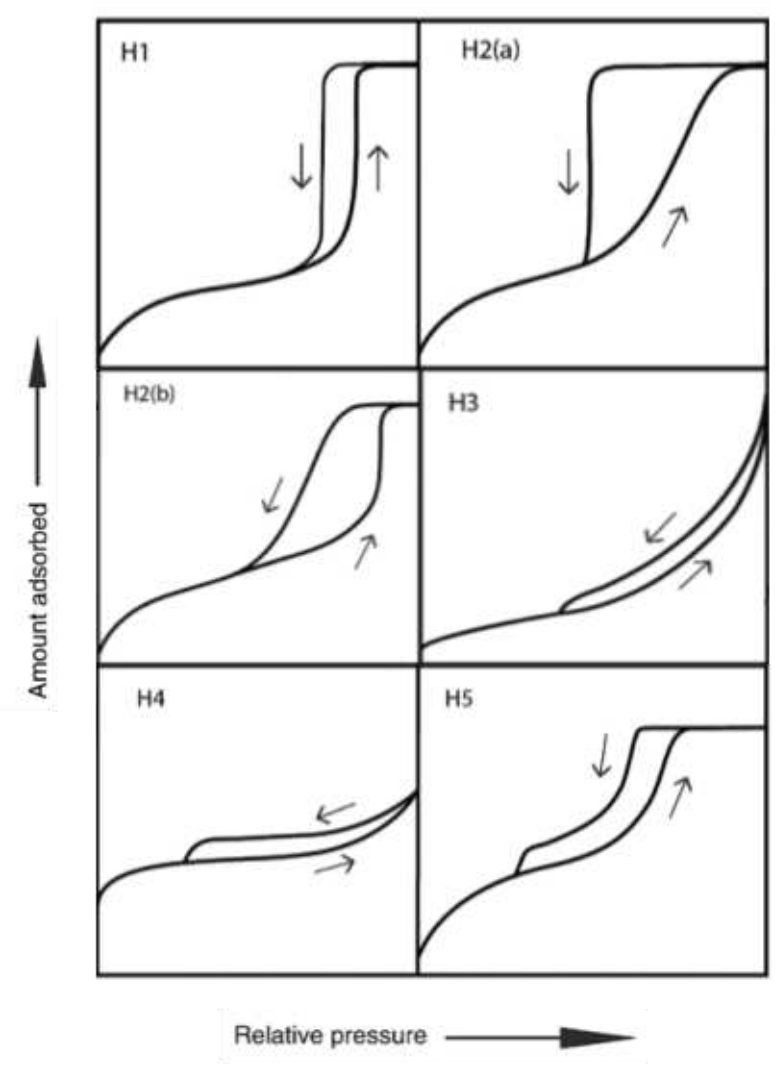

Figure 1.6. IUPAC classifications of hysteresis loops[61]

Type H4 hysteresis loops resemble type I and type II isotherms; higher uptake at low relative pressure indicates the presence of micropores.

Type H5 hysteresis loops are uncommon, and indicative of pore structures containing both open and partially blocked mesopores.[61,108]

Type H3, H4 and H5 hysteresis loops all have a clear closure point where the desorption curve re-joins the adsorption branch. The closure point is characteristic of certain adsorptives at particular temperatures. For nitrogen adsorption conducted at 77 K, the closure point is found in the range $P/P_0 \approx 0.4 – 0.5$.[61,107]

1. 4. 7. Calculating Porosity Values

Sorption isotherm data can be used to calculate a number of porosity values of a material including, surface area, pore volume, pore size distribution and microporosity. BET theory is widely accepted as the standard method for calculating and reporting specific surface area of a material using the sorption isotherm. The BET specific surface area is calculated by estimating the volume of the adsorbed monolayer (V_m) from the linear section of the isotherm curve. The linear section is usually located within the relative pressure range $P/P_0 \approx 0.05 – 0.4$. For a highly microporous material, this linear section should be shifted to a lower relative pressure, and the distinction between monolayer and multilayer adsorption may be less clear.

To estimate V_m, the BET equation in its linear form is applied to the linear section of the isotherm plot:

$$\frac{(P/P_0)}{V(1-(P/P_0))} = \frac{1}{V_m C} + \frac{(C-1)(P/P_0)}{V_m C} \qquad \textbf{Eqn. 1.2}$$

where V is the molar volume of the adsorbate gas at standard temperature and pressure (STP) and C is the intercept. Total surface area (S_{tot}) can then be calculated:

$$S_{tot} = \frac{V_m N_A \sigma_A}{V} \qquad \textbf{Eqn. 1.3}$$

where N_A is Avogadro's number and σ_A is the adsorption cross-sectional area of the adsorbate. Specific surface area (S_{BET}) can then be calculated:

$$S_{BET} = \frac{S_{tot}}{m} \qquad \textbf{Eqn. 1.4}$$

where the specific surface area is defined as the total surface area of a material per unit of mass.[61,106,107,109,110]

Pore volume and pore size information can be calculated from the isotherm data. The total pore volume (TPV) is calculated from the amount of gas adsorbed when relative pressure is close to saturation pressure ($P/P_0 \approx 0.99$). Data is taken from this pressure point, to ensure that the monolayer, multilayer and capillary condensation stages have completed. Assuming

that the adsorbate density is equal to that of the bulk liquid density at saturation pressure, the quantity of gas adsorbed is converted to the corresponding volume of liquid at the adsorption temperature. Therefore, when using nitrogen as the adsorptive, total pore volume (TPV) is calculated by:

$$TPV = Q_{sat}\left(\frac{P_{vap}}{P_{liq}}\right) \qquad \textbf{Eqn. 1.5}$$

where Q_{sat} is the quantity adsorbed at $P/P_0 \approx 0.99$, P_{vap} is the density of N_2 vapour at STP and P_{liq} is the density of liquid N_2 at its boiling point.

The t-plot method was developed by Lippens and De Boer,[111] and is used to calculate the micropore contribution of the total porosity, using the adsorption isotherm. The t-plot calculation is applied to a relative pressure range just above the completion of micropore filling. This is to assume that all micropores are full and capillary condensation has not yet occurred. The t-plot method compares film thickness from the experimental isotherm, to film thickness on a reference standard isotherm, producing a t-curve. The reference isotherm will be type II, and measured on an equivalent, but non-porous sample similar to the experimental material, under the same pressure, temperature and adsorbate conditions as the experimental data. The deviation of adsorption from the reference isotherm

can more accurately locate the point at which micropore filling completes, than using the sorption isotherm alone. The shape of the t-curve can give further information about the porous structure. Linearity of the t-curve with the reference curve at low relative pressures indicates the absence of micropores.[81,111–113] Micropore volume can then be calculated by:

$$V_{micro} = V_{tot} - V_{ext} \qquad \textbf{Eqn. 1.6}$$

where V_{micro} is the micropore contribution to the total pore volume, V_{tot} is the total pore volume and V_{ext} is the external pore volume, defined as the pore volume of the mesopores, macropores and external particle surface. Likewise, the micropore surface area can be calculated by:

$$S_{micro} = S_{tot} - S_{ext} \qquad \textbf{Eqn. 1.7}$$

where S_{micro} is the micropore contribution to the total surface area, S_{tot} is the total surface area and S_{ext} is the external surface area, defined as the surface area of the mesopores, macropores and external particle surface.[112,113]

1. 5. Porous Materials for Gas Adsorption

Many different porous materials are currently being developed for the purpose of post-combustion swing adsorption carbon capture. Each has merits and drawbacks, with research focusing on improving performance and commercial efficiency of the materials. Two major fields of research are metal organic frameworks and zeolites.

1. 5. 1. Metal Organic Frameworks

Metal organic frameworks (MOFs) are crystalline structures comprised of multidentate organic linkers covalently bonded to transition metal centres. First developed in the mid-1990s, the metals and linker molecules used can be varied to create a seemingly infinite number of different MOFs. This allows the development of MOFs suitable for a wide range of applications, such as catalysis, drug delivery, purification and gas separation and storage.[114,115]

MOFs are a promising field of research for carbon capture. By nature, high tailorability allows control over pore size and shape resulting in extraordinarily high surface areas and pore volumes. In 2018, Hönicke *et al*.[116] reported a new MOF, DUT-60, with the highest recorded surface area and accessible pore volume of any material; 7839 m^2 g^{-1} and 5.02 cm^3 g^{-1}

respectively.[116] The ability to increase functionalisation at the molecular level allows increasing uptake ability and selectivity by, for example, introducing polarity.[114,117] A modifiable pore structure results in the ability to create a hierarchical pore structure; an important property for fast diffusion of adsorptive to micropores.[118] MOFs have been shown to exhibit excellent CO_2 uptake capacities at high pressures, compared to alternative commercial sorbents. MOF-210 has a CO_2 uptake of up to 54 mmol g^{-1} at 298 K and 50 bar, while the activated carbon Maxsorb only has an uptake of 36 mmol g^{-1} under the same conditions.[114,115,117–120]

However, MOFs are still some way from commercial viability. Despite impressive performance under high pressure, CO_2 uptake under the low pressure conditions of post-combustion flue gases is poor. The humidity of flue gas streams is often found to degrade or deform MOFs, dramatically reducing uptake ability.[115] Many MOFs show low selectivity for CO_2 over other flue gas components. Generally, MOFs are expensive and time-consuming to produce and have varying associated environmental hazards.[115,119–121]

1. 5. 2. Zeolites

Zeolites are a class of crystalline, microporous aluminosilicates, formed naturally by pre-historic volcanic eruptions, and more recently synthetically, for a range of applications such as molecular sieves, catalysis and gas adsorption.

In terms of suitability for post-combustion CO_2 adsorption, zeolites may be considered to have a slight advantage over MOFs. Often, zeolitic frameworks have a uniform porosity, but can be modified to possess a hierarchical pore structure. As with MOFs, zeolites are very tailorable; the wide variety of possible tetrahedral connections, extra-framework cations and Al:Si:O ratios allow the design of a wide range of frameworks with various pore structures. Exchanging various cations into the framework, such as Na^+, Li^+ or K^+ ions, creates a strong electric field, both increasing selectivity for CO_2 and increasing uptake, due to the quadrupole moment of CO_2. Crucially, zeolites often show an improved low pressure CO_2 uptake compared with MOFs and are comparatively cheaper to produce. However, synthesis is not always straightforward, and zeolites often adsorb water vapour in preference to CO_2, limiting uptake ability. Uptake capacity and selectivity for CO_2 significantly drops at higher pressures, and generally, zeolites show poor hydrothermal stability.[122–129]

1. 5. 3. Porous Carbons

Activated or porous carbons are defined by the IUPAC as carbon materials produced by subjecting a char to various physical or chemical reactions, before, during or after carbonisation, in order to increase their adsorptive properties. Adsorptive properties are enhanced by increasing surface area and volume through the creation or development of small pores within the structure.[130]

The structure of porous carbons varies, depending on the preparation conditions, but they generally have an amorphous, graphitic-like laminar structure.[88,131,132] During activation at high temperatures, carbon atoms preferentially form graphitic-like sheets of sp^2 hybridised carbon that are likely to contain defects. Stacking of graphite sheets is disrupted and disordered, creating slit-shape voids or pores throughout the structure.[131] The higher the degree of activation, the more disordered the graphite stacking, leading to a more porous and amorphous structure. The pore structure is generally hierarchical to various degrees; pores can range from ~ 5 Å in diameter (smaller pore widths are unmeasurable with gas adsorption techniques) to large macropores.[88] The breadth of the PSD is determined by the starting materials and preparation conditions. Due to the nature of graphite stacking, such carbons

are generally assumed to have slit-like pores, however this is not always the case. Defects in the graphite structure such as holes or non-hexagonal rings can cause curvature in the sheets. Templated carbons show the inverse structure of the template used, and pore shape may reflect this. Overall, porous carbons show no long-range order but instead show diverse short-range order.[88,131,132]

Utilisation of porous carbons has been reported for centuries, with porous carbons playing an important role in, among other things, medicine, food production and air and water purification since the 1700s.[88,89,133] Properties of porous carbons are very tailorable, so carbons can be produced that are excellent adsorbents for post-combustion carbon capture. For this purpose, a porous carbon should have a high surface area of at least 1000 $m^2\ g^{-1}$, and large pore volume of at least 0.5 $cm^3\ g^{-1}$. As previously described, gas is preferentially adsorbed into micropores, so a high proportion of microporosity is important, especially due to the low partial pressure of CO_2 (~ 0.15 bar) usually found in flue streams. A hierarchical pore structure allows for fast diffusion of adsorptive through the pore network, however a narrow PSD centred in the micropore region increases the proportion of microporosity. Due to the kinetic

diameter of CO_2, a PSD centred at ~ 7 Å is advantageous for low pressure CO_2 uptake.[88]

In the preparation of porous carbons an activation step is needed to create a pore network. Activation can be done either physically, chemically, or a combination of both. Physical activation uses an oxidising gas and is a two-step process. The first step is pyrolysis of the precursor under inert atmosphere to remove volatiles.[88–90] The second step is partial gasification with an oxidising gas such as CO_2, steam or air. This burns away reactive sites of the carbon skeleton, releasing CO and CO_2 and creating a pore network. Both stages are conducted at temperatures ranging from ~ 400 – 1000 °C.[88,90] The resulting pore structure depends on the precursor used, the activating gas used, the temperatures at both stages and the duration of activation.[88,90,91]

Chemical activation is a one-step process, whereby a chemical activating agent, commonly a strong acid or base, is added to the precursor before pyrolysis under inert atmosphere. Again, high temperatures of ~ 600 – 900 °C are used, with common activating agents including $ZnCl_2$, H_3PO_4, KOH and NaOH.[88–90] $ZnCl_2$ and H_3PO_4 act as dehydrating agents; pores form around the activating agent, which remains within the structure during activation. The release of CO and CO_2 aid development of the

pore structure. KOH and NaOH act as oxidising agents, reacting with the carbon skeleton to form various carbonates. This reaction, along with the decomposition of the carbonates at high temperature, releases H_2, CO and CO_2, which develop the pore network as they escape to the particle surface.[88,91] Subsequent washing steps remove any remnants of the activating agent.[88,90]

The development of pore structure depends on several factors; the precursor used, activating agent and the ratio of the two used, as well as activation temperature and duration. Generally, the development of porosity increases with ratio of activating agent, activation temperature and duration.[88–91] This is often accompanied by broadening of the PSD; as a greater volume of gas is created and escapes to the particle surface, small pores collapse into larger pores. This broadening of the PSD is undesirable in the effort to produce carbons with a narrow PSD centred in the micropore region, suitable for low pressure CO_2 uptake.[88]

Chemical activation is often favoured over physical activation for multiple reasons. It is only a one-step process, and often activation takes places at lower temperatures. Generally, higher carbon yields, surface areas and pore volumes are achieved.

Microporosity is well developed and PSD is narrow and more controllable.[88,90]

KOH is the most commonly reported chemical activating agent. It has been shown to reliably produce carbons with very high surface area and pore volume. Activation with KOH consistently produces carbons with comparatively narrow PSDs with a higher proportion of microporosity. Furthermore, the results of activation reactions conducted with KOH are very predictable, making the tailoring of carbons through the synthesis procedure reasonably straightforward.[90]

Metallic K intercalates into and expands the laminar structure. Reactions with the carbon skeleton are as follows:[89–92]

$$6KOH + 2C \leftrightarrow 2K + 3H_2 + 2K_2CO_3 \qquad \textbf{Eqn. 1.8}$$

The above overall reaction can occur through a series of reactions, such as:[89,90]

$$2KOH \rightarrow K_2O + H_2O \qquad \textbf{Eqn. 1.9}$$

$$C + H_2O \rightarrow CO + H_2 \qquad \textbf{Eqn. 1.10}$$

$$CO + H_2O \rightarrow CO_2 + H_2 \qquad \textbf{Eqn. 1.11}$$

$$CO_2 + K_2O \rightarrow K_2CO_3 \qquad \textbf{Eqn. 1.12}$$

Above 700 °C, K_2CO_3 decomposition occurs and K compounds are reduced to produce metallic K:[88–91]

$$K_2CO_3 \leftrightarrow K_2O + CO_2 \qquad \textbf{Eqn. 1.13}$$

$$CO_2 + C \rightarrow 2CO \qquad \textbf{Eqn. 1.14}$$

$$K_2CO_3 + 2C \rightarrow 2K + 3CO \qquad \textbf{Eqn. 1.15}$$

$$C + K_2O \rightarrow 2K + CO \qquad \textbf{Eqn. 1.16}$$

Porous carbons can also be created using a templating method. A soft template (such as copolymers and surfactants) or a hard template (such as mesoporous silicas or zeolites) are used during the activation stage. The resulting carbon shows a pore structure that is the inverse of the template used. This can result in an ordered pore structure with very controllable characteristics.[87,94,95,134–136] However, this method can be more expensive and the removal of the template post-activation may involve harsh acids such as HF.[137]

There are many reasons why porous carbons are ideal candidates for post-combustion CO_2 capture. An easily tailored pore size and structure means carbons can be created for specific purposes.[88,96,128,138–143] Hierarchical pore networks means fast diffusion rates of adsorptive.[128,142] These factors

combined with good selectivity for CO_2 over other flue gas components such as nitrogen, mean that porous carbons show exceptional CO_2 uptake under post-combustion flue conditions.[138,144,145] Carbons have very high hydro, thermal and chemical stability, meaning they can withstand the conditions in a typical post-combustion flue stream.[88,96,139–144,146] Porous carbons regenerate well after adsorption, leading to high recyclability and a long industrial lifetime.[88,128,139,142,144,145,147] Carbons can also withstand mild compaction, necessary for implementation in an industrial setting.[88,140] These factors, along with being relatively cheap and simple to produce, make porous carbons very commercially viable.[88,96,146–148,128,138–143,145] Such carbons can be produced from a wide range of precursors, including many types of biomass, which has environmental advantages.[88,96,128,138,140–143,145] Finally, the use of porous carbons for post-combustion CO_2 capture presents no hazards to health or the environment.[144]

As previously discussed, porous carbons can be produced from a very wide range of precursors. Porous carbons for various uses have been made from organic metal salts, such as potassium tartrate, sodium citrate, calcium alginate, potassium citrate and potassium gluconate.[149–153] Similarly, organic molecules such as polypyrrole, furfural, cellulose and

acetonitrile are commonly used as carbon precursors.[67,92,136,140,154,155] Other popular precursors include coal[156–158], carbon nanotubes[159–161] and various forms of biomass such as wood, seeds and coconut shells.[141,143,162–164] Different precursors require differing preparation conditions and can affect the pore structure of resulting porous carbons in various ways.

Regardless of the material chosen as a precursor, the preparation of porous carbons allows for many tailoring opportunities in order to create carbons with specific characteristics. As well as the choice of precursor, the choice of preparation and activation conditions affect the resulting material. The choice of activating agent affects the pore development; as mentioned previously, chemical activating agents react in different ways.[88–92] Changes to the ratio of activating agent to precursor, as well as the activation temperature and duration have varying effects on the development of the pore structure. As previously stated, increasing these three factors leads to a more developed porosity, often with increased surface area and pore volume, with smaller pores collapsing into larger ones and broadening the PSD.[88–91]

These tailorable factors allow for extensive investigation into the preparation of carbon materials, providing promising results. Among some of the best recently reported studies, a range of precursors and activation methods have been used to achieve high CO_2 uptake capacity. Estevez et al.[87] made silica-templated hierarchically porous carbons (HPCs) from a sucrose precursor using physical activation with CO_2. Samples with a high microporosity achieved CO_2 uptake of up to 3.7 mmol g^{-1} at 25 °C and 1 bar.[87] Rouzitalab et al.[165] produced N-doped, walnut-shell derived carbons using KOH activation and urea as the nitrogen source. CO_2 uptake of up to 7.42 mmol g^{-1} at 25 °C and 1 bar was reported, using optimal preparation conditions; urea to carbon precursor ratio of 2:1, KOH to carbon precursor ratio of 2:1 and activation at 600 °C for 2 hrs.[165] Tehrani et al.[166] reported N-S-rich carbons prepared from an asphaltene precursor through KOH activation. CO_2 uptake of up to 7.15 mmol g^{-1} at 25 °C and 1 bar was recorded for samples prepared with a KOH to carbon precursor ration of 3:1, activated at 850 °C for 1 hr.[166] Li at al.[167] produced carbons from a rice husk precursor using CO_2 activation at 900 °C for 1 hr. CO_2 uptake of up to 3.1 mmol g^{-1} at 25 °C and 1 bar was reported.[167] Chang et al.[168] used poplar catkins as a precursor to produce self-N-doped HPC microtubes through $ZnCl_2$ activation. CO_2 uptake of 4.05 mmol g^{-1} at 25 °C and 1 bar was

achieved for samples prepared with $ZnCl_2$ to carbon precursor ratio of 4:1, activated at 800 °C for 2 hrs.[168]

This thesis reports 4 investigations into the preparation of porous carbons suitable for post-combustion CO_2 capture, through the tailoring of synthesis conditions. The first investigation addresses the field of doping the carbon structure to improve uptake and selectivity. The research details the effects of doping with various alkali metal ions. The second investigation reports a novel carbonisation method in the preparation of biomass-derived porous carbons. The third investigation details the use of harsh activation conditions on an organic metal salt precursor. The final investigation looks into the use of an alternative hydroxide activating agent.

1. 6. References

1 G. N. Plass, *Ann. N. Y. Acad. Sci.*, 1961, **95**, 61–71.

2 H. Grassl, *Surv. Geophys.*, 2011, 32, 319–328.

3 S. A. Montzka, E. J. Dlugokencky and J. H. Butler, *Nature*, 2011, **476**, 43–50.

4 T. R. Anderson, E. Hawkins and P. D. Jones, *Endeavour*, 2016, **40**, 178–187.

5 T. F. Stocker, D. Qin, G.-K. Plattner, M. Tignor, S. K. Allen, J. Boschung, A. Nauers, Y. Xia, V. Bex and P. M. Midgley, *IPCC, 2013: Annex III: Glossary [Planton, S. (ed.)]. In: Climate Change 2013: The Physical Science Basis. Contribution of Working Group I to the Fifth Assessment Report of the Intergovernmental Panel on Climate Change*, 2013.

6 G. Myhre, D. Shindell, F.-M. Bréon, W. Collins, J. Fuglestvedt, J. Huang, D. Koch, J.-F. Lamarque, D. Lee, B. Mendoza, T. Nakajima, A. Robock, G. Stephens, T. Takemura and H. Zhang, *Anthropogenic and Natural Radiative Forcing. In: Climate Change 2013: The Physical Science Basis. Contribution of Working Group I to the Fifth Assessment Report of the Intergovernmental Panel on Climate Change*, 2013.

7 L. D. D. Harvey, *Energy Policy*, 1993, **21**, 24–34.

8 M. U. F. Kirschbaum, *Environ. Res. Lett.*, 2014, **9**, 1–11.

9 D. L. Hartmann, A. M. G. K. Tank, M. Rusticucci, L. V. Alexander, S. Brönnimann, Y. Charabi, F. J. Dentener, E. J. Dlugokencky, D. R. Easterling, A. Kaplan, B. J. Soden, P. W. Thorne, M. Wild and P. M. Zhai, *Observations: Atmosphere and Surface. In: Climate Change 2013: The Physical Science Basis. Contribution of Working Group I to the Fifth Assessment Report of the Intergovernmental Panel on Climate Change*, 2013.

10 G. Hansen and D. Stone, *Nat. Clim. Chang.*, 2016, **6**, 532–537.

11 P. Bains, P. Psarras and J. Wilcox, *Prog. Energy Combust. Sci.*, 2017, **63**, 146–172.

12 *Global Energy & CO2 Status Report 2017*, 2018.

13 O. Edenhofer, R. Pichs-Madruga, Y. Sokona, E. Farahani, S. Kadner, K. Seyboth, A. Adler, I. Baum, S. Brunner, P. Eickemeier, B. Kriemann, J. Savolainen, S. Schlömer, C. von Stechow, T. Zwickel and J. C. Minx, *IPCC, 2014: Summary for Policymakers. In: Climate Change 2014: Mitigation of Climate Change. Contribution of Working Group III to the Fifth Assessment Report of the Intergovernmental Panel on Climate Change*, 2014.

14 M. Z. Jacobson and M. A. Delucchi, *Energy Policy*, 2011, **39**, 1154–1169.

15 M. Z. Jacobson, M. A. Delucchi, Z. A. F. Bauer, S. C. Goodman, W. E. Chapman, M. A. Cameron, C. Bozonnat, L. Chobadi, H. A. Clonts, P. Enevoldsen, J. R. Erwin, S. N. Fobi, O. K. Goldstrom, E. M. Hennessy, J. Liu, J. Lo, C. B. Meyer, S. B. Morris, K. R. Moy, P. L. O'Neill, I. Petkov, S. Redfern, R. Schucker, M. A. Sontag, J. Wang, E. Weiner and A. S. Yachanin, *Joule*, 2017, **1**, 108–121.

16 IPCC Special Report: *'Global Warming of 1.5°C',* a Summary for Policy makers, 2018, ISBN: 978-92-9169-151-7

17 *Technology Roadmap Energy and GHG reductions in the chemical industry via catalytic processes*, 2013.

18 H. Mikulčić, M. Vujanović and N. Duić, *Appl. Energy*, 2013, **101**, 41–48.

19 R. Kajaste and M. Hurme, *J. Clean. Prod.*, 2016, **112**, 4041–4052.

20 G. Supran and N. Oreskes, *Environ. Res. Lett.*, 2017, **12**, 084019.

21 globalccsinstitute, ute, https://co2degrees.com/learn-more/resources, (accessed 25 June 2019).

22 International Energy Agency*: 'Energy Technology Perspectives 2016'*, 2016, ISBN: 9789264208001

23 Global CCS Institute Projects Database, https://www.globalccsinstitute.com/projects/large-scale-

ccs-projects, (accessed October 2018).

24 O. Miyamoto, C. Maas, T. Tsujiuchi, M. Inui, T. Hirata, H. Tanaka, T. Yonekawa and T. Kamijo, *Energy Procedia*, 2017, **114**, 5616–5623.

25 *International Energy Agency Insights Series: Storing CO2 through Enhanced Oil Recovery*, 2015.

26 M. Bui, C. S. Adjiman, A. Bardow, E. J. Anthony, A. Boston, S. Brown, P. S. Fennell, S. Fuss, A. Galindo, L. A. Hackett, J. P. Hallett, H. J. Herzog, G. Jackson, J. Kemper, S. Krevor, G. C. Maitland, M. Matuszewski, I. S. Metcalfe, C. Petit, G. Puxty, J. Reimer, D. M. Reiner, E. S. Rubin, S. A. Scott, N. Shah, B. Smit, J. P. M. Trusler, P. Webley, J. Wilcox and N. Mac Dowell, *Energy Environ. Sci.*, 2018, **11**, 1062–1176.

27 NRG Case Studies, https://www.nrg.com/case-studies/petra-nova.html, (accessed October 2018).

28 SaskPower Boundary Dam Carbon Capture Project, https://www.saskpower.com/our-power-future/infrastructure-projects/carbon-capture-and-storage/boundary-dam-carbon-capture-project, (accessed October 2018).

29 K. Stéphenne, *Energy Procedia*, 2014, **63**, 6106–6110.

30 A. Manuilova, J. Koiwanit, L. Piewkhaow, M. Wilson, C. W. Chan and P. Tontiwachwuthikul, *Energy Procedia*,

2014, **63**, 7398–7407.

31 *HM Government Statement to Markets Regarding Carbon Capture and Storage Competition, https://www.londonstockexchange.com/exchange/news/market-news/market-news-detail/other/12597443.html, (accessed October 2018)*, .

32 House of Commons Committee of Public Accounts, *Carbon Capture and Storage Sixty-fourth Report of Session 2016–17*, 2017.

33 R. M. Cue´llar-Franca and A. Azapagic, *J. CO2 Util.*, 2015, **9**, 82–102.

34 S. B., A. H. Strømman and E. G. Hertwich, *Int. J. Greenh. Gas Control*, 2011, **5**, 911–921.

35 D. Y. C. Leung, G. Caramanna and M. M. Maroto-Valer, *Renew. Sustain. Energy Rev.*, 2014, **39**, 426–443.

36 M. N. Anwar, A. Fayyaz, N. F. Sohail, M. F. Khokhar, M. Baqar, W. D. Khan, K. Rasool, M. Rehan and A. S. Nizami, *J. Environ. Manage.*, 2018, **226**, 131–144.

37 J. D. Figueroa, T. Fout, S. Plasynski, H. McIlvried and R. D. Srivastava, *Int. J. Greenh. Gas Control*, 2008, **2**, 9–20.

38 E. I. Koytsoumpa, C. Bergins and E. Kakaras, *J. Supercrit. Fluids*, 2018, **132**, 3–16.

39 A. A. Khan, G. N. Halder and A. K. Saha, *Int. J. Greenh.*

Gas Control, 2015, **32**, 15–23.

40 L. S. Tan, A. M. Shariff, K. K. Lau and M. A. Bustam, *J. Ind. Eng. Chem.*, 2012, **18**, 1874–1883.

41 G. T. Rochelle, *Science (80-.).*, 2009, **325**, 1652–1654.

42 B. P. Mandal, A. K. Biswas and S. S. Bandyopadhyay, *Chem. Eng. Sci.*, 2003, **58**, 4137–4144.

43 U. E. Aronu, H. F. Svendsen, K. A. Hoff and O. Juliussen, *Energy Procedia*, 2009, **1**, 1051–1057.

44 B. Dutcher, M. Fan and A. G. Russell, *ACS Appl. Mater. Interfaces*, 2015, **7**, 2137–2148.

45 S. Delgado, B. Valentin, D. Bontemps and O. Authier, *Ind. Eng. Chem. Res.*, 2018, **57**, 6057–6067.

46 S. Freguia and G. T. Rochelle, *AICHe J.*, 2003, **49**, 1676–1686.

47 G. Salazar Duarte, B. Schürer, C. Voss and D. Bathen, *ChemBioEng Rev.*, 2017, **4**, 277–288.

48 Y. Wang, L. Zhao, A. Otto, M. Robinius and D. Stolten, *Energy Procedia*, 2017, **114**, 650–665.

49 J. K. Adewole, A. L. Ahmad, S. Ismail and C. P. Leo, *Int. J. Greenh. Gas Control*, 2013, **17**, 46–65.

50 K. Ramasubramanian and W. S. W. Ho, *Curr. Opin. Chem. Eng.*, 2011, **1**, 47–54.

51 L. Zhao, E. Riensche, L. Blum and D. Stolten, *J. Memb. Sci.*, 2010, **359**, 160–172.

52 W. Yave, A. Car and K. V. Peinemann, *J. Memb. Sci.*, 2010, **350**, 124–129.

53 C. E. Powell and G. G. Qiao, *J. Memb. Sci.*, 2006, **279**, 1–49.

54 M. T. Ho, G. W. Allinson and D. E. Wiley, *Ind. Eng. Chem. Res.*, 2008, **47**, 4883–4890.

55 D. Bahamon, A. Díaz-Márquez, P. Gamallo and L. F. Vega, *Chem. Eng. J.*, 2018, **342**, 458–473.

56 R. Zhao, S. Deng, S. Wang, L. Zhao, Y. Zhang, B. Liu, H. Li and Z. Yu, *Appl. Therm. Eng.*, 2018, **128**, 818–829.

57 R. Ben-Mansour, M. A. Habib, O. E. Bamidele, M. Basha, N. A. A. Qasem, A. Peedikakkal, T. Laoui and M. Ali, *Appl. Energy*, 2016, **161**, 225–255.

58 N. Hedin, L. Andersson, L. Bergström and J. Yan, *Appl. Energy*, 2013, **104**, 418–433.

59 M. G. Plaza, S. García, F. Rubiera, J. J. Pis and C. Pevida, *Chem. Eng. J.*, 2010, **163**, 41–47.

60 M. Radosz, X. Hu, K. Krutkramelis and Y. Shen, *Ind. Eng. Chem. Res.*, 2008, **47**, 3783–3794.

61 M. Thommes, K. Kaneko, A. V Neimark, J. P. Olivier, F. Rodriguez-reinoso, J. Rouquerol and K. S. W. Sing, 2015, **87**, 1051–1069.

62 T. Bligaard and J. K. Nørskov, in *Chemical Bonding at Surfaces and Interfaces*, 2008, pp. 255–321.

63 Z. He, Y. Bai, H. Huang, J. Li, Huhetaoli, N. Kobayashi, Y. Osaka and L. Deng, *Appl. Therm. Eng.*, 2017, **126**, 37–42.

64 M. Woellner, S. Hausdorf, N. Klein, P. Mueller, M. W. Smith and S. Kaskel, *Adv. Mater.*, 2018, **30**, 1–27.

65 C. M. Yon and J. D. Sherman, in *Kirk-Othmer Encyclopedia of Chemical Technology*, 2003, vol. 1, pp. 617–663.

66 Z. Xueping, Z. Jiaojiao, L. Shenglin, Q. Xuanhui, L. Ping, G. Yanbei and L. Weihua, *Int. J. Hydrogen Energy*, 2015, **40**, 10502–10507.

67 B. Adeniran and R. Mokaya, *Nano Energy*, 2015, **16**, 173–185.

68 A. Martin-Calvo, J. J. Gutiérrez-Sevillano, I. Matito-Martos, T. J. H. Vlugt and S. Calero, *J. Phys. Chem. C*, 2018, **122**, 12485–12493.

69 S. Kiefer and E. Robens, *J. Therm. Anal. Calorim.*, 2008, **94**, 613–618.

70 E. Robens and S. A. A. Jayaweera, *Adsorpt. Sci. Technol.*, 2014, **32**, 425–442.

71 In *Bible, Book of Judges, Chpt. VI:33-40*.

72 A. Dabrowski, *Adv. Colloid Interface Sci.*, 2001, **93**, 135–224.

73 R. I. Masel, in *Principles of Adsorption and Reaction on*

Solid Sufaces, 1996, pp. 108–234.

74 I. Langmuir, *J. Am. Chem. Soc.*, 1918, **40**, 1361–1403.

75 S. Brunauer, P. H. Emmett and E. Teller, *J. Am. Chem. Soc.*, 1938, **60**, 309–319.

76 S. Brunauer, L. S. Deming, W. E. Deming and E. Teller, *J. Am. Chem. Soc.*, 1940, **62**, 1723–1732.

77 V. Bolis, in *Calorimetry and Thermal Methods in Catalysis2*, 2013, pp. 3–50.

78 J. Rouquerol, D. Avnir, C. W. Fairbridge, D. H. Everett, J. H. Haynes, N. Pernicone, J. D. F. Ramsay, K. S. W. Sing and K. K. Unger, *Pure Appl. Chem.*, 1994, **66**, 1739–1758.

79 A. J. Burggraaf and L.Cot, in *Fundamentals of Inorganic Membrane Science and Technology*, 1996, p. 71.

80 A. T. Hubbard, in *Encyclopedia of Surface and Colloid Science - Volume 1*, 2002, p. 889.

81 K. Kaneko, *J. Membr. Sci*, 1994, **96**, 59–89.

82 B. D. Zdravkov, J. J. Cermak, M. Sefara and J. Jank, *Cent. Eur. J. Chem.*, 2007, **5**, 385–395.

83 A. T. Hubbard, in *Encylopedia of Surface and Colloid Science - Volume 1*, 2002, p. 943.

84 M. E. Davis, *Nature*, 2002, **417**, 813–821.

85 J.-R. Li, R. J. Kuppler and H.-C. Zhou, *Chem. Soc. Rev.*, 2009, **38**, 1477–1504.

86 H. Furukawa, K. E. Cordova, M. O. Keeffe and O. M. Yaghi, *Science (80-.).*, 2013, **341**, 1230444.

87 L. Estevez, D. Barpaga, J. Zheng, S. Sabale, R. L. Patel, J. Zhang, B. P. Mcgrail and R. K. Motkuri, *Ind. Eng. Chem. Res.*, 2018, **57**, 1262–1268.

88 M. Sevilla and R. Mokaya, *Energy Environ. Sci.*, 2014, **7**, 1250–1280.

89 C. R. Correa and A. Kruse, *Materials (Basel).*, 2018, **11**, 1568.

90 J. Wang and S. Kaskel, *J. Mater. Chem.*, 2012, **22**, 23710–23725.

91 M. A. Lillo-Rodenas, J. Juan-Juan, D. Cazorla-Amor and A. Linares-Solano, *Carbon N. Y.*, 2004, **42**, 1371–1375.

92 M. Sevilla, A. B. Fuertes and R. Mokaya, *Energy Environ. Sci.*, 2011, **4**, 1400.

93 P. González-García, *Renew. Sustain. Energy Rev.*, 2018, **82**, 1393–1414.

94 M. Sun, C. Chen, L. Chen and B. Su, *Front. Chem. Sci. Eng.*, 2016, **10**, 301–347.

95 W. Shen and W. Fan, *J. Mater. Chem. A*, 2013, **1**, 999–1013.

96 C. Lu, Y. H. Huang, Y. J. Wu, J. Li and J. P. Cheng, *J. Power Sources*, 2018, **394**, 9–16.

97 N. Miriyala, D. Ouyang, Y. Perrie, D. Lowry and D. J.

Kirby, *Eur. J. Pharm. Biopharm.*, 2017, **115**, 197–205.

98 R. Liu, F. Yin, J. Zhang, J. Zhang and Z. Zhang, *RSC Adv.*, 2014, **4**, 21465.

99 MicromeriticsInstrumentCorporation, No Title, https://www.micromeritics.com/Repository/Files/Gas_Adsorption_Theory_poster.pdf, (accessed 26 June 2019).

100 M. Aliofkhazraei, N. Ali, W. I. Milne, C. S. Ozkan, S. Mitura and J. L. Gervasoni, in *Graphene Science Handbook: Size-Dependent Properties*, 2016, pp. 64–65.

101 W. Tian, H. Zhang, H. Sun, M. O. Tadé and S. Wang, *Chem. Eng. J.*, 2018, **347**, 432–439.

102 G. Srinivas, V. Krungleviciute, Z.-X. Guo and T. Yildirim, *Energy Environ. Sci.*, 2014, **7**, 335–342.

103 C. Chen, H. Huang, Y. Yu, J. Shi, C. He, R. Albilali and H. Pan, *Chem. Eng. J.*, 2018, **353**, 584–594.

104 D. A. H. Hanaor, M. Ghadiri, W. Chrzanowski and Y. Gan, *Langmuir*, 2014, **30**, 15143–15152.

105 K. Y. Foo and B. H. Hameed, *Chem. Eng. J.*, 2010, **156**, 2–10.

106 K. S. W. Sing, D. H. Everett, R. A. W. Haul, L. Moscou, R. S. Pierotti, J. Rouquerol and T. Siemieniewska, *Pure Appl. Chem.*, 1985, **57**, 603–619.

107 M. Thommes, , DOI:10.1002/cite.201000064.

108 K. S. W. Sing and R. T. Williams, *Adsorpt. Sci. Technol.*,

2004, **22**, 773–782.

109 S. Lowell, J. E. Shields, M. A. Thomas and M. Thommes, in *Characterization of Porous Solids and Powders: Surface Area, Pore Size and Density*, 2004, pp. 101–129.

110 A. K. Ladavos, A. P. Katsoulidis, A. Iosifidis, K. S. Triantafyllidis, T. J. Pinnavaia and P. J. Pomonis, *Microporous Mesoporous Mater.*, 2012, **151**, 126–133.

111 B. C. Lippens and J. H. De Boer, *J. Catal.*, 1965, **4**, 319–323.

112 F. Villemot, A. Galarneau and B. Coasne, *Adsorption*, 2014, **20**, 349–357.

113 A. Galarneau, F. Villemot, J. Rodriguez, F. Fajula and B. Coasne, *Langmuir*, 2014, **30**, 13266–13274.

114 J. D. Evans, B. Garai, H. Reinsch, W. Li, S. Dissegna, V. Bon, I. Senkovska, R. A. Fischer, S. Kaskel, C. Janiak, N. Stock and D. Volkmer, *Coord. Chem. Rev.*, 2019, **380**, 378–418.

115 V. Benoit, N. Chanut, R. S. Pillai, M. Benzaqui, I. Beurroies, S. Devautour-vinot, C. Serre, N. Steunou and P. L. Llewellyn, *J. Mater. Chem. A*, 2018, **6**, 2081–2090.

116 I. M. Hçnicke, I. Senkovska, V. Bon, I. A. Baburin, N. Bçnisch, S. Raschke, J. D. Evans and S. Kaskel, *Angew. Chemie - Int. Ed.*, 2018, **57**, 13780–13783.

117 A. Pal, S. Chand, S. M. Elahi and M. C. Das, *Dalt. Trans.*,

2017, **46**, 15280–15286.

118 A. Kirchon, L. Feng, H. F. Drake, A. Joseph and H. Zhou, *Chem Soc Rev*, 2018, **47**, 8611–8638.

119 H. Ren and X. Zhang, *Energy & Fuels*, 2016, **30**, 526–530.

120 A. Pal, S. Chand and M. C. Das, *Inorg. Chem.*, 2017, **56**, 13991–13997.

121 Q. Mu, H. Wang, L. Li, C. Wang, Y. Wang and X. Zhao, *Chem. Asian J.*, 2015, **10**, 1864–1869.

122 M. Moshoeshoe, M. S. Nadiye-tabbiruka and V. Obuseng, *Am. J. Mater. Sci.*, 2017, **7**, 196–221.

123 M. A. Ghalia and Y. Dahman, *Energy Technol.*, 2017, **5**, 356–372.

124 V. Garshasbi, M. Jahangiri and M. Anbia, *Appl. Surf. Sci.*, 2017, **393**, 225–233.

125 D. P. Bezerra, R. S. Oliveira, R. S. Vieira, C. L. Cavalcante and D. C. S. Azevedo, *Adsorption*, 2011, **17**, 235–246.

126 L. Nie, Y. Mu, J. Jin, J. Chen and J. Mi, *Chinese J. Chem. Eng.*, 2018, **26**, 2303–2317.

127 N. Hedin, L. Chen and A. Laaksonen, *Nanoscale*, 2010, **2**, 1819–1841.

128 A. Samanta, A. Zhao, G. K. H. Shimizu, P. Sarkar and R. Gupta, *Ind. Eng. Chem. Res.*, 2012, **51**, 1438–1463.

129 Y. Li, L. Li and J. Yu, *Chem*, 2017, **3**, 928–949.

130 E. Fitzer, K.-H. Kochling, H. P. Boehm and H. Marsh, *Pure Appl. Chem.*, 1995, **67**, 473–506.

131 A. C. Forse, C. Merlet, P. K. Allan, E. K. Humphreys, J. M. Griffin, M. Aslan, M. Zeiger, V. Presser, Y. Gogotsi and C. P. Grey, *Chem. Mater.*, 2015, **27**, 6848–6857.

132 S. M. Manocha, *Sādhanā*, 2003, **28**, 335–348.

133 T. Gupta, in *Carbon: The Black, the Gray and the Transparent*, 2018, pp. 47–70.

134 E. Masika and R. Mokaya, *RSC Adv.*, 2013, **3**, 17677–17681.

135 M. Sevilla, N. Alam and R. Mokaya, *J. Phys. Chem. C*, 2010, **114**, 11314–11319.

136 E. Masika and R. Mokaya, *Energy Environ. Sci.*, 2014, **7**, 427–434.

137 Z. Chen, S. Deng, H. Wei, B. Wang, J. Huang and G. Yu, *Front. Environ. Sci. Eng.*, 2013, **7**, 326–340.

138 Y. Zhao, X. Liu, K. X. Yao, L. Zhao and Y. Han, *Chem. Mater.*, 2012, **24**, 4725–4734.

139 A. Ganesan and M. M. Shaijumon, *Microporous Mesoporous Mater.*, 2016, **220**, 21–27.

140 B. Adeniran and R. Mokaya, *Chem. Mater.*, 2016, **28**, 994–1001.

141 H. M. Coromina, D. A. Walsh and R. Mokaya, *J. Mater.*

Chem. A, 2016, **4**, 280–289.

142 S. Y. Lee and S. J. Park, *J. Ind. Eng. Chem.*, 2015, **23**, 1–11.

143 W. Sangchoom and R. Mokaya, *ACS Sustain. Chem. Eng.*, 2015, **3**, 1658–1667.

144 M. Sevilla, J. B. Parra and A. B. Fuertes, *ACS Appl. Mater. Interfaces*, 2013, **5**, 6360–6368.

145 A. Alabadi, S. Razzaque, Y. Yang, S. Chen and B. Tan, *Chem. Eng. J.*, 2015, **281**, 606–612.

146 M. Rana, K. Subramani, M. Sathish and U. K. Gautam, *Carbon N. Y.*, 2017, **114**, 679–689.

147 A. L. Yaumi, M. Z. A. Bakar and B. H. Hameed, *Energy*, 2017, **124**, 461–480.

148 A. A. Adelodun, Y. H. Lim and Y. M. Jo, *J. Anal. Appl. Pyrolysis*, 2014, **108**, 151–159.

149 B. Adeniran, E. Masika and R. Mokaya, *J. Mater. Chem. A*, 2014, **2**, 14696.

150 A. B. Fuertes, G. A. Ferrero and M. Sevilla, *J. Mater. Chem. A Mater. energy Sustain.*, 2014, **2**, 14439–14448.

151 C. Zhao, L. Xu, Z. Hu and K. Liu, *RSC Adv.*, 2016, **6**, 47486–47490.

152 M. Sevilla and A. B. Fuertes, *ACS Nano*, 2014, **8**, 5069–5078.

153 M. Sevilla and A. B. Fuertes, *J. Mater. Chem. A*, 2013, **1**,

13738–13741.

154 Z. Yang, Y. Xia and R. Mokaya, *J. Am. Chem. Soc.*, 2007, **129**, 1673–1679.

155 E. Masika and R. Mokaya, *Prog. Nat. Sci.*, 2013, **23**, 308–316.

156 L. Wang, F. Sun, J. Gao, X. Pi, Z. Qu and G. Zhao, *Energy & Fuels*, 2018, **32**, 1255–1264.

157 L. Wang, R. Wang, H. Zhao, L. Liu and D. Jia, *Mater. Lett.*, 2015, **149**, 85–88.

158 J. Zhang, L. Jin, J. Cheng and H. Hu, *Carbon N. Y.*, 2013, **55**, 221–232.

159 Q. Jiang, M. Qu, B. Zhang and Z. Yu, *Carbon N. Y.*, 2002, **40**, 2743–2745.

160 B. Adeniran and R. Mokaya, *J. Mater. Chem. A*, 2015, **3**, 5148–5161.

161 E. Raymundo-Pinero, D. Cazorla-Amoros, A. Linares-Solano, S. Delpeux, E. Frackowiak, K. Szostak and F. Beguin, *Carbon N. Y.*, 2002, **40**, 1614–1617.

162 E. Haffner-Staton, N. Balahmar and R. Mokaya, *J. Mater. Chem. A*, 2016, **4**, 13324–13335.

163 N. Balahmar, A. S. Al-jumialy and R. Mokaya, *J. Mater. Chem. A*, 2017, **5**, 12330–12339.

164 N. Querejeta and I. Nacional, *Greenh. Gases Sci. Technol.*, 2018, **8**, 309–323.

165 Z. Rouzitalab, D. M. Maklavanya, A. Rashidi and S. Jafarinejad, *J. Environ. Chem. Eng.*, 2018, **6**, 6653–6663.

166 N. H. M. H. Tehrani, M. S. Alivand, D. M. Maklavany, A. Rashidi, M. Samipoorgiri, A. Seif and Z. Yousefian, *Chem. Eng. J.*, 2019, **358**, 1126–1138.

167 M. Li and R. Xiao, *Fuel Process. Technol.*, 2019, **186**, 35–39.

168 B. Chang, W. Shi, H. Yin, S. Zhang and B. Yang, *Chem. Eng. J.*, 2019, **358**, 1507–1518.

Chapter 2 - Characterisation Techniques

This chapter details the analytical techniques used to characterise the samples produced in the following studies. The methodology and data output of each technique is described, as well as the reasons for using each technique.

2. 1. CHN Elemental Microanalysis

CHN elemental microanalysis is used to accurately measure the carbon, hydrogen and nitrogen content of a sample. This information can help characterise a sample and detect impurities. Samples are combusted at ~ 1000 °C under a flow of pure oxygen. The combustion products are carried by a flow of helium to thermal conductivity detectors. An oxidation column ensures complete oxidation to CO_2 and H_2O. A reduction column removes excess oxygen and reduces oxides of nitrogen to N_2. A water adsorption trap calculates the amount of water in the gas stream, and so the H content of the sample. A second thermal conductivity trap removes CO_2 from the gas stream, therefore calculating the amount of C in the sample. Finally, the remaining gas stream, of just helium and nitrogen is compared to a reference flow of pure helium to calculate the N content of the sample.[1]

2. 2. Thermal Gravimetric Analysis

Thermal gravimetric analysis (TGA) is a technique primarily used for measuring physical and chemical changes of a material as a function of temperature and/or time. It can be used to provide information about, among other things, thermal decomposition, sorption processes and oxidation and reduction reactions. In this work, TGA was used to assess thermal decomposition. Samples are placed in a platinum or alumina pan, and their masses constantly measured by a highly precise microbalance. A thermocouple close to the sample records temperature increases under controlled gas flow. A plot of temperature vs. mass records how the sample mass changes as temperature increases. A derivative weight loss curve determines the temperature at which largest weight change occurs. In this study, TGA was used to assess thermal stability, material composition and impurity content, by heating a sample in air to cause carbon burn-off. The point of highest burn off indicates the thermal stability of the material, while the sharpness of the burn-off curve indicates a single or multiphase carbon. The residual mass at the end of heating indicates the inorganic impurity content.

2. 3. Scanning Electron Microscopy

Scanning electron microscopy (SEM) generates an image of a material surface by probing the sample surface with a focussed, high-energy electron beam. It is used to provide information on surface topography and composition. Electrons are produced by thermal emission when passing a current through a tungsten filament. Under vacuum, the electron beam is vertically focussed through a series of electromagnetic fields and lenses towards the sample.[2,3]

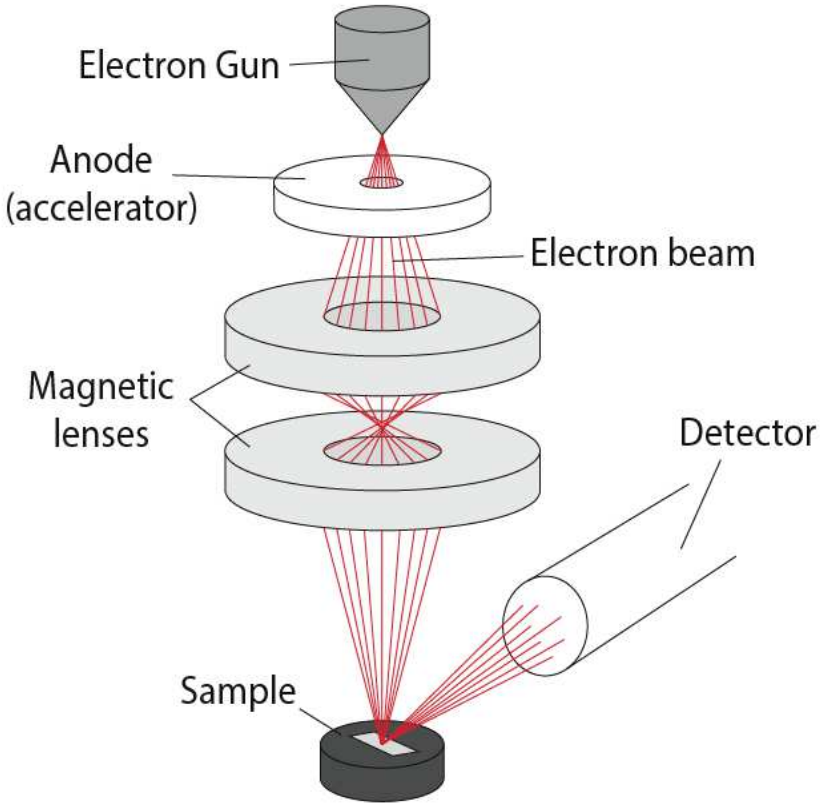

Figure 2.1. Schematic of a typical SEM system[4]

The electron beam penetrates the sample surface layers in a teardrop-shape, the volume of which depends on the energy of the electron beam. Electrons reflected by the sample (backscattered electrons, BSEs) are detected and give compositional information. Heavier atoms deflect more electrons due to their higher density nuclei, so appear relatively brighter on the resulting micrograph.[3,5] Some electrons from the electron beam will cause the ejection of core electrons from surface atoms (secondary electrons, SEs). Outer shell electrons drop down to fill the vacancy and emit a photon characteristic of the element.

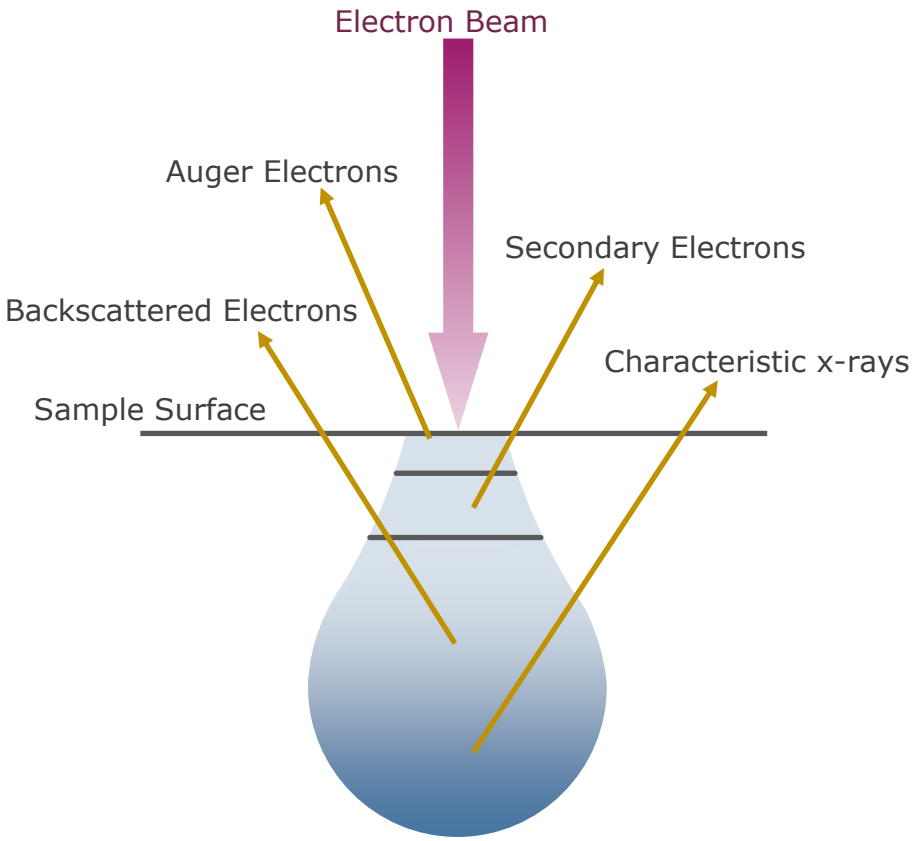

Figure 2.2. Representation of SEM signals

The SEs are detected and produce an image providing information about the surface topography and 3D structure.[2,3,5] More SEs are detected when the beam is perpendicular to the surface, so steep edges appear brighter than flat surfaces. The emitted photon is detected and can be used in combination with energy dispersive x-ray (EDX) analysis to characterise elemental composition across the surface.[2,3,5] In this work, SEM was used to assess surface topography, pore structure and the presence of dopants on the carbon materials.

2. 4. Powder X-Ray Diffraction

Powder x-ray diffraction (PXRD) is used to analyse the crystal structure of a powdered material. The produced diffraction pattern can give information about, among other things, crystallinity, amorphicity, interlayer spacing, graphene stacking and material components.

Electrons are produced from a filament (often tungsten) through thermal emission and accelerated towards a metal target (often copper). Electron bombardment ionises core electrons from metal atoms. Outer shell electrons drop down to fill the vacancies and release photons of x-ray energy, characteristic of the metal target and shell transition. In the case of a copper target, the 2p to 1s transition results in

CuKα radiation with wavelength of 1.5418 Å. This wavelength is on the same scale as interatomic spacings in many materials.[6–8] The material's crystal structure acts as a diffraction grating; constructive interference builds a three-dimensional crystal structure of the material. Bragg's Law (eqn. 2.1) relates the x-ray wavelength to the diffraction angle and lattice spacing of the structure:

$$n\lambda = 2d\sin\theta \qquad \textbf{Eqn. 2.1}$$

where n is an integer, d is the interlayer spacing and θ is the diffraction angle. When the incident x-rays satisfy the Bragg equation, constructive interference occurs and there is a peak in diffraction intensity. Due to the random orientation of a powdered sample, it is scanned through various 2θ angles to

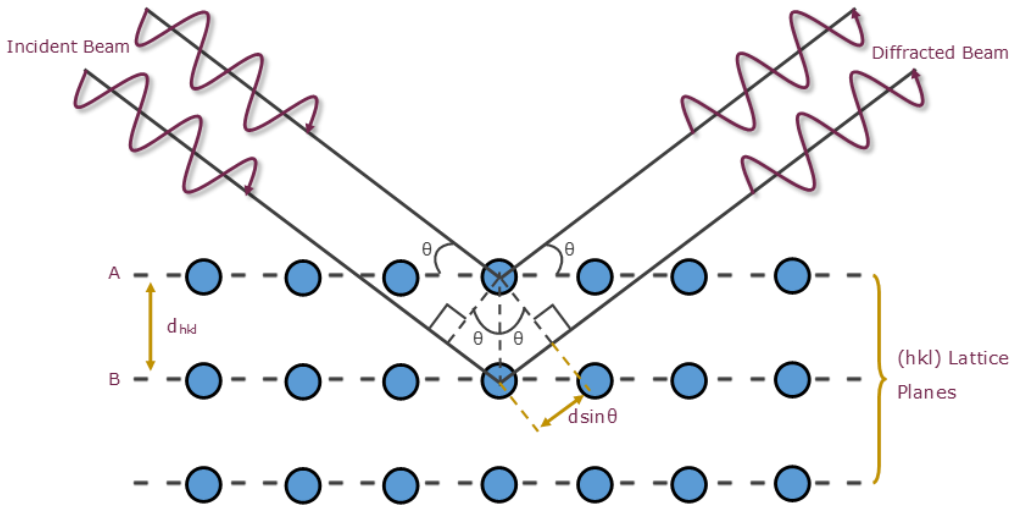

Figure 2.3. Representation of Bragg diffraction

obtain all possible diffraction directions of the structure. A pattern of 2θ vs. diffraction intensity is produced.[6–8]

PXRD patterns of porous carbons show noisy baselines due to the irregular, amorphous structure. Sharp peaks in intensity occur due to inorganic impurities. Peaks at 2θ ≈ 22° and 44° correspond to the diffraction of the 002 and 100 planes of graphene respectively. The intensity and width of these peaks gives information about the regularity and long-range order of the material.[6–8] The height of the peak at 2θ ≈ 22° relative to the baseline can be used in conjunction with the equation:

$$R = B/A \qquad \textbf{Eqn. 2.2}$$

where R represents the average numbers of stacked graphene layers present in the sample, B is the peak intensity at 2θ ≈ 22° and A is the baseline intensity.

2. 5. Gas Sorption Analysis

Gas sorption analysis is a technique used to analyse the textural properties of a material. A non-reactive gas (often N_2 or Ar) is absorbed by a sample over a relative pressure (P/P_0) range of 0 to 1, at a temperature below the critical temperature of the absorbing gas.

A sample is first degassed under vacuum at moderate temperatures for a number of hours, to remove any adsorbed molecules or contaminants. The sample is then held at sub-critical temperature as the absorbing gas is gradually dosed into the sample vessel. After each increment dose, the system is allowed to reach equilibrium, before the system pressure is measured. Graduated measurements take place as gas is dosed until a relative pressure of 1 is reached. The system is then gradually taken back to vacuum and the measurements are repeated to record the desorption process.[9] The resulting isotherm plot of relative pressure vs. quantity absorbed can give information about the textural properties of the sample, as described previously in section 1.4.[9–11] Data from the linear section of the isotherm plot (commonly $P/P_0 \approx 0.05 – 0.4$) can be applied to Bunauer, Emmett and Teller (BET) theory, to calculate surface area, pore volume, microporosity and pore size distribution information.[9,10,12] In this report, replicate analysis of 16 % of samples indicate measurements are within 10.0 % error.

2. 6. CO_2 Uptake

CO_2 uptake can be measured volumetrically or gravimetrically, to assess the efficiency of carbon capture materials. In the case of gravimetric measurement, a sample is first degassed under

vacuum at moderate temperatures for a number of hours to remove any adsorbed molecules or contaminants. For the analysis, a highly accurate microbalance records the changing weight of the sample as CO_2 is dosed into the sample chamber. Measurements are usually recorded from vacuum, to a CO_2 pressure of 20 or 40 bar. The excess uptake of CO_2 is measured, taking into account the compression of CO_2 within the material. Excess adsorption can be calculated using the equation:[13]

$$M_{excess} = \Delta M + V^0_S \times \rho_{gas}(T,p) \qquad \textbf{Eqn. 2.3}$$

where M_{excess} is the excess adsorption, ΔM is the apparent mass change at each sorption step, V^0_s is the skeletal volume of the sample, ρ_{gas} is the gas density at a given pressure and T and p are the temperature and pressure at the isotherm point respectively.

The apparent mass change, ΔM is given by:

$$\Delta M = M_{measured}(T,p) - M^0_s \qquad \textbf{Eqn. 2.4}$$

where $M_{measured}$ is the measured mass at each isotherm point and M^0_s is the dry weight of the sample.

The skeletal volume of the sample, V^0_s is given by:

$$V^0_s = M^0_s/\rho^0_s \qquad \textbf{Eqn. 2.5}$$

where ρ^0_s is the skeletal density of the sample. The consideration of skeletal volume in the calculation of excess adsorption allows for a buoyancy correction of the system.[13] The shape of the resulting isotherm plot provides information on the uptake of CO_2 at various pressures. Replicate analysis of 14 % of the samples indicate measurements are within 7.7 % error.

2. 7. Gas Selectivity Calculations

Calculation of a material's selectivity for CO_2 over N_2 at specific partial pressures is calculated using the ideal adsorbed solution theory (IAST).[14] Sorption isotherms of each gas onto the material are run consecutively, to the respective desired relative partial pressure. In this work, CO_2 uptake was recorded at 0.15 bar while N_2 uptake was recorded at 0.85 bar, to replicate a flue stream gas mixture of CO_2 (15 %) and N_2 (85 %) at atmospheric pressure. IAST predicts mixed gas adsorption isotherms from single component adsorption isotherms.[14] Selectivity of CO_2 over N_2 can be calculated using the equation:[14,15]

$$S = n(CO_2)p(N_2) / n(N_2)p(CO_2) \qquad \textbf{Eqn. 2.6}$$

where S is the selectivity for CO_2, $n(CO_2)$ is the molar uptake of CO_2 at 0.15 bar, $n(N_2)$ is the molar uptake of N_2 at 0.85 bar,

$p(CO_2)$ is the partial pressure of CO_2 and $p(N_2)$ is the partial pressure of N_2.

Selectivity at 1 bar can also be measured using the equilibrium selectivity factor:

$$S_{eq} = n(CO_2)/n(N_2) \qquad \textbf{Eqn. 2.7}$$

where S_{eq} is the equilibrium selectivity for CO_2, $n(CO_2)$ is the molar uptake of CO_2 at 1 bar and $n(N_2)$ is the molar uptake of N_2 at 1 bar.

2. 8. References

1 M. Bird, C. Kietel and W. Meredith, in *Biochar: A Guide to Analytical Methods*, 2017, pp. 39–50.

2 B. D. Ratner, A. S. Hoffman, F. J. Schoen and J. E. Lemons, in *Biomaterials Science - An Introduction to Materials in Medicine (3rd Edition)*, Elsevier, 3rd Editio., 2013, pp. 44–46.

3 J. Goldstein, D. E. Newbury, D. C. Joy, C. E. Lyman, P. Echlin, E. Lifshin, L. Sawyer and J. R. Michael, *Scanning Electron Microscopy and X-Ray Microanalysis Third Edition*, Springer, 2003.

4 University of Cambridge, https://www.eng-atoms.msm.cam.ac.uk/RoyalSocDemos/SEM, (accessed 1 July 2019).

5 J. I. Goldstein, D. E. Newbury, J. R. Michael, N. W. M. Ritchie, J. H. J. Scott and D. C. Joy, *Scanning Electron Microscopy and X-Ray Microanalysis*, Springer, 2017.

6 J. I. Langford and D. Louër, *Reports Prog. Phys.*, 1996, **59**, 131.

7 N. Iwashita, in *Materials Science and Engineering of Carbon - Characterization*, 2016, pp. 7–25.

8 H. G. Brittain, *Spectroscopy*, 2000, **15**, 44.

9 M. Thommes, K. Kaneko, A. V Neimark, J. P. Olivier, F. Rodriguez-reinoso, J. Rouquerol and K. S. W. Sing, 2015, **87**, 1051–1069.

10 M. Thommes, , DOI:10.1002/cite.201000064.

11 A. Dabrowski, *Adv. Colloid Interface Sci.*, 2001, **93**, 135–224.

12 S. Brunauer, P. H. Emmett and E. Teller, *J. Am. Chem. Soc.*, 1938, **60**, 309–319.

13 M. Abunowara, M. A. Bustam, S. Sufian and U. Eldemerdash, *IOP Conf. Ser.Earth Environ. Sci.*, 2016, **36**, 012059.

14 K. S. Walton and D. S. Sholl, *AICHe J.*, 2015, **61**, 2757–2762.

15 B. Adeniran and R. Mokaya, *Chem. Mater.*, 2016, **28**, 994–1001.

Chapter 3 – The Effects of Metal Doping on the Properties of Organic-salt-derived Porous Carbons

3. 1. Abstract

Heteroatom doping has been shown to have the potential to increase the CO_2 uptake capacity of a porous carbon material. This represents a significant advantage in the development of materials to help reduce the effect of CO_2 emissions on the atmosphere. The following study reports the synthesis and analysis of metal doped porous carbons for the application of CO_2 capture. An investigation was carried out into the effects of heteroatom doping in the form of Group 1 and 2 metals on the textural properties, pore structure and CO_2 uptake ability of porous carbons.

Potassium hydrogen phthalate (KHP) was used as a carbon precursor and thermally treated at both 800 and 900 °C to produce carbons with high surface area and pore volume, and a narrow pore size distribution. Samples from each temperature series were subsequently doped with either K, Li, Na or Ba in nitrate form.

Undoped carbon samples had excellent surface areas and pore volumes of up to 1700 $m^2\ g^{-1}$ and 0.86 $cm^3\ g^{-1}$ respectively,

with a highly microporous structure. They exhibited a good CO_2 uptake of up to 4.1 mmol g^{-1} at 1 bar and 25 °C.

Metal doping was found to reduce the accessibility of the carbon pore structure, with this effect generally increasing with decreasing metal ion size. This reduction in measurable porosity resulted in surface areas and pore volumes ranging from 3 – 1655 m^2 g^{-1} and 0.01 – 0.81 cm^3 g^{-1} respectively. CO_2 uptake of the metal doped porous carbons ranged from 0.1 – 3.5 mmol g^{-1} (0.1 – 2.3 mmol cm^{-3}) at 1 bar and 25 °C. Adsorbance selectivity over N_2 under flue gas conditions calculated using the IAST method reached 45, while the equilibrium selectivity factor reached 19.

3. 2. Introduction

Many factors affect the CO_2 uptake capacity of activated carbons. The pore structure has the greatest effect on CO_2 uptake; microporous structures with a narrow pore size distribution (PSD) centred below 10 Å perform well at low pressures ≤ 1 bar. A hierarchical pore structure allows for fast diffusion through pore channels, while a large surface area is the most determining factor when adsorbing CO_2 at higher pressures of 20 – 40 bar.[1–5]

The carbon skeleton can be regarded as disordered planes of graphene with short range order. The aromatic structure gives rise to delocalised π electrons in the carbon basal plane, therefore the carbon skeleton can be considered as inherently basic.[6] However, due to its weak basicity, activated carbon is commonly considered a homogenous surface, with CO_2 molecules adsorbing onto the surface through relatively weak intermolecular forces. This can leave room for improvement in terms of uptake capacity. Heteroatom doping onto the carbon skeleton in order to increase the polarity of the surface and enhance dipole-dipole interactions, is therefore an important area of research within the activated carbon field. As CO_2 is a Lewis acid, research has focused heavily on nitrogen doping in order to form basic nitrogen-containing groups such as amine

and pyridinic groups on the surface, as well as encouraging the formation of hydrogen bonds.[7,8]

Xu *et al*.[9] activated camphor leaves with KOH to produce N-doped porous carbons. The camphor leaves acted as a natural nitrogen source due to the nitrogen found in the DNA and proteins of the plant. The activated carbons were highly microporous with high surface areas of up to 1736 m^2 g^{-1} and nitrogen content up to 3.0 wt%. However, CO_2 uptake at 1 bar and 25 °C was shown to be proportional to the degree of microporosity; the sample with the highest CO_2 uptake at these conditions of 3.74 mmol g^{-1} had the largest proportion of microporosity and a nitrogen content of only 1.5 wt%.[9]

Chen *et al*.[10] produced N-doped porous carbons through KOH activation of crab shells, which acted as both a carbon source and a naturally occurring nitrogen source. The resulting carbons were highly microporous and exhibited CO_2 uptake of up to 4.37 mmol g^{-1} at 1 bar and 25 °C. However, high CO_2 uptake did not correspond with high nitrogen content; the presence of micropores was the dominating factor contributing to high uptake. The sample with the highest nitrogen content (8.5 wt%) exhibited the highest adsorption selectivity over N_2 at 1 bar and 25 °C of 23.1.[10]

Jeon *et al*.[11] produced N-doped porous carbons using resorcinol as a carbon source and melamine as a nitrogen source. It was shown that N-doping reduced the surface area and pore volume when measured through BET analysis. Surface area was reduced by 23 – 86 % while pore volume was reduced by 59 – 94 % compared to the equivalent undoped carbon. CO_2 uptake of the N-doped carbons of up to 2.70 mmol g^{-1} was recorded at 1 bar and 25 °C.[11]

Wang *et al*.[12] produced 3 types of zeolite-templated porous carbons using either furfuryl alcohol or acetonitrile to produce undoped and N-doped carbons respectively. In all 3 cases, the N-doped carbons displayed reduced surface area and pore volume compared to the undoped equivalent samples. However, two of the samples showed improved CO_2 uptake compared with the undoped equivalents, of up to 4.0 mmol g^{-1} at 1 bar and 25 °C.[12]

Park *et al*.[7] produced N-doped porous carbons through KOH activation of a lignin-derived hydrochar. Nitrogen was doped post-activation, using urea as the nitrogen source. Again surface area, and in most cases pore volume, of the N-doped samples were reduced compared with the undoped equivalent. CO_2 uptake at 1 bar and 25 °C increased with nitrogen content;

the sample with the highest nitrogen content of 1.17 wt% exhibited the highest CO_2 uptake of 2.70 mmol g^{-1}.[7]

It is clear that many researchers have produced N-doped carbons that exhibit both excellent low pressure CO_2 uptake and selectivity over N_2. However, some studies cast doubt on the dependence of CO_2 uptake on nitrogen-based functionalities. Adeniran *et al*.[13] produced a series of carbons from various precursors which had equivalent porosities but were either N-doped or N-free. This allowed a systematic assessment of the effect of N-doping on CO_2 uptake. It was shown that N-doping had no beneficial effect on CO_2 uptake, rather it was heavily dependent on the volume of pores sized 5 – 10 Å.[13] Sevilla *et al*.[14] conducted a similar study, whereby N-doped and N-free carbons with equivalent pore structures were compared in terms of CO_2 uptake under flue gas conditions (25 °C and 0 – 1 bar). They also concluded that under such conditions, CO_2 uptake depended on pore size and distribution, and nitrogen content had no effect on uptake.[14]

Activated carbons contain oxygen functionalities inherently, due to the presence of oxygen in precursors and activating agents. Common oxygen functionalities found on the carbon surface include carboxyl, phenol and diketone groups.[6] While pristine graphite is hydrophobic, the polar nature of oxygen

functionalities increases the hydrophilicity of activated carbon, resulting in competition for uptake between CO_2 and H_2O. Due to the natural oxygen content of activated carbons, it is difficult to conduct controlled experiments to assess the impact of oxygen doping on CO_2 uptake.

Sulphur-doped carbons have been explored for various uses and have been synthesised through the use of a sulphur-containing carbon precursor, as well as post-activation hydrogen sulphide (H_2S) reduction of oxygen functionalities.[15–17]

Porous carbons doped with alkaline metal ions is a less commonly researched field of activated carbons. Doping with metal ions would be expected to increase the heterogeneity and polarity of the carbon surface, thereby increasing selectivity and uptake efficiency of CO_2. The formation of metal hydroxides on the surface may further increase the uptake through the formation of hydrogen bonds. Zhao *et al*.[18] synthesised a series of carbons that were either pure carbon, or contained nitrogen, potassium or chlorine ions, or a combination. At 1 bar, samples containing both nitrogen and potassium, and samples containing both nitrogen and chlorine had comparably high CO_2 uptakes of 4.04 and 4.03 mmol g^{-1}, respectively. Samples doped with nitrogen or potassium only, also showed comparable

uptakes. All doped samples showed considerably higher uptakes than the pure carbon control sample, showing that the presence of heteroatoms had a positive effect on CO_2 uptake, although it was difficult to distinguish between the effects of N-doping and K-doping. Samples doped with both nitrogen and potassium demonstrated good selectivity under flue gas conditions of up to 48.[18]

Kim *et al*.[19] investigated the CO_2 uptake and selectivity of N and Na-doped carbons. Carbons containing both N and Na exhibited the highest CO_2 uptake (4.48 mmol g^{-1}) and selectivity for CO_2 over N_2 (69) at 1 bar compared to equivalent N-doped and pristine carbon samples. The high CO_2 selectivity was attributed to the narrow microporous structure (< 7 Å) and the high content of Na and N based, strongly basic sites.[19]

Adelodun *et al*.[20] synthesised micro- and mesoporous carbons from coconut shell and coal that were impregnated with potassium and various amine groups. The amination process was found to stabilise reactive potassium groups resulting in successful doping of the two functionalities. Doping with K and N surface groups reduced pore size, resulting in a more microporous structure seen in the originally more mesoporous structure of the coal-based carbon. The coconut shell-based carbon had a more microporous structure, and had smaller

pores blocked off after doping, resulting in a reduced microporous structure, therefore poorer performance compared with coal-based samples. The combination of K and N-based surface groups provided good CO_2 uptake and selectivity, however there was no clear comparison with equivalent pristine samples.[20]

In 2015, Zhu *et al*.[21] activated carbonised London Plane leaves with KOH and washed only with distilled water. As a result, naturally occurring nitrogen and metal elements were preserved as dopants, specifically Mg and Ca. CO_2 uptake of up to 4.4 mmol g^{-1} at 1 bar and 25 °C was achieved for a sample with surface composition of N (1.3 at%), Mg (0.3 at%) and Ca (1.1 at%). An undoped equivalent sample achieved CO_2 uptake under the same conditions of 4.2 mmol g^{-1}.[21]

In 2016, Zhu *et al*.[22] activated pine cones with KOH and again washed only with distilled water. The resulting porous carbons were naturally doped with Si and Ca. CO_2 uptake of up to 4.8 mmol g^{-1} at 1 bar and 25 °C was achieved for a sample with surface composition of N (0.5 at%), Ca (0.5 at%) and Si (0.6 at%). An equivalent sample washed with acid, with surface composition of N (1.0 at%) and Si (0.5 at%) achieved CO_2 uptake of 4.5 mmol g^{-1}.[22] However, in both studies conducted by Zhu *et al*., the activation condition used produced a more

significant effect on CO_2 uptake than the presence of dopants.[21,22]

Away from activated carbons, Zhang *et al*.[23] synthesised Li and Na-exchanged zeolites, which showed improved CO_2 uptake at 1 bar compared with a control sample. Ca, K, Mg and Ba-exchanged zeolites showed an increasingly negative effect on CO_2 uptake compared to the control. The differences in effect shown by different metal ions was attributed to the differences in the strength of the electrostatic field of each metal-exchanged sample, as well as the differing pore sizes and volumes of each sample.[23]

Cao *et al*.[24] synthesised MOF-199 doped with $LiNO_3$, $NaNO_3$ or KNO_3. Up to an 11 % increase in CO_2 uptake capacity was observed compared with undoped MOF-199 at 25 °C and 18 bar.[24]

Overall, research into metal doped carbons for CO_2 capture has so far been limited. The study reported in this chapter aims to develop the research in this field by investigating the CO_2 uptake capacity of porous carbons doped with Group 1 and 2 metal nitrates. The aim of this study was threefold. Firstly, the efficiency of the chosen doping method was assessed. Secondly, the effect of the presence of the metal ions on the

CO_2 uptake efficiency and selectivity was measured. Finally, the effect of the presence of the metal ions on the accessibility of the carbon pore network was examined.

Potassium hydrogen phthalate (KHP) was chosen as a carbon rich precursor, as it has been shown in previous studies to produce activated carbons reliably, with high surface area and pore volume and a narrow PSD in the small micropore range (5 – 8 Å).[5] KHP is an organic metal salt with a carbon content of 47 % and a C/K molar ratio of 7.8.

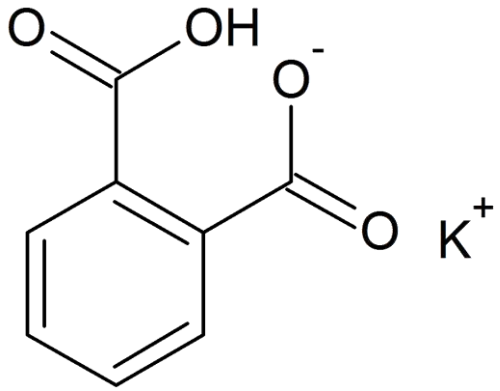

Figure 3.1. Potassium Hydrogen Phthalate (KHP)

KHP is 'self-activating'; KOH is generated upon heating so activated type carbon can be obtained directly, eliminating the need to add an activating agent. The metals were doped on to the carbon structure post-activation in nitrate salt form. The four Group 1 and 2 metals were chosen due to their range in size and electrostatic potential. Carbons were produced at either 800 or 900 °C to investigate the effect of metal ions on different pore structures. Undoped control equivalents were

produced in order to assess the effect of metal doping accurately.

3. 3. Material Synthesis, Characterisation and Analysis

Potassium Hydrogen Phthalate (KHP) was thermally treated as follows; KHP (2 g) (99 %, Alfa Aesar) was heated in a horizontal alumina furnace at a ramp rate of 10 °C min^{-1} to the required temperature (800 or 900 °C) under a flow of nitrogen (100 mL min^{-1}). The samples were held at the target temperature for 1 hr before being allowed to cool to room temperature, all under nitrogen flow. Samples were washed in deionised water (400 mL) for 2 hrs before being collected by vacuum filtration and dried in air at 100 °C for 24 hrs.

Metal doping was carried out by dissolving metal nitrates (10 wt% with respect to activated carbon) in just enough deionised water (~ 2-3 mL) and adding dropwise to the activated carbons. Samples from each temperature series were doped with either lithium nitrate (>98 %, Merck), sodium nitrate (99 %, Sigma Aldrich), potassium nitrate (99 %, Sigma Aldrich) or barium nitrate (99 %, Alfa Aesar). The metal doped samples were dried in air at 80 °C for 12 hrs before being heated in a horizontal alumina furnace in air at 200 °C for 2 hrs. One sample from each activation temperature series was left undoped as a control.

The final samples were denoted KHPx-m, where x represents the activation temperature of the activated carbons (800 or 900 °C) and m represents the doped metal ion (Li, Na, K or Ba).

Various methods were used to characterise and analyse the samples. Elemental analysis was carried out using a CE-440 Elemental Analyzer, Exeter Analytical, INC. Samples were combusted in oxygen at 975 °C.

Scanning electron microscopy was conducted using a Zeiss Evo 10 SEM machine with a tungsten filament, operating with a 10 kV accelerating voltage.

Energy dispersive x-ray spectroscopy analysis was conducted alongside SEM analysis using an EDAX analyser. The presence of C, O, Na and K was confirmed with K_α x-rays. The presence of Ba was confirmed with L_α x-rays.

Thermal gravimetric analysis was carried out using a TA Instruments Analytical SDTQ600 TGA machine. Samples were heated at a ramp rate of 10 °C min^{-1} to 1000 °C in air.

Powder x-ray diffraction analysis was carried out using a PANalytical X'Pet Pro diffractometer using CuKα radiation (λ = 1.5418 Å), operating at 40 kV and 40 mA. A step size of 0.026° and a step time of 300.9 s was used.

Analysis of textural properties was carried out by nitrogen sorption at -196 °C. An initial degassing stage was conducted using a Micromeritics SmartVac Prep degasser wherein samples were held under vacuum at 230 °C for 16 hours. The following analysis was carried out using a Micromeritics 3Flex. Surface areas were calculated using the BET model, from adsorption data within the linear isotherm plot (relative pressure (P/P_0) of 0.04 0.09). Total pore volumes were calculated from the nitrogen uptake close to saturation pressure ($P/P_0 \approx 0.99$). Micropore surface areas and pore volumes were calculated using t-plot analysis. Pore size distributions were determined by applying non-local density functional theory (NLDFT) to the nitrogen adsorption isotherms.

Gas uptakes were measured using a Hiden Isochema XEMIS machine. After an initial degassing stage, where samples were held under vacuum at 230 °C for 14 hours, analysis was carried out with either CO_2 or N_2 as the adsorbing gas, at 25 °C and at pressures from 0 – 40 bar.

3. 4. Results and Discussion

3. 4. 1. Elemental Analysis

The carbon, hydrogen and nitrogen content of all samples, measured by elemental analysis are shown below in Table 3.1.

Due to the differing relative molecular masses of the metals used and the metals being doped on by wt%, the carbon content of the metal doped samples would be expected to be lowest for Li-doped samples. This would be expected to increase for Na-doped samples, then K-doped samples and finally, Ba-doped samples would be expected to show the largest carbon content, in line with the increasing molecular masses of the metals. As expected, this trend is generally seen in both sample sets.

The nitrogen content of the metal doped samples can be attributed to the metals being doped in nitrate form and generally decreases with increasing metal ion size. The hydrogen content is very low in all samples, which is to be expected for porous carbons.

Table 3.1. Elemental analysis results of all samples, calculated through elemental microanalysis

Sample	C%	H%	N%
KHP800-K	63.4	1.0	2.6
KHP800-Li	34.1	1.3	10.3
KHP800-Na	59.7	0.6	5.8
KHP800-Ba	66.3	0.3	2.1
KHP800	71.9	0.7	N/A
KHP900-K	60.1	1.0	2.8
KHP900-Li	38.6	1.8	7.7
KHP900-Na	77.4	0.2	1.8
KHP900-Ba	80.6	N/A	0.9
KHP900	83.7	0.4	N/A

3. 4. 2. Scanning Electron Microscopy and Energy Dispersive X-Ray Spectroscopy Analysis

Scanning electron microscopy was used to produce images of representative samples to give a visual representation of the structure and information about the distribution of metals across the carbon surface. Energy dispersive x-ray (EDX) spectroscopy was used to analyse and map elements on the particle surfaces. Figures 3.2 – 3.6 show the micrographs produced by secondary electron (SE) imaging and EDX mapping and analysis for all samples activated at 900 °C. Figure 3.2 [A] shows a SE produced image of KHP900. The image shows some irregular shaped particles with a high degree of surface roughness, alongside larger particles with a smooth surface. Wide openings of ~ 5 μm show surface access to the internal micropore structure. Figure 3.2 [B] shows a carbon structure with no other detectable elements other than a very low oxygen presence. Figure 3.3 [A] shows the SE image of KHP900-K. As with KHP900, there is a mixture of small, irregular, rough surfaced particles alongside larger, smoother particles with microscale openings. Figure 3.3 [C] shows K dispersed across the entire carbon surface, indicating high metal coverage. Figure 3.3 [D] shows the presence of oxygen on the carbon

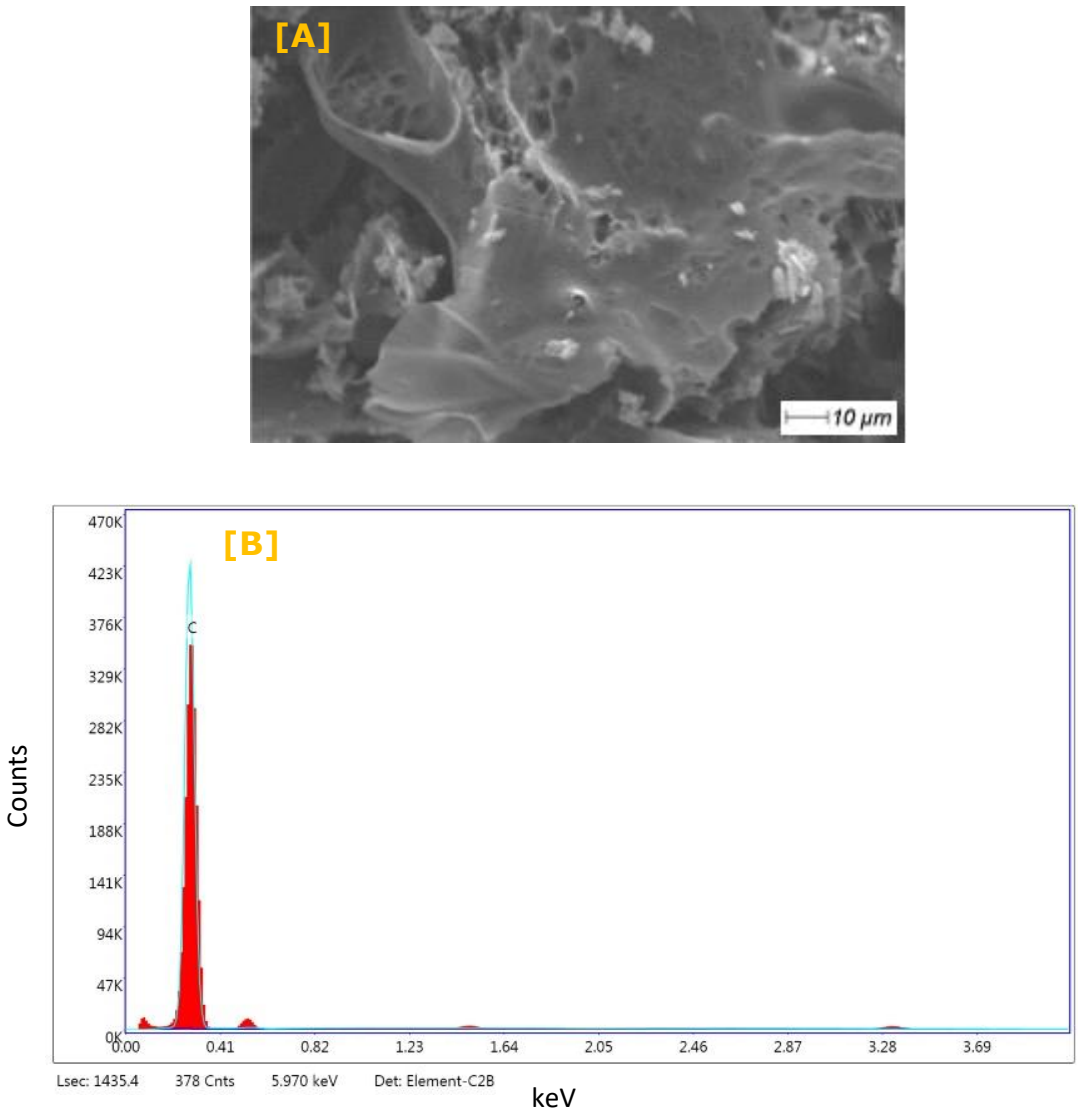

Figure 3.2. SEM images and EDX analysis of KHP900. [A] shows a SE produced image. [B] is the EDX spectrum

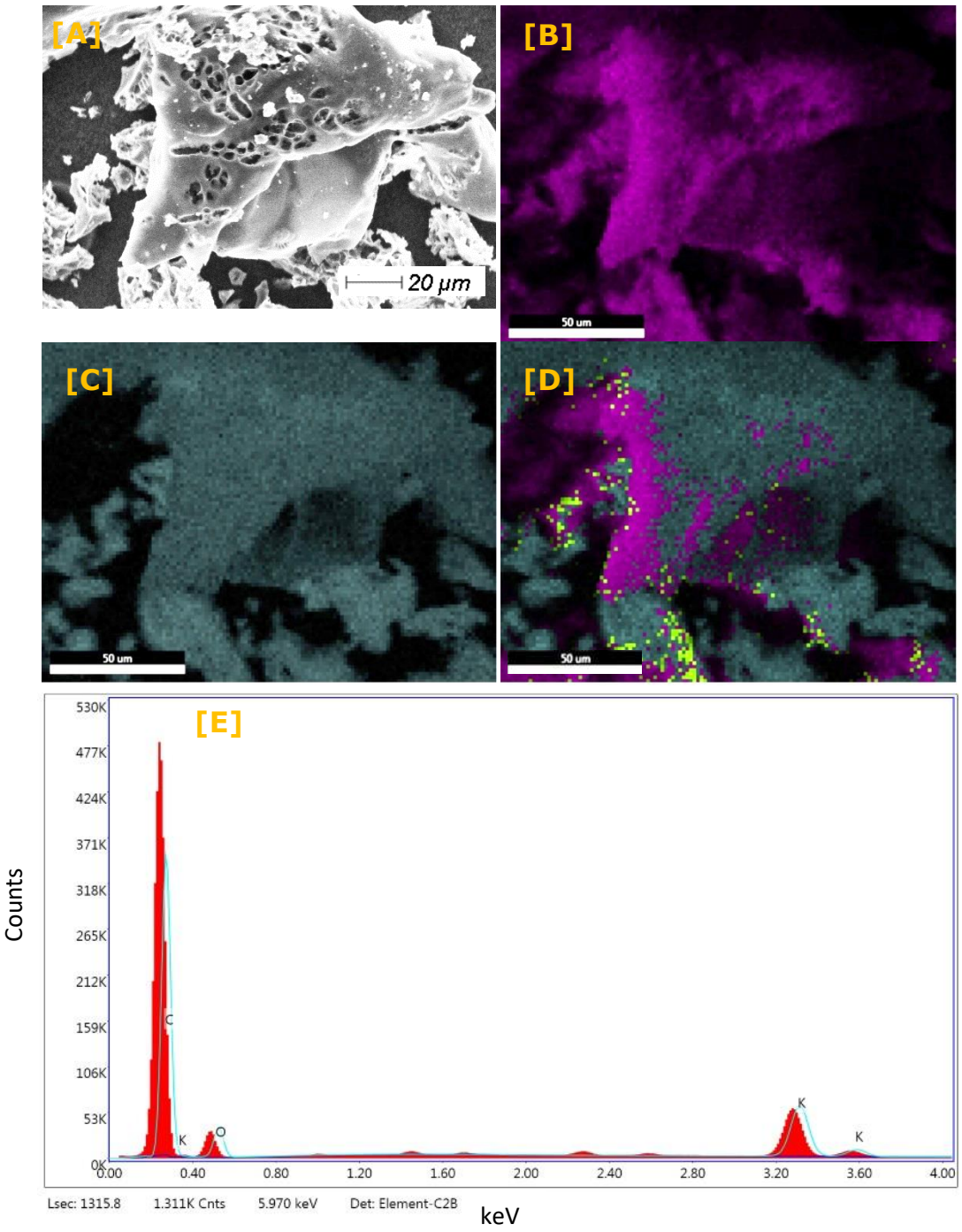

Figure 3.3. SEM images and EDX analysis of KHP900-K. [A] shows a SE produced image. [B] and [C] show elemental mapping of C (purple) and K (dark blue) respectively. [D] shows elemental mapping overlay of C (purple), K (dark blue) and O (green). [E] is the EDX spectrum

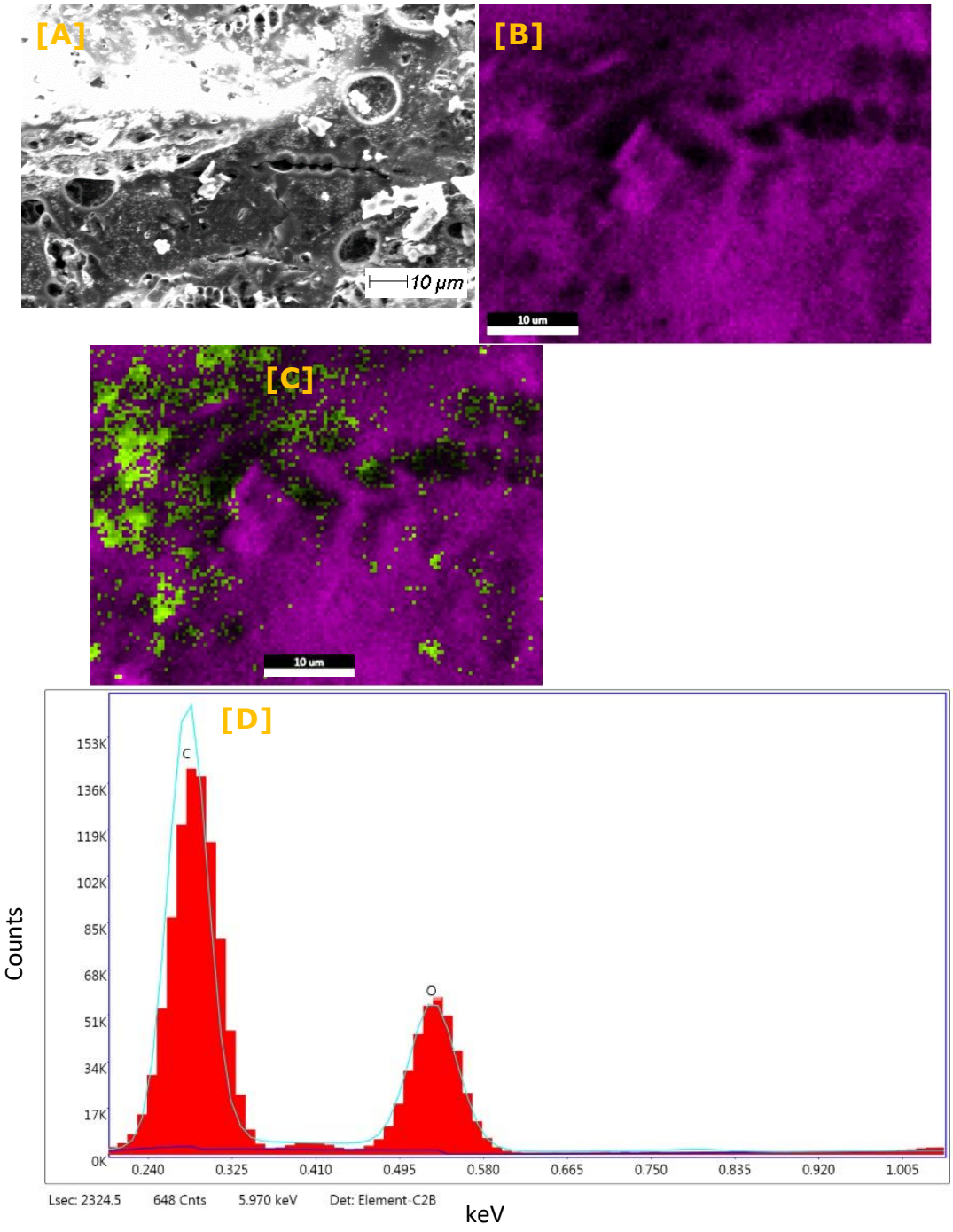

Figure 3.4. SEM images and EDX analysis of KHP900-Li. [A] shows a SE produced image. [B] shows elemental mapping of C (purple). [C] shows elemental mapping overlay of C (purple) and O (green). [D] is the EDX spectrum

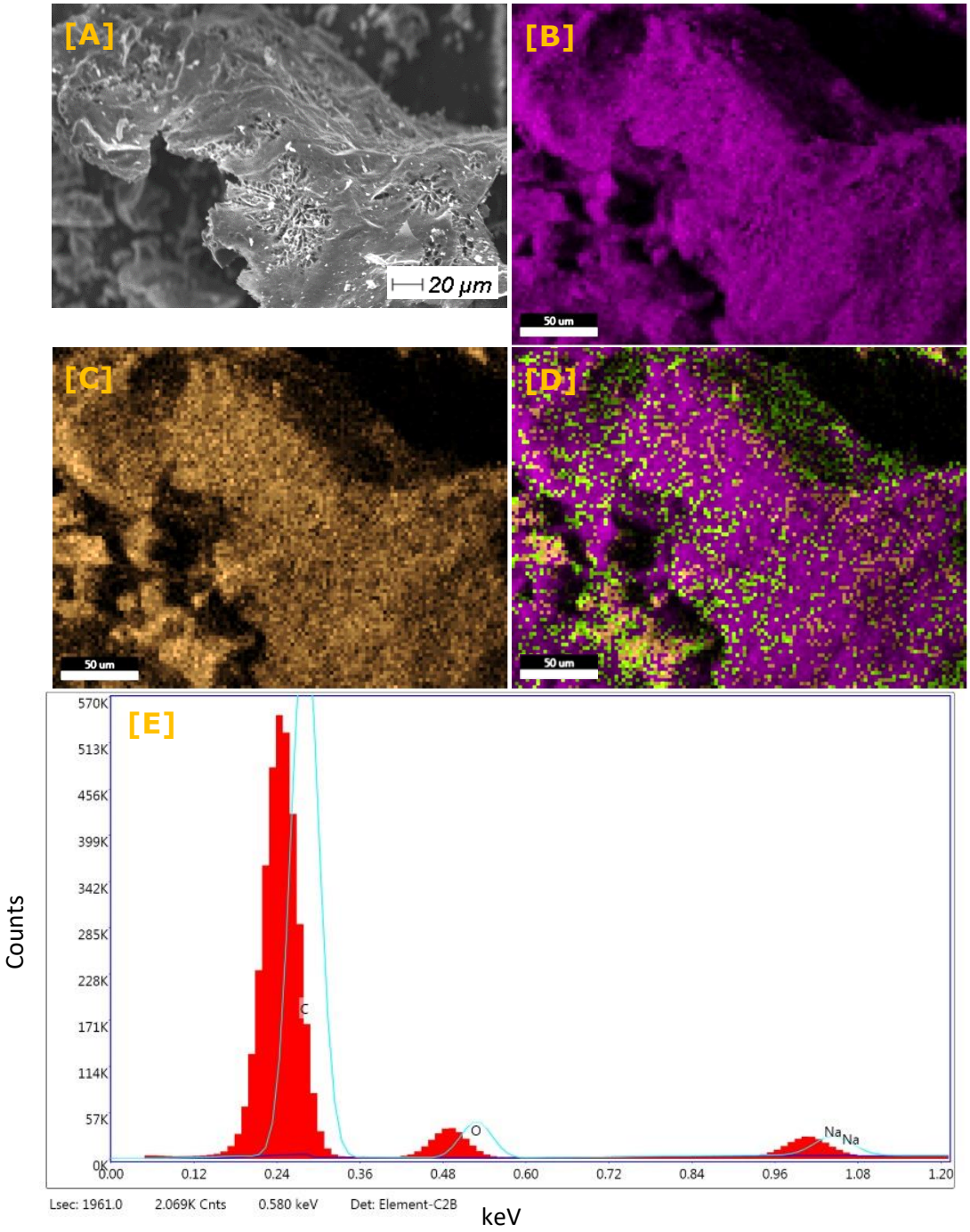

Figure 3.5. SEM images and EDX analysis of KHP900-Na. [A] shows a SE produced image. [B] and [C] show elemental mapping of C (purple) and Na (brown). [D] shows elemental mapping overlay of C (purple), Na (brown) and O (green). [E] is the EDX spectrum

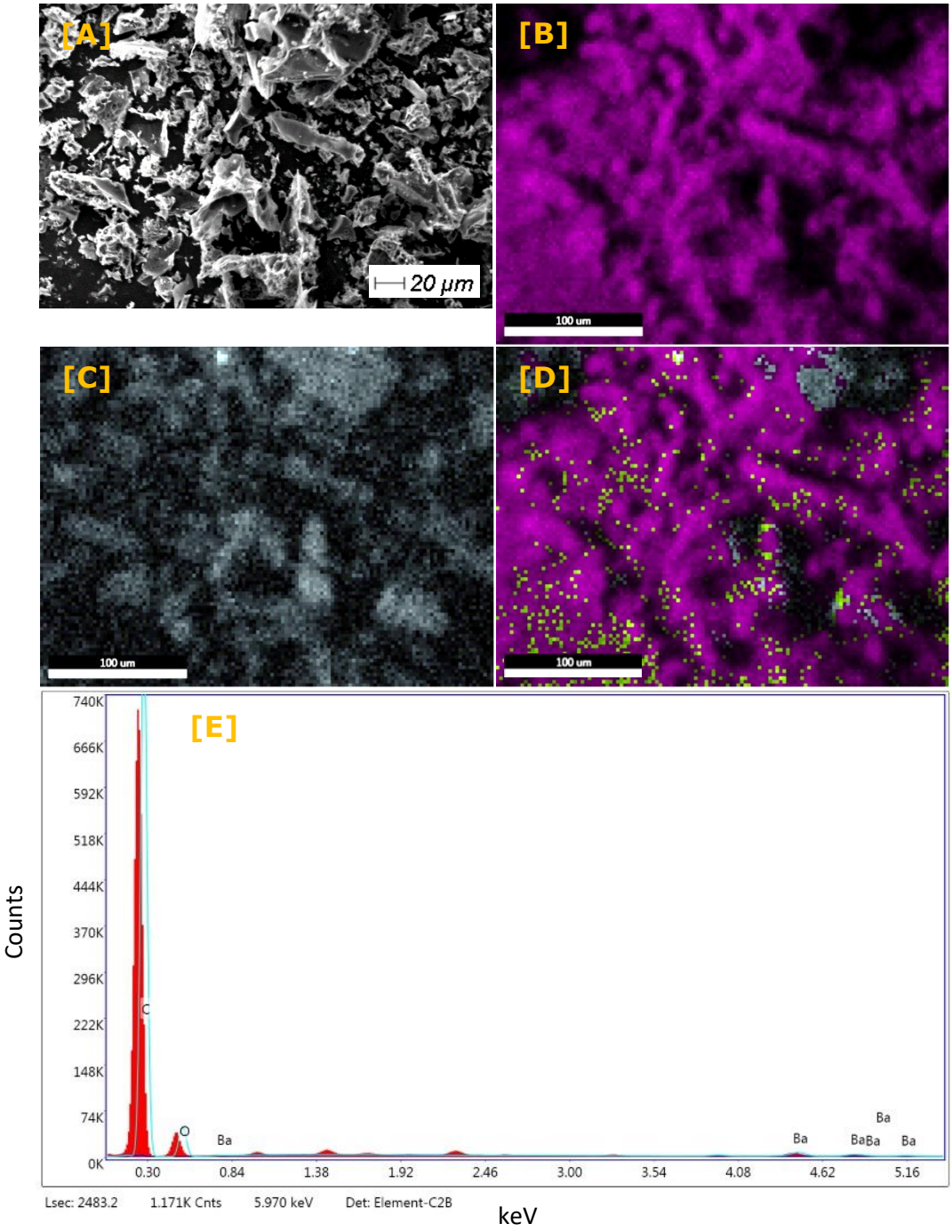

Figure 3.6. SEM images and EDX analysis of KHP900-Ba. [A] shows a SE produced image. [B] and [C] show elemental mapping of C (purple) and Ba (grey). [D] shows elemental mapping overlay of C (purple), Ba (grey) and O (green). [E] is the EDX spectrum

surface. Figure 3.3 [E] shows the EDX spectra for KHP900-K. C, K and O were the only detectable surface elements. Figure 3.4 [A] shows the SE produced image of KHP900-Li. It shows some large conchoidal cavities on the particle surface with some regular microscale openings. Figure 3.4 [B] and [C] show EDX mapping of the carbon surface with oxygen being the only additional element present. Li would not be expected to be detectable through SE imaging or EDX mapping, due to its low atomic weight. However, Li can be assumed to be present in the sample due to the abundant presence of oxygen on the particle surface.

Figure 3.5 [A] shows the SE produced image of KHP900-Na. Areas of regular, layered pore openings are visible on an otherwise relatively smooth particle surface. Figure 3.5 [B], [C] and [D] show EDX mapping of the particle surface. Na is distributed across the whole carbon surface and there is a substantial oxygen presence. Figure 3.5 [E] shows no other elements detected.

Figure 3.6 [A] shows the SE produced image of KHP900-Ba. The image shows small, irregular particles with rough surfaces, and as with other samples, areas of regular, microscale surface openings. Figure 3.6 [B] and [C] show EDX mapping of carbon and Ba on the surface respectively. As with the previous metal

doped samples, Figure 3.6 [C] shows Ba dispersed evenly across the particle surfaces. As with the other metal doped samples, Figure 3.6 [D] shows the presence of oxygen, indicating the metal is present in oxide form. Figure 3.6 [E] shows the EDX spectra for KHP900-Ba, confirming the surface presence of only the 3 expected elements.

EDX mapping shows a pristine carbon particle surface for KHP900, with only negligible oxygen content. For the metal doped samples, an even distribution of metal covers the entire carbon surface, although this is not confirmed for KHP900-Li. Significant oxygen presence only occurs on the surface of metal doped samples. Firstly, this can be used to assume the presence of Li on the surface of KHP900-Li. Secondly, this shows that metal doped carbon reacts in air to form oxygenated surface groups, therefore the metal is present in an oxide form.

Overall, the KHP derived samples comprise of irregularly shaped particles with expanded layering, typical of porous carbons. Large openings of ~ 10 μm demonstrate the porous nature of the samples and provide substantial access to the internal pore system. Metal ions are distributed evenly across the particle surface, accompanied by a high oxygen presence.

3. 4. 3. Thermal Gravimetric Analysis

Thermal gravimetric analysis (TGA) was performed to assess the structure, purity and thermal stability of all the carbon samples. The TGA plots for all samples are shown below in Figures 3.7 and 3.8. Some samples show a small mass loss at ~ 100 °C. This can be attributed to moisture loss and assumed to be associated with the length of time the sample spent exposed to the atmosphere, as opposed to any structural differences.

All samples show a rapid mass loss in the range 260-380 °C. This can be attributed to carbon burn off, and the rapid decrease in weight indicates single phase materials.[25] Generally, all samples activated at 800 °C have a lower thermal stability than the equivalent samples activated at 900 °C. This is to be expected, as exposure to higher temperatures during activation encourages increased formation of thermally stable graphitic domains.

Generally, among the metal doped samples, thermal stability is lowest for the Li-doped samples, which increases for K-doped samples, then Na-doped samples, and finally, Ba-doped samples show the highest thermal stability. This indicates that metal doping has some effect on the carbon structure.

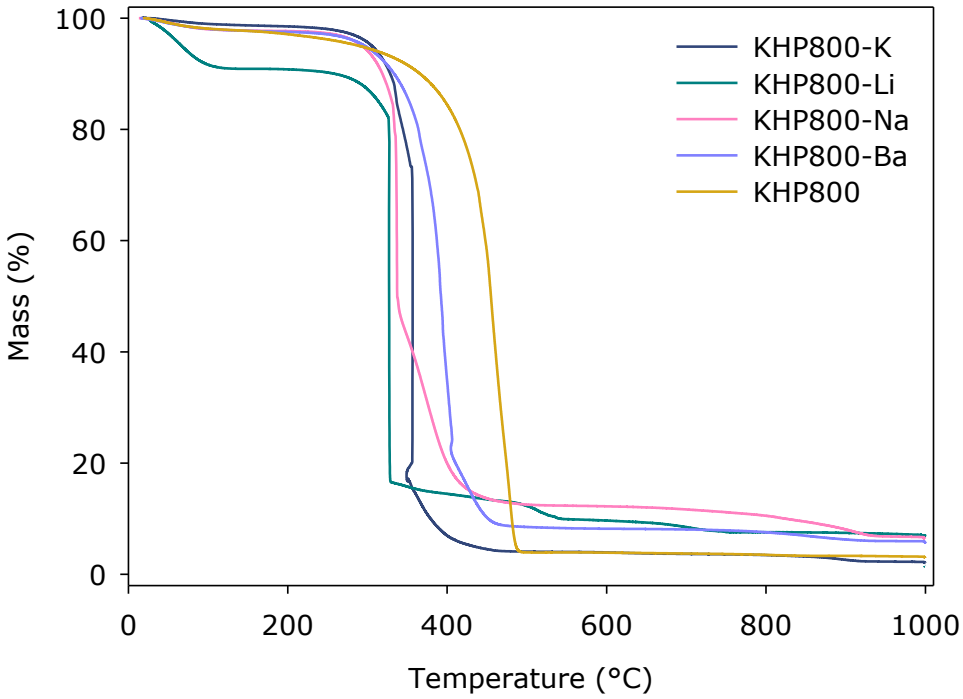

Figure 3.7. TGA plots of samples activated at 800 °C

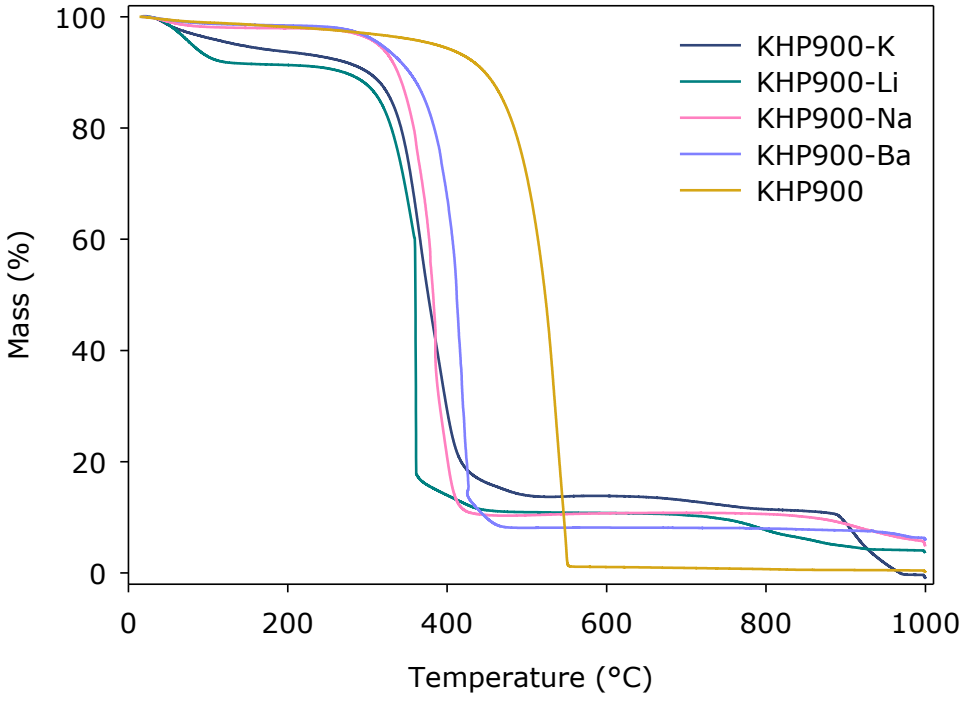

Figure 3.8. TGA plots of samples activated at 900 °C

Intercalation of the metal ions into the laminar carbon structure would cause disruption of any graphitic domains, thereby lowering thermal stability. Thermal stability decreases with the size of doped metal ion, indicating that a higher degree of intercalation and graphitic disruption occurs with the smaller metal ions.

Residual weight is reasonably high for most samples, ranging from 1-12 % for the metal doped samples. This residual weight can be attributed to the metal content of samples, as well as potassium compounds formed during activation and not removed during the washing process. The undoped samples have the two lowest residual weights due to the lack of metal content. Any residual weight in these two samples is attributed to remaining potassium compounds formed during KHP activation.

By factoring out mass loss due to water evaporation and the residual weight of porous carbon at 700 °C, the content of metal compounds can be calculated. Looking at the 900 series, residual mass due to metal compounds at 700 °C for KHP900-K, KHP900-Li, KHP900-Na and KHP900 Ba is 13.1, 10.5, 10.2 and 7.3 % respectively. This gives a metal compound content of 10.2 $\pm$ 2.9 %. Assuming the metal is in nitrate form, this gives a metal content for KHP900-K, KHP900-Li, KHP900-Na

and KHP900-Ba of 5.1, 1.1, 2.8 and 3.8 % respectively. This gives a metal content of 3.1 $\pm$ 2 %.

3. 4. 4. Powder X-Ray Diffraction Analysis

Powder x-ray diffraction (PXRD) was used to assess the purity, structure and level of graphitisation of all the carbon samples. The diffraction patterns are shown below in Figures 3.9 and 3.10. The particular areas of interest of the PXRD patterns are peaks at 2θ ≈ 22° and 44°, as these correspond respectively to diffraction of the (002) and (100) planes of stacked graphite. The very low angle region of the pattern (< 15°) was featureless in regard to the sample analysis, so is not reported here.

The peak centred at 2θ = 22°-26° corresponds to the (002) diffraction plane of graphite and shifts slightly between samples. The intensity of this peak corresponds to the average number of stacked graphene layers within a sample, and therefore the regularity and level of graphitisation of the sample. The peak centred at 2θ ≈ 44° corresponds to the (100) plane. The XRD patterns show that KHP800 and KHP900 both show the expected peaks for amorphous carbon at 2θ = 22° and 44°. For both samples, these peaks are relatively broad and flat, indicating that both the undoped samples have an amorphous structure with low levels of graphitisation. This can be further confirmed by the R value of the peaks at 2θ = 22°, which for both samples is 1.1; nearly all graphene layers are

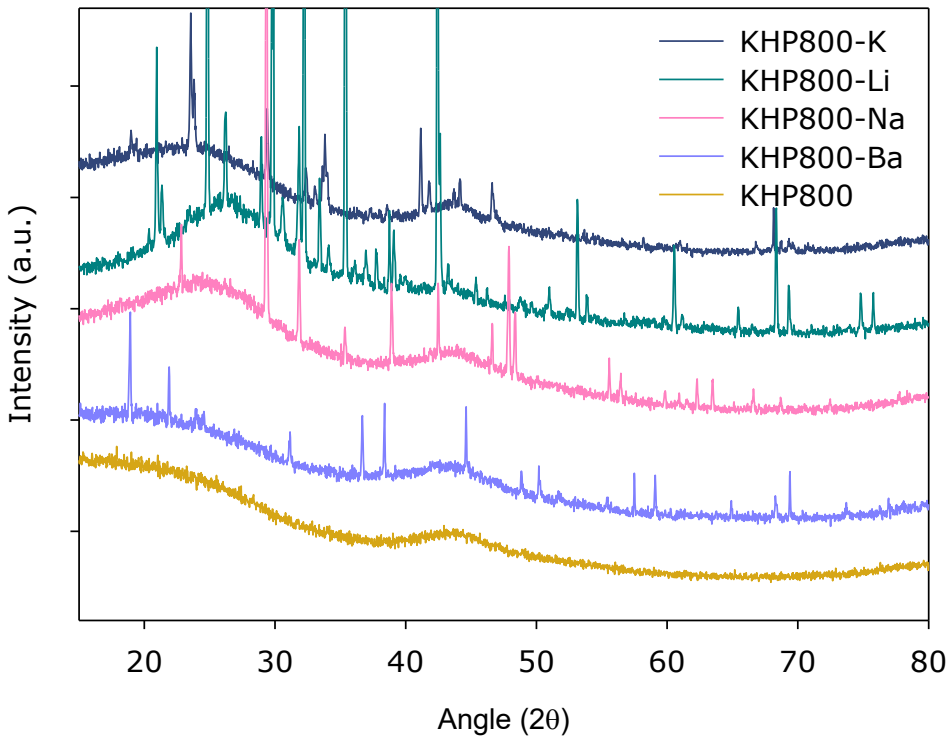

Figure 3.9. PXRD patterns of samples activated at 800 °C

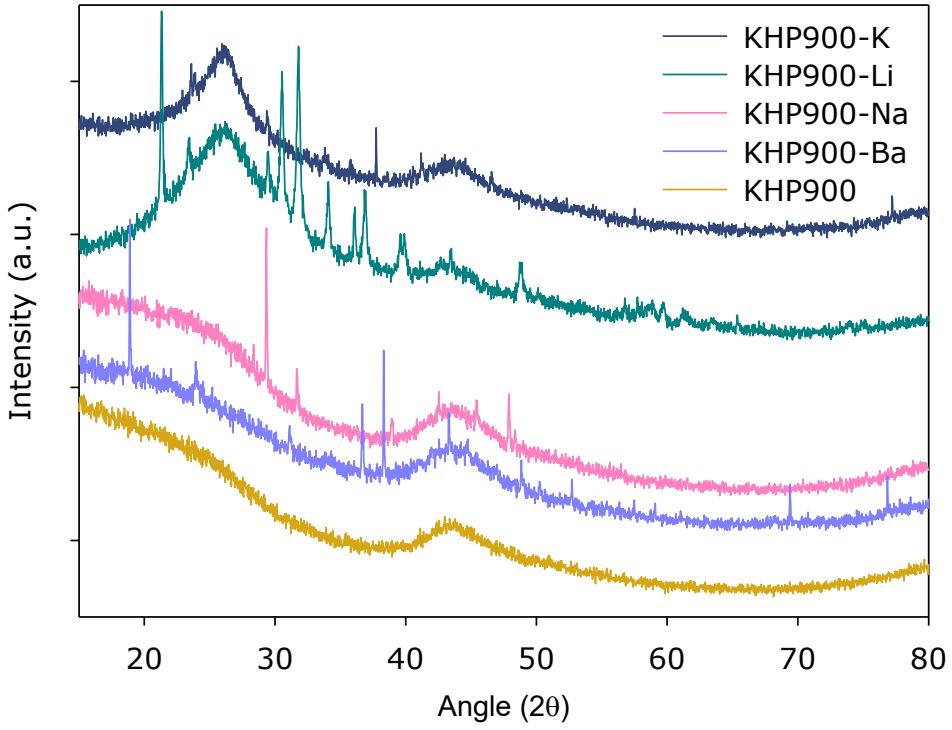

Figure 3.10. PXRD patterns of samples activated at 900 °C

singularly stacked. The lack of sharp peaks on the spectrums for KHP800 and KHP900 indicate clean carbon samples with no impurities.

Both KHP800-Ba and KHP900-Ba have a low and broad peak centred at 2θ ≈ 22°, both with corresponding R values of 1.1, indicating highly amorphous samples that differ little in carbon structure to the equivalent undoped samples. The (002) peak of KHP800-Na is slightly sharper than the equivalent undoped sample, with a corresponding R value of 1.5. KHP900-Na shows a broad flat peak at 2θ ≈ 22°, equivalent to that of KHP900 with a corresponding R value of 1.2. Both KHP800-Li and KHP900-Li show a considerably sharper and more intense (002) peak than the equivalent undoped samples, with corresponding R values of 1.9 and 2.0 respectively. The PXRD pattern therefore appears to indicate that doping with lithium greatly increases the apparent graphitisation and regularity of the carbon structure. KHP800-K and KHP900-k both show a sharper (002) peak than the equivalent undoped samples, with corresponding R values of 1.4 and 1.7 respectively. KHP900-K shows a greater apparent increase in graphiticy compared with KHP800-K.

Overall, doping with barium has little effect on the apparent graphitic structure of the carbon. Generally, doping with sodium, potassium and then lithium has an increasing effect on

the apparent graphitic structure. There is no clear trend in the effect of activation temperature on the regularity of resulting metal doped carbon samples.

As mentioned previously, both undoped samples show the expected peak corresponding to the reflection of the (002) plane of graphite centred at 2θ = 22°. This peak remains at 2θ = 22° for Ba doped samples, but is shifted to 2θ = 25° for Na-doped samples, 2θ = 26° for Li-doped samples and 2θ = 24° and 26° for KHP800-K and KHP900-K respectively. This shift to larger values of 2θ indicates a decrease in interlayer spacing (*d*) of stacked surface graphene layers. The size of the shifts shows that the interlayer spacing generally decreases in the order of Ba-doped samples > K-doped samples > Na-doped samples > Li-doped samples. A possible explanation for this could be the hygroscopic nature of the metal hydroxides. Pristine carbons absorb moisture from the atmosphere onto the surface layers. Metal ions on the particle surface in the form of hygroscopic hydroxides may be absorbing the water molecules, causing contraction of the surface carbon layers. Due to the metal being doped onto the carbon as wt%, a greater number of Li ions will be found on the carbon surface than Ba, Na or K ions; this would result in a greater absorbance of surface moisture and therefore greater contraction of the surface layers. This contraction may

also explain the general increase in regularity of the samples as the respective doped metal ions decrease in size.

All the metal doped samples show very sharp peaks throughout the PXRD spectrums. This confirms the presence of metal on the sample surfaces, and corresponds with different crystalline forms of the metals. They are not seen in the pristine, undoped samples, which can be regarded as 'clean' by TGA analysis. The peaks in the PXRD patterns were compared to peaks in reference patterns of the metals in various forms. As shown below in Figures 3.11 – 3.14, the doped metals were found to be in the nitrate form.

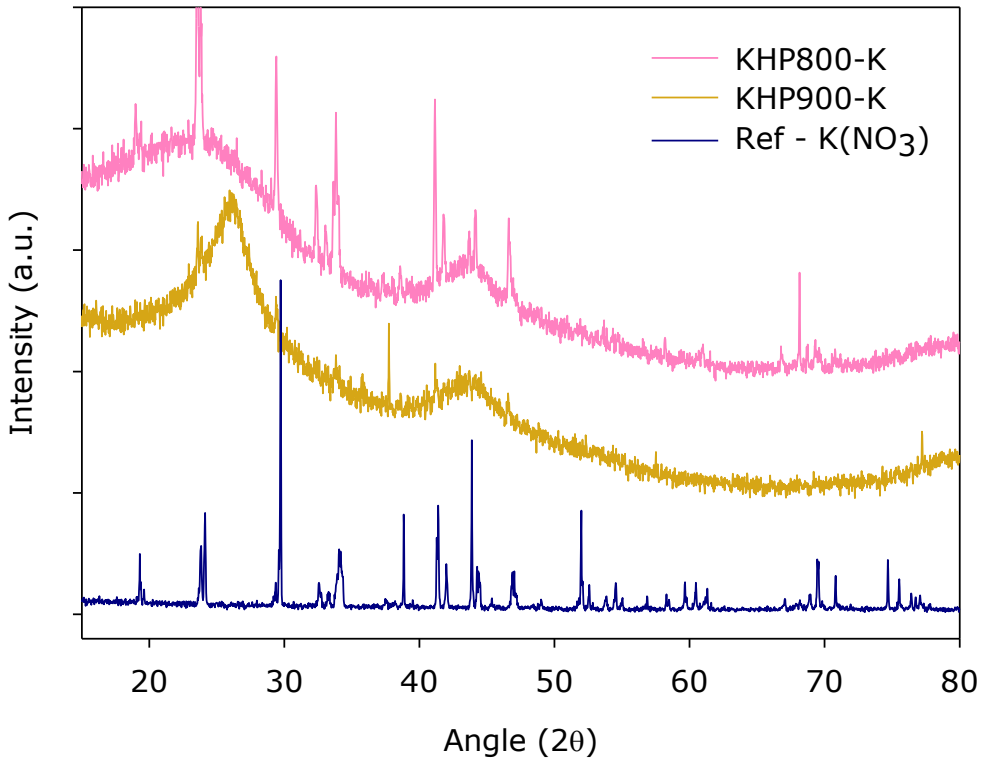

Figure 3.11. Comparative PXRD patterns of KHP800-K, KHP900-K and $K(NO_3)$

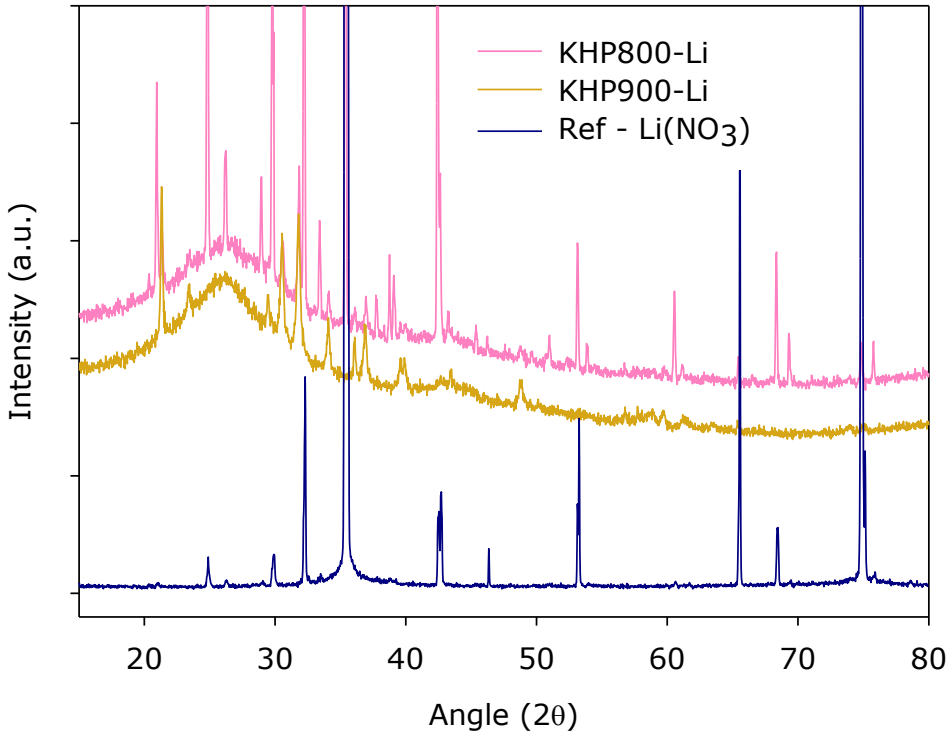

Figure 3.12. Comparative PXRD patterns of KHP800-Li, KHP900-Li and $Li(NO_3)$

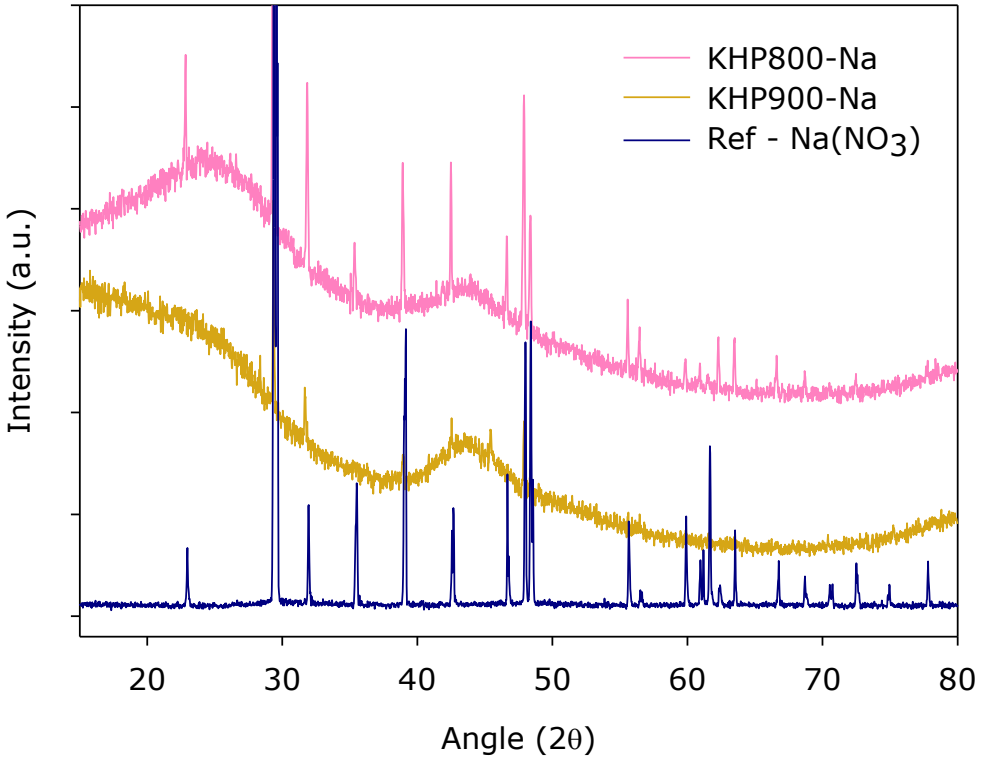

Figure 3.13. Comparative PXRD patterns of KHP800-Na, KHP900-Na and $Na(NO_3)$

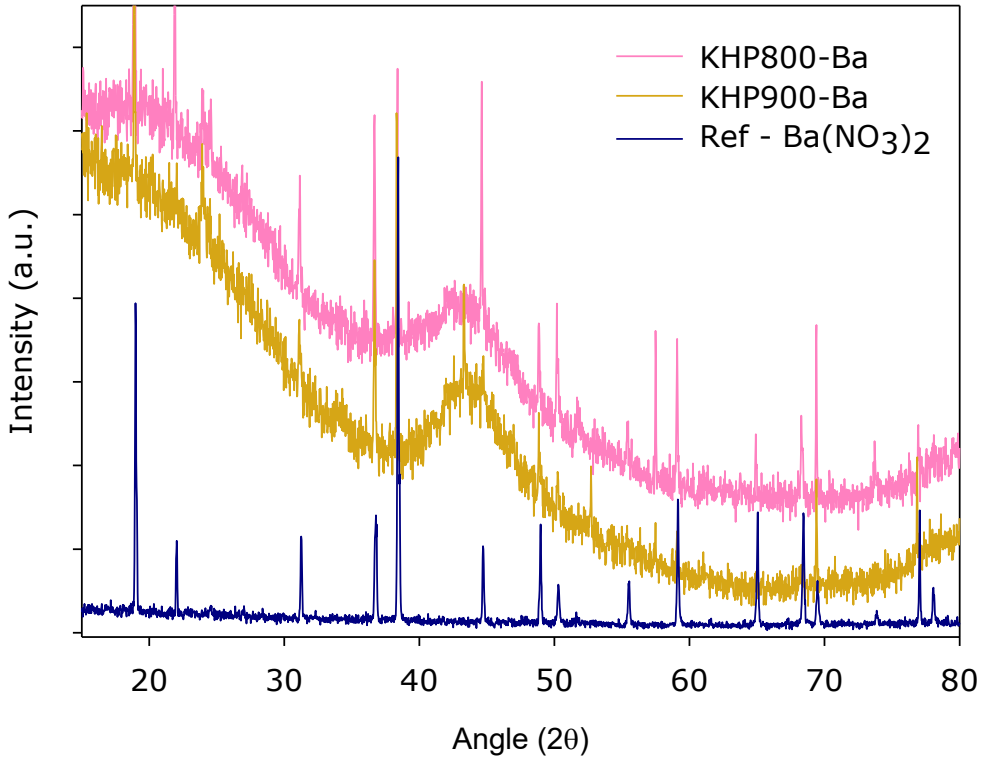

Figure 3.14. Comparative PXRD patterns of KHP800-Ba, KHP900-Ba and $Ba(NO_3)_2$

3. 4. 5. Nitrogen Sorption Isotherms

The N_2 sorption isotherms, recorded at -196 °C are shown below in Figures 3.15 and 3.16.

The undoped samples both show a type I isotherm with high nitrogen uptake, indicating the microporous structure with high surface area that is expected when activating KHP under such conditions.[5] Comparing these isotherms with those for metal doped samples shows that the microporous structure has been retained after metal doping, indicated by the type I isotherms seen for all metal doped samples. However, post-activation metal doping has a large effect on the nitrogen uptake of the carbons, depending on the metal used for doping. Doping with Ba has little effect on the nitrogen uptake, but increasing effect is seen when doping with Na, K and then Li, in the case of both activation temperatures. Nitrogen uptake is a good indicator of sample surface area. Therefore, the isotherms indicate that when compared with undoped samples, Ba-doped samples will show a similar measured surface area, but this decreases when doping with Na, K and mostly with Li. Samples doped with Li show a very low, almost negligible nitrogen uptake. This indicates that metal doping reduces the accessibility of the pore structure in regards to nitrogen uptake. The particular metal used affects the extent of this effect.

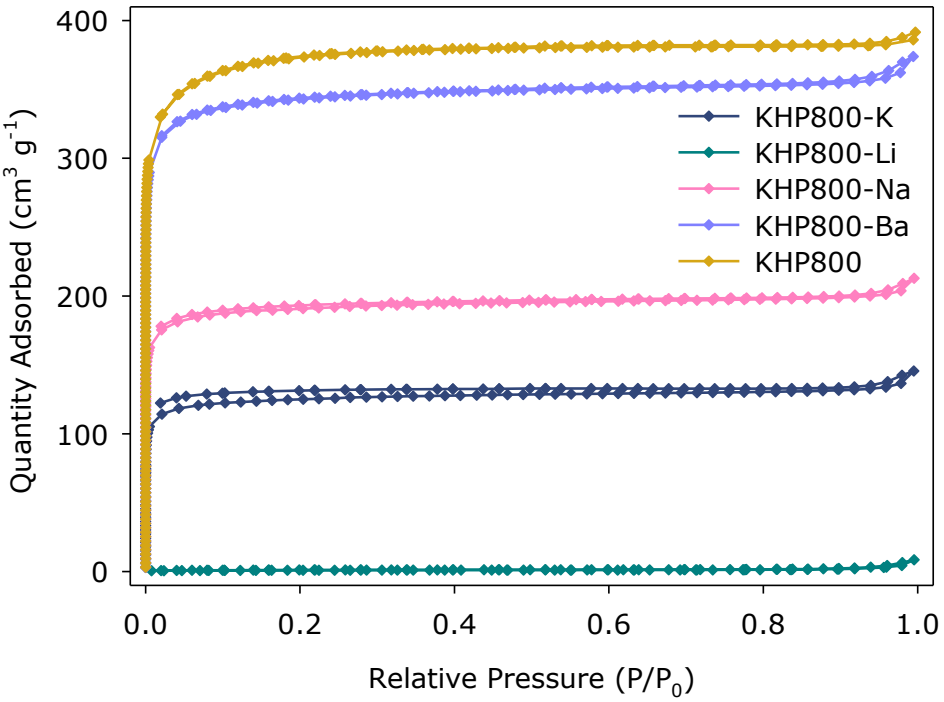

Figure 3.15. Sorption isotherms for samples activated at 800 °C

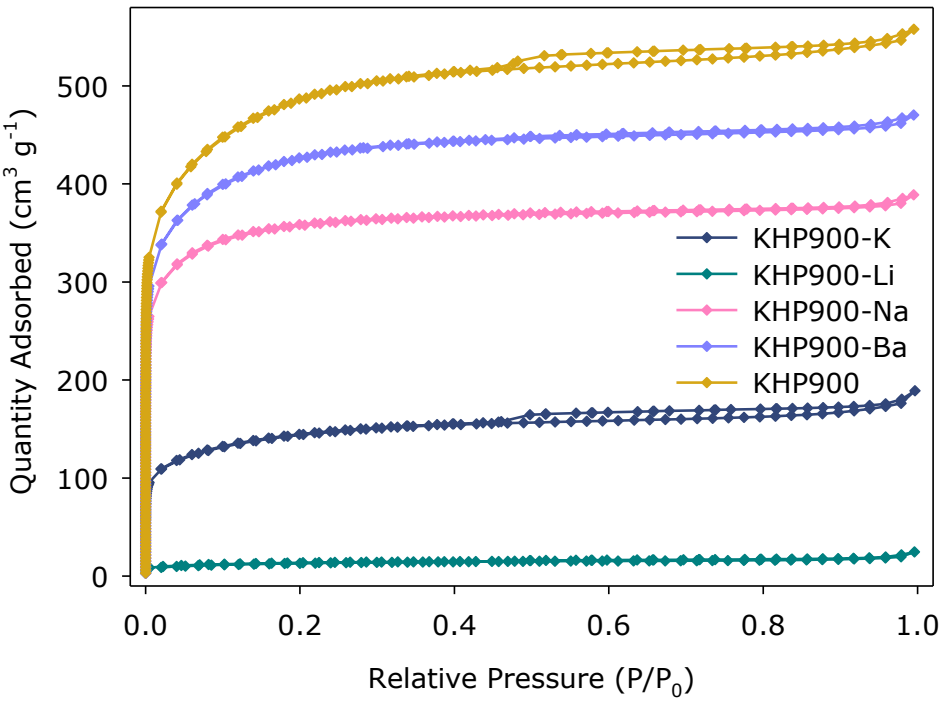

Figure 3.16. Sorption isotherms for samples activated at 900 °C

Samples activated at 900 °C generally display higher nitrogen uptake than samples activated at 800 °C; this can be attributed to higher levels of activation taking place at the higher temperature, leading to a more developed porosity. KHP900-K and KHP900 both show a slight hysteresis, indicating the presence of a small mesoporous volume.

Overall, the isotherms show that all samples have a highly microporous structure with little, if any, mesoporosity. Post activation metal doping has clear negative effects on the nitrogen uptake ability of samples depending on the metal used.

An N_2 molecule has a kinetic diameter of 3.64 Å[26], therefore contraction of surface layers resulting in an interlayer spacing < ~ 3.7 Å would greatly reduce the ability of adsorbing N_2 molecules to enter the internal particle pore network. This would dramatically reduce the internal surface area and pore volume that could be measured during N_2 sorption analysis. K, Na and Li-doped samples all show an interlayer spacing of the (002) plane of < 3.7 Å, which may explain the reduction in N_2 uptake of these samples compared with the undoped equivalents.

3. 4. 6. Textural Properties; Surface Area and Pore Volume

The surface area and pore volume data, calculated from the N_2 sorption isotherms, are displayed below in Tables 3.2 and 3.3.

The undoped samples show the high surface area and high level of microporosity expected from using KHP as the starting material.[5] KHP800 has a surface area and pore volume, with corresponding microporosity of 1324 $m^2\ g^{-1}$ (96 %) and 0.61 $cm^3\ g^{-1}$ (92 %) respectively, while KHP900 has a surface area and pore volume, with corresponding microporosity of 1700 $m^2\ g^{-1}$ (85 %) and 0.86 $cm^3\ g^{-1}$ (76 %) respectively. The higher surface area and pore volume, coupled with a lower proportion of microporosity seen for KHP900 is to be expected, as more extensive activation reactions take place at the higher temperature. This results in greater amounts of gases, such as CO_2 and CO evolving, creating new pores and widening existing channels. Smaller pores collapse into larger pores, contributing to the decrease in microporosity.[27–30]

The surface areas show the trends expected from sorption isotherm analysis. All of the metal doped samples show a reduction in surface area to varying degrees compared with the equivalent undoped samples. KHP800-Ba and KHP900-Ba show only a small reduction in surface area and pore volume

Table 3.2. Surface area of all samples, calculated by BET theory. [a]Proportion of surface area arising from micropores, as a value and as a % of total surface area

Sample	Surface Area ($m^2\ g^{-1}$)	[a]Micropore Surface Area ($m^2\ g^{-1}$)
KHP800-K	444	416 – 94%
KHP800-Li	3	2 – 67 %
KHP800-Na	678	642 – 95%
KHP800-Ba	1220	1167 – 96%
KHP800	1324	1270 – 96%
KHP900-K	505	402 – 80%
KHP900-Li	48	36 – 75 %
KHP900-Na	1263	1177 – 93%
KHP900-Ba	1655	1485 – 90%
KHP900	1700	1447 – 85%

compared with the respective equivalent undoped samples. In the case of KHP900-Ba, this is accompanied by a small increase in microporosity. It may be that large Ba ions are blocking access to some of the larger mesopores, thereby increasing the measured proportion of microporosity.

Table 3.3. Pore volume of samples prepared from KHP. [a]Proportion of pore volume arising from micropores, as a value and as a % of total pore volume

Sample	Pore Volume ($cm^3\ g^{-1}$)	Micropore Volume ($cm^3\ g^{-1}$)
KHP800-K	0.23	0.18 – 78%
KHP800-Li	0.01	N/A
KHP800-Na	0.33	0.28 – 85%
KHP800-Ba	0.58	0.51 – 88%
KHP800	0.61	0.56 – 92%
KHP900-K	0.29	0.18 – 62%
KHP900-Li	0.04	0.02 – 50%
KHP900-Na	0.60	0.52 – 87%
KHP900-Ba	0.81	0.66 – 81%
KHP900	0.86	0.65 – 76%

Na doped samples exhibit the second smallest reduction in surface area and pore volume. KHP800-Na has a surface area of 678 $m^2\ g^{-1}$ and a pore volume of 0.33 $cm^3\ g^{-1}$, which represent a 49 and 46 % decrease respectively, compared with KHP800. KHP900-Na has a surface area of 1263 $m^2\ g^{-1}$ and a

pore volume of 0.6 cm^3 g^{-1}, which represent a 26 and 30 % decrease respectively, compared with KHP900.

K doped samples exhibit the second largest reduction in surface area and pore volume. KHP800-K has a surface area of 444 m^2 g^{-1} and a pore volume of 0.23 cm^3 g^{-1}, which represent a 66 and 62 % decrease respectively, compared with KHP800. KHP900-K has a surface area of 505 m^2 g^{-1} and a pore volume of 0.29 cm^3 g^{-1}, which represent a 70 and 66 % decrease respectively, compared with KHP900.

Finally, Li doped samples show very low levels of porosity; the porosity of KHP800-Li can be regarded as negligible. KHP900-Li has a surface area of 48 m^2 g^{-1} and a pore volume of 0.04 cm^3 g^{-1}, which represent a 97 and 95 % decrease respectively, compared with KHP900.

Overall, these textural properties follow the expected trends predicted from analysis of the N_2 sorption isotherms. Although reasonable microporosity is generally maintained throughout both sample sets, doping with the alkali metals studied has varying negative effects on the measurable porosity of the carbon materials. While doping with Ba has a relatively minimal effect, doping with Li renders the measurable porosity negligible.

3. 4. 7. Textural Properties; Pore Size Distributions

Pore size distributions (PSDs) and pore maxima values for all samples were calculated using non-local density functional theory and are displayed below in Figures 3.17 and 3.18 and Table 3.4.

All samples activated at 800 °C show no volume above a pore width of 15 Å, confirming highly microporous samples. With the exception of KHP800-Li, which displays negligible porosity, all samples activated at 800 °C have pore maxima at widths of 8.6 and 11.8 Å. KHP800-K and KHP800-Na both show pore volume below the minimum pore width seen for KHP800. This may be assumed to be the result of K and Na ions partially blocking surface pores.

With the exception of KHP900-Li, all samples activated at 900 °C show highly microporous structures with low levels of small mesopore volume. This may be attributed to the creation of wider pore channels as well as more extensive pore collapse during activation at the higher temperature. As with the previous sample set, all samples show pore maxima at 8.6 and 11.8 Å. These maxima are consistently retained from the parent carbon. KHP900-Na and KHP900-Ba both show pore volume below the minimum pore width seen for KHP900. Again, this

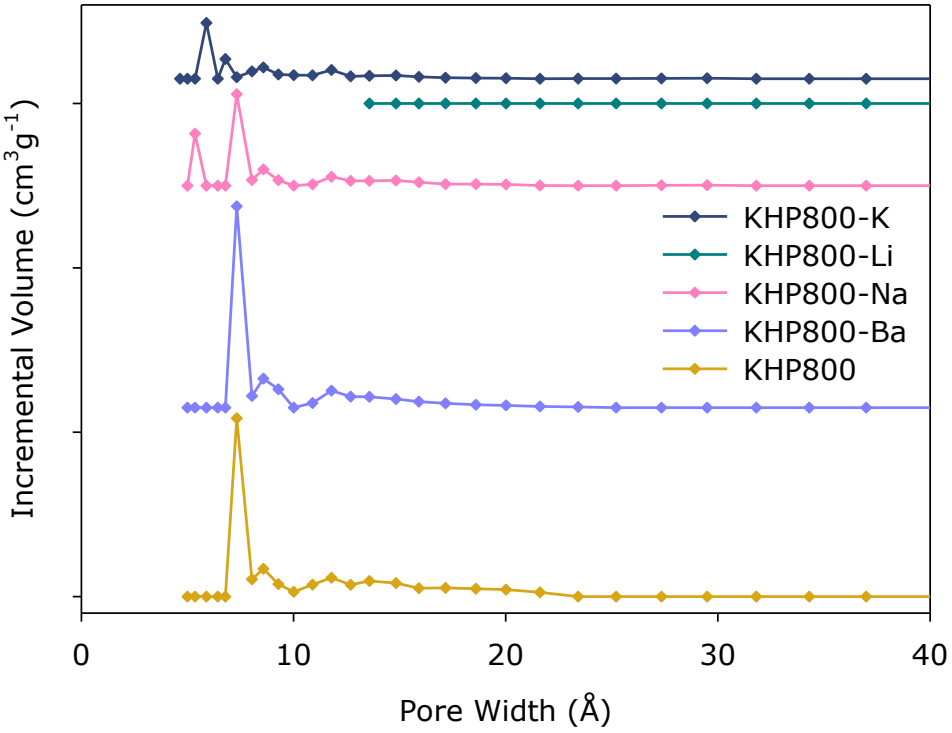

Figure 3.17. PSDs for samples activated at 800 °C

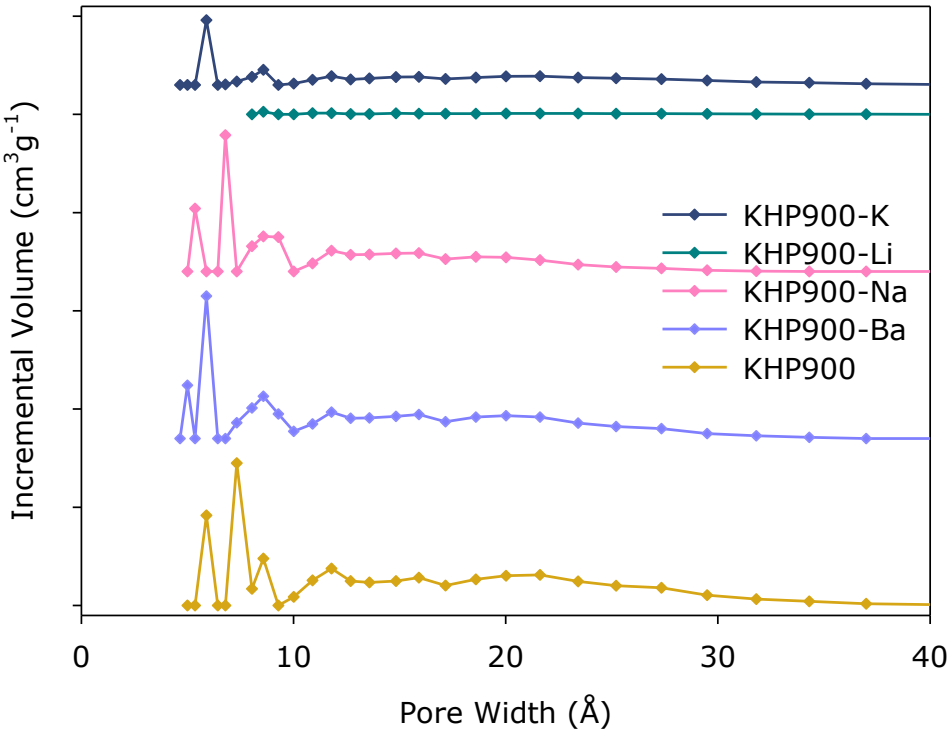

Figure 3.18. PSDs for samples activated at 900 °C

Table 3.4. PSD maxima of samples prepared from KHP, obtained from NLDFT analysis

Sample	Pore Maxima (Å)	
	< 20 Å	**> 20 Å**
KHP800-K	5.9/6.8/8.6/11.8/14.6	N/A
KHP800-Li	N/A	N/A
KHP800-Na	5.4/7.3/8.6/11.8/14.8	N/A
KHP800-Ba	7.3/8.6/11.8/14.8	N/A
KHP800	7.3/8.6/11.8/13.6	N/A
KHP900-K	5.9/8.6/11.8/14.8	21.6
KHP900-Li	8.6/11.8	N/A
KHP900-Na	5.4/6.8/8.6/11.8/15.9	20.0
KHP900-Ba	5.0/5.9/8.6/11.8/15.9	20.0/27.3
KHP900	5.9/7.3/8.6/11.8/15.9	21.6/27.3

may be assumed to be the result of Na and Ba ions partially blocking surface pores.

Overall, all samples, with the exception of Li doped samples, show highly microporous samples with narrow PSDs centred ~ 6 – 8 Å. Such structures would be expected to exhibit high uptake capacities for low pressure CO_2 uptake ≤ 1 bar. Some samples, for example KHP800-K, KHP900-K and KHP900-Ba, have a slightly smaller average pore width than the respective

equivalent undoped carbons. This may be assumed to be due to partial pore blocking by metal ions and may also be due to contraction of surface carbon layers due to presence of hygroscopic metal hydroxides.

3. 4. 8. CO_2 Uptake Analysis

The CO_2 uptake capabilities of the carbon samples were analysed gravimetrically at 25 °C, over a pressure range of 0 – 40 bar. The adsorption isotherms up to 1 bar and 40 bar are shown below in Figures 3.19 – 3.22. The gravimetric and volumetric molar uptakes for the samples at a range of pressures is displayed in Tables 3.5 and 3.6. It is important to analyse CO_2 uptake capabilities at very low pressure of 0.15 bar to simulate typical conditions of a post-combustion flue gas stream. Analysis at 1 bar gives further information about low pressure uptake, while analysis at 20 and 40 bar provides uptake information at medium and high pressure respectively.

KHP800 and KHP900 both show excellent CO_2 uptake across the range of pressures. KHP800 performs better at low pressures of ≤ 1 bar due to its high microporosity; this sample absorbs 1.2 mmol g^{-1} of CO_2 at 0.15, which is among the highest reported in the literature.[5,31–33] KHP900 performs better at 20 and 40 bar due to its high surface area.[4,5,31,32,34,35]

Both KHP800-Li and KHP900-Li show poor CO_2 uptake across the range of pressures due to their low levels of accessible porosity.

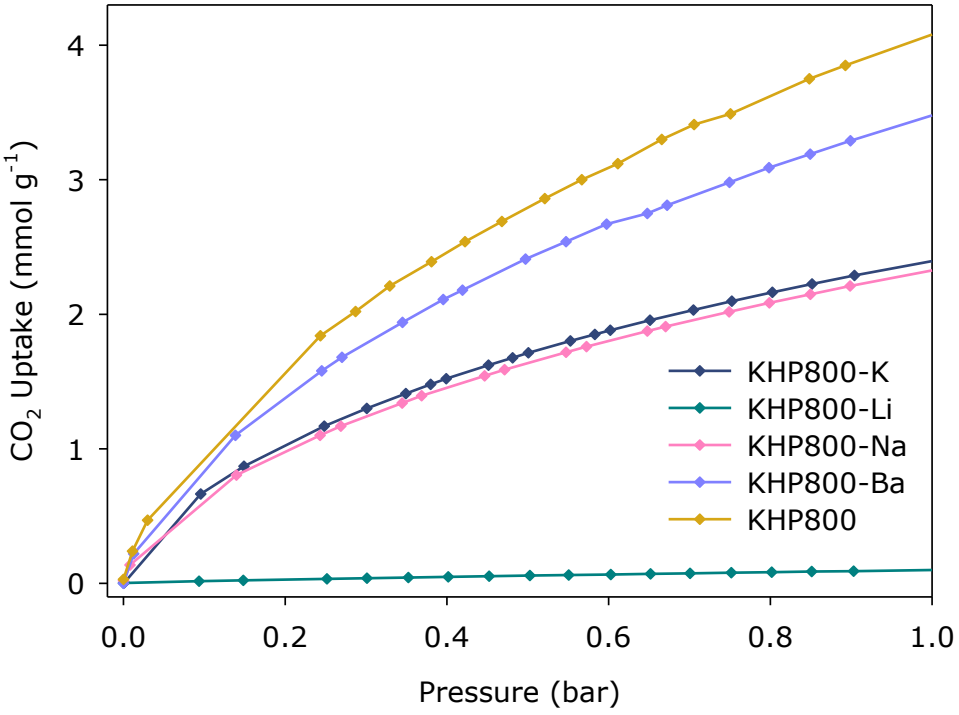

Figure 3.19. CO_2 uptake up to 1 bar for samples activated at 800 °C

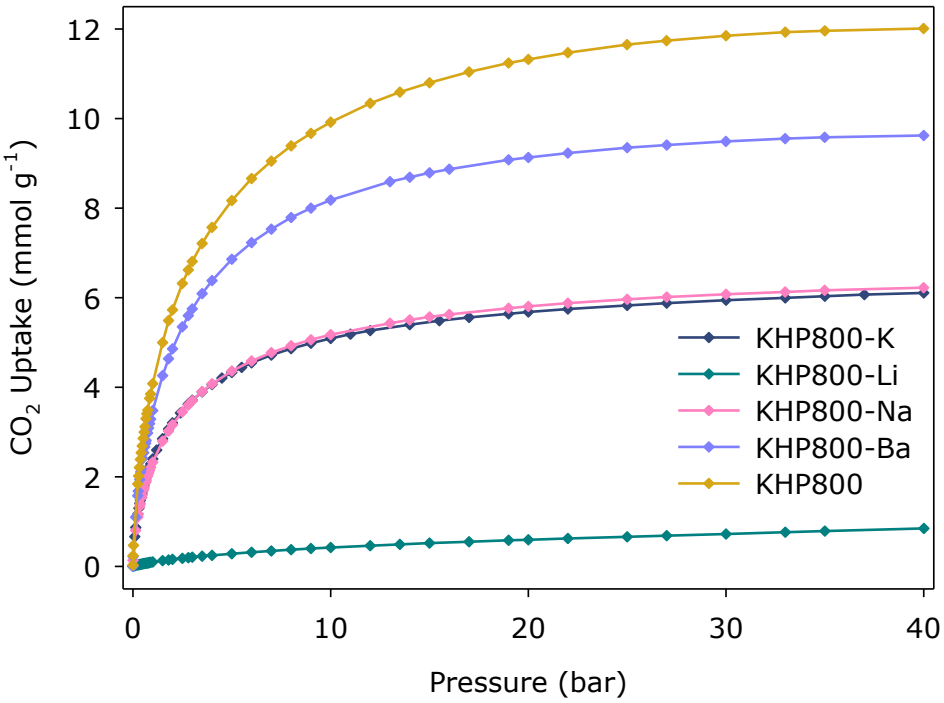

Figure 3.20. CO_2 uptake up to 40 bar for samples activated at 800 °C

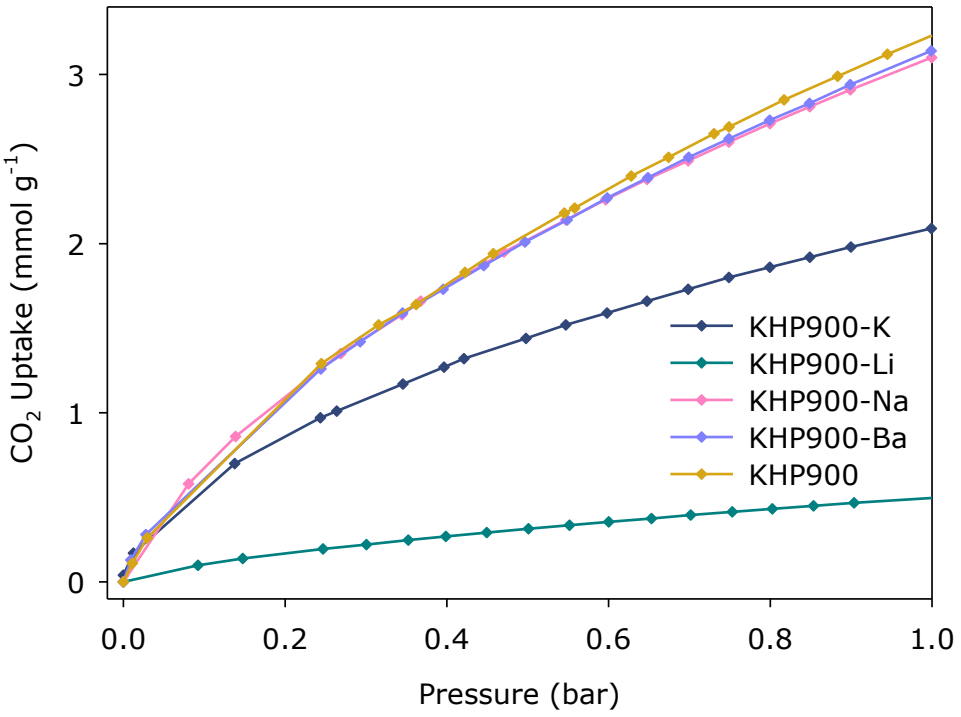

Figure 3.21. CO_2 uptake up to 1 bar for samples activated at 900 °C

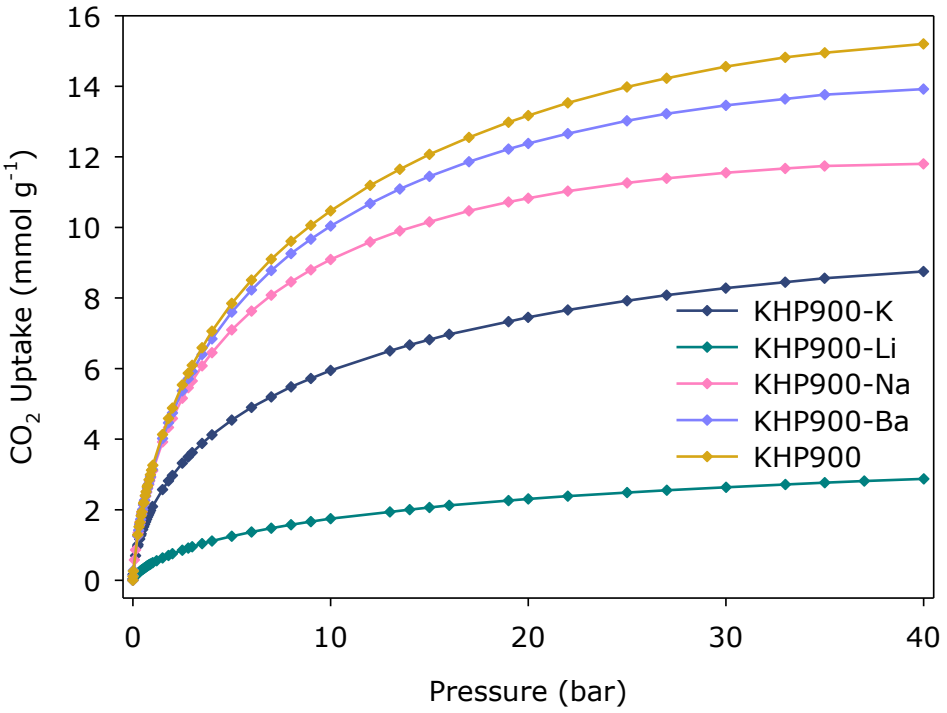

Figure 3.22. CO_2 uptake up to 40 bar for samples activated at 900 °C

Table 3.5. Gravimetric CO_2 uptake at 25 °C over a range of pressures of all samples

Sample	CO_2 Uptake (mmol g^{-1})			
	0.15 bar	**1 bar**	**20 bar**	**40 bar**
KHP800-K	0.9	2.4	5.7	6.1
KHP800-Li	<0.1	0.1	0.6	0.9
KHP800-Na	0.8	2.3	5.8	6.2
KHP800-Ba	1.1	3.5	9.1	9.6
KHP800	1.2	4.1	11.3	12.0
KHP900-K	0.7	2.1	7.4	8.7
KHP900-Li	0.1	0.5	2.3	2.9
KHP900-Na	0.9	3.1	10.8	11.8
KHP900-Ba	0.8	3.1	12.4	14.0
KHP900	0.8	3.2	13.2	15.2

In order to compare the effects of metal doping on the CO_2 uptake capacities of activated carbon, it is more meaningful to analyse the volumetric CO_2 uptake (Table 3.6). This takes into account the various densities of the different metal dopants, therefore allowing accurate comparison. When studying the 800 series, KHP800-Ba consistently performs better in terms of CO_2 uptake than the equivalent undoped sample (KHP800) across all pressures. As KHP800-Ba has lower surface area,

Table 3.6. Volumetric CO_2 uptake at 25 °C over a range of pressures of all samples

Sample	CO_2 Uptake (mmol cm^{-3})			
	0.15 bar	**1 bar**	**20 bar**	**40 bar**
KHP800-K	0.7	1.9	4.4	4.7
KHP800-Li	<0.1	0.1	0.7	1.0
KHP800-Na	0.6	1.8	4.5	4.8
KHP800-Ba	0.7	2.3	5.9	6.3
KHP800	0.6	2.1	5.7	6.1
KHP900-K	0.3	0.9	3.2	3.8
KHP900-Li	0.1	0.3	1.6	2.0
KHP900-Na	0.5	1.7	5.6	6.4
KHP900-Ba	0.5	1.8	7.1	8.0
KHP900	0.5	1.8	7.6	8.8

pore volume and proportion of microporosity than KHP800 (Tables 3.2 and 3.3), the higher volumetric CO_2 uptake confirms that Ba-doping is beneficial.

KHP800-K and KHP800-Na exhibit lower CO_2 uptake than KHP800 at all pressures. However, although KHP800-K and KHP800-Na both show considerably lower surface area and pore volume than KHP800, the reduction in CO_2 uptake capacity is

only slight. Therefore, it can be concluded that the presence of the metal ions is having a beneficial effect on the uptake of CO_2.

When studying the 900 series, the performance of KHP900-Ba is equivalent to that of KHP900 ≤ 1 bar, and only slightly lower ≥ 20 bar. This may be expected as KHP900-Ba possesses slightly lower surface area and pore volume than KHP900. KHP900-K and KHP900-Na adsorb less CO_2 than KHP900 ≥ 20 bar. Again, this may be expected as KHP900-Na and, to a greater extent, KHP900-K have considerably lower surface area and pore volume than KHP900.

Overall, metal doping has a positive effect in terms of CO_2 uptake on highly microporous samples. The benefit is particularly noticeable at higher pressures ≥ 20 bar, where a high surface area is necessary for high CO_2 uptake. The presence of Group 1 and 2 metal ions therefore goes some way to alleviating the disadvantage of lower surface area in highly microporous samples.

Metal doping has a more negligible effect in terms of CO_2 uptake on more mesoporous samples. It is clear from this study that porous structure has a greater impact on CO_2 uptake capacity, in particular the need for high surface areas when studying high pressure CO_2 uptake.

3. 4. 7. Selectivity Measurements

To predict the industrial efficiency of the synthesised carbons more effectively, the selectivity of the carbons for CO_2 over N_2 must be considered. A typical flue gas stream from a coal or gas burning power station is composed of approximately 85% N_2 and 15% CO_2 at atmospheric pressure. Low concentrations of other components may be found, including steam, acids and metal contaminants.[36,37] The Ideal Adsorbed Solution Theory (IAST) method of calculating selectivity estimates the relative uptake of two gases in a binary mixture and has been used in this study alongside the equilibrium pressure at 1 bar. A good IAST selectivity for a carbon of CO_2 over N_2 may be considered as being ~ 20 or above under flue gas conditions.[33]

Table 3.7 shows both the IAST and equilibrium selectivity values calculated for all samples, with low pressure CO_2 and N_2 adsorption isotherms shown in Appendix Figures 3.A1 to 3.A10. Within the 800 series, IAST selectivity for the metal doped samples ranges between 16 and 22, which all represent an increase in selectivity over KHP800. Under flue gas conditions, KHP800-K provides excellent selectivity of 22. The same trend is seen when comparing equilibrium selectivity, with all metal doped samples performing better than KHP800. However,

Table 3.7. Selectivity of CO_2 over N_2. [a]Under flue gas conditions (85%N_2/15%CO_2) at 1 bar and 25°C, calculated from the IAST equation. [b]At 1 bar and 25 °C. All values calculated from volumetric gas uptake

Sample	IAST Selectivity Factor[a]	Equilibrium Selectivity Factor[b]
KHP800-K	22	9
KHP800-Li	16	10
KHP800-Na	18	8
KHP800-Ba	17	8
KHP800	14	7
KHP900-K	23	10
KHP900-Li	12	6
KHP900-Na	15	8
KHP900-Ba	45	19
KHP900	13	8

under these conditions, KHP800-Li exhibits the highest selectivity of 10, among the highest values most often seen for porous carbons.[38–41]

Within the 900 series, similar trends are observed. With the exception of KHP900-Li, all metal doped samples display higher or equivalent selectivity in regards to both the IAST and

equilibrium selectivity factors. KHP900-K has both an excellent IAST selectivity factor of 23 and an equilibrium selectivity factor of 10, among the highest often reported for porous carbons. KHP900-Ba shows exceptional selectivity. An IAST selectivity factor of 45 is among the highest reported for porous carbons, while an equilibrium selectivity factor of 19 far exceeds values often seen for porous carbons.[5,13,18,33] Under flue gas conditions, KHP900 exhibits a slightly lower IAST selectivity value than KHP800, which can be attributed to the wider PSD.

Overall, metal doping improves selectivity for CO_2 to varying degrees in almost all cases. All metal doped samples show a reduced accessible surface area and pore volume than the equivalent undoped samples. Therefore, increased selectivity can be attributed to the reduction in pore size seen for metal doped samples, as well as the presence of metal ions creating a more desirable heterogeneous adsorption surface.

In both temperature series, K-doped samples show excellent selectivity under flue gas conditions despite their low accessible surface areas and pore volumes. Ba-doped samples show good selectivity values, particularly KHP900-Ba. Despite exhibiting slightly lower CO_2 uptake than KHP900, which can be attributed to a slightly lower accessible surface area and pore volume,

KHP900-Ba far outperforms KHP900 in terms of selectivity; another indication of a positive impact of Ba-doping.

3. 5. Conclusions

A series of metal doped porous carbons was synthesised through activation of KHP at 800 and 900 °C. The carbons were subsequently doped with either K, Li, Na or Ba in nitrate form. The structural characteristics and CO_2 uptake ability of the resulting metal doped carbons were analysed and compared to control undoped carbons.

SEM and EDX analysis revealed that the samples were comprised of irregularly shaped particles with some degree of expanded ordered layering, typical of porous carbons. EDX mapping of the metal doped samples showed an even distribution of metal ions across the carbon surface, accompanied by a high oxygen content which is not seen in the undoped equivalent samples.

TGA analysis showed that thermal stability of metal doped samples decreases with metal ion size. This indicates that a greater degree of intercalation within the laminar structure takes place, disrupting any graphitic domains. Metal compound content was found to be 10.2 $\pm$ 2.9 % for the 900 series.

Undoped samples exhibited excellent surface area and pore volume up to 1700 $m^2\ g^{-1}$ and 0.86 $cm^3\ g^{-1}$ respectively, with type I isotherms indicating highly microporous structures. Metal

doping reduces the accessibility of the pore structure in all cases, with the effect increasing as metal ion size decreases. This may be due to a combination of possible reasons. Firstly, smaller metal ions may sit within the pores, reducing pore size and therefore access to the internal pore structure for adsorbing N_2 molecules. Secondly, a greater hygroscopic effect from a greater presence of smaller ions, may result in greater contraction of the carbon structure. This effect further reduces the number of pores large enough to be measured by N_2 uptake.

Metal doping has a clear positive effect on the CO_2 uptake of highly microporous carbons. In the 800 series, despite considerable reduction of accessible pore structure after metal doping, there is only a minor reduction in CO_2 uptake capacity, thereby confirming the benefit of metal doping. The improved uptake can be attributed to the presence of metal ions as well as the increased surface oxygen presence as a result of metal doping. Improved uptake may also be due to reduction of pore size as a result of metal doping, creating a more desirable microporous structure.

In the more mesoporous 900 series, it is clear that pore structure still has a greater impact on CO_2 uptake than the presence of any heteroatom dopants.

Metal doping generally increases the selectivity of the carbons. Metal doping creates a more heterogeneous surface through the presence of metal ions and the resulting additional oxygen presence. The added heterogeneity increases polarity and enhances the dipole-dipole interactions that take place during CO_2 uptake.

It is difficult to determine the effect of Li-doping, as it renders the accessible surface area and pore volume too small to draw accurate conclusions from the surface adsorption measurements.

3. 6. Future Work

Metal doping was found to block access to the pore structure to varying degrees, reducing the pore size. In samples with a larger porosity this was found to be beneficial, creating a larger network of smaller pores, encouraging low pressure CO_2 uptake. However, in highly microporous samples, reduction of the pore size resulted in pore channels becoming inaccessible for adsorbing CO_2 and N_2 molecules.

Repeating the study using a mesoporous carbon would allow further investigation into the effects of metal doping. A high surface area carbon with high pore volume and low microporosity would be expected to show low CO_2 uptake ≤ 1 bar. Doping with Group 1 and 2 metal ions may reduce the size of the accessible pore size to create a more favourable, microporous structure, while retaining the high surface area and volume of the carbon. Additionally, the added benefit of a highly heterogenous carbon surface may further improve the uptake and selectivity of the carbon material.

3. 7. References

1 C. Chen, H. Huang, Y. Yu, J. Shi, C. He, R. Albilali and H. Pan, *Chem. Eng. J.*, 2018, **353**, 584–594.

2 A. Samanta, A. Zhao, G. K. H. Shimizu, P. Sarkar and R. Gupta, *Ind. Eng. Chem. Res.*, 2012, **51**, 1438–1463.

3 S. Y. Lee and S. J. Park, *J. Ind. Eng. Chem.*, 2015, **23**, 1–11.

4 W. Sangchoom and R. Mokaya, *ACS Sustain. Chem. Eng.*, 2015, **3**, 1658–1667.

5 B. Adeniran, E. Masika and R. Mokaya, *J. Mater. Chem. A*, 2014, **2**, 14696.

6 D. Saha and M. J. Kienbaum, *Microporous Mesoporous Mater.*, 2019, **287**, 29–55.

7 S. Park, M. S. Choi and H. S. Park, *Carbon Lett.*, 2019, **29**, 289–296.

8 W. Xing, C. Liu, Z. Zhou, L. Zhang, J. Zhou, S. Zhuo, Z. Yan, H. Gao, G. Wanga and S. Z. Qiao, *Energy Environ. Sci.*, 2012, **5**, 7323–7327.

9 J. Xu, J. Shi, H. Cui, N. Yan and Y. Liu, *Chem. Phys. Lett.*, 2018, **711**, 107–112.

10 T. Chen, S. Deng, B. Wang, J. Huang, Y. Wang and G. Yu, *RSC Adv.*, 2015, **5**, 48323–48330.

11 D. Jeon, B. Min, J. G. Oh, C. Nah and S. Park, *Carbon Lett.*, 2015, **16**, 57–61.

12 L. Wang and R. T. Yang, *J. Phys. Chem. C*, 2012, **116**, 1099–1106.

13 B. Adeniran and R. Mokaya, *Chem. Mater.*, 2016, **28**, 994–1001.

14 M. Sevilla, J. B. Parra and A. B. Fuertes, *ACS Appl. Mater. Interfaces*, 2013, **5**, 6360–6368.

15 Y. Shin, G. E. Fryxell, W. Um, K. Parker, S. V Mattigod and R. Skaggs, *Adv. Funct. Mater.*, 2007, **17**, 2897–2901.

16 M. Seredych, M. Khine and T. J. Bandosz, *ChemSusChem*, 2011, **4**, 139.

17 Y. Xia, Y. Zhu and Y. Tang, *Carbon N. Y.*, 2012, **50**, 5543–5553.

18 Y. Zhao, X. Liu, K. X. Yao, L. Zhao and Y. Han, *Chem. Mater.*, 2012, **24**, 4725–4734.

19 Y. K. Kim, G. M. Kim and J. W. Lee, *J. Mater. Chem. A*, 2015, **3**, 10919–10927.

20 A. A. Adelodun, Y. H. Lim and Y. M. Jo, *J. Anal. Appl. Pyrolysis*, 2014, **108**, 151–159.

21 B. Zhu, K. Qiu, C. Shang and Z. Guo, *J. Mater. Chem. A*,

2015, **3**, 5212–5222.

22 B. Zhu, C. Shang and Z. Guo, *ACS Sustain. Chem. Eng.*, 2016, **4**, 1050.

23 J. Zhang, R. Singh and P. A. Webley, *Microporous Mesoporous Mater.*, 2008, **111**, 478–487.

24 Y. Cao, Y. Zhao, F. Song and Q. Zhong, *J. Energy Chem.*, 2014, **23**, 468–474.

25 E. Masika and R. Mokaya, *Prog. Nat. Sci.*, 2013, **23**, 308–316.

26 C. A. Scholes, S. E. Kentish and G. W. Stevens, *Recent Patents Chem. Eng.*, 2008, **1**, 52.

27 M. Sevilla and R. Mokaya, *Energy Environ. Sci.*, 2014, **7**, 1250–1280.

28 C. R. Correa and A. Kruse, *Materials (Basel).*, 2018, **11**, 1568.

29 J. Wang and S. Kaskel, *J. Mater. Chem.*, 2012, **22**, 23710–23725.

30 M. A. Lillo-Rodenas, J. Juan-Juan, D. Cazorla-Amor and A. Linares-Solano, *Carbon N. Y.*, 2004, **42**, 1371–1375.

31 H. M. Coromina, D. A. Walsh and R. Mokaya, *J. Mater. Chem. A*, 2016, **4**, 280–289.

32 E. Hirst, A. Taylor and R. Mokaya, *J. Mater. Chem. A*,

2018, **6**, 12393–12403.

33 N. Balahmar, A. S. Al-jumialy and R. Mokaya, *J. Mater. Chem. A*, 2017, **5**, 12330–12339.

34 E. Haffner-Staton, N. Balahmar and R. Mokaya, *J. Mater. Chem. A*, 2016, **4**, 13324–13335.

35 B. Adeniran and R. Mokaya, *J. Mater. Chem. A*, 2015, **3**, 5148–5161.

36 R. Zhao, S. Deng, S. Wang, L. Zhao, Y. Zhang, B. Liu, H. Li and Z. Yu, *Appl. Therm. Eng.*, 2018, **128**, 818–829.

37 D. Bahamon, A. Díaz-Márquez, P. Gamallo and L. F. Vega, *Chem. Eng. J.*, 2018, **342**, 458–473.

38 M. Sevilla, C. Falco, M. Titirici and A. B. Fuertes, *RSC Adv.*, 2012, **2**, 12792–12797.

39 M. Sevilla, P. Valle-vigón and A. B. Fuertes, *Adv. Funct. Mater.*, 2011, **21**, 2781–2787.

40 M. Sevilla and A. B. Fuertes, *Energy Environ. Sci.*, 2011, **4**, 1765–1771.

41 M. Sevilla and A. B. Fuertes, *J. Colloid Interface Sci.*, 2012, **366**, 147–154.

3. 8. Appendix

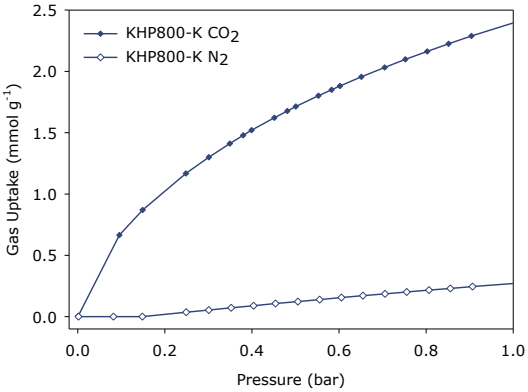

Figure 3.A1. CO_2 and N_2 uptake up to 1 bar at 25 °C of KHP800-K

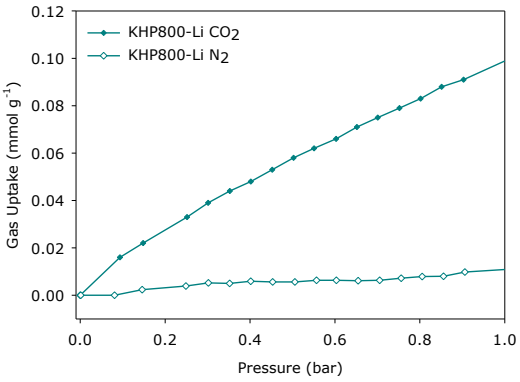

Figure 3.A2. CO_2 and N_2 uptake up to 1 bar at 25 °C of KHP800-Li

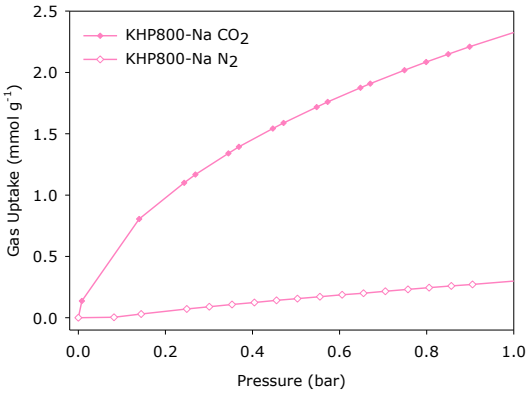

Figure 3.A3. CO_2 and N_2 uptake up to 1 bar at 25 °C of KHP800-Na

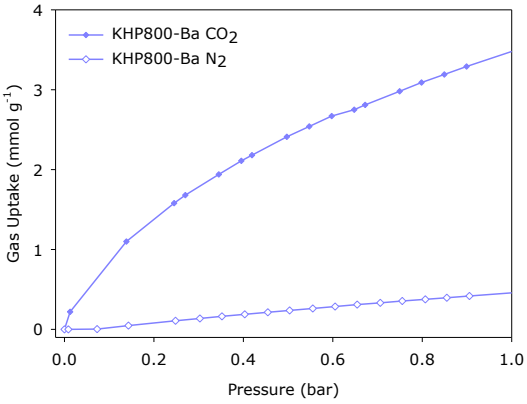

Figure 3.A4. CO_2 and N_2 uptake up to 1 bar at 25 °C of KHP800-Ba

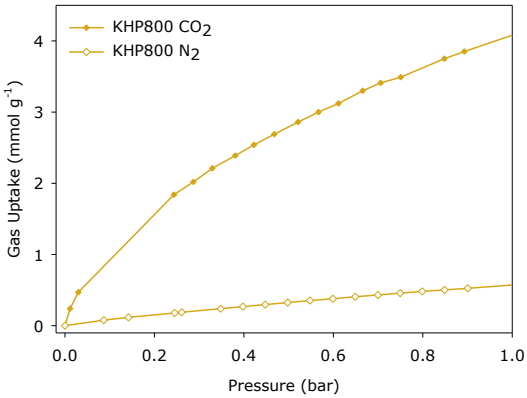

Figure 3.A5. CO_2 and N_2 uptake up to 1 bar at 25 °C of KHP800

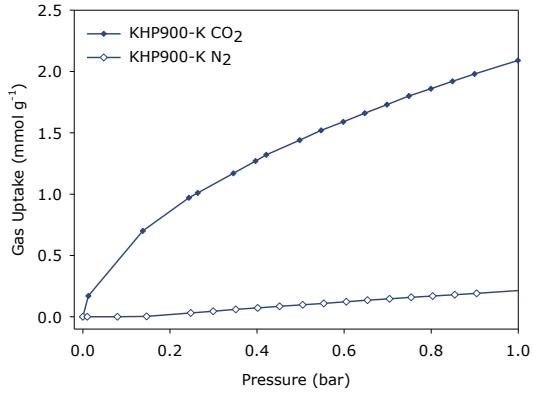

Figure 3.A6. CO_2 and N_2 uptake up to 1 bar at 25 °C of KHP900-K

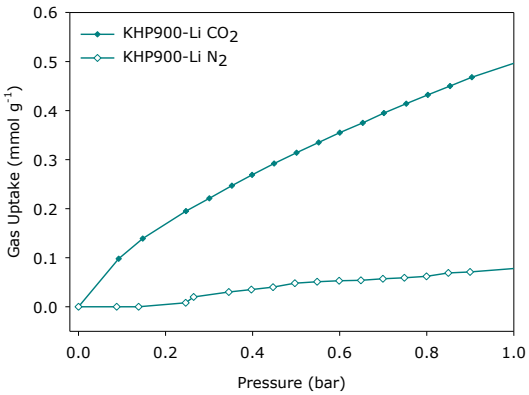

Figure 3.A7. CO_2 and N_2 uptake up to 1 bar at 25 °C of KHP900-Li

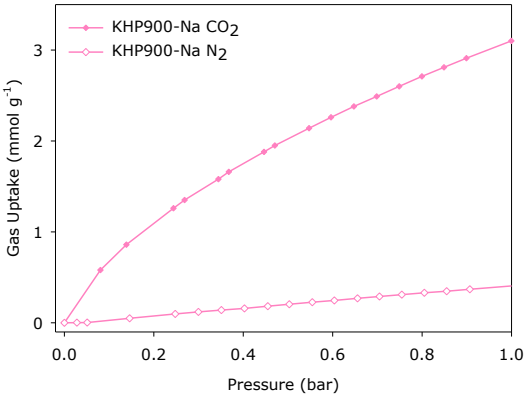

Figure 3.A8. CO_2 and N_2 uptake up to 1 bar at 25 °C of KHP900-Na

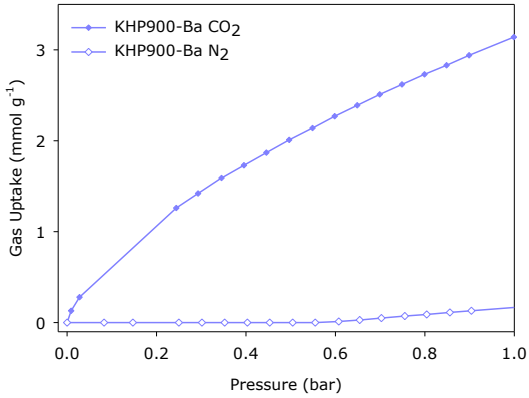

Figure 3.A9. CO_2 and N_2 uptake up to 1 bar at 25 °C of KHP900-Ba

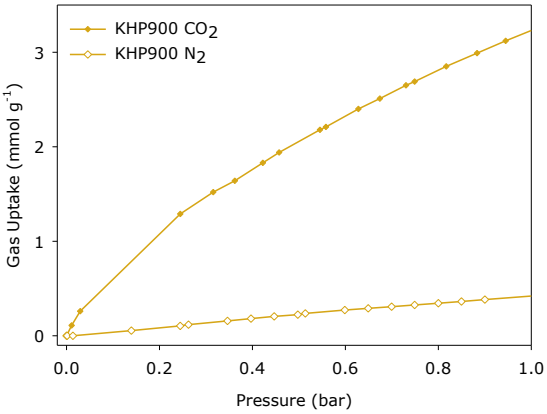

Figure 3.A10. CO_2 and N_2 uptake up to 1 bar at 25 °C of KHP900

Chapter 4 – Pre-Activation Treatment of Biomass Derived Porous Carbons

4. 1. Abstract

This study presents an investigation into a novel biomass carbonisation method, herein referred to as 'flash air-carbonisation'. Initial studies[1,2] showed air-carbonisation to be an effective carbonisation process with the potential to provide a precursor suitable for the synthesis of porous carbons with superior CO_2 uptake performance. It was also shown that air-carbonisation is less energy intensive and higher yielding than traditional methods. This study analyses the properties of so called 'airchar' and a wide range of airchar-derived porous carbons. The carbons produced exhibited excellent surface area and pore volume of up to 3159 $m^2\ g^{-1}$ and 1.82 $cm^3\ g^{-1}$ respectively. The airchar-derived carbons also have very high ambient temperature (25 °C) CO_2 uptake, at low pressures of 0.15 bar and 1 bar, of 1.1 and 4.5 mmol g^{-1}, respectively.

In a direct comparison, this study compares novel air-carbonisation with the traditional hydrothermal carbonisation method. The effect of wood type on the air-carbonisation process was also explored.

4. 2. Introduction

Biomass is a term that encompasses all plant and animal matter and is a widely used starting material for the synthesis of porous carbons; it is cheap, readily available and renewable. Biomass as a starting material is a step closer towards carbon neutrality than alternative precursors and has been shown to produce excellent carbons that are easily tailorable to a range of uses.[3–10] Many studies have been published that utilise various forms of biomass, ranging from plant seeds[4–6,8] and pine needles,[7] to seaweeds[9,10] and coffee grounds[11,12] to name but a few. Biomass produced as a waste product from industry may be preferred; this can further reduce the cost, as well as providing opportunities for valorisation of waste material. Importantly, it also goes some way towards alleviating various environmental issues, such as waste disposal and effective land use. For these reasons, wood and coconut shells are among the most popular biomass starting materials for the synthesis of activated carbons.[3,13]

The three main components of biomass are lignin, cellulose and hemicellulose. Cellulose is a linear polysaccharide with a repeating D-glucose unit. Lignin is an aromatic heterogeneous polymer consisting of phenylpropane units linked together by ether and carbon-carbon bonds.[14–18] Biomass can be classified

as 'hard' (lignin rich), for example wood, coconut shells and fruit stones, or 'soft' (cellulose rich), for example straw and grasses.[18]

Due to these structural properties, raw biomass is difficult to directly activate, particularly lignin. Therefore, a carbonisation step is required before activation can take place, to break down the large, aromatic structures into smaller, more reactive and readily activated molecules. The carbonisation process enriches carbon content, by converting biomass precursor to a carbon-rich carbonaceous char.[2] Cellulose and hemicellulose are the more volatile components, meaning that lignin is the main source of char formation.[17,19,20] Chars from lignin-rich precursors have been shown to have a higher yield and pore volume than those from cellulose-rich precursors.[21,22] It has been shown that chars with a higher proportion of lignin have lower reactivity, due to their highly cross-linked nature and are therefore harder to activate.[23,24] However, the chars produced have a larger surface area and pore volume, and are more microporous than chars with a higher proportion of cellulose, which exhibit a wider pore size range.[25]

Among the most common methods for biomass carbonisation are hydrothermal carbonisation and pyrolysis. Hydrothermal carbonisation is the thermal treatment under autogenous

pressure of biomass material in water, at temperatures of 150 – 350 °C. The result of this process is a solution of dissolved organic molecules and a carbon-rich char – so called 'hydrochar'.[26,27] Hydrothermal carbonisation replicates the natural process of coal generation. The resulting hydrochar is rich in oxygen functional groups, with a low degree of aromaticity.[26,27] Previous studies[26–28] have shown that hydrothermal carbonisation of cellulose produces agglomerates of micron-sized spherical particles with hydrophobic cores and hydrophilic shells. However, it has been shown that when the same treatment is applied to wood, the resulting hydrochar particles retained the cellular appearance of the raw precursor, with a surface covering of microspheres.[27,29] It is assumed that the microspheres are generated due to the conversion of the cellulosic component, while the retention of cellular appearance is due to the lignin component of the raw wood.[27,29] Despite being an effective process for the production of carbon-rich chars, hydrothermal carbonisation has some drawbacks. The hydrochar requires extensive washing with copious amounts of water to remove the soluble organics, and the char has negligible surface area and porosity.[26]

Hydrothermal carbonisation is a popular choice of carbonisation method in the synthesis of biomass-derived activated carbons,

and excellent results have previously been reported. Matabosch Coromina *et al*.[30] conducted hydrothermal carbonisation of Jujun grass and *Camellia japonica*. The resulting char was activated with KOH to yield activated carbons with surface area and pore volume up to 3537 m^2 g^{-1} and 1.85 cm^3 g^{-1} respectively. The carbons were highly microporous and exhibited CO_2 uptake of up to 5.0 mmol g^{-1} at 1 bar and 25 °C.[30] Sevilla *et al*.[31] performed hydrothermal carbonisation of both cellulose and potato starch. The chars were activated with KOH to produce carbons with similar textural properties. Cellulose-derived carbons had surface area and pore volume of up to 3100 m^2 g^{-1} and 1.46 cm^3 g^{-1}, and CO_2 uptake of up to 2.8 mmol g^{-1} at 1 bar and 25 °C. Starch-derived carbons had surface area and pore volume of up to 3000 m^2 g^{-1} and 1.41 cm^3 g^{-1} respectively, and CO_2 uptake also of up to 2.8 mmol g^{-1} at 1 bar and 25 °C.[31] The results showed that the use of the cellulose or starch, two structurally similar polymers, had little effect on the resulting hydrochars. In another study, Sevilla *et al*.[32] hydrothermally carbonised a mixture of protein-rich microalgae and glucose. KOH activation of the resulting hydrochar produced N-doped carbons with surface area and pore volume of up to 2390 m^2 g^{-1} and 1.15 cm^3 g^{-1} respectively and CO_2 uptake of up to 4.5 mmol g^{-1} at 1 bar and 25 °C.[32]

Pyrolysis is another commonly used method for the carbonisation of biomass. Pyrolysis is the process of thermally converting organic matter at moderate temperatures between 500 – 800 °C under an inert atmosphere.[33–36] Pyrolysis of biomass produces three products; a carbon-rich solid char, so called 'biochar', a liquid component composed of various organic molecules, known as 'bio-oil' and syngas, composed of mainly H_2, CO, CO_2, H_2O and various hydrocarbons. The liquid and gas fractions of the pyrolysis products can be further processed into fuels with commercial value in the energy sector.[14,36] Alterations to the pyrolysis temperature, heating rate and exposure time give control over the ratio of the three products, although conversion always takes place via three main processes; char formation, depolymerisation and fragmentation. During char formation, intra- and intermolecular rearrangement reactions occur to form benzene rings in a polycyclic structure. The resulting solid biochar has increased levels of reticulation and thermal stability. During depolymerisation, bonds between monomer units of polymer chains break. Resulting molecules become volatile and are often found in the liquid fraction of the pyrolysis products. Finally, during fragmentation, linkage of covalent bonds within polymer and monomer units produces volatile molecules found in both the liquid and gas fractions of pyrolysis products.[14,36]

Biochar has been produced from a range of biomass materials and widely utilised as a carbon-rich precursor in the synthesis of activated carbons. Recent studies have detailed the synthesis of porous carbons with well-developed porosity and CO_2 uptake. Singh *et al*.[37] pyrolysed lotus seeds and activated the resulting biochar with KOH. Porous carbon materials were produced with surface area and pore volume of up to 2230 $m^2\ g^{-1}$ and 0.96 $cm^3\ g^{-1}$ respectively, with CO_2 uptake of up to 3.1 mmol g^{-1} at 1 bar and 25 °C.[37] Li *et al*.[38] pyrolysed dates and activated the resulting biochar with KOH. The produced carbons exhibited excellent pore development, with surface area and pore volume up to 3337 $m^2\ g^{-1}$ and 2.05 $cm^3\ g^{-1}$ respectively. The carbons also showed high CO_2 uptake at 1 bar and 25 °C of up to 4.4 mmol g^{-1}.[38] Chang *et al*.[39] activated a poplar catkin-derived biochar with $ZnCl_2$, to achieve carbons with surface area and pore volume of up to 1455 $m^2\ g^{-1}$ and 0.78 $cm^3\ g^{-1}$ respectively. CO_2 uptake of up to 4.1 mmol g^{-1} was recorded at 1 bar and 25 °C. The carbons also exhibited exceptional CO_2 uptake at very low pressure of 0.15 bar, of 1.1 mmol g^{-1} at 25 °C.[39] Yang *et al*.[40] pyrolysed coconut shells and activated the resulting biochar with KOH. The porous carbons produced exhibited surface area and pore volume of up to 1817 $m^2\ g^{-1}$ and 0.69 $cm^3\ g^{-1}$. The carbons also exhibited excellent CO_2 uptake at 1 bar and 25 °C of 4.2 mmol g^{-1}.[40]

Despite the popularity of both hydrothermal carbonisation and pyrolysis as biomass pre-treatment in the synthesis of activated carbons, both processes are very energy intensive and are low yielding.

In September 2014, the nearly fully completed Carbon Neutral Laboratory (CNL) building at the University of Nottingham was destroyed by a fire. The building had been constructed almost entirely of wood, requiring ~ 100 spruce trees sourced from Bavarian forest. Following the fire, the Mokaya research group at the University of Nottingham obtained a short length (~ 60 cm) of charred wooden beam (Fig. 4.1). As seen in Figure 4.1, the core of the beam is presumed to be pristine wood, while the outside of the beam had been carbonised in the fire. It was acknowledged that the charred wood had been subjected to a novel carbonisation method in air, which was termed 'air-carbonisation'. Mokaya *et al*.[1] conducted a study to investigate the properties and activation potential of the novelly carbonised spruce wood. It was found that the air-carbonised wood, so called 'airchar' had surface area and pore volume of 100 $m^2\ g^{-1}$ and 0.06 $cm^3\ g^{-1}$ respectively, with microporosity accounting for 79 % of the surface area, thus proving more porous than chars produced by traditional hydrothermal or pyrolysis methods.[1,41]



Figure 4.1. Charred beam obtained from CNL fire

The airchar was activated with KOH under various conditions, to produce a range of porous carbons with high surface area and pore volume of up to 2487 m^2 g^{-1} and 1.16 cm^3 g^{-1} respectively, and high levels of microporosity of up to 96 %.[1] As mentioned previously, in most studies of activated carbons, surface area and pore volume increases as activation conditions become harsher. However, this is accompanied by a broadening of the pore size distribution (PSD), which is undesirable for the purpose of adsorbing CO_2 as this favours a narrow PSD, centred at ~ 6 – 8 Å.[41–44] However, the investigated air char showed

high resistance to KOH activation, retaining a higher level of microporosity as activation conditions harshened. A high surface area and pore volume combined with narrow microporosity proved ideal for low pressure CO_2 uptake, with the carbons exhibiting uptake of up to 5 mmol g^{-1} at 1 bar and 25 °C.[1]

Heating biomass in air results in combustion, and to the best of our knowledge, has not been explored for biomass pre-treatment in the synthesis of porous carbons. Air-carbonisation offers a carbonisation method that is less energy intensive than alternative methods and has the potential to produce more efficient porous carbons for gas adsorption. However, in order for the novel air-carbonisation method to be considered as a viable alternative to traditional methods, it has to be reproducible. In 2018, Mokaya *et al*.[2] published a study of lab-synthesised airchar and the resulting activated carbons. To replicate the conditions of the CNL fire, eucalyptus sawdust was heated to 400 °C under inert atmosphere. At 400 °C, the wood was subject to air flow for 10 mins, before being cooled to room temperature under inert atmosphere. The conditions were chosen to promote conservative combustion in a limited oxygen atmosphere. The process, so called 'flash-air carbonisation' produced an airchar with similar properties to that of the

original CNL airchar.[1,2] A small range of activated carbons were produced from the lab-synthesised airchar, with equally promising surface area and pore volume of up to 2610 m^2 g^{-1} and 1.15 cm^3 g^{-1}, with CO_2 uptake of up to 4.0 mmol g^{-1} at 1 bar and 25 °C.

The study reported here, is a development of the investigation into the novel flash air-carbonisation method and its aims are threefold. Firstly, airchar was produced in the lab, from the pristine spruce wood of the beam core (Fig. 4.1) to confirm reproducibility. A wide range of activated carbons were produced from the airchar to comprehensively study the effects of airchar as a precursor. Secondly, a detailed comparison between novel air-carbonisation and traditional hydrothermal carbonisation was conducted. A range of analogous samples was synthesised, prepared from hydrochar. The hydrochar was produced using the same pristine spruce wood as the airchar. The third aim of the investigation was to compare the effect of using two different biomass sources. To achieve this, air-carbonisation of eucalyptus wood was conducted. The resulting airchar was analysed, a range of activated carbons produced and the results compared with those of the spruce airchar-derived activated carbons.

For the purpose of this study, KOH was used as the activating agent as its use is highly effective and well documented. The range of activating conditions was chosen to represent 'standard conditions' (carbon:KOH ratio of 1:2, temperature of 800 °C, duration of 1 hr) and the effects of increased concentration of activating agent, lower temperatures and longer activation durations.

4. 3. Materials Synthesis, Characterisation and Analysis

Activated carbons were synthesised by pre-treating spruce wood chippings (Fig. 4.2) and eucalyptus sawdust (Fig. 4.3) through either a hydrothermal carbonisation or an air carbonisation method, prior to activation.



Figure 4.2. Spruce wood chippings



Figure 4.3. Eucalyptus sawdust

Hydrothermal Carbonisation Pre-Treatment

An aqueous suspension of wood chippings (3.2 g) in deionised water (10 mL) was placed in a stainless steel autoclave and heated at a ramp rate of 5 °C min^{-1} to 250 °C. The suspension was held at this temperature for 2 hrs before being allowed to cool to room temperature. The resulting 'hydrochar', denoted HC-WC (hydrochar wood chippings), was collected by vacuum filtration and washed thoroughly with deionised water before being dried in air at 100 °C for 48 hrs. The yield of this hydrothermal carbonisation process was 38 %.

Air Carbonisation Pre-Treatment

Wood chippings (~2 g), or separately, sawdust (~2 g) were heated in a horizontal alumina furnace at a ramp rate of 10 °C min^{-1} to 400 °C under a flow of nitrogen (100 mL min^{-1}). When the furnace reached 400 °C, the gas flow was changed to air (100 mL min^{-1}) and the sample was held under these conditions for 10 mins. After this time, the gas flow was changed back to nitrogen (100 mL min^{-1}) and the sample was allowed to cool to room temperature. The resulting 'airchar' was denoted AC-WC, (air-carbonised wood chippings) and AC-SD, (air-carbonised sawdust). The yield of this air carbonisation process was 24 % for AC-WC and 28 % for AC-SD.

Activation

All samples underwent the same activation procedure. Typically, carbonised material (either hydrothermally or air-carbonised) was ground in a pestle and mortar with KOH (Fisher Scientific) in a KOH:C weight ratio of either 2:1 or 4:1. The mixture (3 g) was heated in a horizontal alumina furnace at a ramp rate of 3 °C min^{-1} to either 600, 700 or 800 °C under a flow of nitrogen (100 mL min^{-1}). The samples were held at the target temperature for either 1, 5 or 10 hrs before being allowed to cool to room temperature, all under nitrogen flow. Samples were washed several times in HCl (10 wt%, 400 mL) (Fisher Scientific) before being collected by vacuum filtration, neutralised with deionised water and dried in air at 100 °C for 24 hrs. The average yield of the activation process was 47 % for activation of AC-WC, 18 % for activation HC-WC and 38 % for activation of AC-SD.

The final samples were denoted either HC-WC(x)T-y, for samples prepared via hydrothermal carbonisation, or either AC-WC(x)T-y for samples prepared from wood chippings via air carbonisation, or AC-SD(x)T-y for samples prepared from sawdust via air carbonisation. x represents the KOH:C ratio, T represents the activation temperature in degrees Celsius and y represents the activation time in hours.

Various methods were used to characterise and analyse the samples. Thermal gravimetric analysis was carried out using a TA Instruments Analytical TGAQ500 machine. Samples were heated at a ramp rate of 10 °C min^{-1} to 1000 °C in air.

Elemental analysis was carried out using a CE-440 Elemental Analyzer, Exeter Analytical, Inc. Samples were combusted in oxygen at 975 °C.

Powder x-ray diffraction analysis was carried out using a PANalytical X'Pet Pro diffractometer using CuKα radiation (λ = 1.5418 Å), operating at 40 kV and 40 mA. A step size of 0.026° and a step time of 30.6 s was used.

Analysis of textural properties was carried out by nitrogen sorption at -196 °C. An initial degassing stage was conducted using a Micromeritics SmartVac Prep degassing unit wherein samples were held under vacuum at 230 °C for 16 hours. The following analysis was carried out using a Micromeritics 3Flex. Surface areas were calculated using BET theory, from adsorption data within the linear isotherm plot (relative pressure (P/P_0) of 0.04 – 0.09). Total pore volumes were calculated from the nitrogen uptake close to saturation pressure ($P/P_0 \approx 0.99$). Micropore surface areas and pore volumes were calculated using t-plot analysis. Pore size distributions were

determined by applying non-local density functional theory (NLDFT) to the nitrogen adsorption isotherms.

Gas uptakes were measured using a Hiden Isochema XEMIS machine. After an initial degassing stage, where samples were held under vacuum at 230 °C for 3 hours, analysis was carried out with CO_2 as the adsorbing gas, at 25 °C and at pressures from 0 – 40 bar.

SEM was conducted using a JEOL 7100F microscope with a tungsten filament, operating at an accelerating voltage of 10 – 15 kV.

4. 4. Results and Discussion

4. 4. 1. Elemental Analysis and Yield

The elemental analysis (C, H, O analysis) and average yields for all the chars and activated carbon samples are shown below in Tables 4.1 – 4.4. Nitrogen content is not reported for the samples as in all cases its presence was negligible. The carbon and hydrogen content of the organic component of the materials were measured and the remaining content assumed to be oxygen.

The elemental analyses for samples prepared from air-carbonised spruce wood chippings are shown in Table 4.1. In all cases, activation increases the C/O ratio. The smallest increase in carbon content is seen for AC-WC(2)600-1, the sample activated under the gentlest conditions, giving an increase of 67.8 % for AC-WC to 73.9 %. The largest increase was shown by AC-WC(2)800-1, where carbon content was increased to 86.0 % compared with the airchar. This corresponds with AC-WC(2)600-1 and AC-WC(2)800-1 having among the smallest and largest decrease in oxygen content respectively. AC-WC(2)800-5 and AC-WC(4)800-5 were both activated under relatively harsh conditions and subsequently show large increases in carbon content. AC-WC(2)800-1, AC-WC(2)800-5

Table 4.1. C, H and O content by wt% in samples prepared from air-carbonised wood chippings. C and H content was calculated though elemental microanalysis. The remaining content was assumed to be O. The atomic C/O ratio was calculated from these values

Sample	C%	H%	O%	C/O
AC-WC	67.8	2.8	29.4	3.1
AC-WC(2)800-1	86.0	0.1	13.9	8.2
AC-WC(4)800-1	74.6	0.0	25.4	3.9
AC-WC(2)600-1	73.9	1.0	25.1	3.9
AC-WC(4)600-1	77.0	0.5	22.5	4.6
AC-WC(2)800-5	85.5	0.5	14.0	8.1
AC-WC(4)800-5	84.7	0.3	15.0	7.5
AC-WC(2)600-5	75.1	1.2	23.7	4.2
AC-WC(4)600-5	75.3	0.6	24.1	4.2

and AC-WC(4)800-5 show the greatest carbon enrichment of this sample set and the largest increase of C/O ratio.

The elemental analysis for samples prepared from hydrothermally-carbonised spruce wood chippings are shown in Table 4.2. Activation does not necessarily result in an increase of carbon content. HC-WC(4)600-1, HC-WC(4)600-5 and HC-WC(4)800-5 all have decreased carbon content compared with HC-WC, decreasing from 57.4 % to 46.1, 52.6 and 39.4 %

Table 4.2. C, H and O content by wt% in samples prepared from hydrothermally-carbonised wood chippings. C and H content was calculated though elemental microanalysis. The remaining content was assumed to be O. The atomic C/O ratio was calculated from these values

Sample	C%	H%	O%	C/O
HC-WC	57.4	5.5	37.1	2.1
HC-WC(2)800-1	84.4	0.2	15.4	7.3
HC-WC(4)800-1	74.8	0.1	25.1	4.0
HC-WC(2)600-1	74.8	1.1	24.1	4.1
HC-WC(4)600-1	46.1	0.5	53.4	1.1
HC-WC(2)800-5	81.0	0.7	18.3	5.9
HC-WC(4)800-5	39.4	0.1	60.5	0.9
HC-WC(2)600-5	72.4	1.5	26.1	3.7
HC-WC(4)600-5	52.6	0.8	46.6	1.5

respectively. These three samples showed an increase in oxygen content, resulting in corresponding decreases in C/O ratio. Generally, this trend was shown by samples activated with a higher proportion of activating agent, which may be responsible for the higher oxygen content. The biggest increase in oxygen content of 57.4 to 84.4 % was shown by HC-WC(2)800-1, corresponding to the largest increase in C/O ratio.

Table 4.3. C, H and O content by wt% in samples prepared from air-carbonised sawdust. C and H content was calculated though elemental microanalysis. The remaining content was assumed to be O. The atomic C/O ratio was calculated from these values

Sample	C%	H%	O%	C/O
AC-SD	72.4	3.2	24.4	3.9
AC-SD(2)800-1	76.4	0.2	23.4	4.4
AC-SD(2)800-5	84.1	0.0	15.9	7.1
AC-SD(2)800-10	88.1	0.0	11.9	9.9
AC-SD(4)800-1	85.0	0.1	14.9	7.6
AC-SD(4)800-5	91.2	0.0	8.8	13.8
AC-SD(4)800-10	91.1	0.0	8.9	13.6
AC-SD(2)700-1	76.8	1.3	21.9	4.7
AC-SD(2)700-5	59.7	2.9	37.4	2.1
AC-SD(2)700-10	63.8	2.7	33.5	2.5
AC-SD(2)600-1	70.5	2.3	27.2	3.5

In both the AC-WC and HC-WC sample sets, activation conditions of '(2)800-1' resulted in the best carbon enrichment of the char. Comparing the two chars (AC-WC and HC-WC), AC-WC has a higher C/O ratio, which may be a result of flash combustion in air and may cause the airchar to be more resistant to chemical activation. It is clear that air-carbonisation exhibits more efficient carbon enrichment than hydrothermal-carbonisation.

Table 4.4. Average synthesis yields of all carbon samples. Averages calculated from the yield of each sample produced

Sample	Average Yield (%)
AC-WC	26
Activated AC-WC	47
HC-WC	38
Activated HC-WC	18
AC-SD	28
Activated AC-SD	38

The elemental analysis for samples prepared from air-carbonised eucalyptus sawdust are shown in Table 4.3. Activation does not necessarily result in carbon enrichment. AC-SD(2)700-5, AC-SD(2)700-10 and AC-SD(2)600-1 all show a decrease in carbon content compared with AC-SD, decreasing from 72.4 % to 59.7, 63.8 and 70.5 % respectively. As a result, these samples show a decrease in C/O ratio. The remaining samples in this set show a large increase in carbon content. AC-SD(4)800-5 shows the largest increase in carbon content, from 72.4 to 91.2 %, resulting in an increase of C/O ratio from 3.9 to 13.8. The char, AC-SD shows the highest C/O ratio of the three chars, confirming that air-carbonisation is a more efficient carbon enrichment method than hydrothermal-carbonisation. It is clear that wood composition (ratio of

lignin/cellulose/hemicellulose) does have an effect on the resulting elemental composition.

The average synthesis yields for all samples are shown in Table 4.4. Hydrothermal carbonisation provides a high char yield of 38 % compared with 26 and 28 % for AC-WC and AC-SD respectively. However, upon activation, airchar provides a much higher yield, indicating a higher resistance to KOH activation. Activated AC-WC samples and activated AC-SD samples have average yields of 47 and 38 % respectively, compared with an average yield of 18 % for activated HC-WC samples.

There is a clear difference when comparing overall yield of activated carbon with respect to the starting biomass of either spruce wood chippings or eucalyptus sawdust. Preparing activated carbons from spruce wood via hydrothermal-carbonisation results in an overall yield of 7 %. Preparing activated carbons via air-carbonisation from spruce and eucalyptus wood results in overall yields of 12 and 11 %, respectively.

Overall, there is a general trend that a higher activation temperature results in a higher carbon content, which is the trend found in previous studies.[2,10,30,45] However, there is no

consistent trend concerning activation time or activating agent ratio.

4. 4. 2. Scanning Electron Microscopy

Scanning electron microscopy (SEM) images for representative chars and activated samples are shown below in Figure 4.4. The morphology of the 3 chars, AC-WC (Fig. 4.4 [A]), HC-WC (Fig. 4.4 [C]) and AC-SD (Fig. 4.4 [E]) is typical of chars formed from lignocellulosic biomass.[1] Retention of the pre-carbonisation structure of wood is clear, especially in the airchars (Fig. 4.4 [A] and [E]), characterised by cellular monolith-like formations with an extended honeycomb structure. Although still exhibiting a woody, cellular-like structure, HC-WC (Fig. 4.4 [C]) has less regular, long-range order than the airchars and is distinctly more broken down and fragmented.

Figure 4.4 [B] and [D] (SEM images of AC-WC(2)800-1 and HC-WC(2)800-1) are representative of the activated samples. The hydrochar-derived activated carbon (Fig. 4.4 [D]) is comprised of irregularly shaped particles with sharp corners, large conchoidal cavities and a high degree of surface roughness, characteristic of microporous activated carbons.[10,30,46] Drastic morphological change results in no retention of the parent char, with micron-sized surface openings indicating the porosity developed through activation.

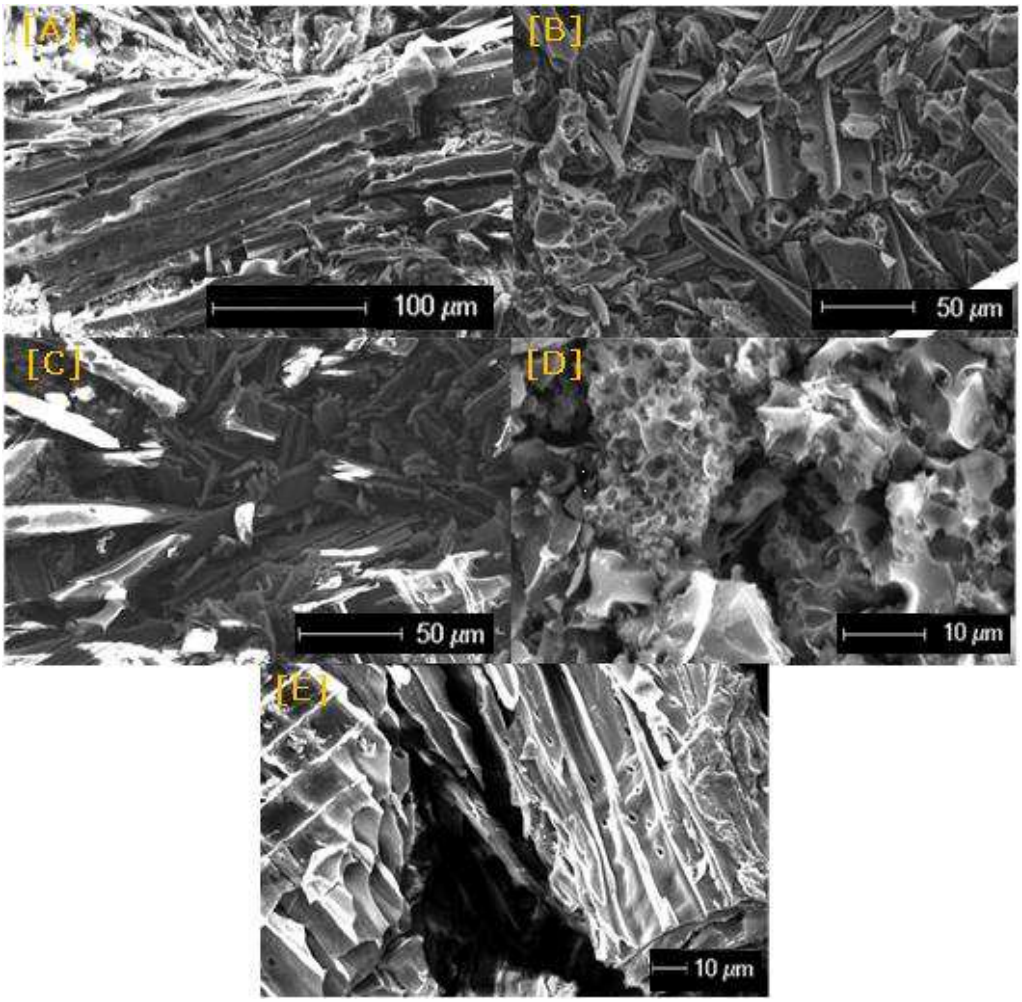

Figure 4.4. SEM images of [A] AC-WC, [B] AC-WC(2)800-1, [C] HC-WC, [D] HC-WC(2)800-1 and [E] AC-SD

Activated carbon derived from airchar has significantly different morphology to that derived from hydrochar. Clear retention of the lignocellulosic structure results in fragments of monolith-like particles interspersed with areas of porous openings and irregularly shaped particles with conchoidal cavities. It is clear that flash air-carbonisation allows for the preservation of the raw material's woody morphology to a greater extent than hydrothermal carbonisation. Resistance of airchar to KOH

activation compared to hydrochar is evident from the comparatively low levels of particle disruption seen during activation.[2]

4. 4. 3. Thermal Gravimetric Analysis

Thermal gravimetric analysis (TGA) of all activated samples and the three carbonised starting materials (AC-WC, HC-WC and AC-SD) was performed to assess the structure, purity and thermal stability of the materials. The TGA curves of all samples are shown in Figures 4.5 – 4.13. Across all plots, some samples show a small mass loss at ~ 100 °C. This can be attributed to moisture loss and can be assumed to be associated with the length of time the sample spent exposed to the atmosphere, as opposed to any structural differences. All the activated samples show a single sharp burn-off within the approximate range 400 – 600 °C. This burn-off range is indicative of amorphous carbon, while a single burn-off curve indicates single phase carbon.[47] As mentioned in previous chapters, activation conditions have an effect on thermal stability of resulting activated carbons. Samples activated above ~ 750 °C are expected to show some graphitic domains, leading to higher thermal stability.[1]

With a few exceptions, most sample sets show only small deviations in burn-off temperature, indicating that activating agent ratio and activation time have minimal effect on the thermal stability of resulting materials. However, AC-WC800

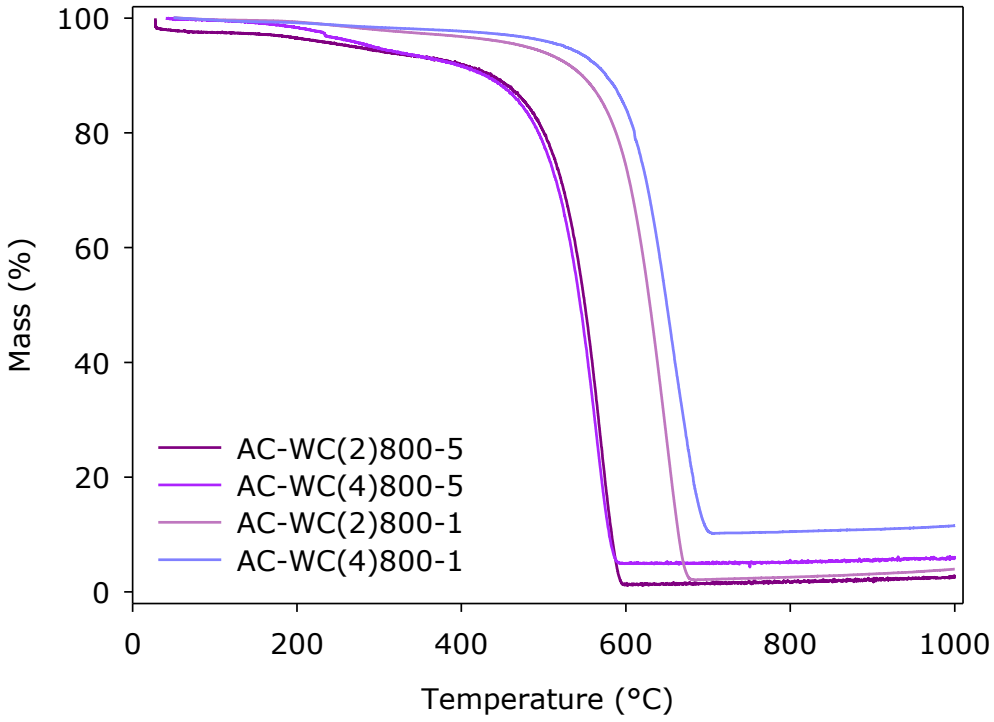

Figure 4.5. TGA plots of samples prepared from air-carbonised wood chippings at 800 °C

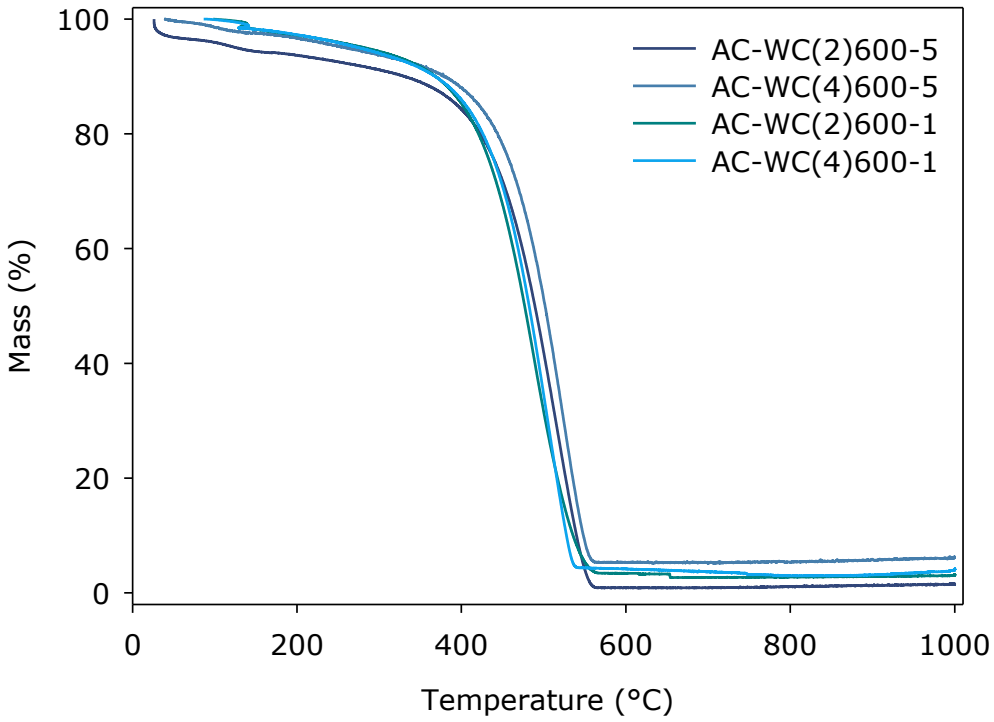

Figure 4.6. TGA plots of samples prepared from air-carbonised wood chippings at 600 °C

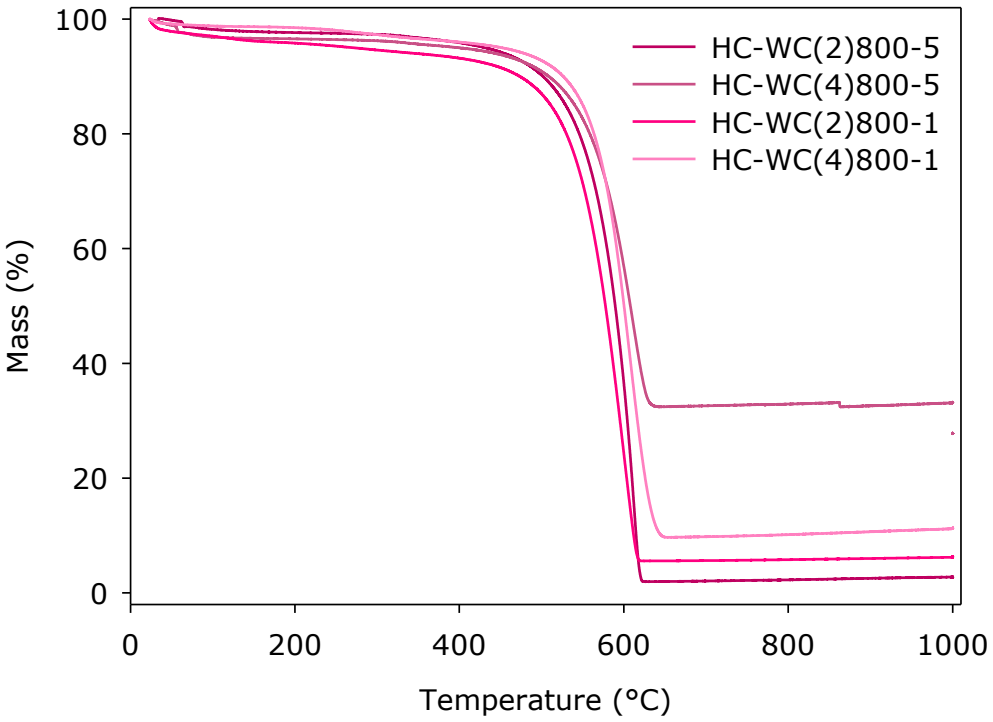

Figure 4.7. TGA plots of samples prepared from hydrothermally-carbonised wood chippings at 800 °C

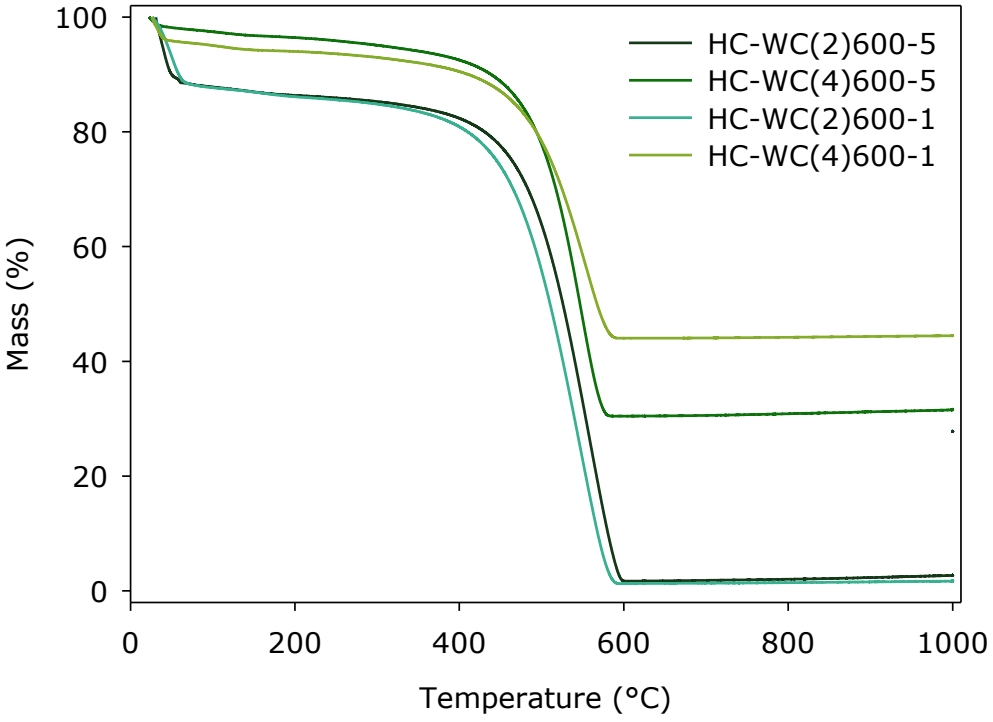

Figure 4.8. TGA plots of samples prepared from hydrothermally-carbonised wood chippings at 600 °C

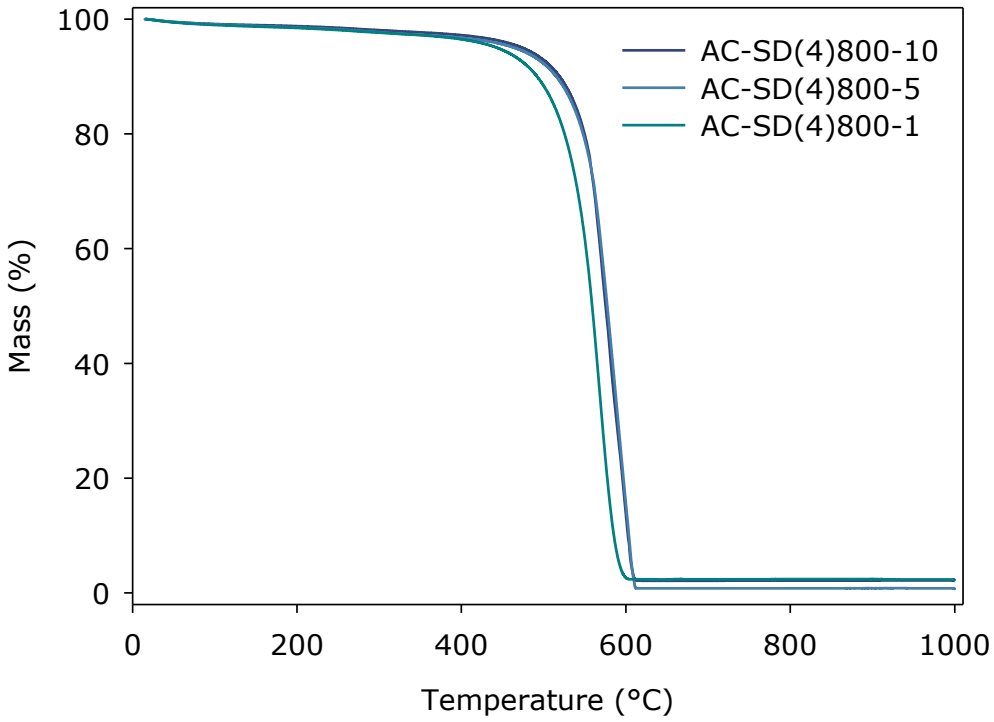

Figure 4.9. TGA plots of samples prepared from air-carbonised sawdust at 800 °C, C:KOH ratio of 1:4

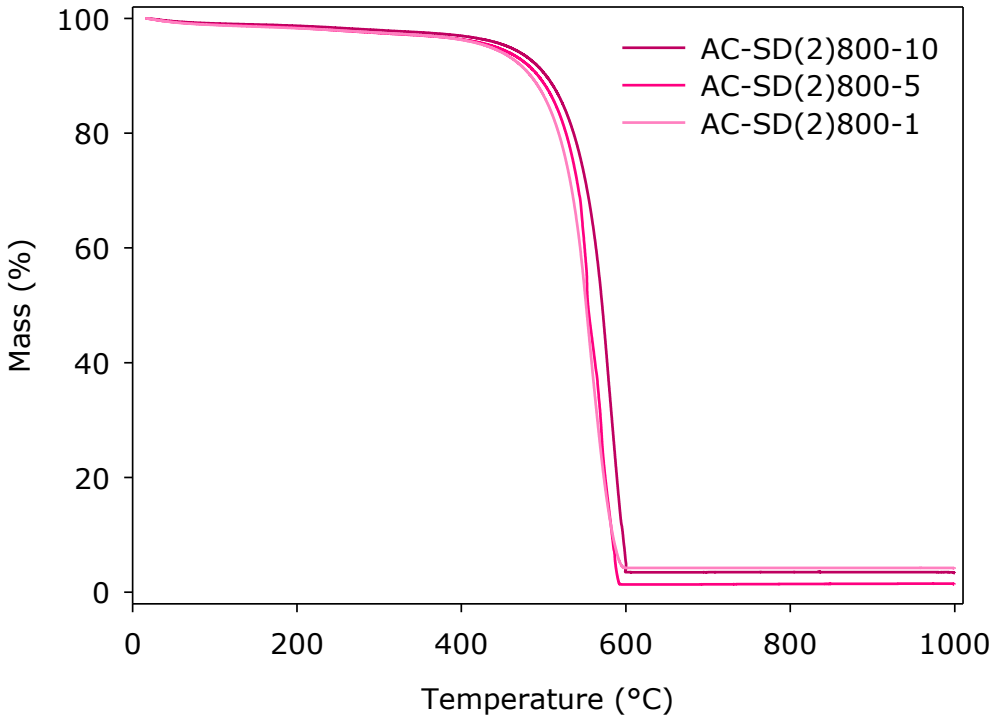

Figure 4.10. TGA plots of samples prepared from air-carbonised sawdust at 800 °C, C:KOH ratio of 1:2

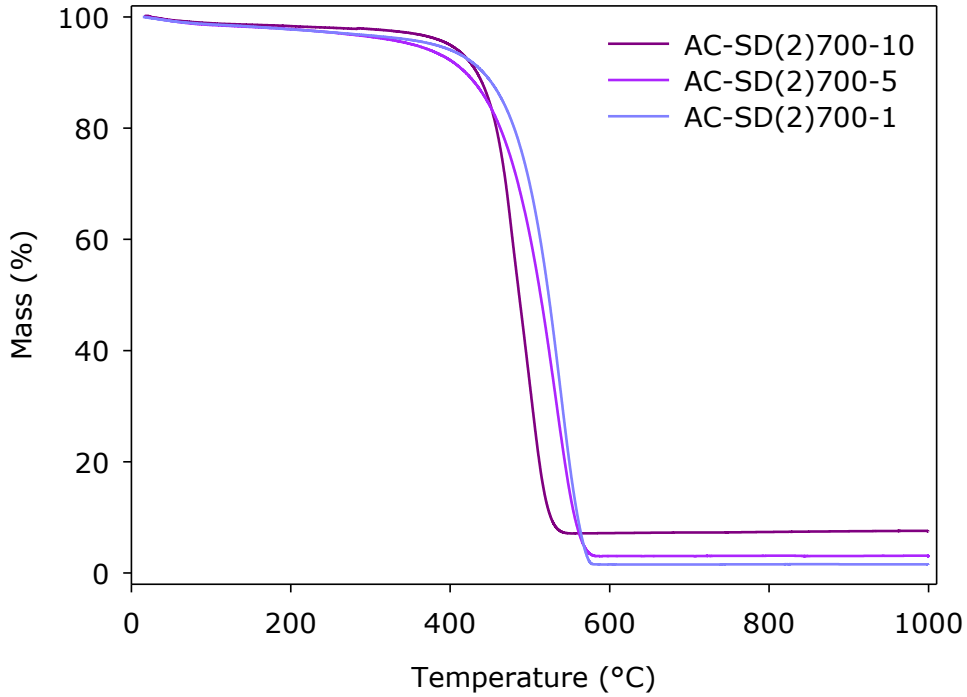

Figure 4.11. TGA plots of samples prepared from air-carbonised sawdust at 700 °C, C:KOH ratio of 1:2

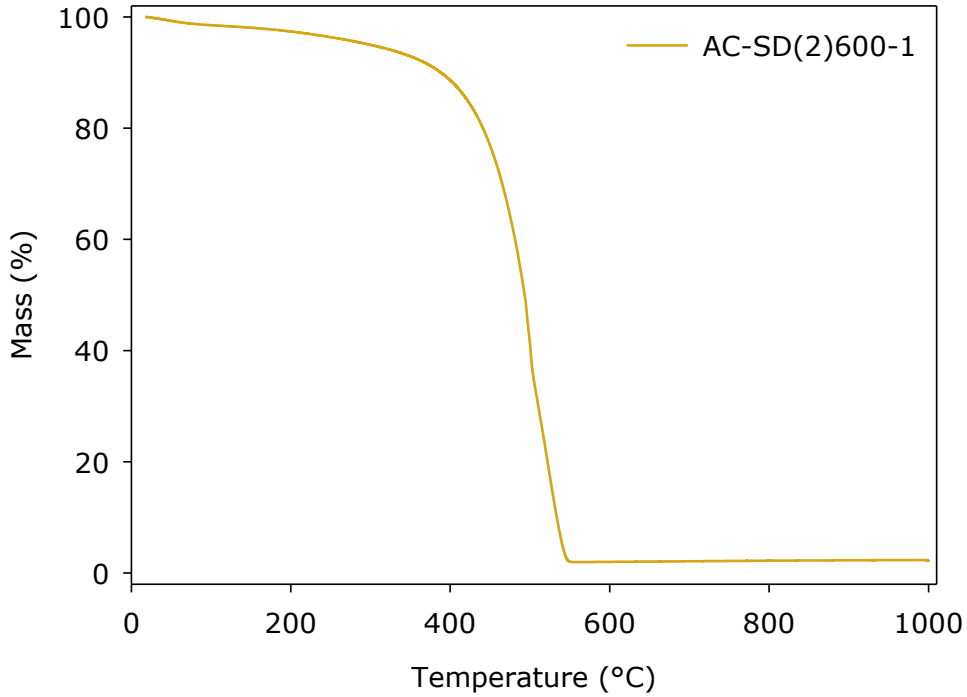

Figure 4.12. TGA plots of samples prepared from air-carbonised sawdust at 600 °C, C:KOH ratio of 1:2

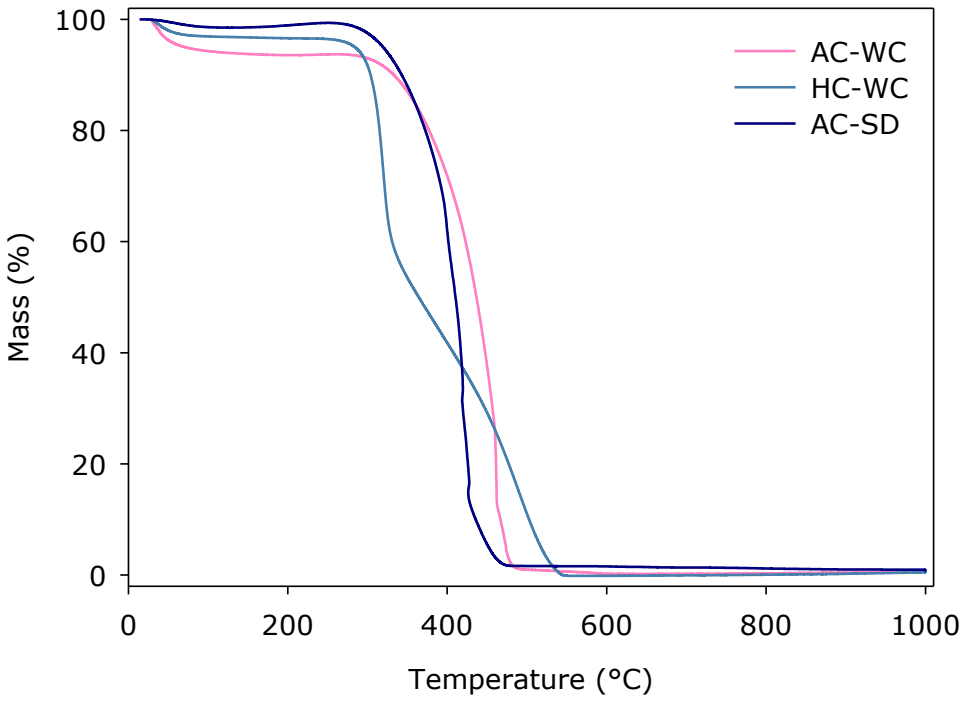

Figure 4.13. TGA plots of air-carbonised wood chippings, hydrothermally-carbonised wood chippings and air-carbonised sawdust

samples (Fig. 4.5) shows a clear difference in thermal stability between samples with an activation time of 5 hrs compared to 1 hr. The longer activation time results in lower thermal stability, suggesting that extensive activation at high temperature leads to 'over-activation'; continued activation reactions cause small pores to collapse into larger ones. This may result in a less regular structure and reduction in graphitisation, hence a lower thermal stability. TGA plots for AC-WC600 samples (Fig. 4.6) all show similar thermal stability, indicated by similar burn-off onset temperatures. AC-WC(4)600-5 shows the highest thermal stability. In the case of lower activation temperature, higher activating agent ratio and

activation time do not have the same effect on structure as at 800 °C. Instead, greater activation creates a more stable structure. HC-WC800 samples (Fig. 4.7) all show similar thermal stabilities, with the gentlest activation conditions (HC-WC(2)800-1) resulting in the lowest thermal stability. Samples having undergone prolonged activation, HC-WC(2)800-5 and HC-WC(4)800-5 do not show the highest thermal stability. As before, at the higher temperature of 800 °C, prolonged activation may result in some structural collapse, reducing the structural regularity.

TGA plots for the HC-WC600 sample set (Fig. 4.8) also show a clear difference in thermal stabilities. However, in this case, a lower activation agent ratio results in a lower thermal stability. This could suggest that at the lower temperature of 600 °C, a high ratio of activating agent results in further activation, but not excessive to the point of structural collapse.

AC-SD samples (Fig. 4.9 – 4.11) generally show a sharper carbon burn-off curve than samples derived from spruce wood chippings. This indicates that there is less variation in the carbon structure of samples derived from eucalyptus sawdust, therefore, the composition of the wood precursor may play a part in final sample structure. As with samples derived from wood chippings, AC-SD sample sets show conflicting trends.

AC-SD(2)800 samples (Fig. 4.10) show increasing thermal stability with activation time, however, AC-SD700 samples (Fig. 4.11) show decreasing thermal stability with increasing activation time.

Overall, the TGA plots show that harsher activation conditions leading to a more extensive activation, increases thermal stability to a point, after which excessive activation can become detrimental to structural stability. When analysing samples prepared from spruce wood chippings, those prepared at 600 °C (Fig. 4.6 and 4.8) have a shallower burn off curve than those prepared at 800 °C (Fig. 4.5 and 4.7). This may be a result of remaining volatiles present in the samples prepared at the lower temperature.[48] Carbonisation method does not have a clear effect on thermal stability. Wood composition may have an effect on the resulting carbon structure.

A clear way to compare the effects of carbonisation and activation conditions on thermal stability is to compare the average burn-off temperature of each sample set. The average burn off temperature for sample sets AC-WC800 and AC-WC600 (Fig. 4.5 and 4.6) is 565 and 509 °C respectively. This rises to 609 and 552 °C for HC-WC800 and HC-WC600 sample sets (Fig. 4.7 and 4.8) respectively. Not only does this confirm the higher thermal stabilities produced by a higher activation temperature,

but also that carbons prepared from a hydrochar precursor are on average, 43.5 °C more thermally stable than their airchar equivalents. Analysing the average burn-off temperature for sample sets prepared from eucalyptus sawdust demonstrates a clear that trend that thermal stability increases with harsher activation conditions; AC-SD600 (Fig. 4.12), AC-SD700 (Fig. 4.11), AC-SD(2)800 (Fig. 4.10) and AC-SD(4)800 (Fig. 4.9) have increasing thermal stabilities of 499, 520, 561 and 580 °C respectively.

There is a small variation in the level of remaining impurities after carbon burn-off, despite all activated samples being subjected to the same level of washing. Any remaining mass can be assumed to be potassium compounds derived from the KOH activation agent. Generally the samples can be considered to be clean, with most samples containing < 5 % impurities. Hydrothermally-carbonised samples (Fig. 4.7 and 4.8, with repeat measurements shown in Appendix Fig.'s 4.A1-4.A2) had noticeably higher levels of impurity. This may be due to hydrothermal carbonisation resulting in a char that, on activation, forms a structure that traps products of the activation procedure within the carbon structure. This would be assumed to have a detrimental effect on accessible pore structure and therefore gas uptake.

The TGA plots for the carbonised woods, AC-WC, HC-WC and AC-SD (Fig. 4.13) generally show lower thermal stability than the activated samples. This is to be expected, as they have been subjected to lower temperatures. The carbonised woods contain very low levels of impurities, < 2 %, confirming that any impurities found in the activated samples are formed in the activation process. The two air-carbonised woods show reasonably sharp burn-off curves, indicating single phase carbon, whereas hydrothermally-carbonised wood chippings has a two stage burn-off. This could suggest that air carbonisation is a more effective carbonisation method than hydrothermal carbonisation, as the resulting char is a more homogenous carbon material.

4. 4. 4. Powder X-Ray Diffraction Patterns

Powder x-ray diffraction (PXRD) was used to assess the purity, structure and graphitisation of all the carbon samples. The diffraction patterns are shown below in Figures 4.14 – 4.22. The particular areas of interest of the PXRD patterns are peaks at 2θ ≈ 22° and 44°, as these correspond respectively to diffraction of the (002) and (100) planes of stacked graphite. The very low angle region of the pattern (< 15°) was featureless in the context of the sample analyses, so is not reported here.

The PXRD patterns for samples prepared from air-carbonised wood chippings are shown in Figures 4.14 and 4.15. None of the 8 samples show any discernible peak at 2θ ≈ 22°. Any increased intensity may be partially obscured by background disturbances in the baseline, although it is clear that all eight samples display a highly amorphous and disordered carbon structure, with very few, if any, graphitic domains.[1] For this reason, the R value calculation of the 2θ ≈ 22° peak is not applicable; R can be assumed to equal 1, indicating that all graphene sheets are singularly distributed.[49] Peaks at 2θ ≈ 44° are broad and of low intensity, confirming little regularity of the carbon structure. All of the activated airchar samples show some level of impurity, indicated by sharp peaks of high intensity relative to

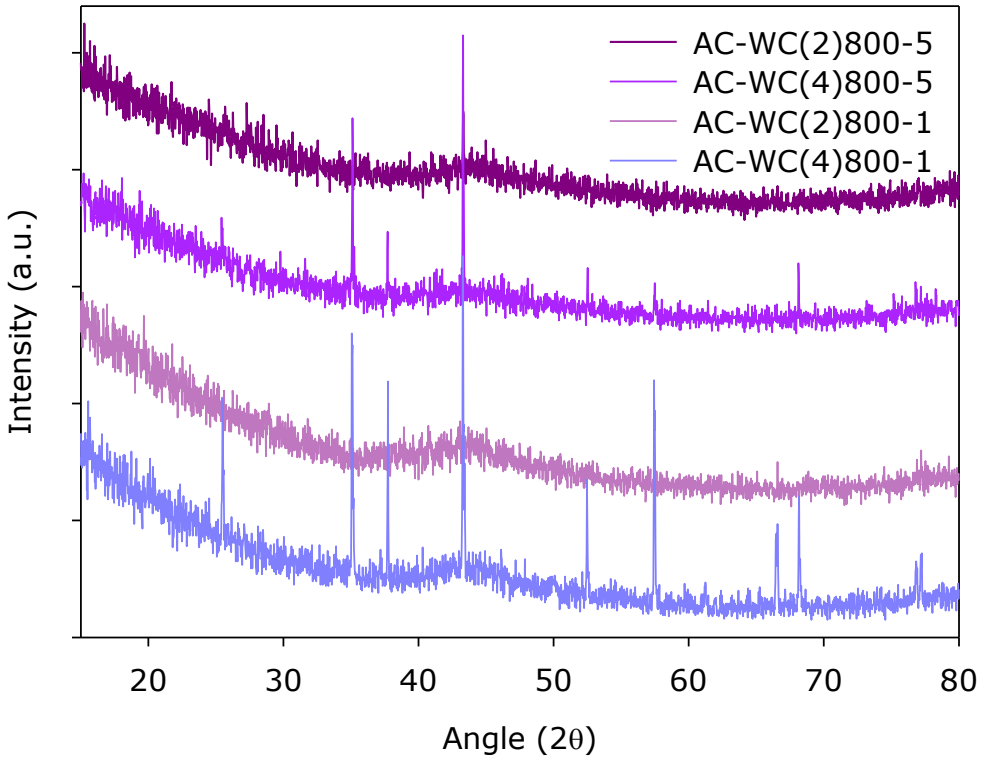

Figure 4.14. PXRD patterns of samples prepared from air-carbonised wood chippings at 800°C

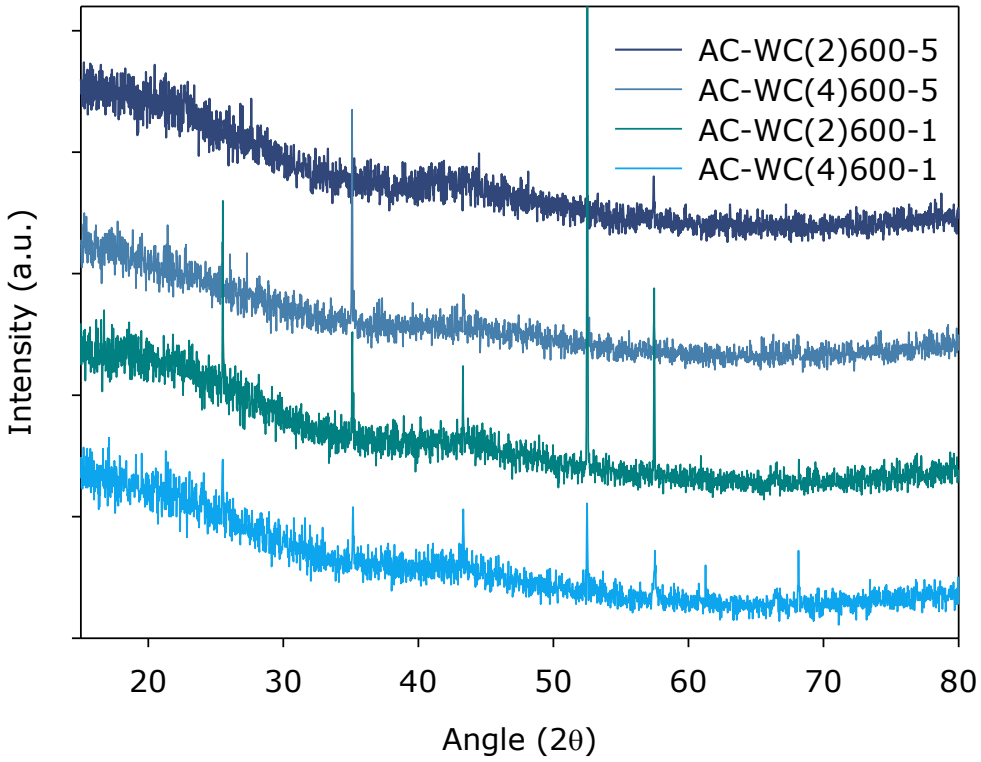

Figure 4.15. PXRD patterns of samples prepared from air-carbonised wood chipping at 600°C

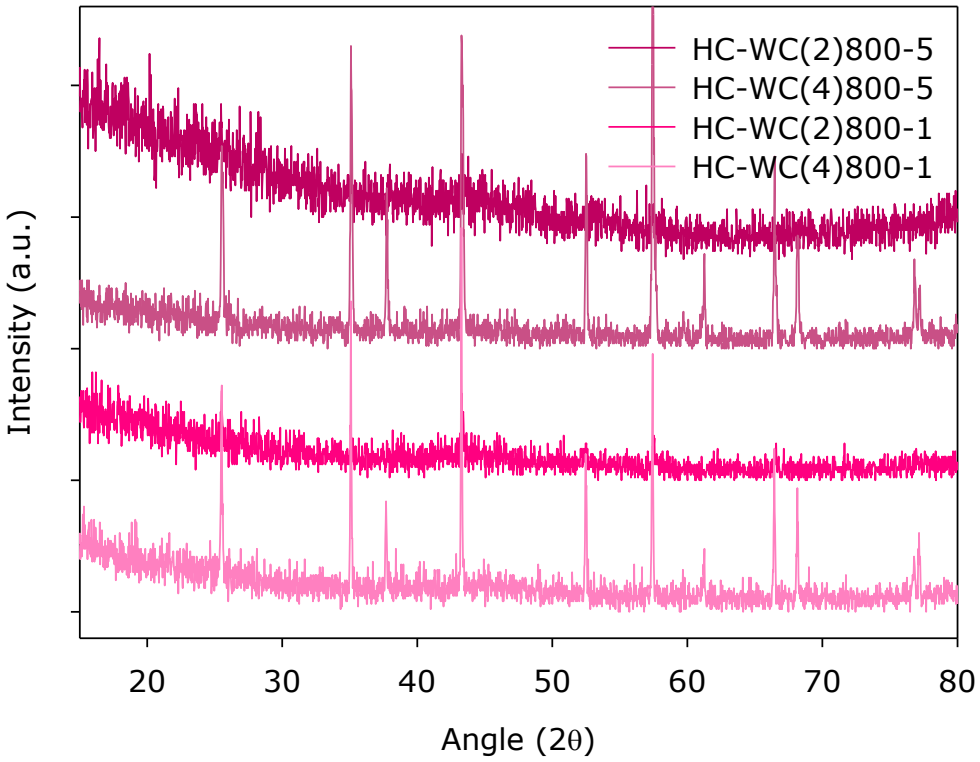

Figure 4.16. PXRD patterns of samples prepared from hydrothermally-carbonised wood chipping at 800°C

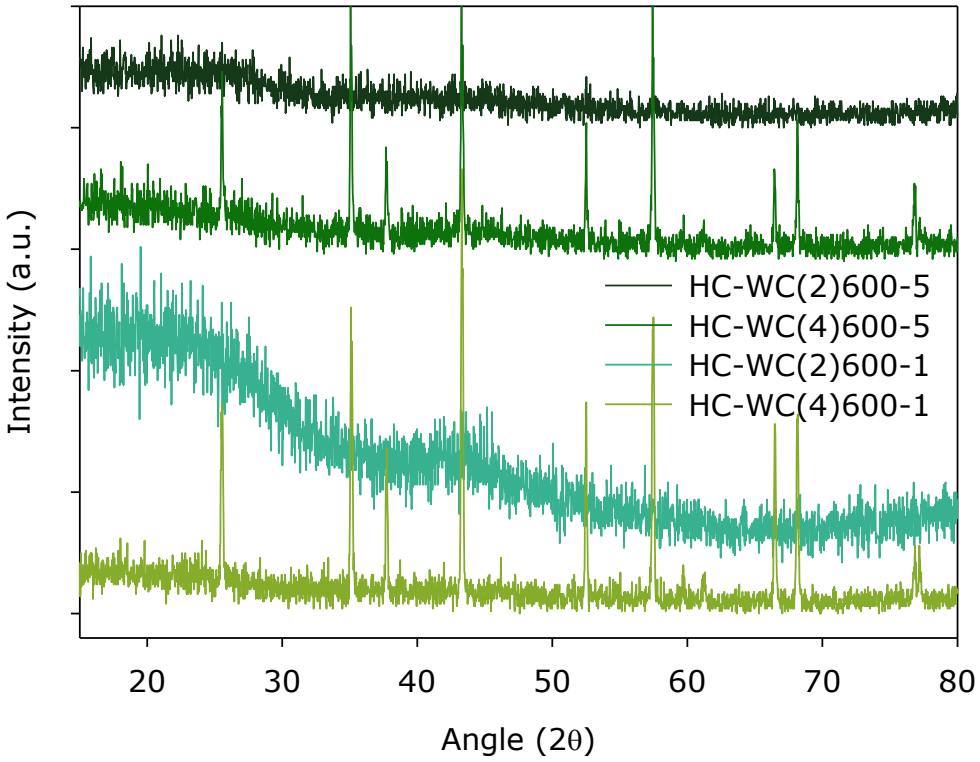

Figure 4.17. PXRD patterns of samples prepared from hydrothermally-carbonised wood chipping at 600°C

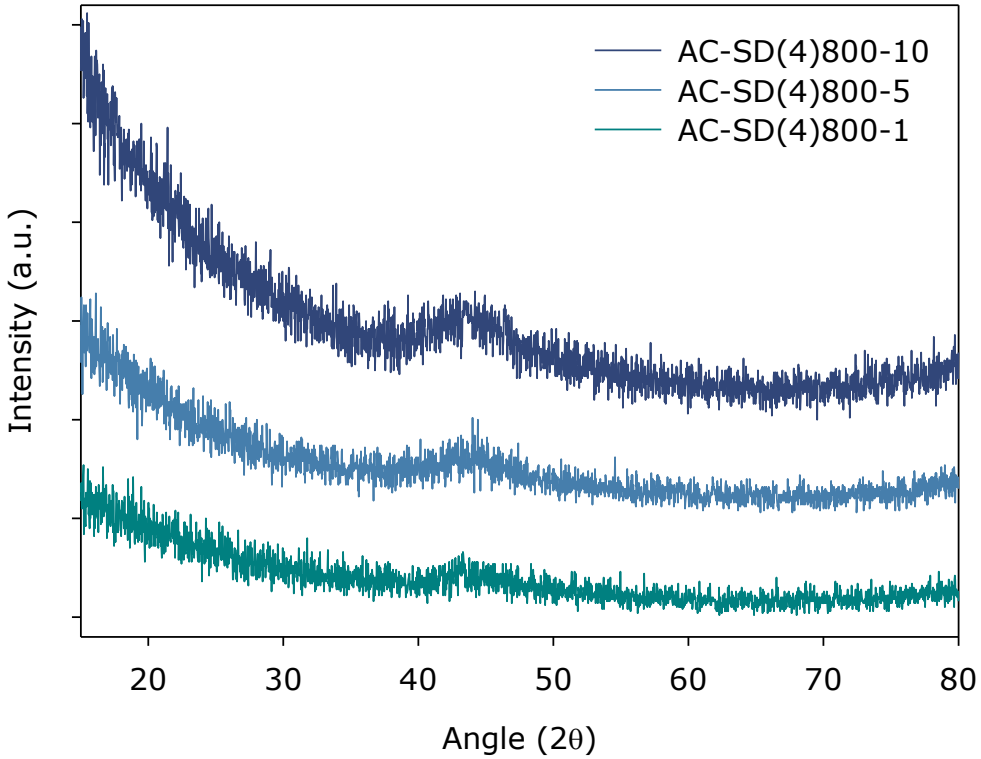

Figure 4.18. PXRD patterns of samples prepared from air-carbonised sawdust at 800°C, C:KOH = 1:4

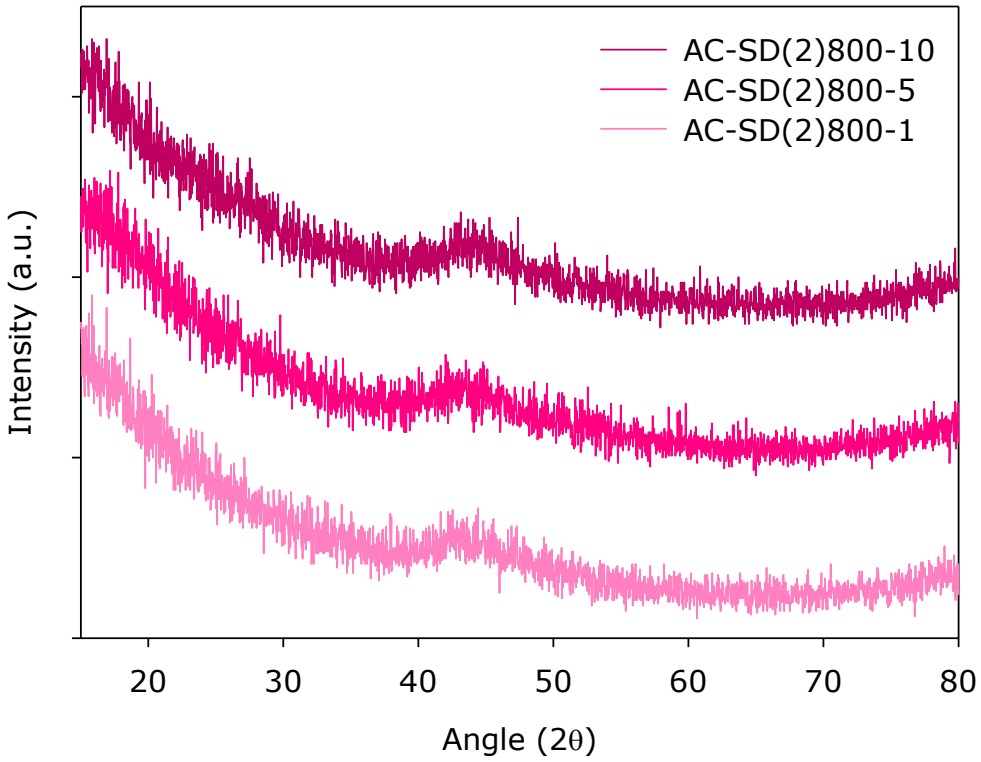

Figure 4.19. PXRD patterns of samples prepared from air-carbonised sawdust at 800°C, C:KOH = 1:2

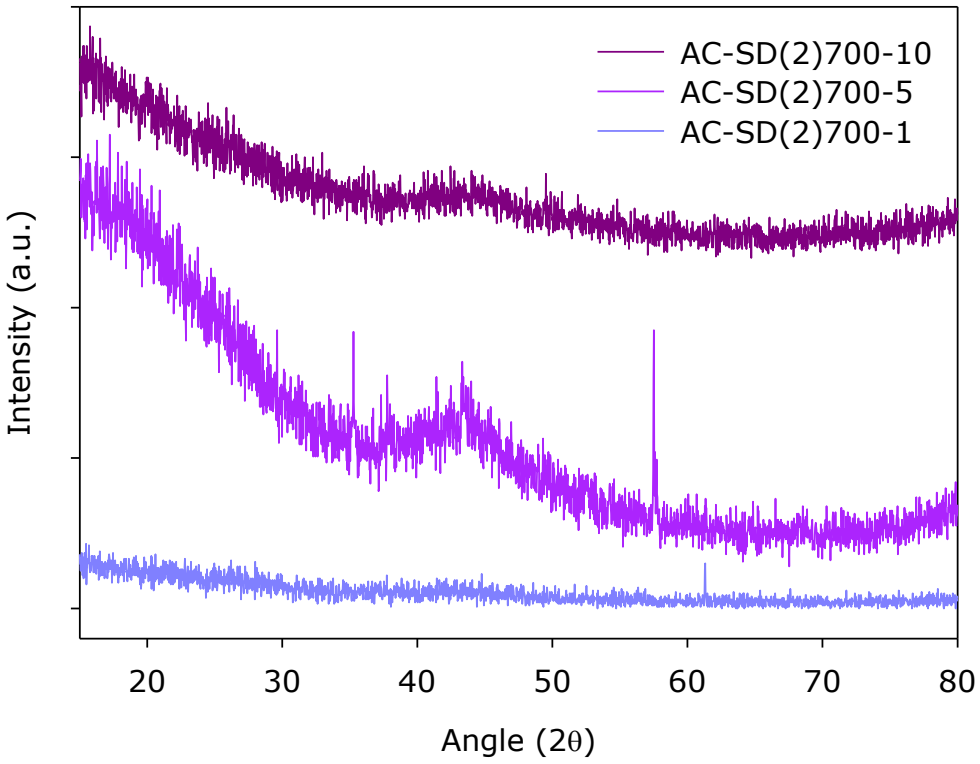

Figure 4.20. PXRD patterns of samples prepared from air-carbonised sawdust at 700°C

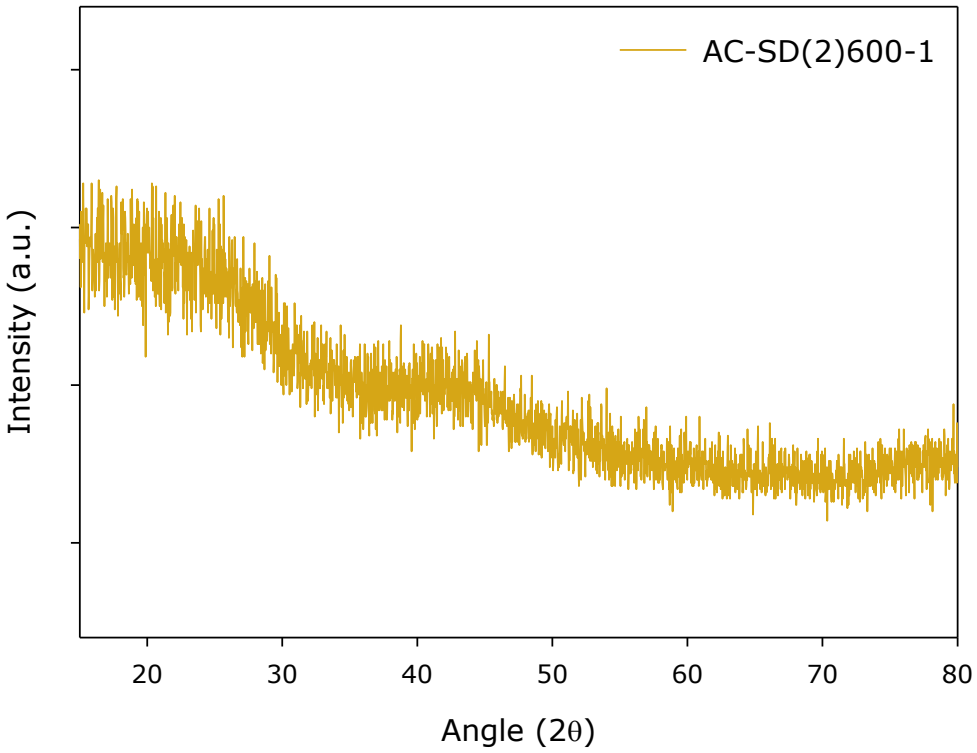

Figure 4.21. PXRD patterns of samples prepared from air-carbonised sawdust at 600°C

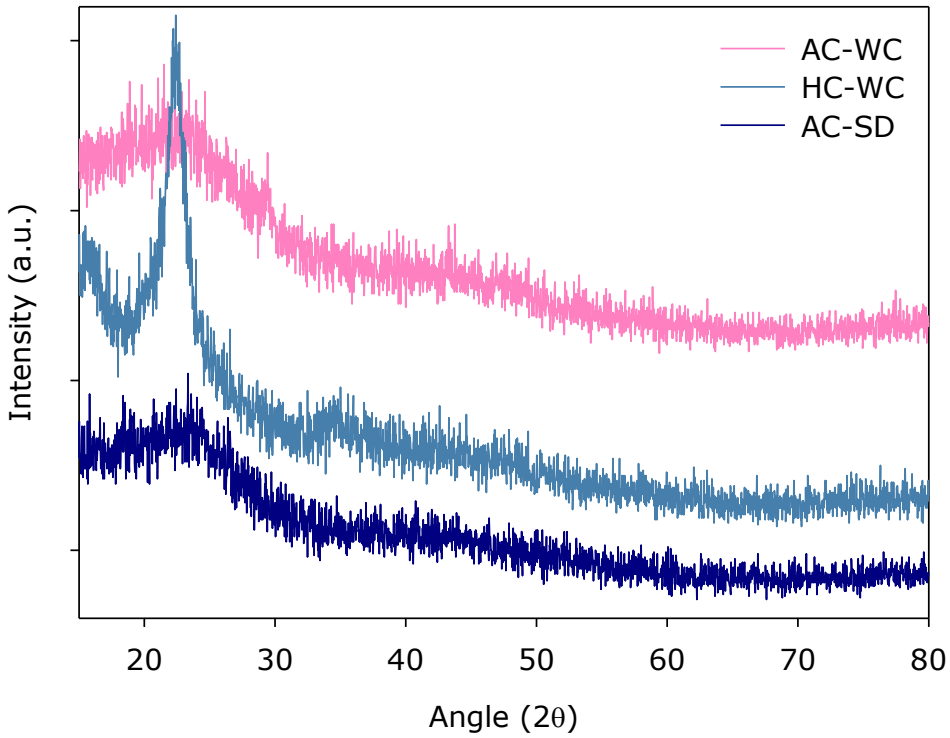

Figure 4.22. PXRD patterns of air-carbonised wood chippings, hydrothermally-carbonised wood chippings and air-carbonised sawdust

the baseline. As mentioned previously, any impurities can be assumed to be potassium-based compounds formed during activation. AC-WC(4)800-1 has the most abundant impurity peaks, corresponding with the conclusions drawn from the TGA.

The PXRD patterns for activated hydrochar samples (Fig. 4.16 and 4.17) show similar results to those of their airchar equivalents. Any increase of intensity at 2θ ≈ 22° is virtually indiscernible, again indicating that all 8 samples are highly amorphous with few graphitic domains. R can be assumed to equal 1 in all cases. Peaks at 2θ ≈ 44° are low intensity and broad, in line with amorphous, turbostratic carbons. The

samples generally show higher levels of impurity than the airchar equivalents, corresponding with the high impurity levels shown by TGA.

Samples prepared from air-carbonised sawdust and activated at 800 °C (Fig. 4.18 and 4.19) show similar PXRD patterns to the samples mentioned previously, with no discernible peaks at 2θ ≈ 22° and low, broad peaks at 2θ ≈ 44°. R values at 2θ ≈ 22° can be assumed to equal 1, indicating amorphous, turbostratic carbon structures. There are virtually no sharp peaks indicative of impurities, which reflect the TGA curves.

Samples prepared from air-carbonised sawdust and activated at 700 °C and 600 °C (Fig. 4.20 and 4.21) show a slightly higher degree of regularity than the previous activated samples. Low intensity, broad peaks at 2θ = 25° provide an R value of 1.5, 1.5 and 1.2 for AC-SD(2)700-5, AC-SD(2)700-1 and AC-SD(2)600-1 respectively.

Figure 4.22 shows the PXRD patterns for the carbonised precursors, AC-WC, HC-WC and AC-SD. All three samples show a clear peak at 2θ ≈ 22°; AC-WC and HC-WC show increased intensity centred at 2θ = 22° with R values of 1.7 and 3.4 respectively. AC-SD shows increased intensity centred at 2θ = 24° with an R value of 1.8. It is clear that both airchar

precursors have a similarly regular structure and that air-carbonisation causes a certain level of graphitisation that is independent of wood type. Hydrothermal carbonisation produces carbons with a significantly more regular structure, with a higher proportion of graphitic domains and longer-range order than air-carbonised equivalents. This higher level of graphitisation may be an explanation for the higher thermal stabilities of activated hydrochar samples seen on the TGA curves; a greater level of graphitisation remains in these samples after activation, which is immeasurable by PXRD. The lack of sharp impurity peaks in the PXRD patterns of these three samples confirms that impurities found in activated samples were formed during the activation process.

It is clear from the PXRD patterns that in all cases, activation causes a significant decrease in the graphene stacking of the carbonised precursors. All activated samples show PXRD patterns associated with amorphous, turbostratic carbons, with a high level of irregularity and few graphitic domains. Carbonisation method has a significant effect on the resulting carbon structure; air-carbonisation is more effective at breaking down the complex organic structure of the wood precursor than hydrothermal-carbonisation. From studying the PXRD patterns, the type of wood precursor does not appear to have any

significant effect on either the efficiency of air-carbonisation, or the subsequent activation step.

4. 4. 5. Nitrogen Sorption Isotherms

The N_2 sorption isotherms recorded at -196 °C are shown below in Figures 4.23 – 4.31. The N_2 sorption isotherms for samples prepared from air-carbonised wood chippings are shown in Figures 4.23 and 4.24. All eight samples generally show type I isotherms; sharp N_2 uptake at low relative pressure followed by a plateau, indicates highly microporous samples. Carbons activated at 600 °C (Fig. 4.24) exhibit steep N_2 uptake at $P/P_0 < 0.04$, followed by a sharp knee, which then plateaus. The consistent shape of the isotherms indicates similar PSDs. Carbons activated at 800 °C (Fig. 4.23) generally show a broader knee than those activated at 600 °C, indicating a broader range of micropore widths. AC-WC(4)800-1 and AC-WC(4)800-5 have significantly broader knees, with AC-WC(4)800-5 showing some type IV(b) character, indicating the presence of small mesopores. As well as broadening of the isotherm knee, activation at 800 °C also shows an increase in N_2 uptake; two indications of increased porosity that are consistent with previous studies.[10,30,45,49–52] The breakdown of K_2CO_3 at 800 °C releases CO_2 and CO, widening pore channels and increasing porosity.

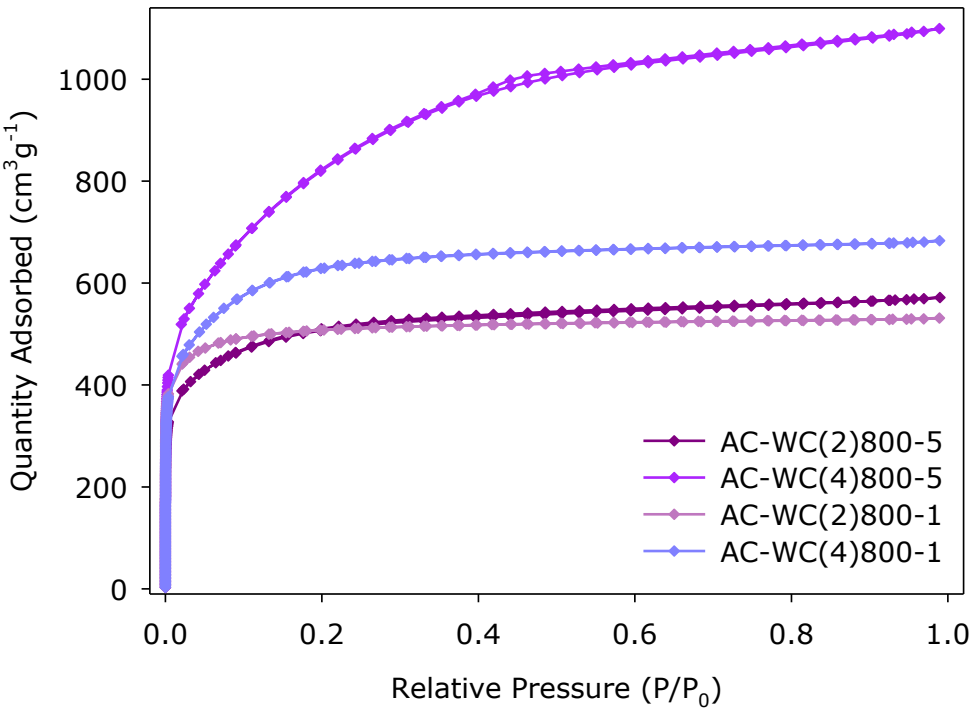

Figure 4.23. Sorption isotherms of samples prepared from air-carbonised wood chippings at 800 °C

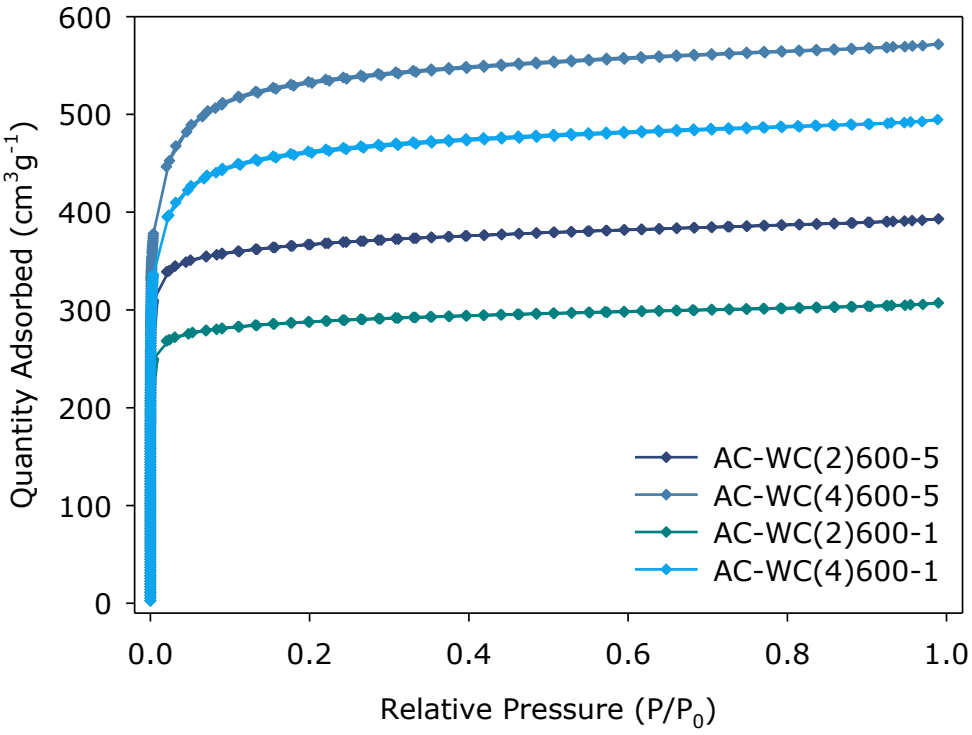

Figure 4.24. Sorption isotherms of samples prepared from air-carbonised wood chippings at 600 °C

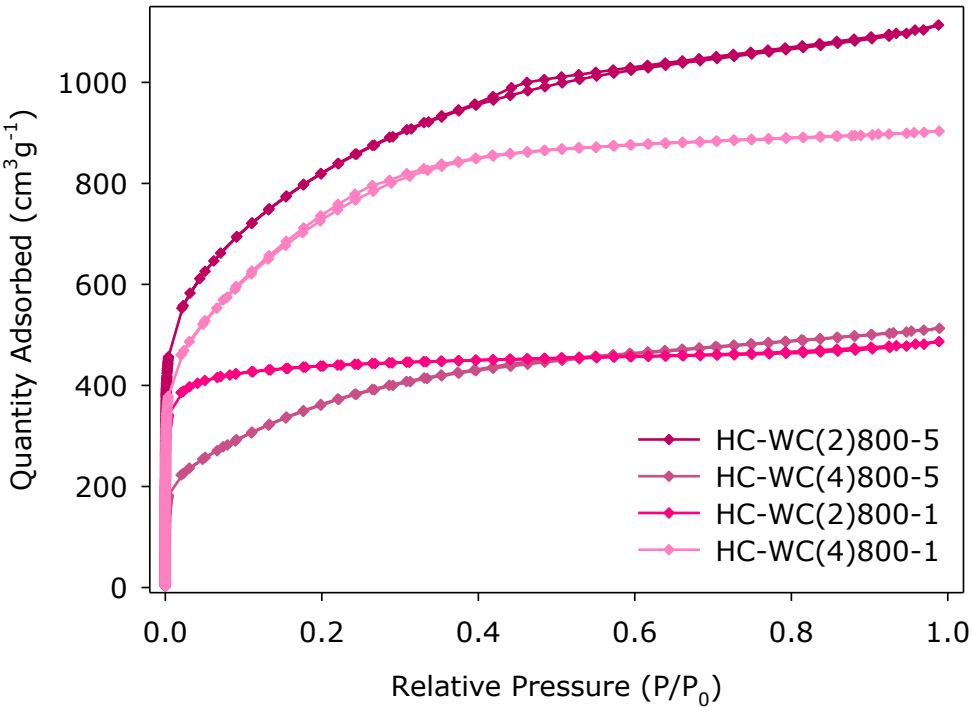

Figure 4.25. Sorption isotherms of samples prepared from hydrothermally-carbonised wood chippings at 800 °C

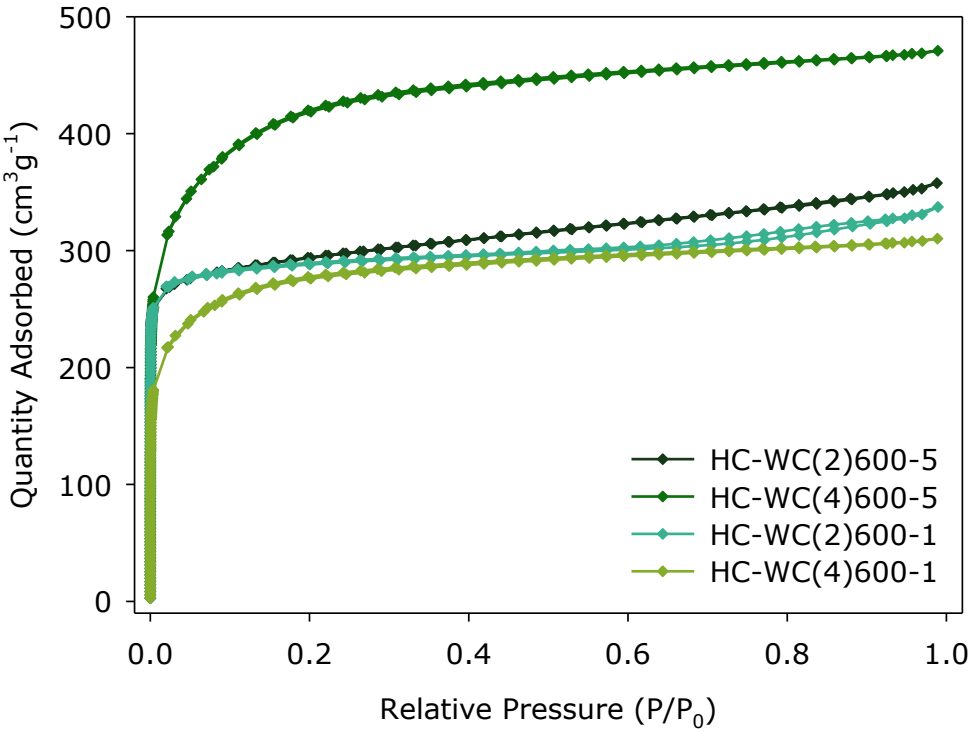

Figure 4.26. Sorption isotherms of samples prepared from hydrothermally-carbonised wood chippings at 600 °C

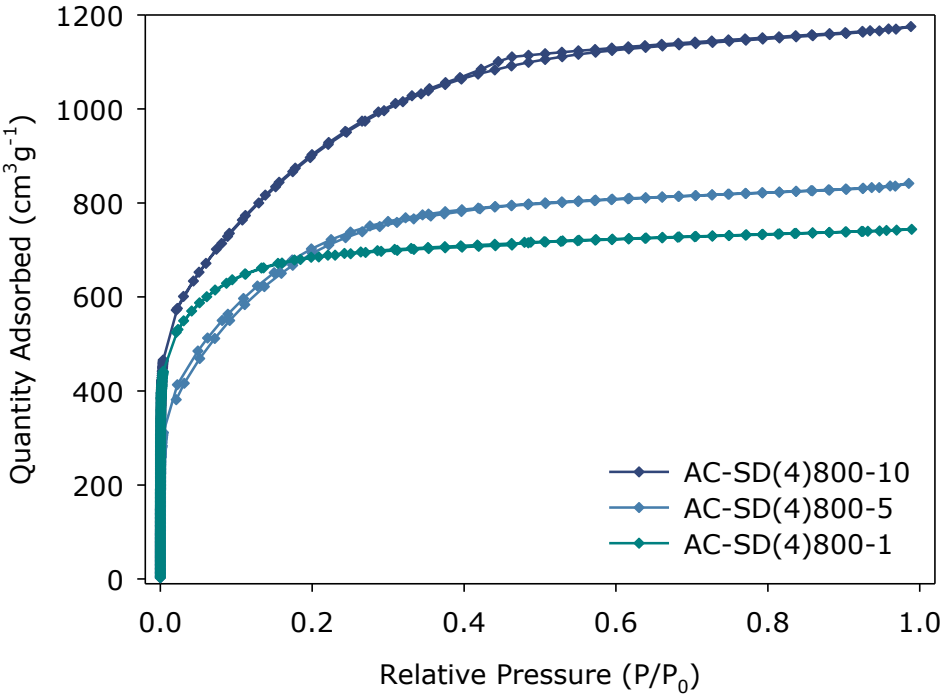

Figure 4.27. Sorption isotherms of samples prepared from air-carbonised sawdust at 800 °C, C:KOH ratio of 1:4

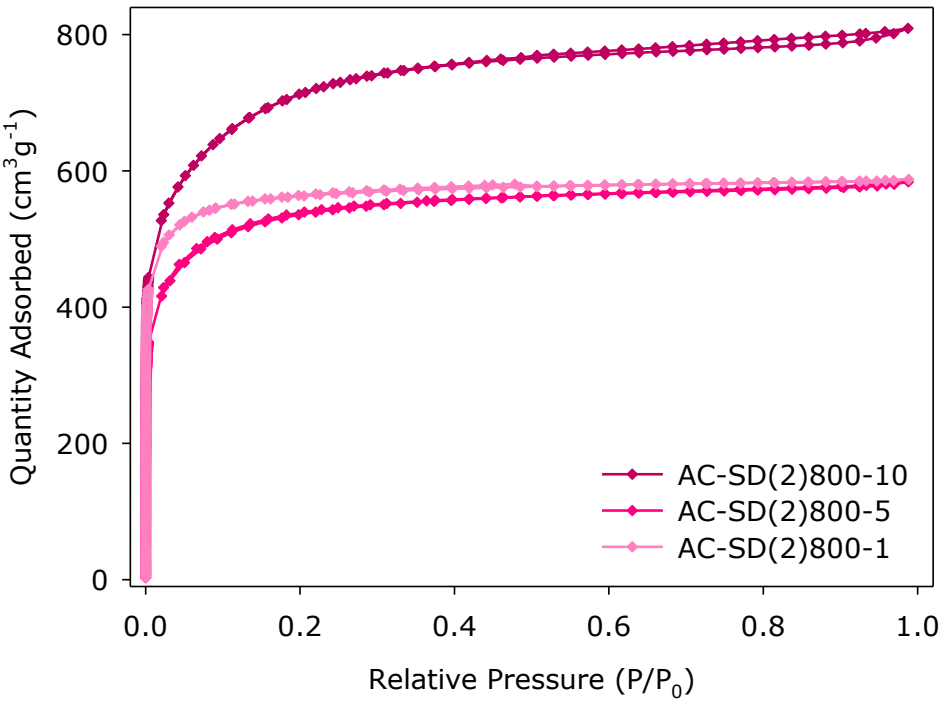

Figure 4.28. Sorption isotherms of samples prepared from air-carbonised sawdust at 800 °C, C:KOH ratio of 1:2

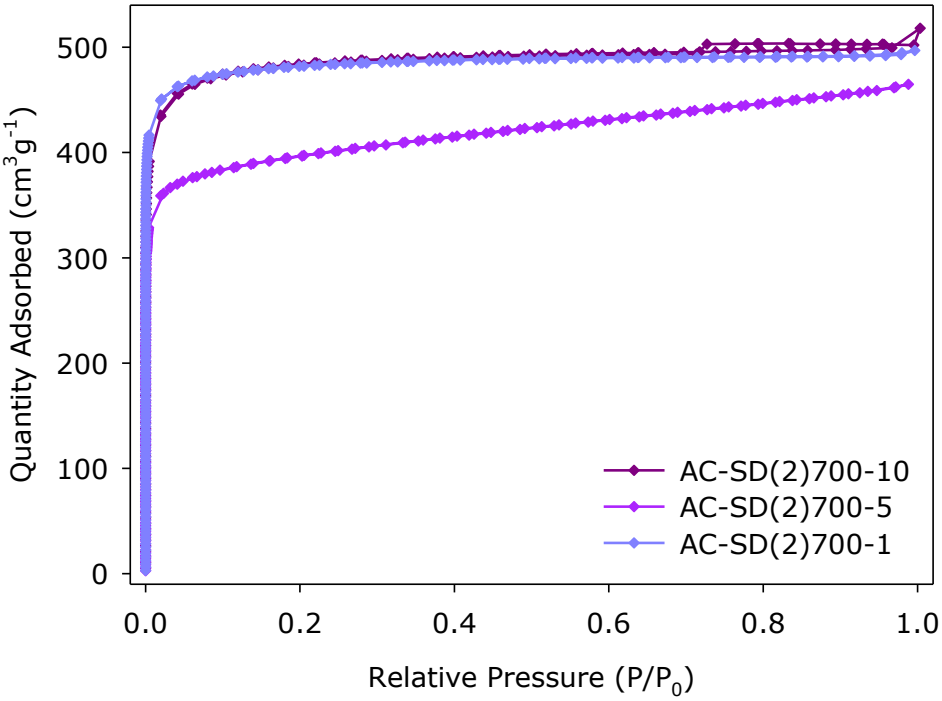

Figure 4.29. Sorption isotherms of samples prepared from air-carbonised sawdust at 700 °C, C:KOH ratio of 1:2

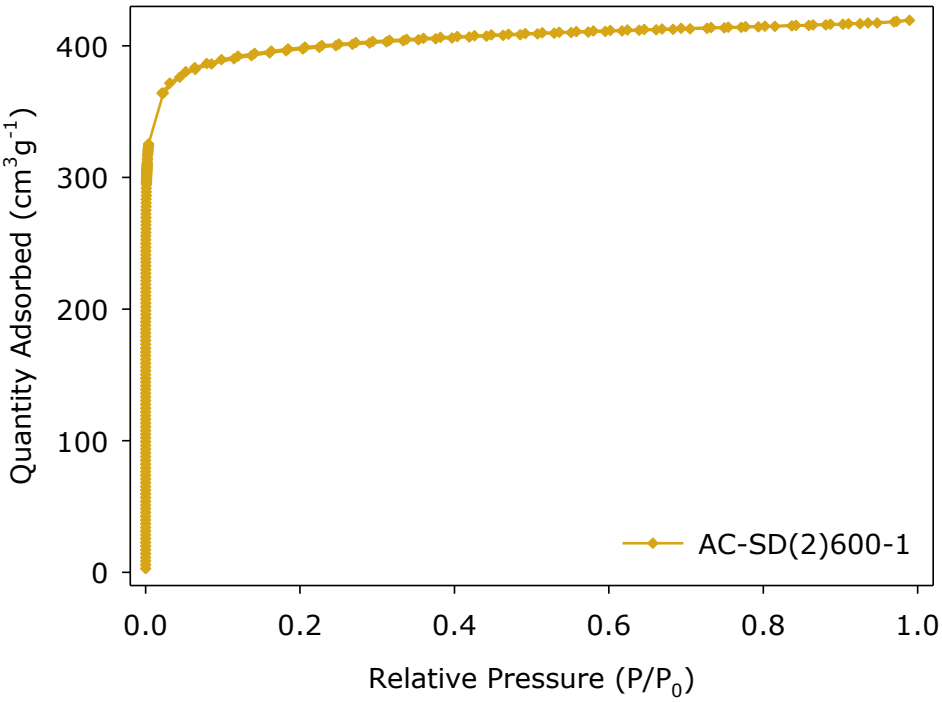

Figure 4.30. Sorption isotherms of samples prepared from air-carbonised sawdust at 600 °C, C:KOH ratio of 1:2

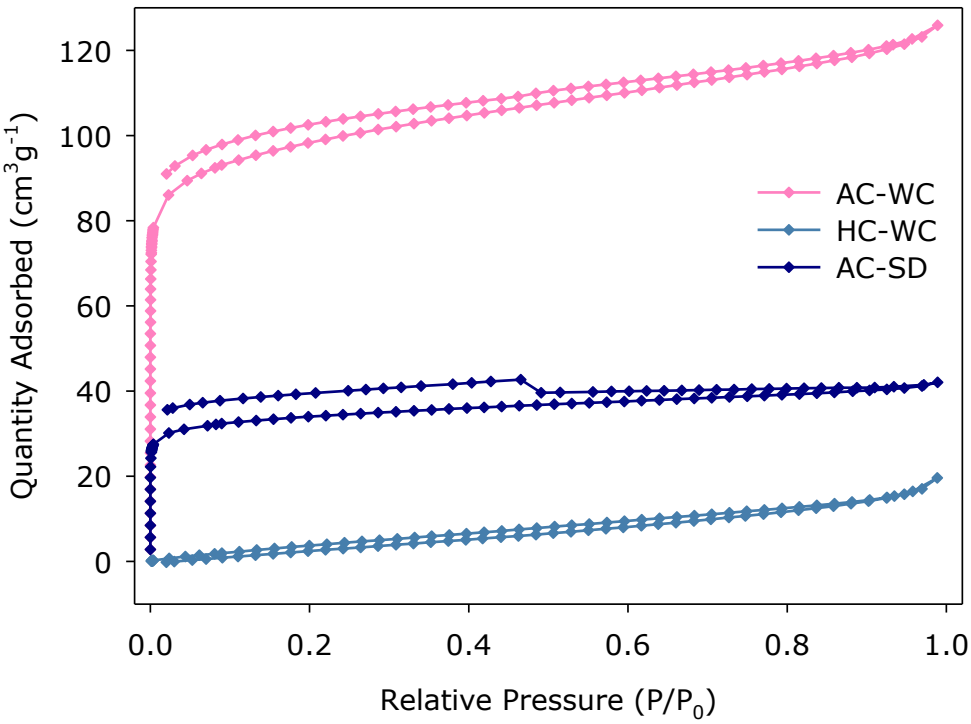

Figure 4.31. Sorption isotherms of air-carbonised wood chippings, hydrothermally wood chippings and air-carbonised sawdust

Samples with a KOH:carbon ratio of 4 exhibit a more developed porosity, as a larger ratio of K_2CO_3 breaks down, creating new pores and widening existing pores.[41–44] From Figure 4.23 (AC-WC800), it is clear that, although a longer activation time also results in a more developed porosity, the effect is not as significant as an increased activating agent ratio.

The N_2 sorption isotherms for samples prepared from hydrothermally-carbonised wood chippings are shown in Figures 4.25 and 4.26. The samples generally show type I isotherms, with some showing type IV characteristics,

indicating the presence of small mesopores. Isotherms for samples activated at 600 °C (Fig. 4.26) are highly microporous, indicated by sharp knees followed by plateaus. Although overall N_2 uptake is lower, uptake is complete at P/P_0 = 0.08. Isotherms for samples activated at 800 °C are shown in Figure 4.25. As before, activation at the higher temperature results in higher N_2 uptake and broadening of the isotherm knee as a result of a more developed porosity. Again, this increased porosity can be attributed to the decomposition of K_2CO_3 at 800 °C.

HC-WC(4)800-1 and HC-WC(2)800-5 both show type IV characteristics. Both isotherms show a broad knee, which is evidence of a broadened PSD and the presence of a significant volume of small mesopores. HC-WC(2)800-5 shows an isotherm close to type IV(b); N_2 uptake continually increases after an initial knee, indicating multilayer adsorption taking place in mesopores. As with the equivalent airchar samples, increasing activating temperature, time and activating agent ratio increases pore development, resulting in higher levels of porosity and a widening of the PSD. This can be attributed to increased release of CO_2 and CO as K_2CO_3 breaks down and is represented by higher N_2 uptake, broader knees and uptake at higher relative pressure of the sorption isotherm. HC-

WC(4)800-5 is an exception to this trend and may be an example of 'over-activation'. The harshest activation conditions may cause pores to collapse, blocking pore channels and broadening the PSD, reducing both microporosity and overall porosity.

Sorption isotherms for samples prepared from air-carbonised sawdust are shown in Figures 4.27 – 4.30. Carbons activated at 600 °C and 700 °C (Fig. 4.30 and 4.29) show type I isotherms, with very high N_2 uptake at $P/P_0 < 0.02$, followed by sharp knees and plateaus to indicate micropore saturation. These samples can all be assumed to be highly microporous with a narrow PSD. Samples activated at 800 °C with a KOH:carbon ratio of 2, show increased N_2 uptake and broader knees than the equivalent samples activated at lower temperatures, but still exhibit steep uptake at very low relative pressure and micropore saturation. Samples activated at 800 °C with a KOH:carbon ratio of 4 exhibit the highest N_2 uptake and very broad knees for AC-SD(4)800-10 and AC-SD(4)800-5.

Generally, all the activated samples produce a type I isotherm, although some samples activated under harsher conditions begin to show type IV characteristics. The activation conditions have a clear effect on the isotherm shape, with higher activating agent ratios and a temperature over 800 °C having the most

significant effect. Under these conditions, there is greater breakdown of K_2CO_3 into CO_2 and CO, widening existing pores and creating new ones. This more developed porosity and widened PSD are represented by higher N_2 uptake, broader knees and some mesopore adsorption on the sorption isotherms. Samples prepared from air-carbonised wood exhibit higher degrees of microporosity than those prepared from hydrothermal carbonisation, suggesting that the airchar is more resistant to excessive activation. The type of wood used seems to have little effect on the isotherm shape of the final samples.

The sorption isotherms for the carbonised chars are shown in Figure 4.31. AC-WC has a type I isotherm with notable N_2 uptake and a sharp knee. This is uncommon for carbonised chars and indicates a carbon with an established degree of porosity. HC-WC shows negligible N_2 uptake; the isotherm indicates a non-porous char. AC-SD shows an isotherm with some type I character, with a relatively sharp knee, followed by a plateau. Some degree of microporosity is indicated by N_2 uptake at very low relative pressure. However, overall N_2 uptake is significantly lower than that seen for AC-WC, indicating that the wood composition of eucalyptus is less amenable to porosity development during carbonisation that spruce wood.

It is clear that air-carbonisation produces a char with some degree of microporosity, most notably when using spruce wood as a precursor. When using eucalyptus wood as a precursor, porosity development occurs to a lesser extent, and is on the macropore scale. The process of air-carbonisation allows porosity to develop as volatiles are burnt off and escaping gases create pore channels. However, the composition of the wood precursor does have an effect on the efficiency of this process. Hydrothermal carbonisation creates a virtually non-porous char; the process does not allow for the removal of volatiles through gaseous escape. In all cases, activation has a great effect on the pore development of the chars.

4. 4. 6. Textural Properties; Surface Area and Pore Volume

The surface area and pore volume measurements, calculated from N_2 sorption data, are displayed below in Tables 4.5 – 4.10. The surface area and pore volume data for samples prepared from air-carbonised wood chippings is reported in Tables 4.5 and 4.8 respectively. The activated samples show a broad range of surface areas, pore volumes and proportion of microporosity. AC-WC(2)600-1 was activated under the gentlest conditions and as expected, shows the lowest level of porosity, with a surface area and pore volume of 1085 $m^2\ g^{-1}$ and 0.48 $cm^3\ g^{-1}$ respectively. However, this sample possesses one of the highest

Table 4.5. Surface area of samples prepared from air-carbonised wood chippings, calculated by BET theory. [a]Proportion of surface area arising from micropores, as a value and as a % of total surface area

Sample	Surface Area ($m^2\ g^{-1}$)	[a]Micropore Surface Area ($m^2\ g^{-1}$)
AC-WC	366	267 – 73%
AC-WC(2)800-1	1944	1672 – 86%
AC-WC(4)800-1	2373	1507 – 64%
AC-WC(2)600-1	1085	966 – 89%
AC-WC(4)600-1	1756	1465 – 83%
AC-WC(2)800-5	1914	1161 – 61%
AC-WC(4)800-5	2913	212 – 7%
AC-WC(2)600-5	1387	1219 – 88%
AC-WC(4)600-5	2038	1680 – 82%

levels of microporosity, with micropores responsible for 89 % of surface area and 82 % of pore volume. AC-WC(4)800-5 was activated under the harshest conditions and exhibits the most developed porosity, with a surface area and pore volume of 2913 $m^2\ g^{-1}$ and 1.71 $cm^3\ g^{-1}$ respectively. AC-WC(4)800-5 also possesses the lowest level of microporosity, with micropores responsible for only 7 % of surface area and 5 % of pore volume. This data trend can be explained by harsher activation

Table 4.6. Surface area of samples prepared from hydrothermally-carbonised wood chippings, calculated by BET theory. [a]Proportion of surface area arising from micropores, as a value and as a % of total surface area

Sample	Surface Area ($m^2\ g^{-1}$)	[a]Micropore Surface Area ($m^2\ g^{-1}$)
HC-WC	17	-
HC-WC(2)800-1	1666	1405 – 84%
HC-WC(4)800-1	2568	75 – 3%
HC-WC(2)600-1	1087	960 – 88%
HC-WC(4)600-1	1048	735 – 70%
HC-WC(2)800-5	2944	646 – 22%
HC-WC(4)800-5	1275	-
HC-WC(2)600-5	1098	880 – 80%
HC-WC(4)600-5	1570	932 – 59%

conditions causing more extensive reactions of KOH with the carbon skeleton and the breakdown of K_2CO_3 releasing higher volumes of CO_2 and CO. The result is the creation of new pores and widening of existing pores, increasing surface area, broadening the PSD and reducing microporosity. These results were predicted by analysis of the N_2 sorption isotherms (Fig. 4.23 and 4.24), where AC-WC(2)600-1 has steep uptake at low

Table 4.7. Surface area of samples prepared from air-carbonised sawdust, calculated by BET theory. [a]Proportion of surface area arising from micropores, as a value and as a % of total surface area

Sample	Surface Area ($m^2\ g^{-1}$)	[a]Micropore Surface Area ($m^2\ g^{-1}$)
AC-SD	127	97 – 76%
AC-SD(2)800-1	2150	1861 – 87%
AC-SD(2)800-5	2051	1477 – 72%
AC-SD(2)800-10	2661	1555 – 58%
AC-SD(4)800-1	2610	1892 – 72%
AC-SD(4)800-5	2562	161 – 6%
AC-SD(4)800-10	3159	88 – 3%
AC-SD(2)700-1	1715	1658 – 97%
AC-SD(2)700-5	1495	1224 – 82%
AC-SD(2)700-10	1716	1645 – 96%
AC-SD(2)600-1	1426	1094 – 77%

relative pressure followed by a sharp knee with low N_2 uptake, whereas AC-WC(4)800-5 shows a broad knee, with high N_2 uptake extending into higher relative pressure. Further analysis of the textural properties of this data set confirm the effect of activation conditions on resulting porosity. AC-WC(2)800-1 was activated under 'standard conditions' and exhibits surface area,

Table 4.8. Pore volume of samples prepared from air-carbonised wood chippings. [a]Proportion of pore volume arising from micropores, as a value and as a % of total pore volume

Sample	Pore Volume ($cm^3\ g^{-1}$)	[a]Micropore Volume ($cm^3\ g^{-1}$)
AC-WC	0.20	0.11 – 55%
AC-WC(2)800-1	0.82	0.67 – 82%
AC-WC(4)800-1	1.06	0.59 – 56%
AC-WC(2)600-1	0.48	0.39 – 81%
AC-WC(4)600-1	0.77	0.58 – 75%
AC-WC(2)800-5	0.89	0.46 – 52%
AC-WC(4)800-5	1.71	0.08 – 5%
AC-WC(2)600-5	0.61	0.50 – 82%
AC-WC(4)600-5	0.89	0.67 – 75%

pore volume and corresponding microporosity (%) of 1944 $m^2\ g^{-1}$ (86 %) and 0.82 $cm^3\ g^{-1}$ (82 %) respectively. The effect of increasing activating agent ratio is exhibited by AC-WC(4)800-1. This sample has a surface area of 2373 $m^2\ g^{-1}$, a 22 % increase on standard conditions, with a corresponding decrease in micropore surface area of 26 %. In terms of pore volume, AC-WC(4)800-5 has a pore volume of 1.06 $cm^3\ g^{-1}$, a 29 % increase on standard conditions, with a corresponding decrease

Table 4.9. Pore volume of samples prepared from hydrothermally-carbonised wood chippings. [a]Proportion of pore volume arising from micropores, as a value and as a % of total pore volume

Sample	Pore Volume ($cm^3\ g^{-1}$)	[a]Micropore Volume ($cm^3\ g^{-1}$)
HC-WC	0.03	-
HC-WC(2)800-1	0.76	0.56 – 74%
HC-WC(4)800-1	1.40	0.03 – 2%
HC-WC(2)600-1	0.52	0.39 – 75%
HC-WC(4)600-1	0.48	0.29 – 60%
HC-WC(2)800-5	1.73	0.26 – 15%
HC-WC(4)800-5	0.80	-
HC-WC(2)600-5	0.56	0.36 – 64%
HC-WC(4)600-5	0.73	0.36 – 49%

in micropore volume of 32 %. Increasing the ratio of activating agent generates a substantial increase in porosity, seen by an increased surface area and pore volume, but coupled with the development of some mesoporosity, resulting in a reduction of microporosity.

The effect of increasing activation time is shown by AC-WC(2)800-5. This sample has a surface area of 1914 $m^2\ g^{-1}$,

Table 4.10. Pore volume of samples prepared from air-carbonised sawdust. [a]Proportion of pore volume arising from micropores, as a value and as a % of total pore volume

Sample	Pore Volume ($cm^3\ g^{-1}$)	[a]Micropore Volume ($cm^3\ g^{-1}$)
AC-SD	0.06	0.04 – 67%
AC-SD(2)800-1	0.91	0.74 – 81%
AC-SD(2)800-5	0.91	0.58 – 64%
AC-SD(2)800-10	1.26	0.61 – 48%
AC-SD(4)800-1	1.15	0.74 – 64%
AC-SD(4)800-5	1.30	0.03 – 2%
AC-SD(4)800-10	1.82	0.04 – 2%
AC-SD(2)700-1	0.77	0.72 – 94%
AC-SD(2)700-5	0.72	0.50 – 69%
AC-SD(2)700-10	0.80	0.72 – 90%
AC-SD(2)600-1	0.72	0.44 – 61%

a 2 % decrease compared with standard conditions, with a corresponding 29 % decrease in micropore surface area. AC-WC(2)800-5 has a pore volume of 0.89 $cm^3\ g^{-1}$, a 9 % increase compared with standard conditions, with a corresponding decrease in micropore volume of 37 %. Increasing activation

time has a negligible effect on overall porosity, but causes a significant decrease in microporosity.

The effect of activation temperature is shown by AC-WC(2)600-1. This sample has a surface area of 1085 m^2 g^{-1}, a 44 % decrease compared with standard conditions, with a corresponding 3 % in microporosity. AC-WC(2)600-1 has a pore volume of 0.48 cm^3 g^{-1}, a 41 % decrease compared with standard conditions, with a corresponding 1 % decrease in microporosity. Activation temperature can be assumed to have a negligible effect on microporosity in this case, but significant increase in overall porosity with temperature.

The airchar, AC-WC shows reasonable surface area, pore volume and microporosity for a carbonised precursor, of 366 m^2 g^{-1} and 0.2 cm^3 g^{-1} respectively, with corresponding microporosities of 73 % and 55 %.

The surface area and pore volume data for samples prepared from hydrothermally-carbonised wood chippings are reported in Tables 4.6 and 4.9. The activated samples show a broad range of surface areas, pore volumes and proportions of microporosity. HC-WC(4)600-1 was activated under reasonably gentle conditions and possesses the lowest surface area of the sample set of 1048 m^2 g^{-1}, with a micropore surface area of 70

%. HC-WC(2)800-5 was activated under reasonably harsh conditions and possesses the highest surface area of the sample set, of 2944 m^2 g^{-1}, with a micropore surface area of 22 %. Although the trend of harsher activating conditions resulting in a higher level of porosity but reduced microporosity, reflects the trend seen in the AC-WC sample set, it is not the equivalent samples showing the most extreme results. The highest proportion of micropore surface area is exhibited by HC-WC(2)600-1 (88 %), while the lowest proportion is exhibited by HC-WC(4)800-1 (3 %). Micropore data for HC-WC(4)800-5 could not be reported and can be assumed to be too low for accurate measurements, however this has not been confirmed.

HC-WC(4)600-1 and HC-WC(2)800-5 also show the lowest (0.48 cm^3 g^{-1}) and highest (1.73 cm^3 g^{-1}) pore volumes of the sample set respectively. They exhibit corresponding micropore volumes of 60 % and 15 % respectively. The highest proportion of micropore volume (75 %) is exhibited by HC-WC(2)600-1, with the lowest proportion (2 %) exhibited by HC-WC(4)800-1. The pore volume data therefore follows the same trend as the surface area data.

To thoroughly analyse the effect of carbonisation method on the activation process, the effect of activation conditions on hydrochars was calculated. HC-WC(2)800-1, activated under

'standard conditions', exhibited a surface area, pore volume and corresponding microporosity (%) of 1666 m^2 g^{-1} (84 %) and 0.76 cm^3 g^{-1} (74 %) respectively. HC-WC(4)800-1 was activated with double the ratio of activating agent. HC-WC(4)800-1 has a surface area of 2568 m^2 g^{-1}, a 54 % increase on standard conditions with a corresponding 96 % decrease in micropore surface area. HC-WC(4)800-1 has a pore volume of 1.40 m^2 g^{-1}, an 84 % increase on standard conditions, with a corresponding 97 % decrease in micropore volume. Compared with the effect of increased activating agent ratio on airchars, the effect on hydrochars is the same, but seen to a much more drastic extent.

HC-WC(2)800-5 has a longer activation time compared with standard conditions. HC-WC(2)800-5 has a surface area of 2944 m^2 g^{-1}, a 77 % increase on standard conditions, with a corresponding 74 % decrease in micropore surface area. HC-WC(2)800-5 has a pore volume of 1.73 cm^3 g^{-1}, a 127 % increase on standard conditions, with a corresponding decrease in micropore volume of 80 %. Although increasing activation time of an airchar has a negligible effect on porosity, it significantly increases porosity of a hydrochar, accompanied with a big reduction in microporosity.

HC-WC(2)600-1 was activated at a lower temperature compared with standard conditions. HC-WC(2)600-1 has a surface area of 1087 m^2 g^{-1}, a 35 % decrease compared with standard conditions, with a corresponding 5 % increase in micropore surface area. HC-WC(2)600-1 has a pore volume of 0.52 cm^3 g-1, a 32 % decrease compared with standard conditions, with a corresponding increase of micropore volume of 1 %. The effect of temperature on porosity is slightly smaller than that seen with the airchar samples, but still has a negligible effect on microporosity.

HC-WC has a very low surface and porosity. Microporosity was unable to be reported, so is assumed to be negligible. These results confirm that the hydrothermal-carbonisation technique does not allow porosity development.

Overall, when comparing the two carbonisation techniques, KOH activation generally has a more drastic effect on hydro char than on airchar. This suggests that airchar is more resistant to KOH activation; increasing surface area is accompanied by a more moderate decrease in microporosity. Samples derived from airchar have, on average, higher surface areas and proportions of microporosity. Pore volume is equivalent in both sets of activated samples, however it is clear that a greater proportion of that volume is due to mesopores in

samples prepared from hydrochar. This is further reflected in the N_2 sorption isotherms.

The surface area and pore volume data for samples prepared from air-carbonised sawdust is shown in Tables 4.7 and 4.10. The sample set shows a broad range of surface areas and pore volumes, with AC-SD(2)600-1 (activated under the gentlest conditions) having the lowest surface of 1426 m^2 g^{-1}. The highest surface area of 3159 m^2 g^{-1} is reported by the sample activated under the harshest conditions, AC-SD(4)800-10. The sample with the highest proportion of micropore surface area is AC-SD(2)700-1 (97 %), also activated under gentle conditions. AC-SD(4)800-10 possesses the lowest proportion of micropore surface area, of just 3 %. The pore volume data corresponds closely with the surface area data; the lowest pore volume of 0.72 cm^3 g^{-1} is shown by both AC-SD(2)600-1 and AC-SD(2)700-1. AC-SD(2)700-1 has the highest proportion of micropore volume, at 94 %. AC-SD(4)800-10 has the highest pore volume, of 1.82 cm^3 g^{-1}. AC-SD(4)800-10 and AC-SD(4)800-5 have the lowest proportion of micropore volume, of just 2 %. The trend in effect of activation conditions corresponds with the previous two data sets, however, as with the HC-WC data set, it is not always equivalent samples that show the most extreme porosity characteristics.

The effect of activation conditions on porosity development can be further analysed by comparing to 'standard conditions'. AC-SD(2)800-1 was activated under standard conditions and exhibits a surface area of 2150 m^2 g^{-1}, with a corresponding proportion of micropore surface area of 87 %. AC-SD(2)800-1 exhibits a pore volume of 0.91 cm^3 g^{-1}, with a corresponding micropore volume proportion of 81 %. AC-SD(4)800-1 was activated with double the ratio of activating agent compared with standard conditions. As a result, it possesses a surface area of 2610 m^2 g^{-1}, a 21 % increase on standard conditions, with a corresponding 17 % decrease in micropore surface area. AC-SD(4)800-1 has a pore volume of 1.15 cm^3 g^{-1}, a 26 % increase compared with standard conditions, with a corresponding decrease in micropore volume of 21 %. Increasing the ratio of activating agent has the same effect as seen with the AC-WC sample set, of increasing porosity, while decreasing microporosity. The extent of the effect seen with AC-SD samples is similar, if slightly lower than with AC-WC samples.

AC-SD(2)800-5 was activated for a greater duration than standard conditions. AC-SD(2)800-5 has a surface area of 2051 m^2 g^{-1}, a 5 % decrease compared with standard conditions, corresponding with a 17 % decrease in micropore surface area.

AC-SD(2)800-5 has a pore volume of 0.91 $cm^3\ g^{-1}$, equal to that of standard conditions, with a corresponding 21 % decrease in micropore volume. As seen with the AC-WC sample set, a longer activation time has a negligible effect on porosity of AC-SD samples, and a similar, if not slightly lower decrease in microporosity.

AC-SD(2)600-1 was activated at a temperature lower than that of standard conditions. AC-SD(2)600-1 has a surface area of 1426 $m^2\ g^{-1}$, a 34 % decrease compared to standard conditions, with a corresponding 12 % decrease in micropore surface area. AC-SD(2)600-1 has a pore volume of 0.72 $cm^3\ g^{-1}$, a 21 % decrease compared with standard conditions, with a corresponding 25 % decrease in micropore volume. Decreasing activation temperature has a similar effect on AC-SD samples as on AC-WC samples of decreasing porosity, however it is accompanied by a moderate decrease in microporosity.

Overall, the AC-SD sample set shows the same trends as the AC-WC sample set, to the same, if not slightly lower extent. It is clear that char type (airchar or hydrochar) does have a substantial effect on activation efficiency, although the effect of wood composition is significantly less.

4. 4. 7. Textural Properties; Pore Size Distributions

Pore size distributions (PSDs) for all carbon samples were calculated using non-local density functional theory and are displayed below in Figures 4.32 – 4.40. The PSDs for samples prepared from air-carbonised wood chippings are shown in Figures 4.32 and 4.33. Most samples show a similar porosity dominated by micropores, which is in line with isotherm and textural data. The main pore size maxima sit in a narrow range between 5.9 and 10 Å. All samples also show significant pore volume at 11.8 Å, except AC-WC(2)600-1 and AC-WC(2)600-5, the two samples activated under the gentlest conditions. AC-WC(4)800-5 is the only sample of these sets to show any substantial broadening of the PSD to include some small mesopore volume. This is to be expected from analysis of the textural data.

PSDs for samples prepared from hydrothermally-carbonised wood chippings are shown in Fig.'s 4.34 and 4.35. As seen with the activated AC-WC samples, and as predicted from isotherm and textural properties data, the PSDs for the majority of the samples are predominantly microporous. The main pore size maxima occupy a slightly broader range in the micropore region of 5.9 to 11.8 Å. As with the previous set, most samples show significant pore volume at 11.8 Å, excluding HC-WC(2)600-5

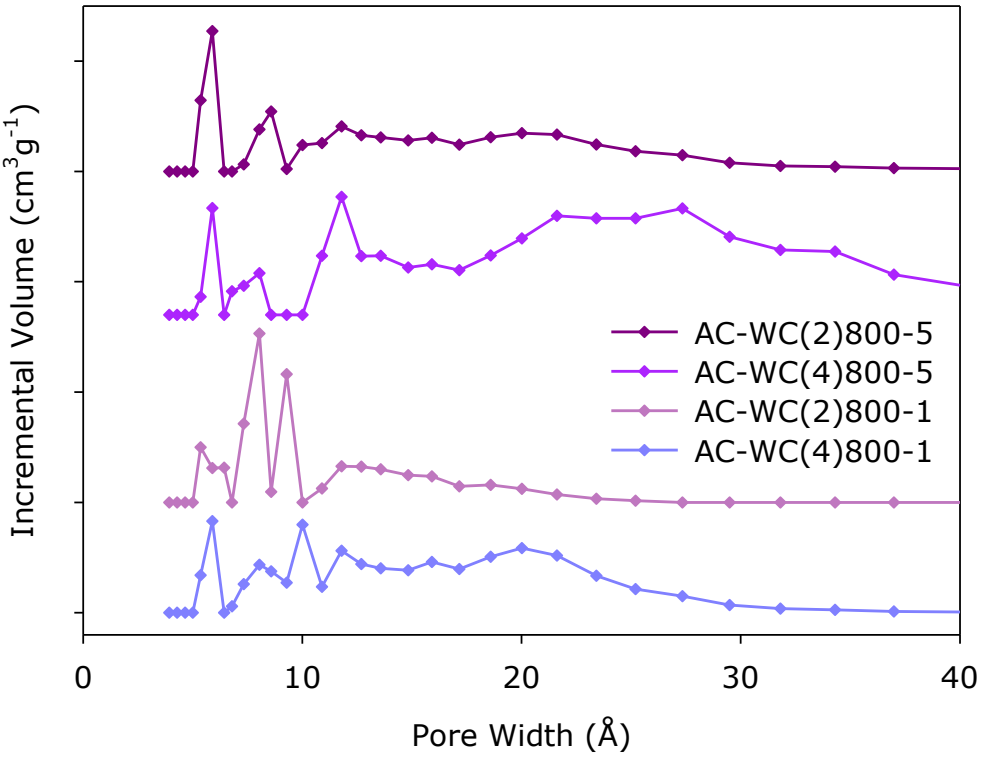

Figure 4.32. PSDs of samples prepared from air-carbonised wood chippings at 800 °C

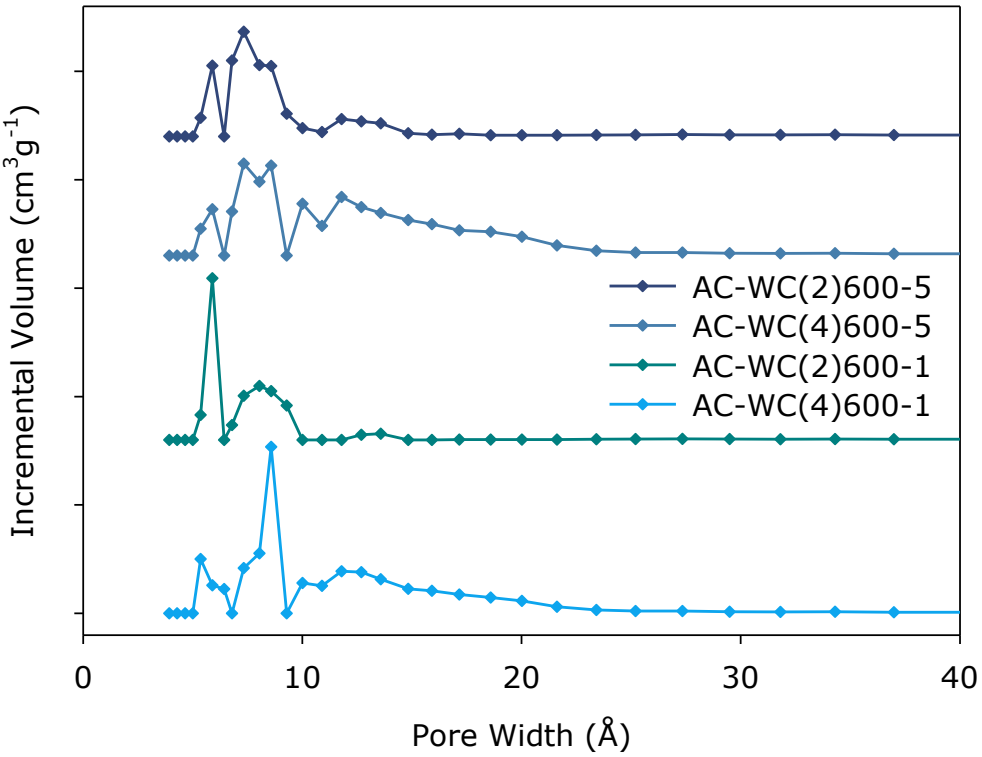

Figure 4.33. PSDs of samples prepared from air-carbonised wood chippings at 600 °C

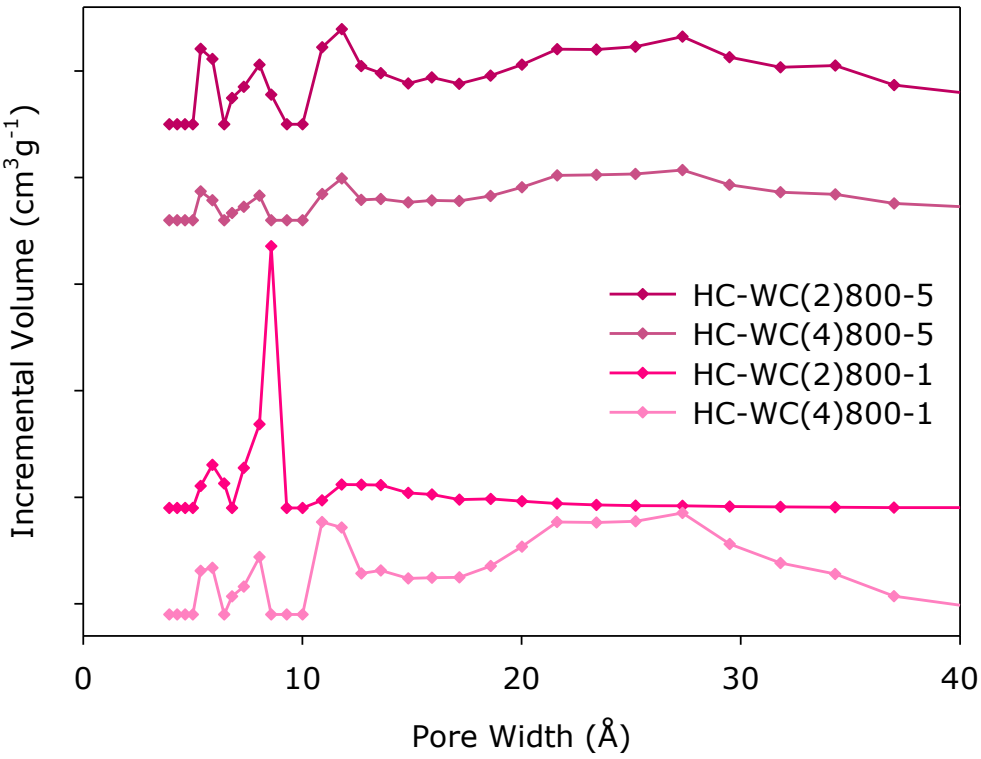

Figure 4.34. PSDs of samples prepared from hydrothermally-carbonised wood chippings at 800 °C

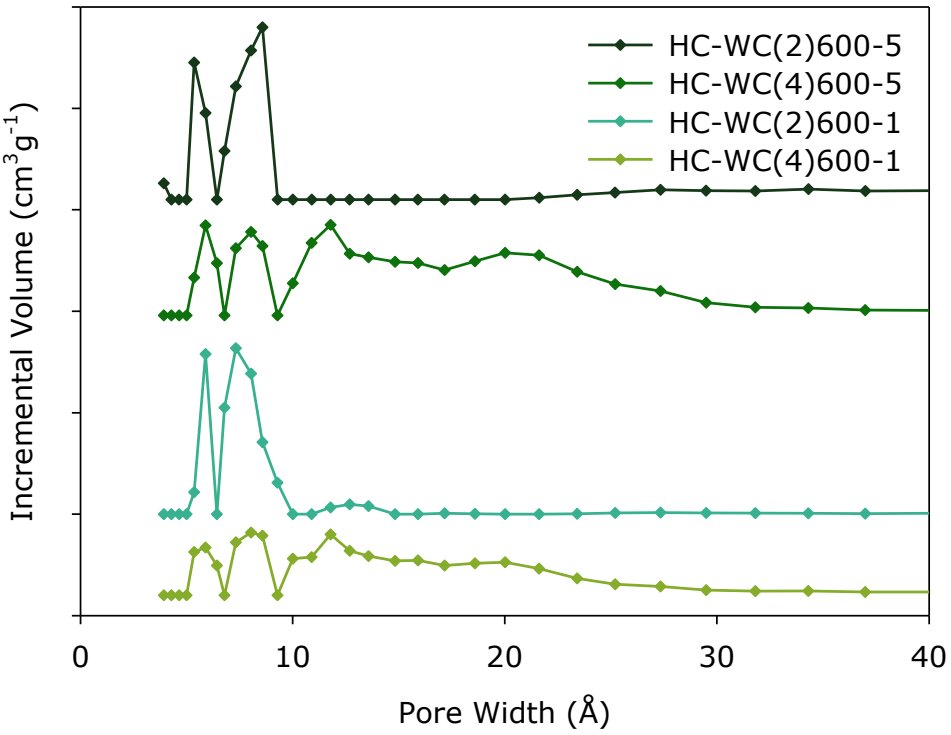

Figure 4.35. PSDs of samples prepared from hydrothermally-carbonised wood chippings at 600 °C

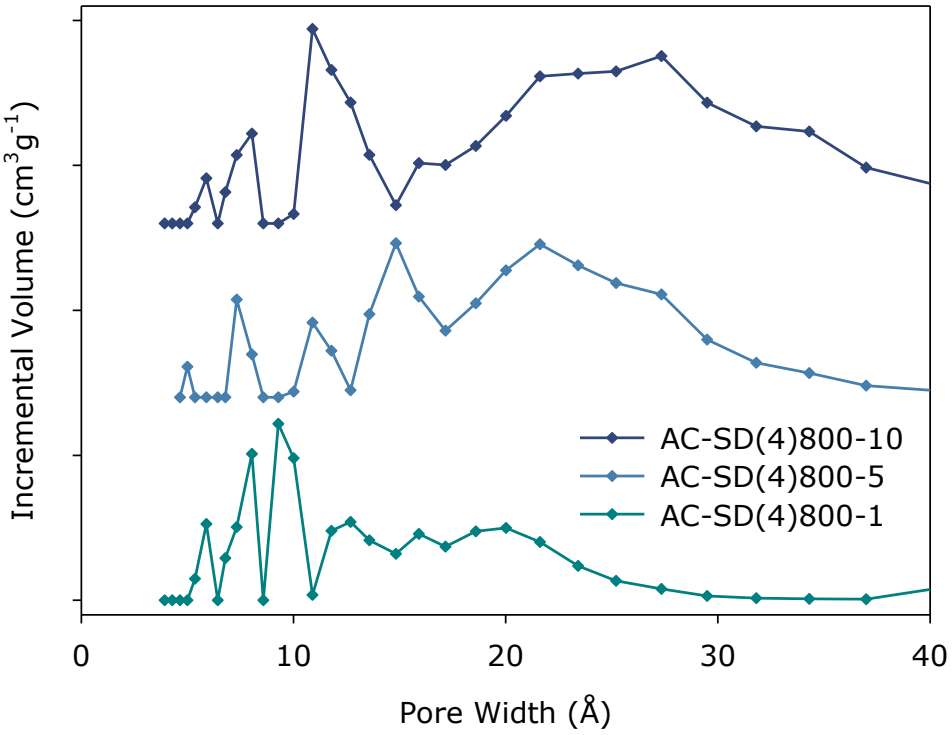

Figure 4.36. PSDs of samples prepared from air-carbonised sawdust at 800 °C, C:KOH ratio of 1:4

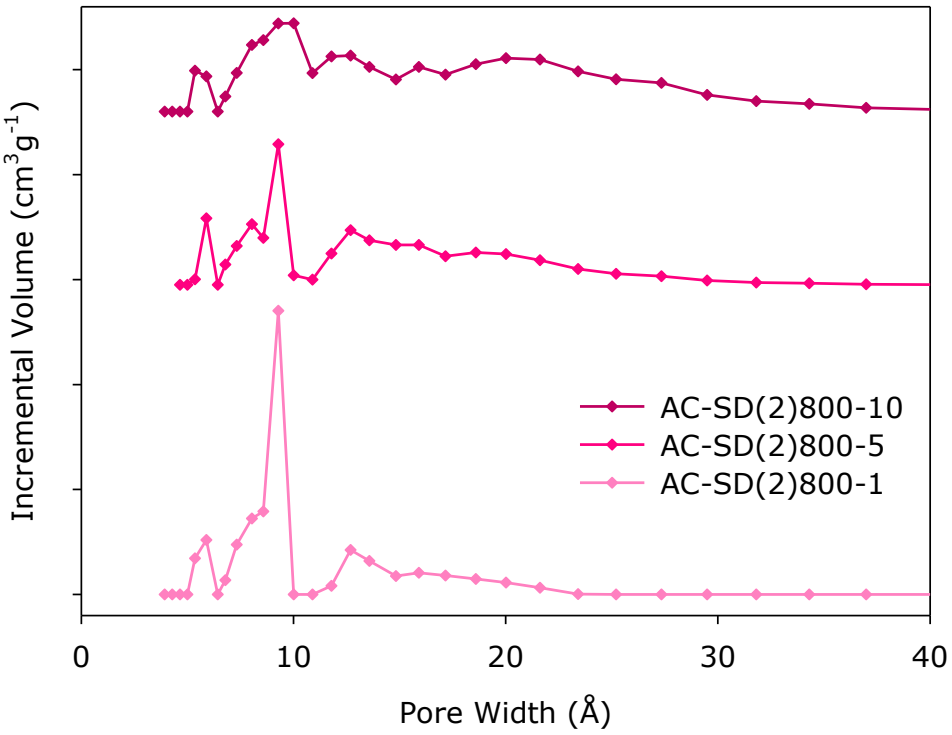

Figure 4.37. PSDs of samples prepared from air-carbonised sawdust at 800 °C, C:KOH ratio of 1:2

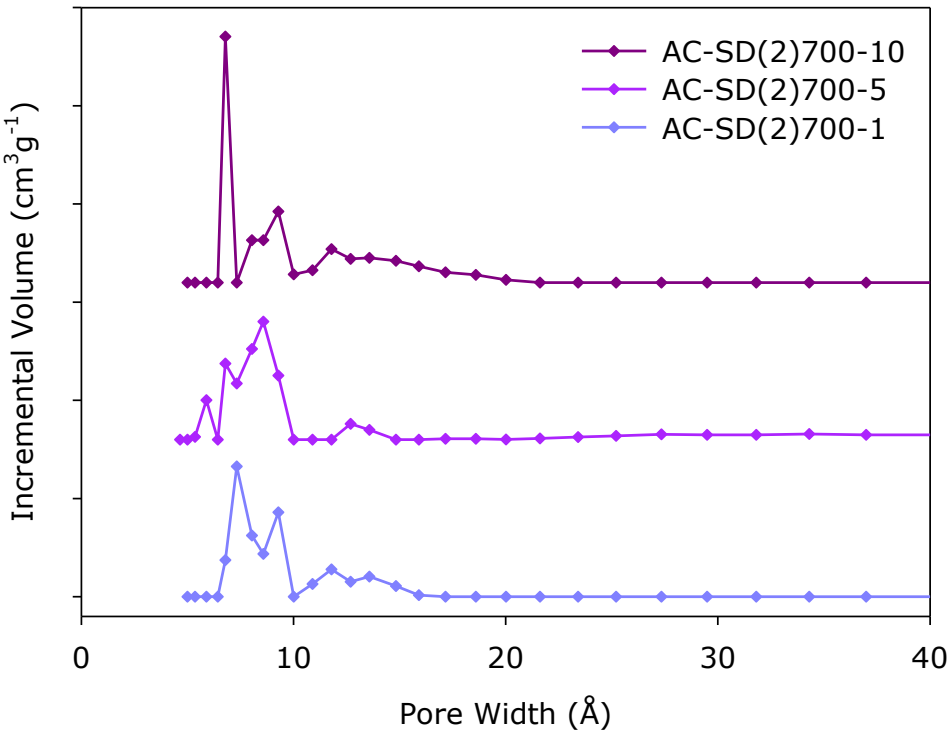

Figure 4.38. PSDs of samples prepared from air-carbonised sawdust at 700 °C, C:KOH ratio of 1:2

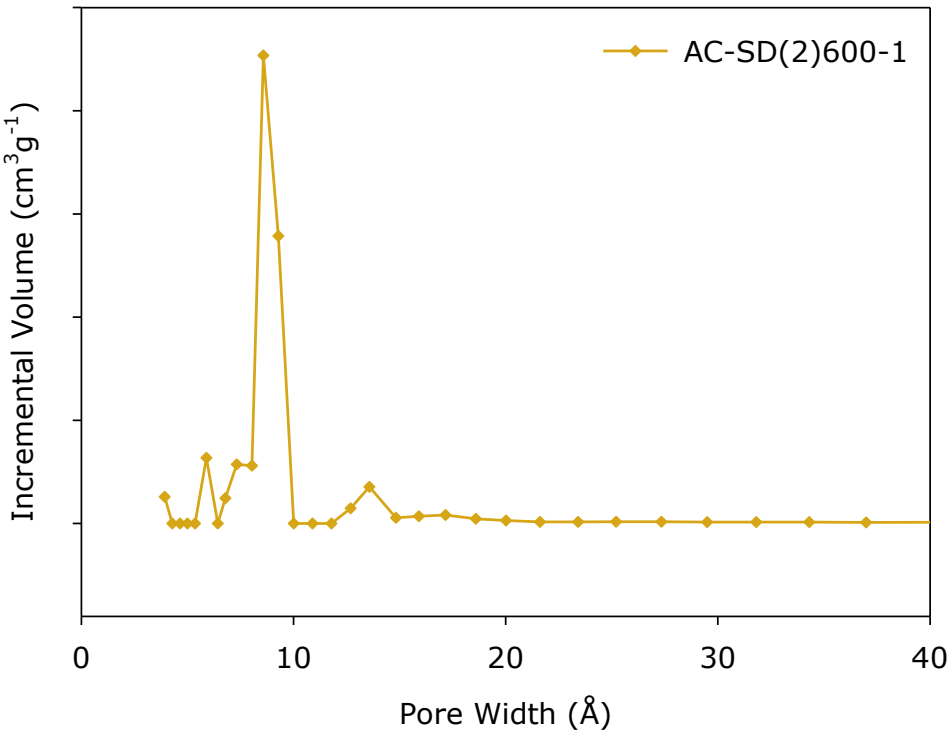

Figure 4.39. PSDs of samples prepared from air-carbonised sawdust at 600 °C, C:KOH ratio of 1:2

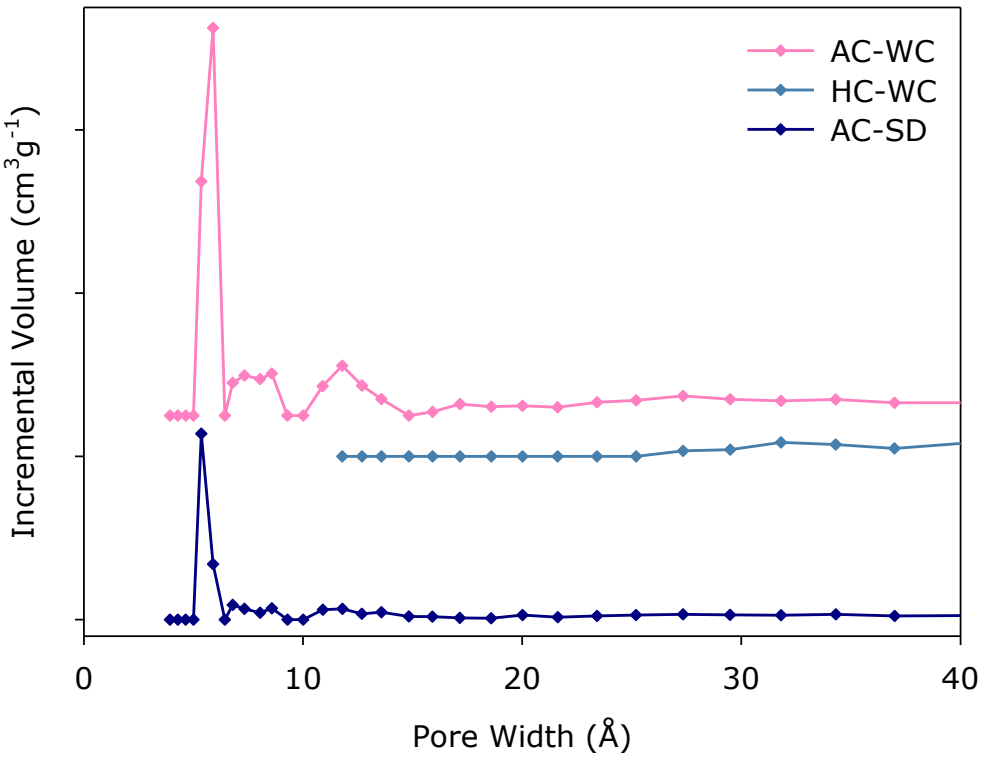

Figure 4.40. PSDs of air-carbonised wood chippings, hydrothermally-carbonised wood chippings and air-carbonised sawdust

and HC-WC(2)600-1. It is clear that the formation of pores of width 11.8 Å is due to more extensive activation conditions. All samples in both sample sets show significant pore volume at 5.9 Å, suggesting that under harsher conditions, more extensive activation causes the collapse of small pores of width 5.9 Å, into larger pores of width 11.8 Å. AC-WC(2)600-1, AC-WC(2)600-5, HC-WC(2)600-1 and HC-WC(2)600-5 all show a larger proportion of pores of width 5.9 Å compared with the rest of the sample set.

Table 4.11. PSD maxima of samples prepared from air-carbonised wood chippings, obtained from NLDFT analysis

Sample	Pore Maxima (Å)	
	< 20 Å	**≥ 20 Å**
AC-WC(2)800-1	5.4/8.0/9.3/11.8	N/A
AC-WC(4)800-1	5.9/8.0/10.0/11.8	20.0
AC-WC(2)600-1	5.9/8.0	N/A
AC-WC(4)600-1	5.4/8.6/11.8	N/A
AC-WC(2)800-5	6.0/8.5/11.8	N/A
AC-WC(4)800-5	5.9/8.0/11.8	21.6/27.3
AC-WC(2)600-5	5.9/7.4	N/A
AC-WC(4)600-5	5.9/7.4/8.6/10.0/11.8	N/A

A larger number of samples in the HC-WC set show broadening of the PSD into the mesopore region, and to a greater extent compared with samples in the AC-WC set. HC-WC(2)800-5, HC-WC(4)800-5, HC-WC(4)800-1 and HC-WC(4)600-5 show particularly substantial mesoporous volume, corresponding with isotherm and textural properties data. Hydrochar shows less resistance to KOH activation in terms of PSD broadening than airchar.

The PSDs of samples prepared from air-carbonised sawdust are shown in Fig.'s 4.36 – 4.39. The samples are all predominantly

Table 4.12. PSD maxima of samples prepared from hydrothermally-carbonised wood chippings, obtained from NLDFT analysis

Sample	Pore Maxima (Å)	
	< 20 Å	**≥ 20 Å**
HC-WC(2)800-1	6.0/8.6/11.8	N/A
HC-WC(4)800-1	5.9/8.0/10.9	27.3
HC-WC(2)600-1	6.0/7.3	N/A
HC-WC(4)600-1	6.0/8.0/11.8	20.0
HC-WC(2)800-5	5.4/8.0/11.8	27.3
HC-WC(4)800-5	5.4/8.0/11.8	27.3
HC-WC(2)600-5	5.3/8.6	N/A
HC-WC(4)600-5	6.0/8.0/11.8	20.0

microporous. Samples activated at 600 and 700 °C have very narrow PSD with no porosity > 20 Å. The main pore maxima fall between 6.8 and 8.6 Å. Samples activated at 800 °C with a carbon:KOH ration of 1:2 show a slight broadening of the PSD to include low volumes of small mesopores < 30 Å. The main pore maxima are slightly larger, at 9.3 Å and 9.7 Å. The PSDs of samples activated at 800 °C with a carbon:KOH ratio of 1:4 broaden to include large pore volumes in the range 20 – 30 Å.

Table 4.13. PSD maxima of samples prepared from air-carbonised sawdust, obtained from NLDFT analysis

Sample	Pore Maxima (Å)	
	< 20 Å	**≥ 20 Å**
AC-SD(2)700-1	7.4/9.3/11.8/13.6	N/A
AC-SD(2)700-5	5.9/6.8/8.6/12.7	N/A
AC-SD(2)700-10	6.8/9.3/11.8	N/A
AC-SD(2)800-1	5.9/9.3/12.7/15.9	N/A
AC-SD(2)800-5	5.9/8.0/9.3/12.7/15.9	20.0
AC-SD(2)800-10	5.4/9.7/12.7/15.9	20.0
AC-SD(4)800-1	5.9/8.0/9.4/12.7/15.9	20.0
AC-SD(4)800-5	5.0/7.3/10.9/14.9	21.7
AC-SD(4)800-10	5.9/8.0/10.9	21.7/27.3
AC-SD(2)600-1	5.9/8.6/13.6	N/A

Pore maxima range from 9.4 to 14.9 Å, with the proportion of mesoporosity increasing with activation time.

Across the three sample sets, the majority of samples are predominantly microporous. The PSD broadens into the small mesopore region as activation time, temperature and KOH ratio increases, decreasing the proportion of microporosity and confirming trends seen in the previous data. There is also evidence for the broadening of pore channels, and collapse of

Table 4.14. PSD maxima of air-carbonised wood chippings, hydrothermally-carbonised wood chippings and air-carbonised sawdust, obtained from NLDFT analysis

Sample	Pore Maxima (Å)	
	< 20 Å	≥ 20 Å
AC-WC	5.9/8.9/11.8	N/A
HC-WC	N/A	N/A
AC-SD	5.4/6.8/8.6/11.8/13.6	20.0

small pores into larger pores as activation conditions intensify. The PSDs provide further evidence that airchar is more resistant to KOH activation; a greater amount of microporosity is retained as activation conditions increase, compared with hydrochar.

The PSDs for the three chars are displayed in Figure 4.40. AC-WC shows a very narrow PSD centred at 5.9 Å, with negligible mesoporosity. The carbonisation process creates a porous structure of primarily 5.9 Å diameter pores. Upon activation, the majority of this volume is retained, with broadening of the pores being seen as activation conditions intensify. HC-WC displays negligible pore volume as expected, indicating that a porous structure is only formed during the activation process.

AC-SD displays a narrow microporosity, similar to that seen for AC-WC, with no significant mesoporosity. The PSD is centred at 5.4 Å, which expands into larger micropores upon activation.

It is clear that both the carbonisation method and the wood composition have a significant effect on the pore formation process and resulting porous structure.

4. 4. 8. CO_2 Uptake Analysis

The CO_2 uptake capabilities of the activated carbon samples were analysed gravimetrically at 25 °C, over a pressure range of 0 – 40 bar. The adsorption isotherms up to 1 bar and 40 bar are shown below in Figures 4.41 – 4.56. The molar uptakes for the samples at a range of pressures is displayed in Tables 4.15 – 4.17. It is important to analyse CO_2 uptake capabilities at very low pressure of 0.15 bar, to simulate typical conditions of a post-combustion flue gas stream. Analysis at 1 bar gives further information about low pressure uptake, while analysis at 20 and 40 bar provides uptake information at medium and high pressure respectively.

The CO_2 uptake isotherms for samples prepared from air-carbonised wood chippings are displayed below in Figures 4.41 to 4.44, with quantitative data recorded in Table 4.15. CO_2 uptake at 0.15 bar ranges between 0.3 and 1.1 mmol g^{-1}, which is among the highest uptakes at this pressure recorded in previous studies.[2,10,30,53] Uptake of 1.1 mmol g^{-1} is exhibited by both AC-WC(2)600-1 and AC-WC(2)600-5; the samples activated under

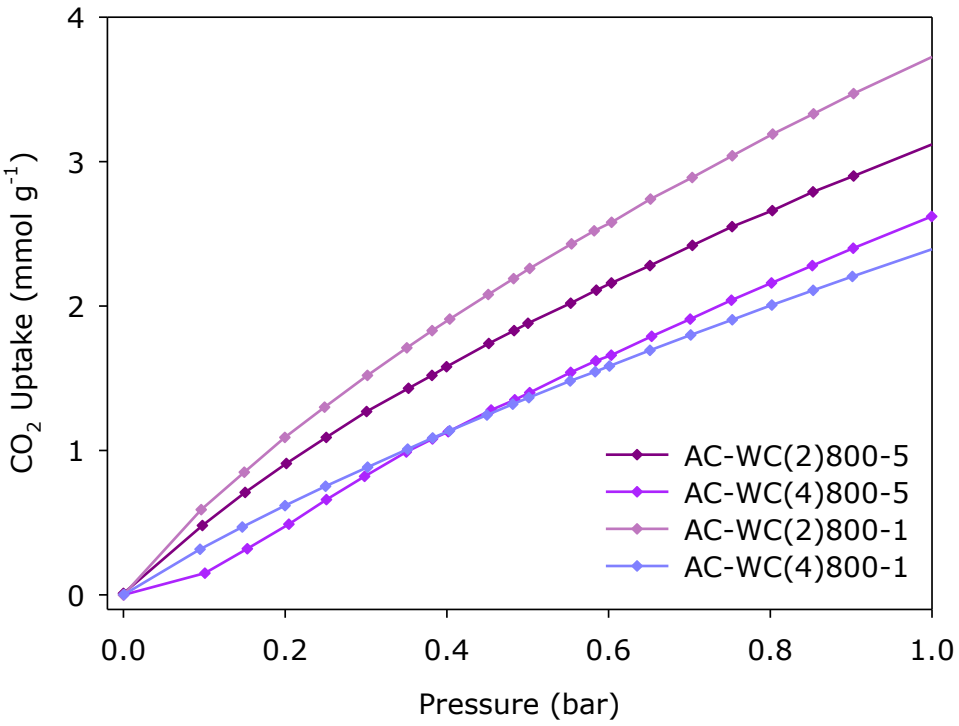

Figure 4.41. CO_2 uptake up to 1 bar of samples prepared from air-carbonised wood chippings at 800 °C

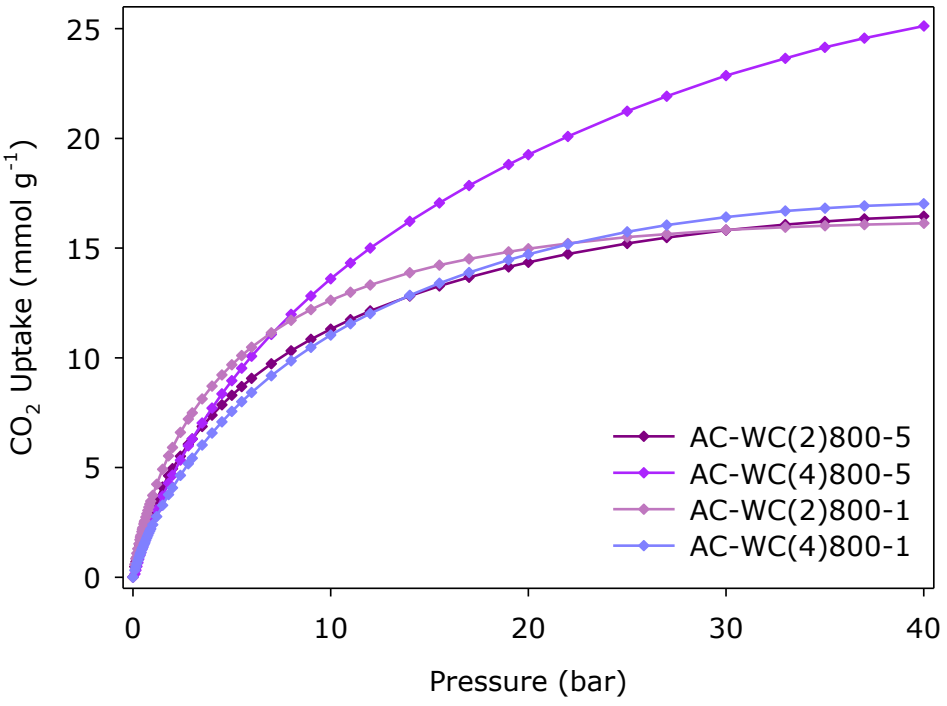

Figure 4.42. CO_2 uptake up to 40 bar of samples prepared from air-carbonised wood chippings at 800 °C

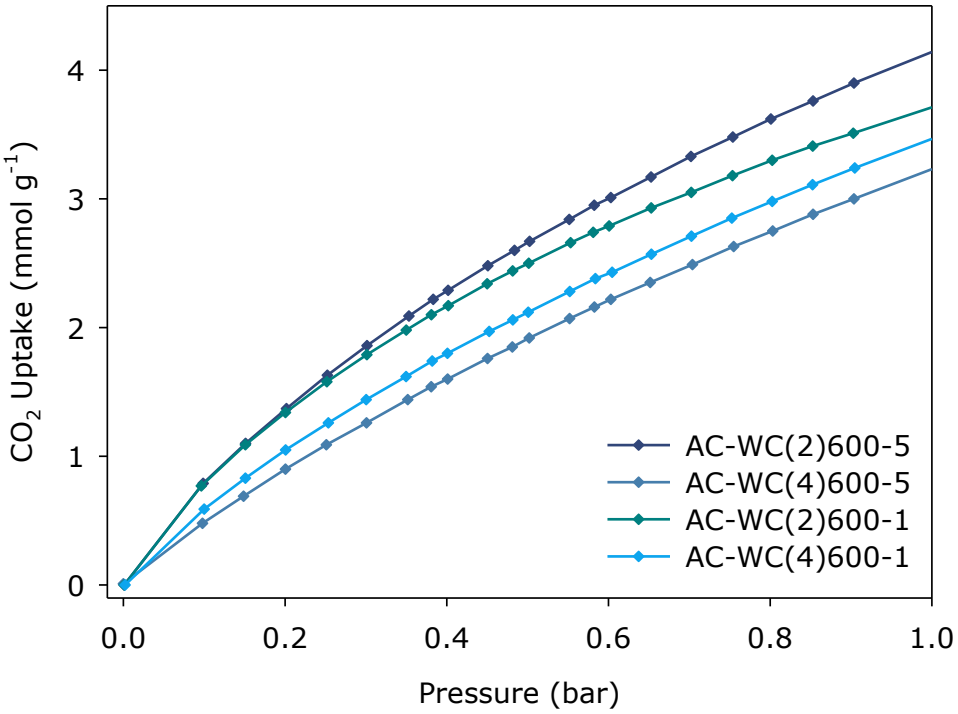

Figure 4.43. CO_2 uptake up to 1 bar of samples prepared from air-carbonised wood chippings at 600 °C

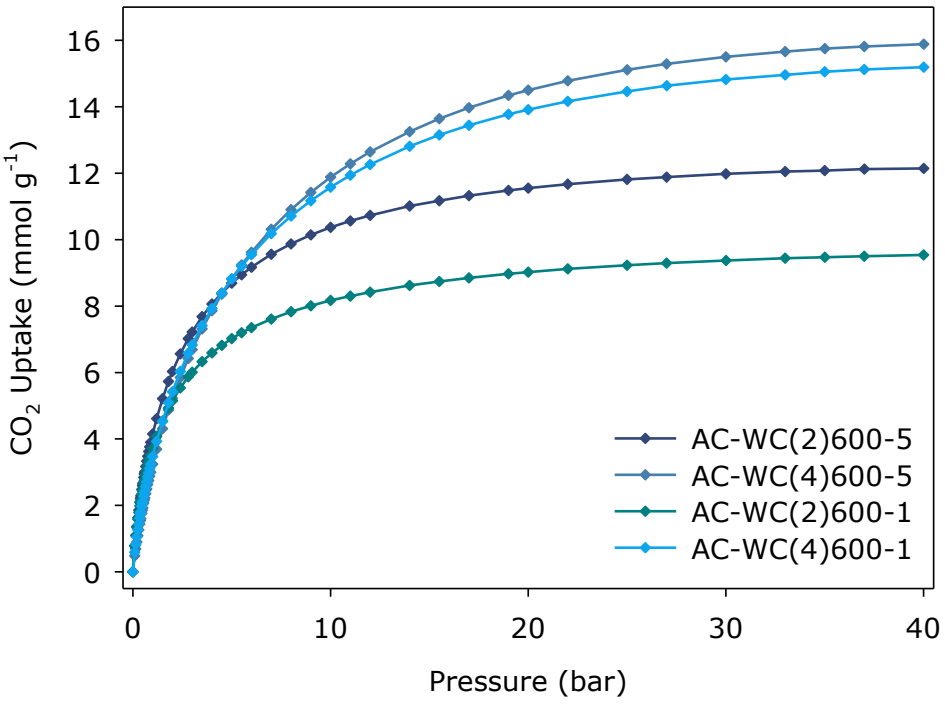

Figure 4.44. CO_2 uptake up to 40 bar of samples prepared from air-carbonised wood chippings at 600 °C

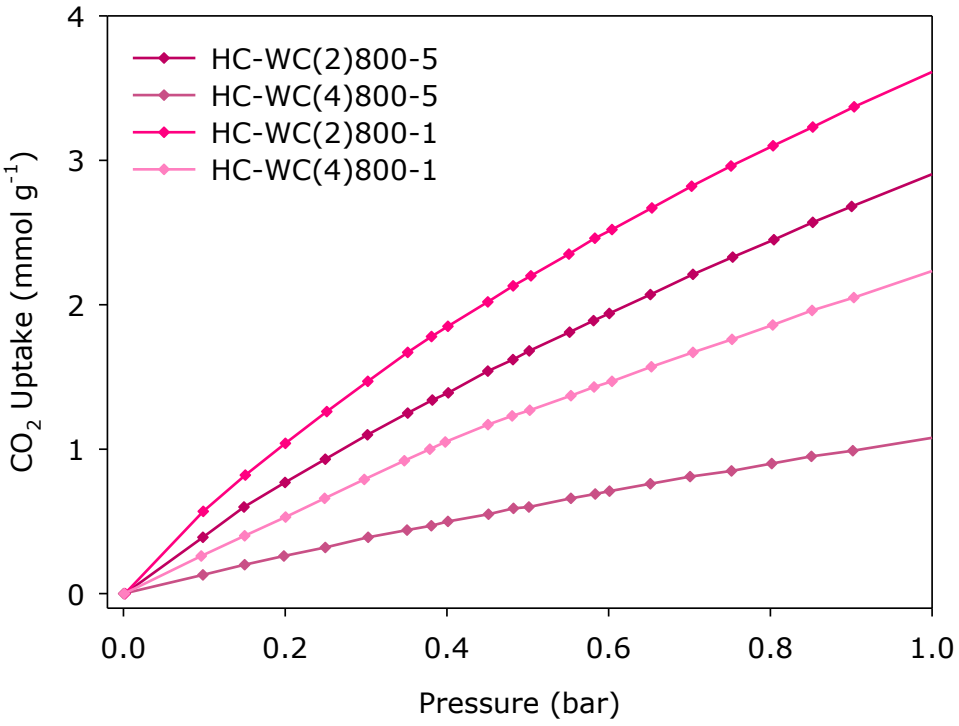

Figure 4.45. CO_2 uptake up to 1 bar of samples prepared from hydrothermally-carbonised wood chippings at 800 °C

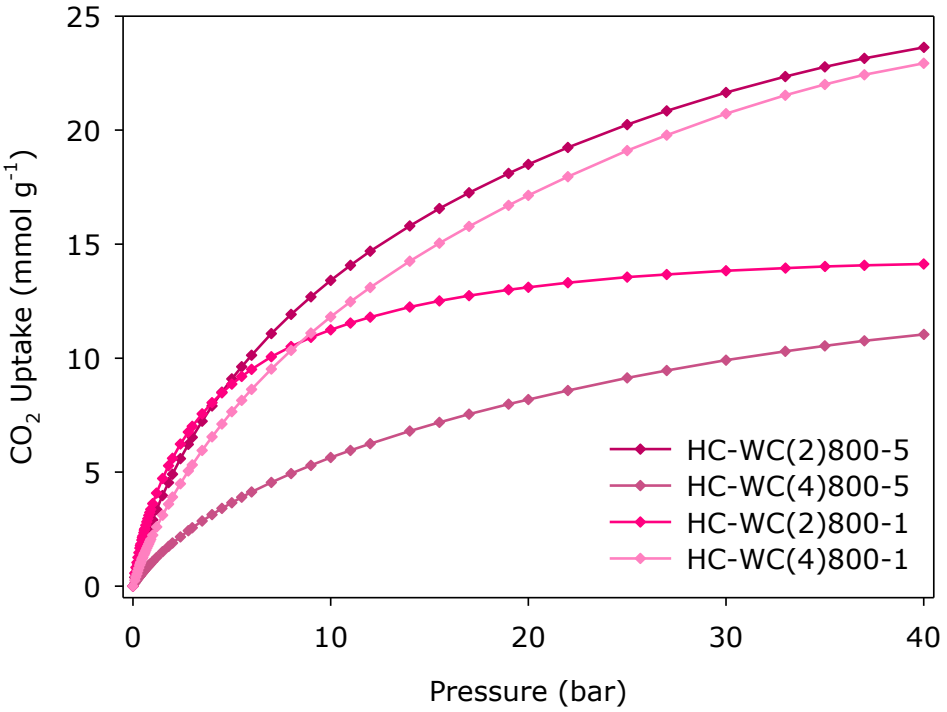

Figure 4.46. CO_2 uptake up to 40 bar of samples prepared from hydrothermally-carbonised wood chippings at 800 °C

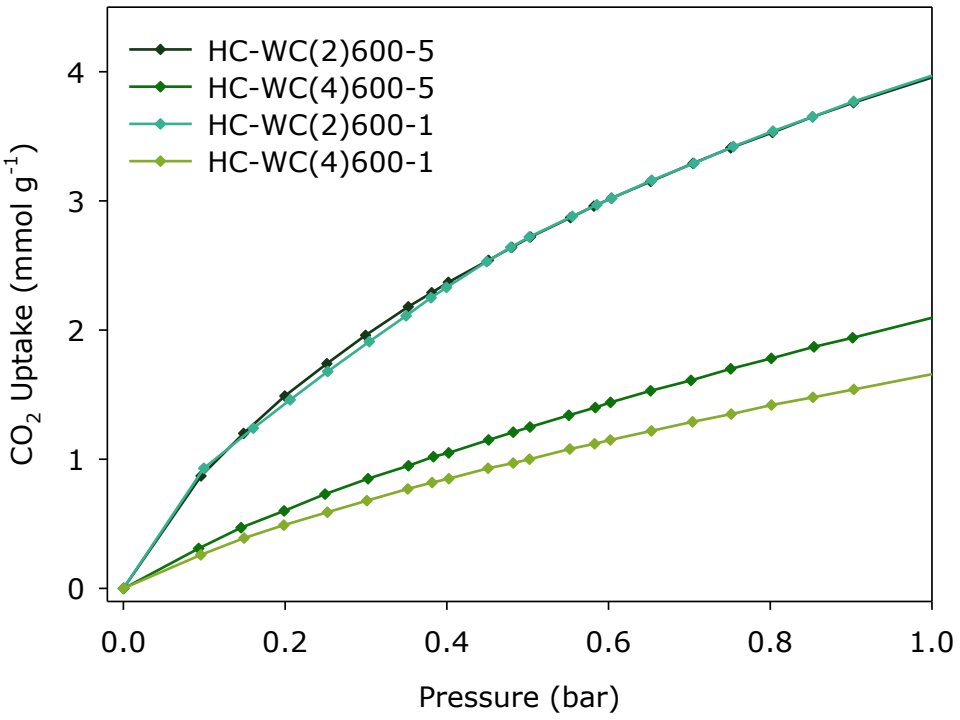

Figure 4.47. CO_2 uptake up to 1 bar of samples prepared from hydrothermally-carbonised wood chippings at 600 °C

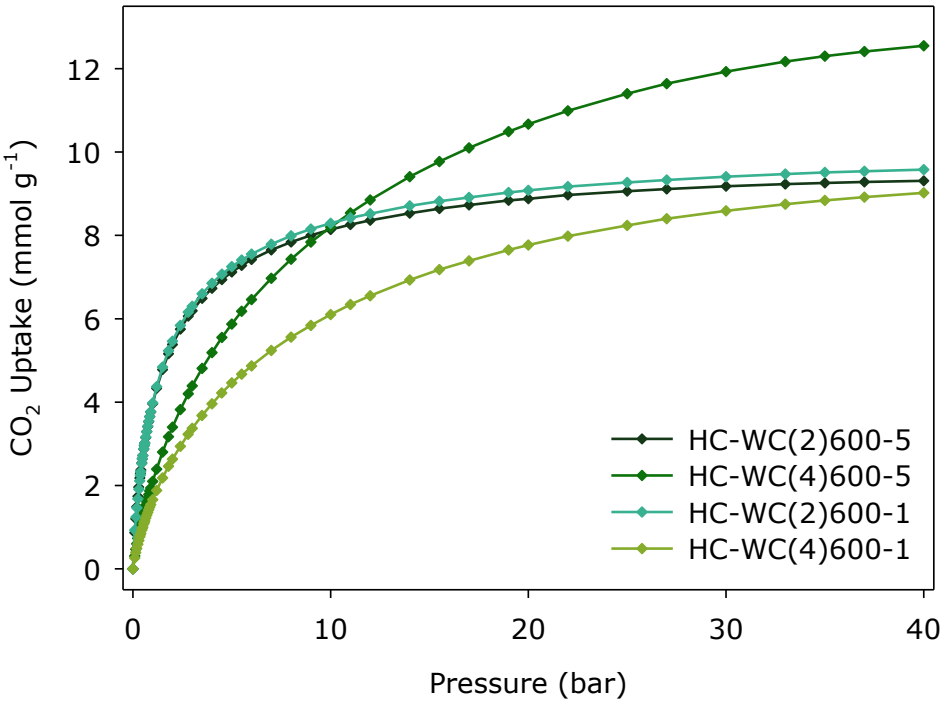

Figure 4.48. CO_2 uptake up to 40 bar of samples prepared from hydrothermally-carbonised wood chippings at 600 °C

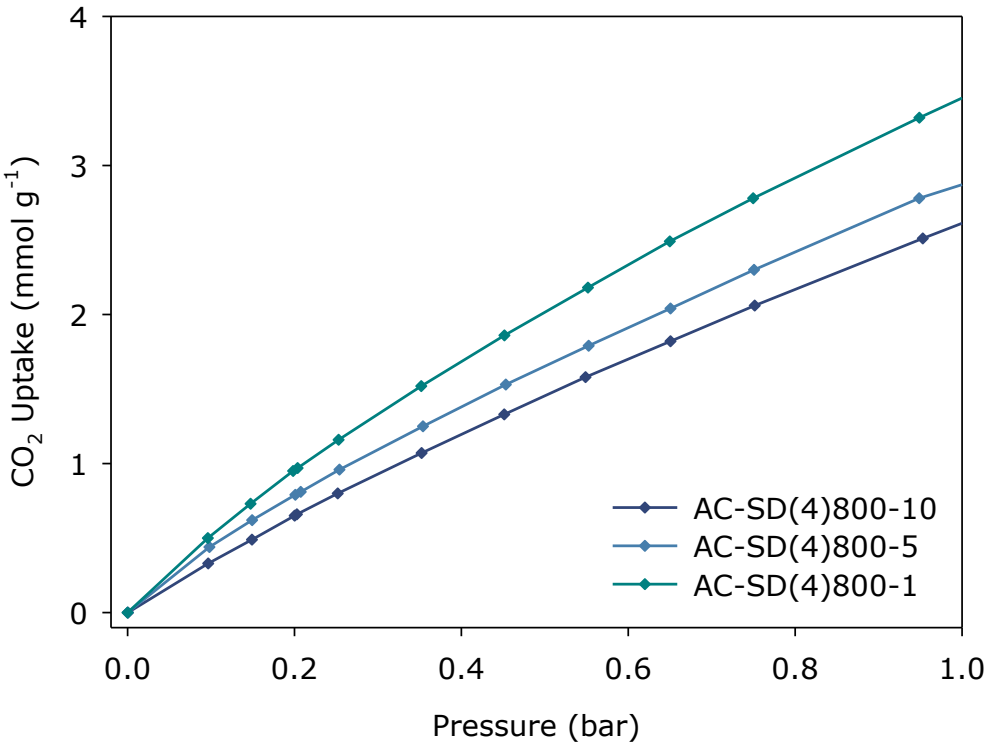

Figure 4.49. CO_2 uptake up to 1 bar of samples prepared from air-carbonised sawdust at 800 °C, C:KOH ratio of 1:4

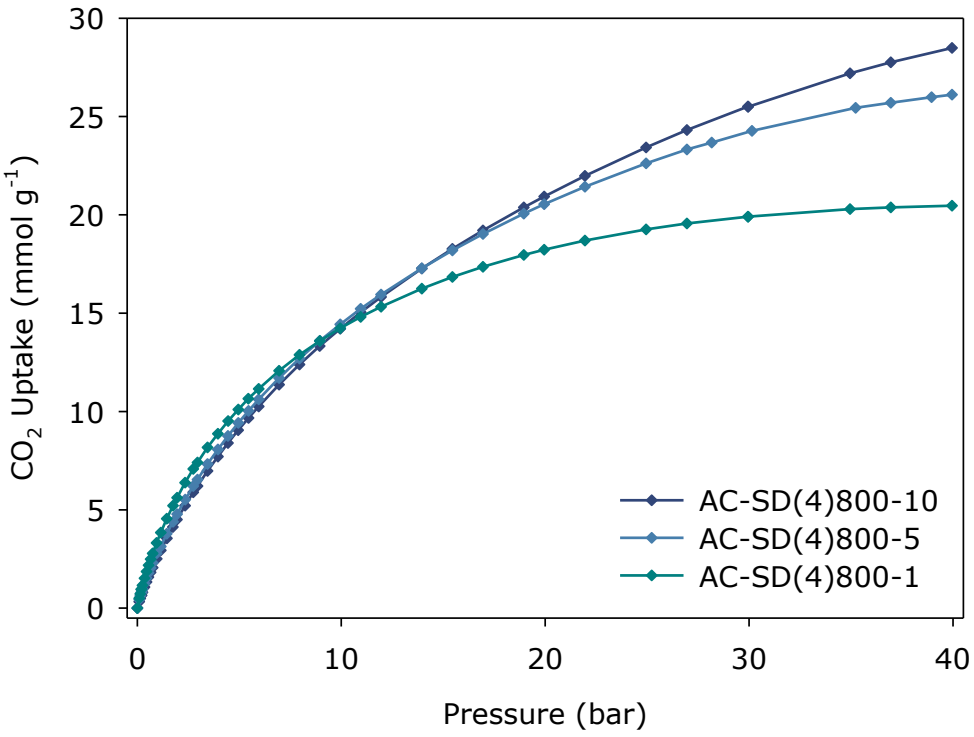

Figure 4.50. CO_2 uptake up to 40 bar of samples prepared from air-carbonised sawdust at 800 °C, C:KOH ratio of 1:4

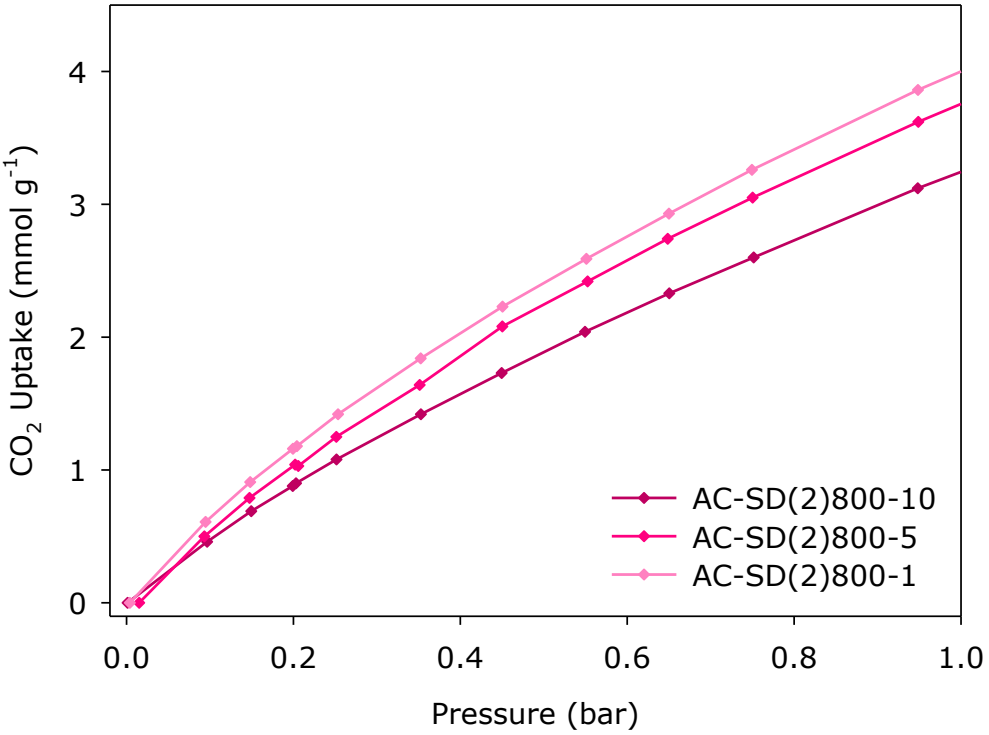

Figure 4.51. CO_2 uptake up to 1 bar of samples prepared from air-carbonised sawdust at 800 °C, C:KOH ratio of 1:2

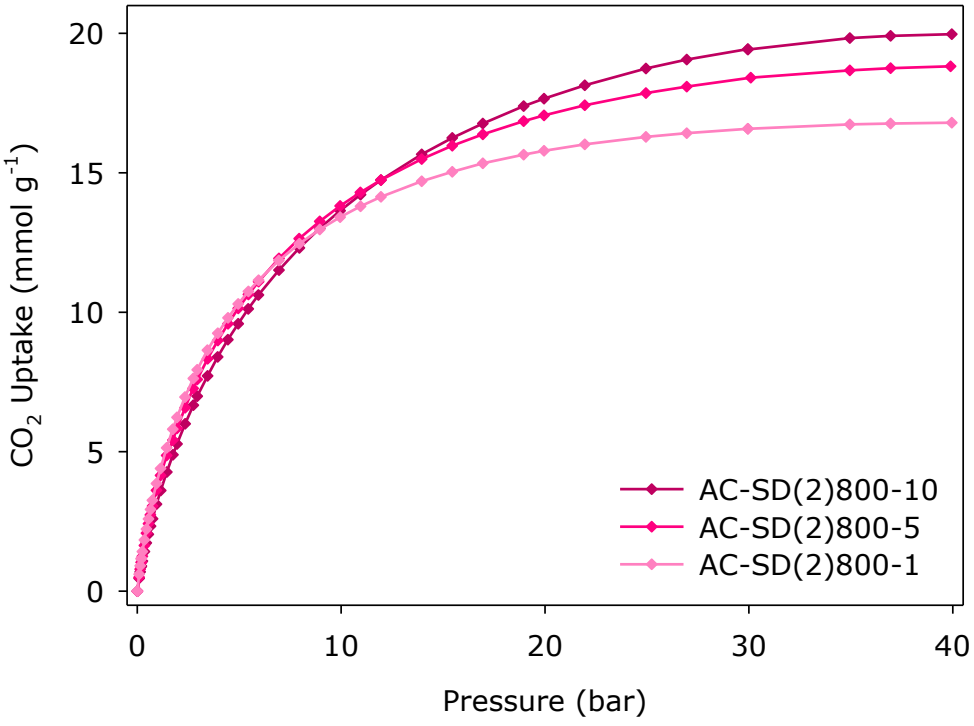

Figure 4.52. CO_2 uptake up to 40 bar of samples prepared from air-carbonised sawdust at 800 °C, C:KOH ratio of 1:2

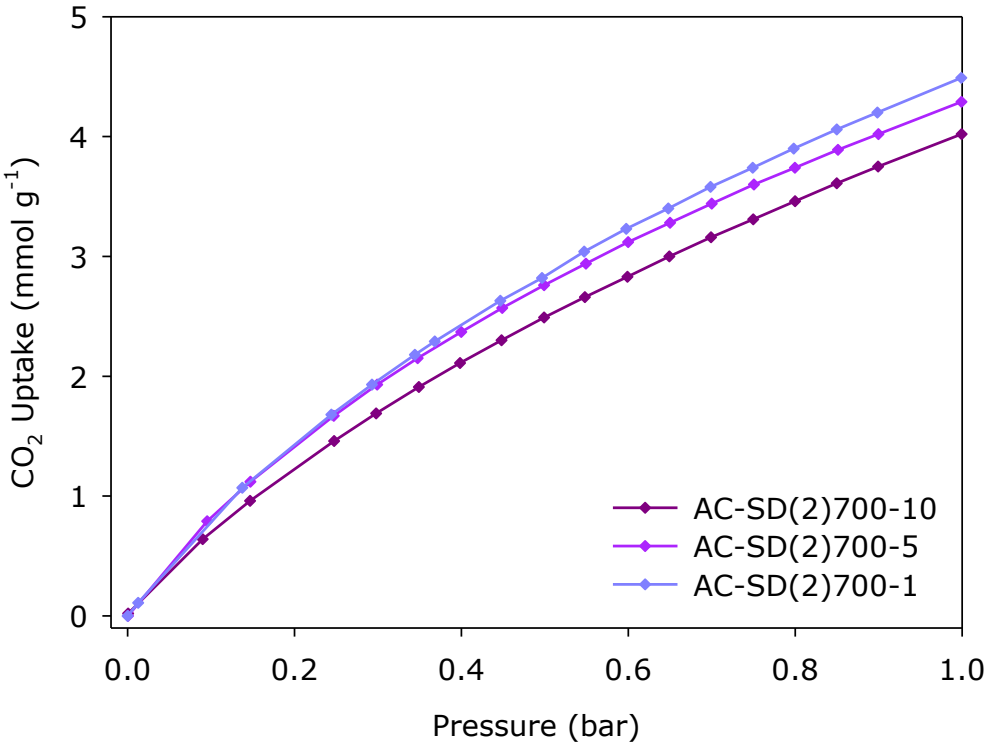

Figure 4.53. CO_2 uptake up to 1 bar of samples prepared from air-carbonised sawdust at 700 °C, C:KOH ratio of 1:2

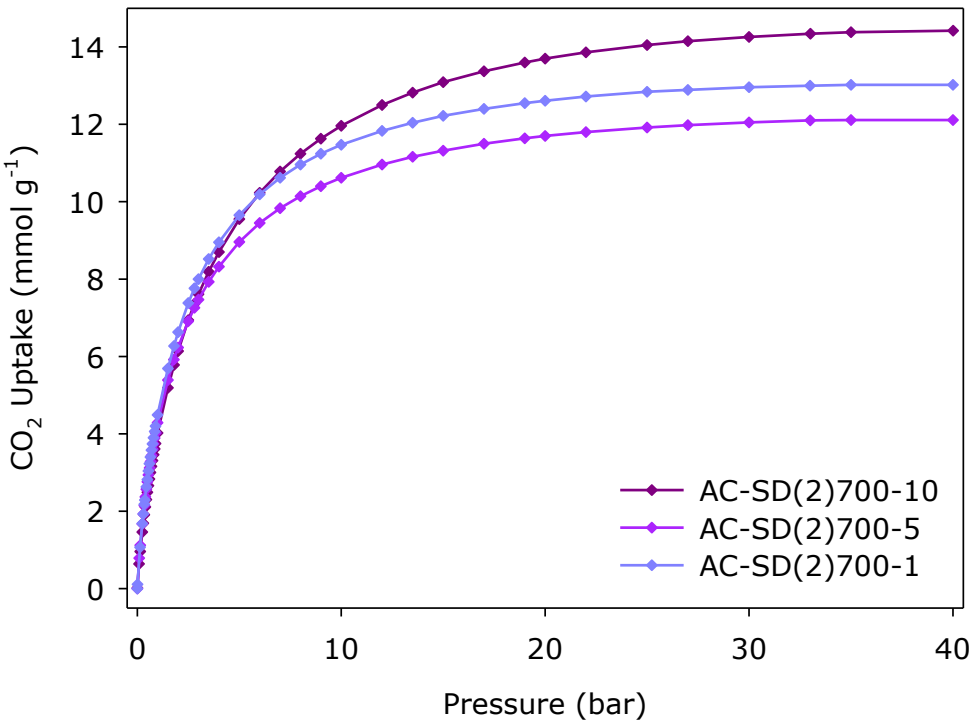

Figure 4.54. CO_2 uptake up to 40 bar of samples prepared from air-carbonised sawdust at 700 °C, C:KOH ratio of 1:2

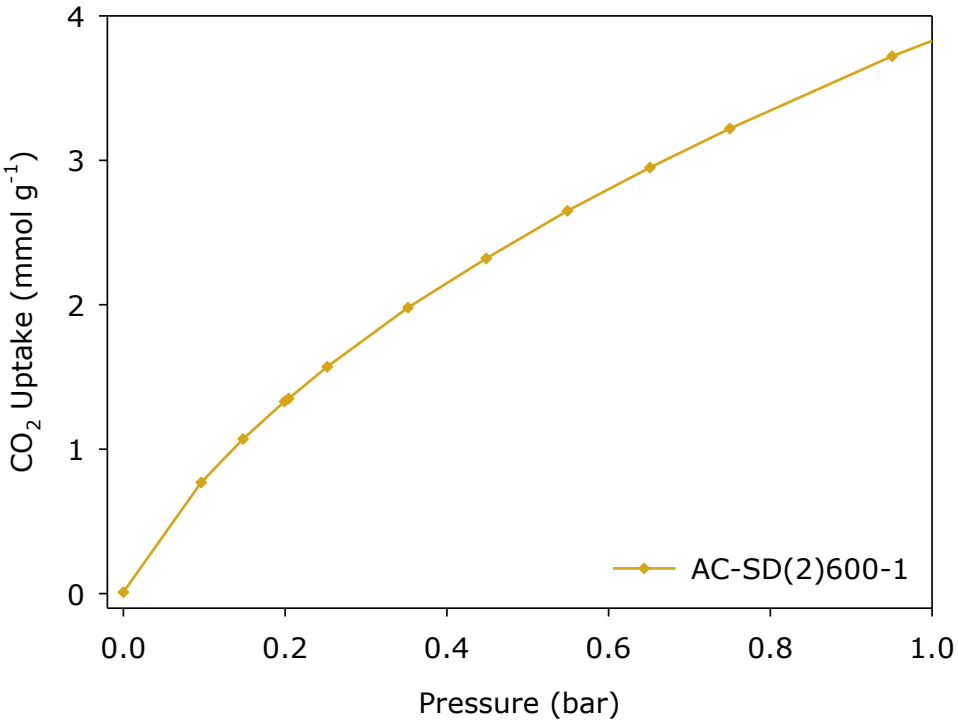

Figure 4.55. CO_2 uptake up to 1 bar of the sample prepared from air-carbonised sawdust at 600 °C, C:KOH ratio of 1:2

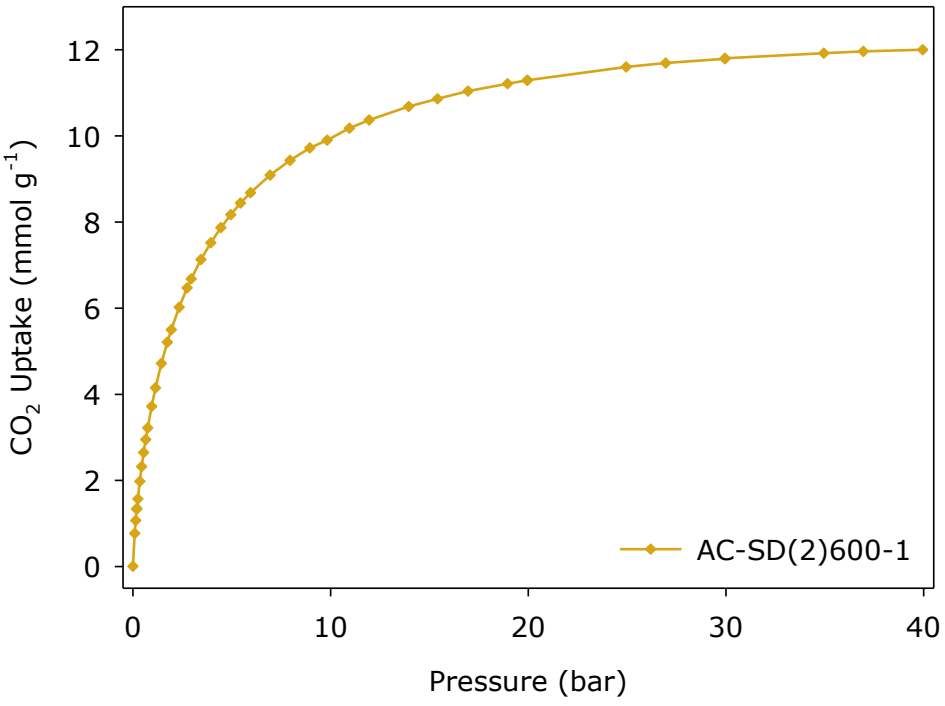

Figure 4.56. CO_2 uptake up to 40 bar of the sample prepared from air-carbonised sawdust at 600 °C, C:KOH ratio of 1:2

Table 4.15. CO_2 uptake at 25 °C over a range of pressures of samples prepared from air-carbonised wood chippings

Sample	CO_2 Uptake (mmol g^{-1})			
	0.15 bar	**1 bar**	**20 bar**	**40 bar**
AC-WC(2)800-1	0.9	3.7	15.0	16.1
AC-WC(4)800-1	0.5	2.4	14.7	17.0
AC-WC(2)600-1	1.1	3.7	9.0	9.5
AC-WC(4)600-1	0.8	3.5	13.9	15.2
AC-WC(2)800-5	0.7	3.1	14.4	16.5
AC-WC(4)800-5	0.3	2.6	19.3	25.1
AC-WC(2)600-5	1.1	4.2	11.6	12.1
AC-WC(4)600-5	0.7	3.2	14.5	15.9

the gentlest conditions, possess the lowest surface area and pore volume, and highest proportion of microporosity of this sample set. Previous studies have shown a link between porosity and CO_2 uptake at various pressures.[1,2,30,45,49,53] The common trend is that at very low pressures (≤ 1 bar), uptake is dependent on the presence of small micropores of ~ 6 – 8 Å.[30,45,51,53] However, at high pressures (≥ 20 bar), uptake becomes dependent on surface area.[1,2,30,45,49,53] Generally, as seen in this study, surface area increases while microporosity

Table 4.16. CO_2 uptake at 25 °C over a range of pressures of samples prepared from hydrothermally-carbonised wood chippings

Sample	CO_2 Uptake (mmol g^{-1})			
	0.15 bar	**1 bar**	**20 bar**	**40 bar**
HC-WC(2)800-1	0.8	3.6	13.1	14.1
HC-WC(4)800-1	0.4	2.2	17.1	22.9
HC-WC(2)600-1	1.2	4.0	9.1	9.6
HC-WC(4)600-1	0.4	1.7	7.8	9.0
HC-WC(2)800-5	0.6	2.9	18.5	23.6
HC-WC(4)800-5	0.2	1.1	8.2	11.0
HC-WC(2)600-5	1.2	4.0	8.9	9.3
HC-WC(4)600-5	0.5	2.1	10.7	12.6

decreases when activation conditions are intensified, resulting in different samples performing to varying degrees as pressure increases. Therefore, it is to be expected that samples AC-WC(2)600-1 and AC-WC(2)600-5 show the highest uptake at 0.15 bar, as they possess the highest proportion of small micropores, centred between 5.4 – 8.0 Å. Following this trend, AC-WC(4)800-5 exhibits the lowest CO_2 uptake of 0.3 mmol g^{-1}. This sample was activated under the harshest conditions, consequently possessing the highest surface area

Table 4.17. CO_2 uptake at 25 °C over a range of pressures of samples prepared from air-carbonised sawdust

Sample	CO_2 Uptake (mmol g^{-1})			
	0.15 bar	**1 bar**	**20 bar**	**40 bar**
AC-SD(2)700-1	1.1	4.5	12.6	13.0
AC-SD(2)700-5	1.1	4.3	11.7	12.1
AC-SD(2)700-10	1.0	4.0	13.7	14.4
AC-SD(2)800-1	0.9	4.0	15.8	16.8
AC-SD(2)800-5	0.8	3.8	17.1	18.8
AC-SD(2)800-10	0.7	3.2	17.7	19.9
AC-SD(4)800-1	0.7	3.5	18.2	20.4
AC-SD(4)800-5	0.6	2.9	20.6	26.1
AC-SD(4)800-10	0.5	2.7	21.0	28.5
AC-SD(2)600-1	1.1	3.8	11.3	12.0

and pore volume, and the lowest proportion of microporosity of the sample set. At 1 bar, CO_2 uptake ranges from 2.4 – 4.2 mmol g^{-1}. AC-WC(4)800-1 was activated under reasonably gentle conditions, showing the lowest uptake of 2.4 mmol g^{-1}. AC-WC(2)600-5, activated under reasonably harsh conditions exhibited the highest 1 bar uptake of 4.2 mmol g^{-1}. At 20 bar, uptake ranges from 9.0 – 19.3 mmol g^{-1} and there is a change to samples with the larger porosities showing higher uptakes.

The lowest uptake (9.0 mmol g^{-1}) was shown by the sample with the least developed porosity (AC-WC(2)600-1), while the highest uptake was shown by AC-WC(4)800-5. At 40 bar, this trend is confirmed, with AC-WC(2)600-1 and AC-WC(4)800-5 showing the lowest and highest uptakes of 9.5 and 25.1 mmol g^{-1} respectively. The isotherms (Fig. 4.42 and 4.44) of all samples, with the exception of AC-WC(4)800-5, reach CO_2 saturation by 40 bar, with AC-WC(2)600-1 and AC-WC(2)600-5 reaching saturation by ~ 15 bar.

The CO_2 uptake isotherms for samples prepared from hydrothermally-carbonised wood chippings are shown in Figures 4.45 to 4.48, with quantitative uptake data recorded in Table 4.16. Uptake at 0.15 bar is in the range 0.2 – 1.2 mmol g^{-1}, again among the highest recorded.[2,10,30,53] The lowest uptake of 0.2 mmol g^{-1} was recorded by HC-WC(4)800-5. Activated under the harshest conditions, the sample has a broad PSD with very little microporosity and a mid-range surface area. The highest uptake of 1.2 mmol g^{-1} was recorded by HC-WC(2)600-1 and HC-WC(2)600-5, the two samples activated under the gentlest conditions. The two samples have among the lowest surface area and highest microporosity for this sample set. They both display a very narrow PSD with the majority of pore volume < 10 Å.

This trend continues at 1 bar, with HC-WC(4)800-5 exhibiting the lowest CO_2 uptake of 1.1 mmol g^{-1}, and both HC-WC(2)600-1 and HC-WC(2)600-5 showing the highest CO_2 uptake of 4.0 mmol g^{-1}. At 20 bar, the shift starts towards samples with higher microporosity showing lower uptakes while those with higher surface area show the highest uptakes. HC-WC(4)600-1 exhibits the lowest uptake of 7.8 mmol g^{-1} while HC-WC(2)800-5 shows the highest uptake of 18.5 mmol g^{-1}. At 40 bar, this trend is confirmed. HC-WC(4)600-1 has the lowest surface area of the sample set (1048 m^2 g^{-1}) with a fairly high microporosity. As a result, it exhibits the lowest CO_2 uptake of 9 mmol g^{-1}. HC-WC(2)800-5 has the highest surface area (2944 m^2 g^{-1}) and among the lowest recorded proportion of microporosity. As a result, it exhibits the highest CO_2 uptake of 23.6 mmol g^{-1}.

Generally, the HC-WC set of samples exhibit lower CO_2 uptakes than the analogous AC-WC samples across all pressure ranges. At each pressure (0.15, 1, 20 and 40 bar) the uptake range is larger than those of AC-WC samples, reflecting the broader range of pore structures. This provides further confirmation that hydrochar is less resistant to KOH activation than airchar.

The CO_2 uptake isotherms for samples prepared from air-carbonised sawdust are displayed in Figures 4.49 – 4.56, with quantitative uptake data displayed in Table 4.17. Uptake at

0.15 bar is in the range 0.5 – 1.1 mmol g^{-1}. AC-SD(4)800-10 was activated under the harshest conditions of the sample set, and consequently possesses the highest surface area, lowest proportion of microporosity and a broad PSD that extends into the small mesopore region. As a result, it shows the lowest CO_2 uptake at 0.15 bar of 0.5 mmol g^{-1}. The highest uptake of 1.1 mmol g^{-1} is exhibited by AC-SD(2)600-1, AC-SD(2)700-1 and AC-SD(2)700-5, the three samples activated under the gentlest conditions of the sample set. These three samples show the lowest surface areas, among the highest proportions of microporosity and very narrow PSDs, with little or no porosity > 15 Å.

CO_2 uptake at 1 bar ranges from 2.7 to 4.5 mmol g^{-1}, which is among the highest recorded CO_2 uptake at 1 bar for porous carbon materials. As before, AC-SD(4)800-10 shows the lowest uptake of 2.7 mmol g^{-1}, while the highest uptake of 4.5 mmol g^{-1} is displayed by AC-SD(2)700-1. Although AC-SD(2)700-1 was not activated under the gentlest conditions, it displays the highest proportion of microporosity of the sample set, and possesses a larger surface area than AC-SD(2)600-1.

CO_2 uptake at 20 bar ranges from 11.3 – 21.0 mmol g^{-1}. The switch toward uptake being dependent on surface area becomes apparent. The lowest uptake of 11.3 mmol g^{-1} is exhibited by

AC-SD(2)600-1 which has the lowest surface area of the sample set. The highest uptake of 21.0 mmol g^{-1} is exhibited by AC-SD(4)800-10, which has the highest surface area of the sample set.

CO_2 uptake at 40 bar ranges from 12.0 – 28.5 mmol g^{-1}. As seen at 20 bar, the lowest uptake of 12.0 mmol g^{-1} is exhibited by AC-SD(2)600-1, while the highest uptake of 28.5 mmol g^{-1} is exhibited by AC-SD(4)800-10.

The isotherms for this sample set (Fig. 4.50, 4.52, 4.54 and 4.56) show that all samples activated at 600 and 700 °C, as well as AC-SD(2)800-1 are fully saturated with CO_2 by 20 bar. AC-SD(4)800-5 and AC-SD(4)800-10 are not fully saturated at 40 bar.

The AC-SD sample set show a similar range of CO_2 uptake to the AC-WC sample set, however they generally show higher uptake values. On average, AC-SD samples have higher surface area and pore volume, but slightly lower proportions on microporosity than equivalent AC-WC samples.

The CO_2 uptakes for all activated samples mostly follow the trends expected from analysis of the textural data. It is clear that samples prepared from airchar perform better in terms of CO_2 uptake than those prepared from hydrochar across all

pressure ranges. Overall, all sample sets show good CO_2 uptakes compared with values reported in the literature for porous carbon materials.

4. 5. Conclusions

Air-carbonisation was successfully carried out within a laboratory setting and the properties of the resulting airchar analysed. A wide range of activated carbons were synthesised from the airchar. The textural properties and CO_2 uptake capacities of the airchar-derived carbons were assessed. In a direct comparison, the effects of air-carbonisation were compared with those of the traditional hydrothermal carbonisation method. The effect of wood type on the air-carbonisation process was also investigated.

Airchar was shown to produce higher yielding porous carbons than hydrochar. Activated AC-WC samples and activated AC-SD samples have average yields of 47 and 38 % respectively, compared with an average yield of 18 % for activated HC-WC samples. This indicates airchar has a higher resistance to KOH activation than hydrochar. Preparing activated carbons through air-carbonisation provides a higher overall yield than through hydrothermal-carbonisation.

SEM images showed that cellular morphology is retained during the air-carbonisation process, in contrast to hydrothermal carbonisation. This is presumably due to the more volatile cellulose and hemicellulose components burning away, leaving

a lignin-rich char. Porosity data shows that while the hydrochar possessed negligible porosity, the process of air-carbonisation creates low levels of porosity. The extent of this porosity development is dependent on wood type.

Activated carbons synthesised from airchar showed superior textural properties and CO_2 uptake capacity. Excellent surface area and pore volume of up to 3159 $m^2\ g^{-1}$ and 1.82 $cm^3\ g^{-1}$ respectively was exhibited. The airchar-derived carbons also showed very high CO_2 uptake at low pressures of 0.15 bar and 1 bar, of 1.1 and 4.5 mmol g^{-1} respectively at 25 °C.

From the range of analysis carried out, it is clear that airchar is more resistant to KOH activation the conventional hydrochar. As shown by pore size distribution plots, less expansion of pore channels occurred under hasher activation conditions during airchar activation than hydrochar activation. This resulted in airchar-derived carbons with high surface area and pore volume, combined with a narrower, small-micropore centred PSD than equivalent hydrochar-derived samples, which is advantageous for CO_2 uptake.

Air-carbonisation is less energy intensive than traditional carbonisation methods and in this study has demonstrated to

be much higher yields, therefore making it a promising step in the synthesis of porous carbons.

Wood type has been shown to have some effect on the char produced via air-carbonisation. This may be assumed to be related to the specific lignin, cellulose and hemicellulose ratios of different wood species. However, upon activation, these differences become negligible, and there is no significant effect of wood type on the structure of resulting porous carbons.

4. 6. Future Work

Calculation of the specific lignin, cellulose and hemicellulose ratios of different wood types would help to investigate and account for the differences in char properties of the spruce-derived char and the eucalyptus-derived char.

Investigating new ways of carrying out air-carbonisation may allow development of an even less energy intensive, and higher yielding process.

Studying the effect of air-carbonisation on non-biomass precursors, e.g. plastics and man-made fibres may expand the potential of the process.

4. 7. References

1 E. Haffner-Staton, N. Balahmar and R. Mokaya, *J. Mater. Chem. A*, 2016, **4**, 13324–13335.

2 E. Hirst, A. Taylor and R. Mokaya, *J. Mater. Chem. A*, 2018, **6**, 12393–12403.

3 P. González-García, *Renew. Sustain. Energy Rev.*, 2018, **82**, 1393–1414.

4 S. Deng, B. Hu and T. Chen, *Adsorption*, 2015, **21**, 125–133.

5 T. Ramesh, N. Rajalakshmi and K. S. Dhathathreyan, *J. Energy Storage*, 2015, **4**, 89–95.

6 M. Stojmenovi, M. C. Pagnacco and M. Popovi, *Colloids Surfaces A Physicochem. Eng. Asp.*, 2017, **522**, 83–96.

7 F. Zhang, G. Li and J. Chen, *J. Colloid Interface Sci.*, 2008, **327**, 108–114.

8 K. S. K. R. A. Al and S. C. Srinivasakannan, 2015, 959–966.

9 M. C. Ncibi, R. Ranguin, M. J. Pintor, V. Jeanne-rose, M. Sillanpää and S. Gaspard, *J. Anal. Appl. Pyrolysis*, 2014, **109**, 205–214.

10 N. Balahmar, A. S. Al-jumialy and R. Mokaya, *J. Mater. Chem. A*, 2017, **5**, 12330–12339.

11 S. Liu and Y. Huang, *J. Clean. Prod.*, 2018, **175**, 354–360.

12 W. Travis, S. Gadipelli and Z. Guo, *RSC Adv.*, 2015, **5**, 29558–29562.

13 M. Yang, L. Guo, G. Hu, X. Hu, L. Xu, J. Chen, W. Dai and M. Fan, *Environ. Sci. Technol.*, 2015, **49**, 7063–7070.

14 O. Paris, C. Zollfrank and G. A. Zickler, *Carbon N. Y.*, 2005, **43**, 53–66.

15 C. Xu and M. Strømme, *Nanomaterials*, 2019, **9**, 103.

16 C. Rodríguez Correa, M. Stollovsky, T. Hehr, Y. Rauscher, B. Rolli and A. Kruse, *ACS Sustain. Chem. Eng.*, 2017, **5**, 8222–8233.

17 Suhas, P. J. M. Carrott and M. M. L. R. Carrott, *Bioresour. Technol.*, 2007, **98**, 2301–2312.

18 F. H. Isikgor and C. R. Becer, *Polym. Chem.*, 2015, **6**, 4497–4559.

19 J. J. M. Órfão, F. J. A. Antunes and J. L. Figueiredo, *Fuel*, 1999, **78**, 349–358.

20 J. F. González, J. M. Encinar, J. L. Canito, E. Sabio and M. Chacón, *J. Anal. Appl. Pyrolysis*, 2003, **67**, 165–190.

21 K. Gergova, N. Petrov and S. Eser, *Carbon N. Y.*, 1994,

32, 693–702.

22 R. Zanzi, K. Sjöström and E. Björnbom, *Biomass Bioenergy*, 2002, **23**, 357–366.

23 W. M. A. W. Daud and W. S. W. Ali, *Bioresour. Technol.*, 2004, **93**, 63–69.

24 R. K. Sharma, J. B. Wooten, V. L. Baliga, X. Lin, W. G. Chan and M. R. Hajaligol, *Fuel*, 2004, **83**, 1469–1482.

25 M. Jagtoyen and F. Derbyshire, *Carbon N. Y.*, 1998, **36**, 1085–1097.

26 M. Sevilla and A. B. Fuertes, *Carbon N. Y.*, 2009, **47**, 2281–2289.

27 M. Sevilla, A. B. Fuertes and R. Mokaya, *Energy Environ. Sci.*, 2011, **4**, 1400.

28 M. Sevilla and A. B. Fuertes, *Chem. A Eur. J.*, 2009, **15**, 4195–4203.

29 M. Sevilla, G. A. Ferrero and A. B. Fuertes, *Carbon N. Y.*, 2017, **114**, 50–58.

30 H. M. Coromina, D. A. Walsh and R. Mokaya, *J. Mater. Chem. A*, 2016, **4**, 280–289.

31 M. Sevilla, W. Sangchoom, N. Balahmar, A. B. Fuertes and R. Mokaya, *ACS Sustain. Chem. Eng.*, 2016, **4**, 4710–4716.

32 M. Sevilla, C. Falco, M. Titirici and A. B. Fuertes, *RSC Adv.*, 2012, **2**, 12792–12797.

33 S. Mandal, A. Kunhikrishnan, N. S. Bolan, H. Wijesekara and R. Naidu, in *Environmental Materials and Waste: Resource Recovery and Pollution Prevention*, Elsevier Inc., 2016, pp. 73–89.

34 A. V Bridgwater, *Biomass and Bioenergy*, 2012, **38**, 68–94.

35 D. J. Roddy and C. Manson-Whitton, in *Reference Module in Earth Systems and Environmental Sciences Comprehensive Renewable Energy*, Elsevier Ltd., 2012, vol. 5, pp. 133–153.

36 F. Collard and J. Blin, *Renew. Sustain. Energy Rev.*, 2014, **38**, 594–608.

37 G. Singh, K. S. Lakhi, K. Ramadass, C. I. Sathish and A. Vinu, *ACS Sustain. Chem. Eng.*, 2019, **7**, 7412–7420.

38 J. Li, B. Michalkiewicz, J. Min, C. Ma, X. Chen, J. Gong, E. Mijowska and T. Tang, *Chem. Eng. J.*, 2019, **360**, 250–259.

39 B. Chang, W. Shi, H. Yin, S. Zhang and B. Yang, *Chem. Eng. J.*, 2019, **358**, 1507–1518.

40 J. Yang, L. Yue, X. Hu, L. Wang, Y. Zhao, Y. Lin, Y. Sun, H. Dacosta and L. Guo, *Energy & Fuels*, 2017, **31**, 4287–

4293.

41 M. Sevilla and R. Mokaya, *Energy Environ. Sci.*, 2014, **7**, 1250–1280.

42 C. R. Correa and A. Kruse, *Materials (Basel).*, 2018, **11**, 1568.

43 J. Wang and S. Kaskel, *J. Mater. Chem.*, 2012, **22**, 23710–23725.

44 M. A. Lillo-Rodenas, J. Juan-Juan, D. Cazorla-Amor and A. Linares-Solano, *Carbon N. Y.*, 2004, **42**, 1371–1375.

45 W. Sangchoom and R. Mokaya, *ACS Sustain. Chem. Eng.*, 2015, **3**, 1658–1667.

46 M. Sevilla, P. Valle-vigón and A. B. Fuertes, *Adv. Funct. Mater.*, 2011, **21**, 2781–2787.

47 E. Masika and R. Mokaya, *Prog. Nat. Sci.*, 2013, **23**, 308–316.

48 J. Song, W. Shen, J. Wang and W. Fan, *Carbon N. Y.*, 2014, **69**, 255–263.

49 B. Adeniran and R. Mokaya, *J. Mater. Chem. A*, 2015, **3**, 5148–5161.

50 D. Li, Y. Tian, L. Li, J. Li and H. Zhang, *J. Porous Mater.*, 2015, **22**, 1581–1588.

51 M. Sevilla and A. B. Fuertes, *Energy Environ. Sci.*, 2011,

4, 1765–1771.

52 D. Lozano-Castello, M. A. Lillo-Rodenas, D. Cazorla-Amoros and A. Linares-Solano, *Carbon N. Y.*, 2001, **39**, 741–749.

53 B. Adeniran, E. Masika and R. Mokaya, *J. Mater. Chem. A*, 2014, **2**, 14696.

4.8. Appendix

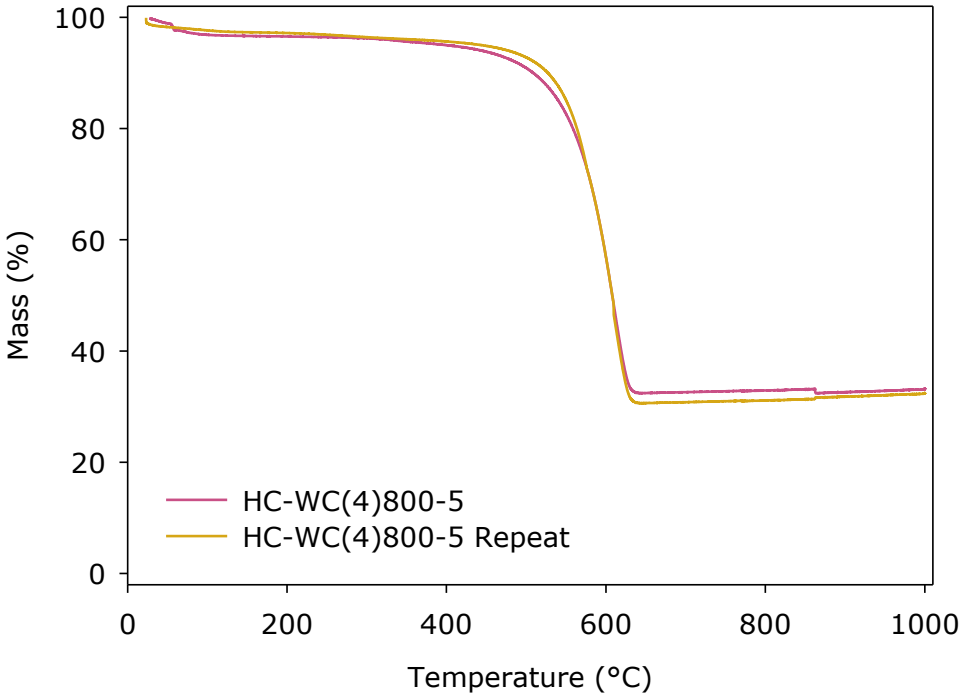

Figure 4.A1. Repeat TGA measurement of HC-WC(4)800-5

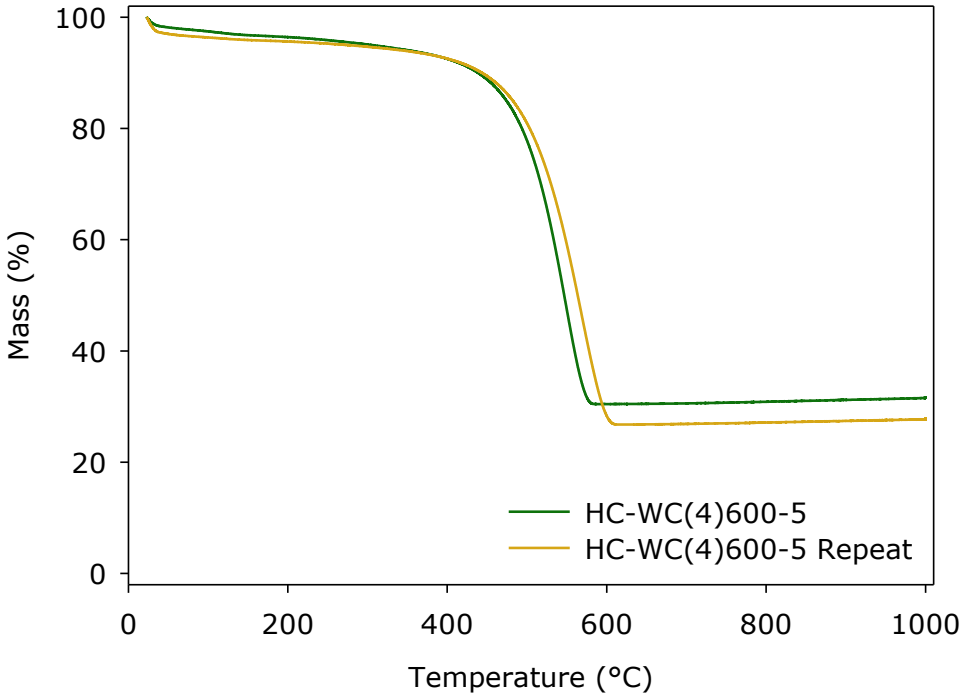

Figure 4.A2. Repeat TGA measurement of HC-WC(4)600-5

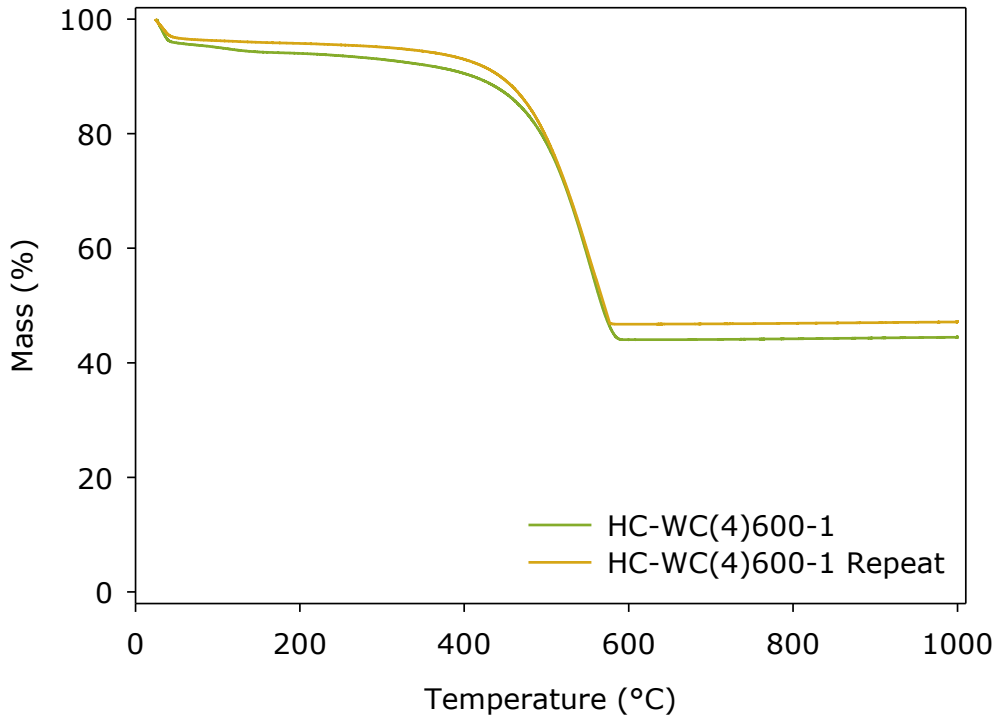

Figure 4.A3. Repeat TGA measurement of HC-WC(4)600-1

Chapter 5 – An Alternative Activating Agent in the Synthesis of Activated Carbons

5. 1. Abstract

The study reported in this chapter is an investigation into the activation ability of calcium hydroxide ($Ca(OH)_2$). The aim of the study was to assess the suitability of $Ca(OH)_2$ as a less corrosive, less aggressive alternative to the most commonly reported chemical activating agent, potassium hydroxide (KOH), in the synthesis of porous carbons for the purpose of CO_2 uptake.

Eucalyptus-derived hydrochar was activated with $Ca(OH)_2$ under a range of activation conditions to produce a series of porous carbons. The resulting carbons were mainly mesoporous, with varying degrees of micro and macroporosity. Surface area and pore volume of up to 562 $m^2\ g^{-1}$ and 1.07 $cm^3\ g^{-1}$ respectively were obtained. CO_2 uptake reached a maximum of 0.9, 2.3, 5.6 and 6.8 mmol g^{-1} at 0.15, 1, 20 and 40 bar respectively and 25 °C. Selectivity of CO_2 over N_2 calculated using IAST theory under flue gas conditions reached a maximum of 35 and the equilibrium selectivity factor at 1 bar reached 14.

5. 2. Introduction

In the synthesis of activated carbons, an activation step is needed to generate enhanced porosity. The role of an activating agent is to develop a pore structure, thereby increasing the surface area and pore volume of the material.[1,2] As well as the activating conditions used (temperature, duration, heating ramp rate and amount of activating agent), the activation agent chosen has a significant effect on the pore structure of resulting carbons.[2–5] Activated carbons with different porous structures are suitable for a range of applications. While a narrow pore size distribution centred at 6 – 8 Å is ideal for CO_2 uptake ≤ 1 bar,[2,6,7] a large surface area is important for efficient H_2 storage.[8,9] A hierarchical pore structure allows for fast diffusion kinetics and is therefore suitable for applications such as electrode materials[10,11] and catalyst supports.[12,13] Large pore sizes are desirable in applications such as pollutant removal.[14,15]

As stated in Chapter 1 (section 1. 5. 3.), activation of a material can be either chemical, physical or a combination of both. Therefore, activating agents act via either chemical or physical processes to create a pore structure in a variety of ways.

Physical activation involves the use of an oxidising gas such as CO_2, steam or air for partial gasification of the carbon precursor.

This process burns away reactive sites of the carbon skeleton, releasing CO and CO_2, to create a pore network. An initial pyrolysis step is required under an inert atmosphere to remove volatiles.[2–4]

Chemical activation is a one-step process, with the most commonly used activating agents being either dehydrating or oxidising reagents. Popular dehydrating activating agents include $ZnCl_2$, $MgCl_2$, $AlCl_3$ and H_3PO_4.[2,3,16,17] During heating under inert atmosphere, dehydration of the carbon-based precursor occurs around the activating agent. The expected shrinking of the dehydrated skeleton is inhibited due to the presence of the activating agent remaining within the structure. Therefore, the activating agent acts as a template for the creation of a pore network.[2,17,18]

KOH and NaOH are commonly used oxidising activating agents and, as discussed in Chapter 1 (section 1. 5. 3.), several studies have detailed the redox reaction mechanism between these hydroxides and a carbon skeleton.[2–5,19–21] The overall reaction of KOH and NaOH respectively, with a carbon precursor can be summarised as follows:[21]

$$6KOH + 2C \leftrightarrow 2K + 3H_2 + 2K_2CO_3 \qquad \textbf{Eqn. 5.1}$$

$$6NaOH + 2C \leftrightarrow 2Na + 3H_2 + 2Na_2CO_3 \qquad \textbf{Eqn. 5.2}$$

Above 700 °C, the respective metal carbonates decompose to release CO_2 as follows:[21]

$$K_2CO_3 \leftrightarrow K_2O + CO_2 \qquad \textbf{Eqn. 5.3}$$

$$Na_2CO_3 \leftrightarrow Na_2O + CO_2 \qquad \textbf{Eqn. 5.4}$$

Metallic K has been shown to intercalate into and expand the laminar carbon structure, further contributing to pore development.[16,22] The reaction between KOH and carbon begins at ~ 570 °C, whereas the reaction between NaOH and carbon begins at ~ 400 °C.[21]

KOH is by far the most commonly used chemical reagent in the activation of carbon materials. Its popularity is due to the porous structures it generates having narrow pore size distribution and a high proportion of microporosity. KOH has been shown to create carbons reliably, with high surface area and pore volume. The results it produces are predictable, making tailoring of synthesis procedures simple.[4,23]

However, there are many disadvantages associated with using KOH as a chemical activating agent. Its highly corrosive nature results in safety and handling issues, as well as potential damage to equipment. It is also considered an aggressive activating agent, resulting in low carbon yields of only ~ 20 –

30 %.[17,23] For these reasons, studies have started to explore alternative, more industrially viable chemical activating agents.

Many studies have investigated alternative K-based or metal hydroxide activating agents. Potassium bicarbonate ($KHCO_3$) is a mildly alkaline, less corrosive potassium salt. Deng *et al*.[24] activated various forms of biomass with $KHCO_3$ to produce hierarchically porous carbons for use as electrode materials. The materials exhibited well developed porosity with surface area and pore volume up to 1893 $m^2\ g^{-1}$ and 1.37 $cm^3\ g^{-1}$ respectively.[24] Sevilla *et al*.[25] activated a biomass hydrochar with $KHCO_3$ to produce carbons with high surface area and pore volume of up to 2305 $m^2\ g^{-1}$ and 1.36 $cm^3\ g^{-1}$ respectively. The carbons were highly microporous and provided a yield of 33 %, compared with a yield of only 23 % for equivalent carbons activated with KOH.[25]

In a separate study, Sevilla *et al*.[23] activated biomass hydrochar with an alternative potassium salt, potassium oxalate ($C_2K_2O_4$). Potassium oxalate is a weakly acidic carboxylic acid that is significantly less corrosive than KOH. Carbons were produced with surface area and pore volume of only up to 1600 $m^2\ g^{-1}$ and 0.71 $cm^3\ g^{-1}$ respectively. However, the carbons exhibited up to 90 % microporosity.[23]

Alternative alkali metal hydroxides have also been studied as activating agents. NaOH is the most commonly used alternative; although it has shown to produce well developed microporous structures, it is also highly corrosive. Volperts *et al*.[26] activated biomass with NaOH to produce highly microporous carbons with very high surface area and pore volume of up to 2845 $m^2\ g^{-1}$ and 1.41 $cm^3\ g^{-1}$ respectively. Dobele *et al*.[27] activated pyrolysed biomass impregnated with NaOH to produce high yielding (up to 38 %), highly microporous carbons. The carbons exhibited reasonable surface area and pore volume of up to 1348 $m^2\ g^{-1}$ and 1.35 $cm^3\ g^{-1}$ respectively, with the majority of the pore volume in the supermicropore range (7 – 20 Å).[27]

Tamarkina *et al*.[28] conducted an extensive comparison of three alkali metal hydroxides; KOH, NaOH and LiOH. Activation efficiency of coal increased in the order LiOH < NaOH < KOH and it was concluded that KOH was 10x more effective than NaOH and 16x more effective than LiOH. As a result, when using the same weight ratio of metal hydroxide, KOH, NaOH and LiOH resulted in carbon yields of 20, 24 and 44 % respectively. Maximum surface area obtained with KOH, NaOH and LiOH was 680, 450 and 400 $m^2\ g^{-1}$ respectively.[28]

Despite the interest in the use of Group 1 metal hydroxides as oxidising activating agents, particularly KOH and NaOH, no studies have been found reported in the literature regarding the use of Group 2 metal hydroxides. Danish *et al*.[29] activated raw biomass with calcium oxide (CaO) to produce activated carbon with low porosity. The carbon material presented a type II isotherm with an H3 hysteresis, indicating a non-porous or macroporous structure constructed of plate-like particles with slit-shaped pores. Gas sorption analysis measured a surface area and pore volume of 65 m^2 g^{-1} and 0.09 cm^3 g^{-1} respectively. The degree of microporosity was negligible.[29]

The investigation here is a study of the use of $Ca(OH)_2$ as an oxidising chemical activating agent, which is little reported in the literature. As an alkali metal hydroxide, $Ca(OH)_2$ may be expected to react with the carbon skeleton via a similar mechanism to that of the more reported KOH and NaOH. Metallic Ca, being of a similar size to metallic K, can be expected to intercalate into and expand the laminar carbon structure, contributing to pore development as seen with the use of KOH. For these reasons, $Ca(OH)_2$ could prove to be an effective carbon activating agent, having the advantage over KOH of being less corrosive and not as strongly alkaline. This leads to safer and therefore cheaper industrial handling, and the

potential for higher carbon yields due to the less aggressive nature of Group 2 metal hydroxides.

Due to the favourability of biomass precursors both environmentally and economically,[30,31] hydrothermally carbonised eucalyptus sawdust was chosen as a carbon source. The hydrochar was activated with $Ca(OH)_2$ at a range of temperatures, durations and char:$Ca(OH)_2$ ratios. The aim of the study was firstly to analyse the activating ability of $Ca(OH)_2$ and how this is affected by changes to the activation conditions. The secondary aim of the study was to assess the suitability of $Ca(OH)_2$-activated porous carbons as solid CO_2 adsorbents over a range of pressures.

5. 3. Material Synthesis

Activated carbons were synthesised by pre-treating sawdust through hydrothermal carbonisation before activation.

Hydrothermal Carbonisation Pre-Treatment

An aqueous suspension of sawdust (Eucalyptus wood) (3.2 g) in deionised water (10 mL) was placed in a stainless steel autoclave and heated at a ramp rate of 5 °C min^{-1} to 250 °C. The suspension was held at this temperature for 2 hrs before being allowed to cool to room temperature. The resulting 'hydrochar' was collected by vacuum filtration and washed thoroughly with deionised water before being dried in air at 100 °C for 48 hrs. The yield of this hydrothermal carbonisation process was 57 %.

Activation

Sawdust derived hydrochar was ground in a pestle and mortar with $Ca(OH)_2$ (Sigma Aldrich) in a $Ca(OH)_2$:C weight ratio of either 2 or 4. The mixture (3 g) was heated in a horizontal alumina furnace at a ramp rate of 5 °C min^{-1} to either 500, 600, 800 or 1000 °C under a flow of nitrogen (100 mL min^{-1}). The samples were held at the target temperature for either 1 or 5 hrs before being allowed to cool to room temperature, all under nitrogen flow. Samples were washed several times in HCl (10

wt%, 400 mL) (Fisher Scientific) before being collected by vacuum filtration, neutralised with deionised water and dried in air at 100 °C for 24 hrs. The yield of the activation process ranged from 19 – 45 %.

The final samples were denoted Ca(x)T-y, where x represents the $Ca(OH)_2$:C ratio, T represents the activation temperature in degrees Celsius and y represents the activation time in hours.

Various methods were used to characterise and analyse the samples. Thermal gravimetric analysis was carried out using a TA Instruments Analytical TGAQ500 machine. Samples were heated at a ramp rate of 10 °C min^{-1} to 1000 °C in air.

Elemental analysis was carried out using a CE-440 Elemental Analyzer, Exeter Analytical, INC. Samples were combusted in oxygen at 975 °C.

Powder x-ray diffraction analysis was carried out using a PANalytical X'Pet Pro diffractometer using CuKα radiation (λ = 1.5418 Å), operating at 40 kV and 40 mA. A step size of 0.026° and a step time of 30.6 s was used.

Analysis of textural properties was carried out by nitrogen sorption at -196 °C. An initial degassing stage was conducted using a Micromeritics SmartVac Prep degassing unit wherein samples were held under vacuum at 230 °C for 16 hours. The

following analysis was carried out using a Micromeritics 3Flex. Surface areas were calculated using BET theory from adsorption data within the linear isotherm plot (relative pressure (P/P_0) of 0.04 – 0.09). Total pore volumes were calculated from the nitrogen uptake close to saturation pressure ($P/P_0 \approx 0.99$). Micropore surface areas and pore volumes were calculated using t-plot analysis. Pore size distributions were determined by applying non-local density functional theory (NLDFT) to the nitrogen adsorption isotherms.

Gas uptakes were measured using a Hiden Isochema XEMIS machine. After an initial degassing stage, where samples were held under vacuum at 230 °C for 3 hours, analysis was carried out with either CO_2 or N_2 as the adsorbing gas, at 25 °C and at pressures from 0 – 40 bar.

Scanning electron microscopy was conducted using a Zeiss Evo 10 SEM machine with a tungsten filament, operating with a 20 kV accelerating voltage.

5. 4. Results and Discussion

5. 4. 1. Elemental Analysis and Carbon Yield

The elemental analysis (C, H, O analysis) and average yields for all samples are shown below in Tables 5.1 and 5.2. Nitrogen content is not reported for the samples as in all cases its presence was negligible. The carbon and hydrogen content of the organic component of the materials were measured, and the remaining content assumed to be oxygen.

Activation increases carbon content with respect to the hydrochar in all cases. The largest increase in carbon content of 59.4 to 91.6 % is shown by Ca(4)800-1. Overall, samples activated at 800 °C showed the greatest carbon enrichment. The smallest increase in carbon content of 59.4 to 74.6 % was shown by Ca(4)500-1. Overall, samples activated at 500 °C showed the lowest degree of carbon enrichment. This can be explained by the low level of reactions taking place between the activating agent and the carbon skeleton at 500 °C. Increased levels of carbon burn off as CO monoxide can be assumed to occur at an activation temperature over 800 °C.[3] Ca(4)800-1 and Ca(4)500-1 therefore show the largest and smallest corresponding decrease in oxygen content, respectively.

Table 5.1. Elemental analysis results of all samples. C and H content was calculated though elemental microanalysis. The remaining content was assumed to be O. The atomic C/O ratio was calculated from these values

Sample	C%	H%	O%	C/O
Ca(2)1000-1	86.7	0.4	12.9	8.9
Ca(4)1000-1	85.7	0.3	14.0	8.1
Ca(2)800-5	90.9	0.5	8.6	14.0
Ca(4)800-5	87.9	0.6	11.5	10.2
Ca(2)800-1	91.1	N/A	8.9	13.6
Ca(4)800-1	91.6	N/A	8.4	14.4
Ca(2)600-5	85.3	1.4	13.3	8.6
Ca(4)600-5	84.3	1.7	14.0	8.0
Ca(2)600-1	84.5	2.4	13.1	8.6
Ca(4)600-1	85.4	2.2	12.4	9.1
Ca(2)500-1	76.3	2.6	21.1	4.8
Ca(4)500-1	74.6	2.5	22.9	4.3
HC-SD	59.4	5.2	35.4	2.2

Increasing activation temperature increases the degree of carbon enrichment up to 800 °C, after which this trend seems to reverse. No consistent trend is observed with respect to activating agent ratio. Generally, a shorter activation time results in a higher carbon content; reactions over an extended

Table 5.2. Carbon yield from hydrochar of all samples. Averages calculated from the yield of each sample produced

Sample	Carbon Yield (%)
Ca(2)1000-1	39
Ca(4)1000-1	23
Ca(2)800-5	23
Ca(4)800-5	19
Ca(2)800-1	29
Ca(4)800-1	27
Ca(2)600-5	29
Ca(4)600-5	28
Ca(2)600-1	32
Ca(4)600-1	27
Ca(2)500-1	45
Ca(4)500-1	34

period of time encourage greater carbon burn-off. The carbon content (59.4 %) and yield (57 %) of the hydrochar precursor is in line with similar chars reported in previous studies.[19,32–35] The yields of the activated samples range between 19 – 45 %, which covers the range commonly seen for carbons prepared from KOH activation of hydrochar.[32,36,37] Therefore, using $Ca(OH)_2$ as an activating agent has no disadvantage in terms of yield compared with the more corrosive KOH. The yields are

slightly lower for samples activated with a char:$Ca(OH)_2$ ratio of 1:4, as a higher proportion of activating agent results in more extensive etching of the carbon surface.

5. 4. 2. Scanning Electron Microscopy

Scanning electron microscopy (SEM) images for representative samples are shown below in Figure 5.1. Ca(2)500-1 (Fig. 5.1 [A]) is comprised of large particles. The particle surface is a mixture of irregular structures and areas of woody, cellular structures with lamellar regularity, alongside honeycomb structures retained from the parent char (Fig. 5.1 [D]). This shows that low temperature activation results in little breakdown of the hydrochar particles.

Ca(2)800-1 and Ca(2)1000-1 (Fig. 5.1 [B] and [C], respectively) show similar morphology, consisting of considerably smaller particles of varying sizes. Figure 5.1 [B] is an image formed by backscattered electrons and shows a mixture of irregularly shaped particles and woody, cellular-like monolith structures, indicating retention of the parent hydrochar.

Sample Ca(2)1000-1 is comprised of slightly larger particles and exhibits conchoidal etching on the larger particle surfaces.

It is clear that the higher the activation temperature, the greater the breakdown of the hydrochar particles. Although some retention of the parent char is apparent in all 3 activated samples, the higher the activation temperature used, the

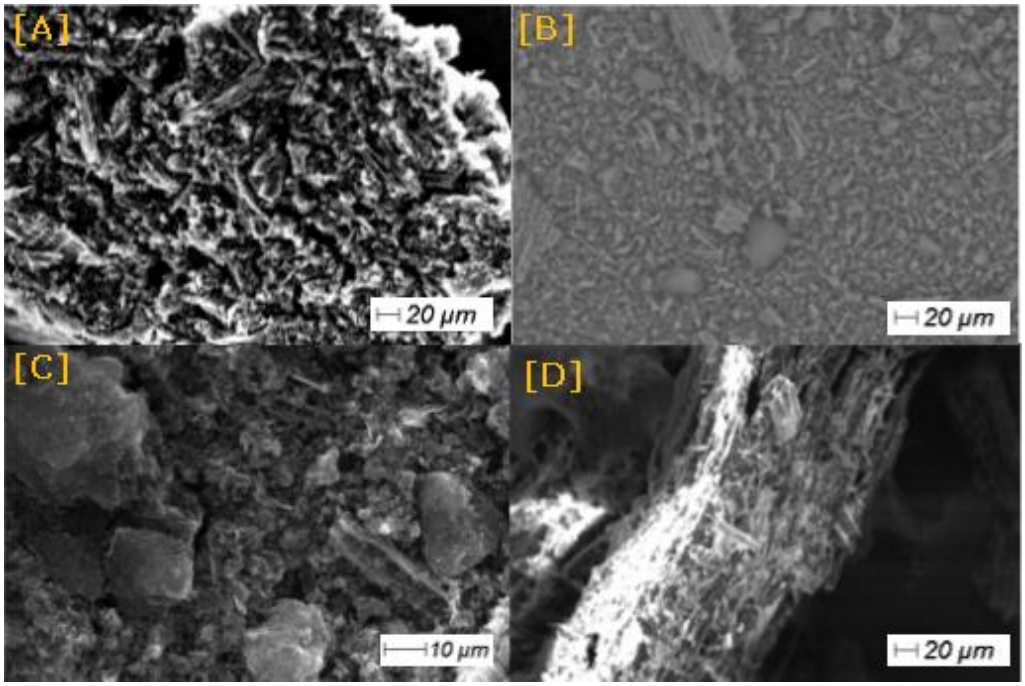

Figure 5.1. SEM images of [A] Ca(2)500-1, [B] Ca(2)800-1, [C] Ca(2)1000-1 and [D] SD-HC

greater the irregularity and surface etching of the resulting activated carbon particles.

5. 4. 3. Thermal Gravimetric Analysis

Thermal gravimetric analysis (TGA) of all the activated samples was conducted to assess the structure, purity and thermal stability. The TGA plots of all samples are shown in Figures 5.2 – 5.5. Across all plots, some samples show a small mass loss at ~ 100 °C. This can be attributed to moisture loss and can be assumed to be associated with the length of time the sample spent exposed to the atmosphere, as opposed to any structural differences. Most samples show a single sharp burn-off curve within the approximate range 400 – 600 °C. This burn-off range is indicative of amorphous carbon, while a single burn-off curve indicates single phase carbon.[8]

As described in previous chapters, activation conditions have an effect on thermal stability of resulting activated carbons. Samples activated above ~ 750 °C are expected to show some graphitic domains, leading to higher thermal stability.[38] Indeed, samples activated at both 1000 and 800 °C (Fig. 5.2 and 5.3) show the highest thermal stability of the sample set with burn-off maxima ranging between 539 – 586 °C. Thermal stability reduces with activation temperature, with samples activated at 600 and 500 °C showing burn-off maxima that range between 479 – 504 °C and 455 – 487 °C respectively (Fig. 5.4 and 5.5).

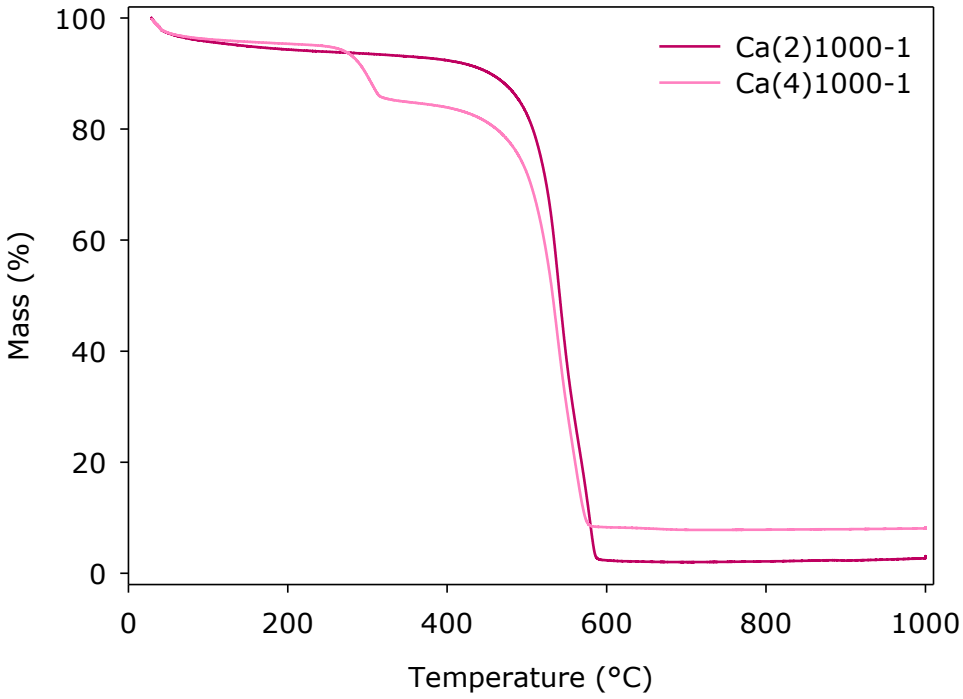

Figure 5.2. TGA plots of samples activated at 1000 °C

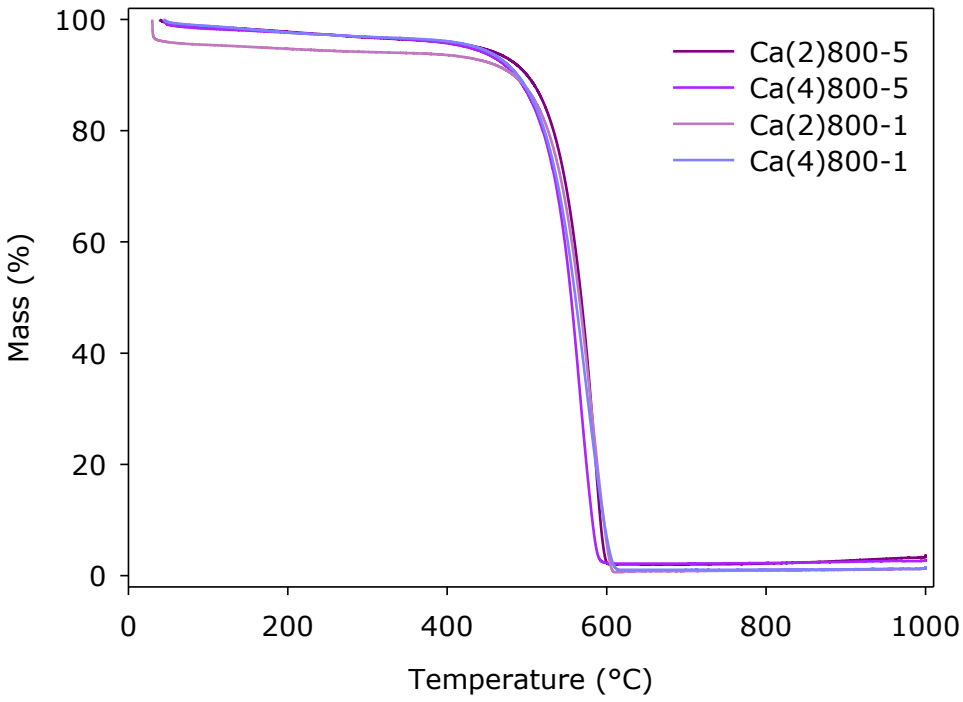

Figure 5.3. TGA plots of samples activated at 800 °C

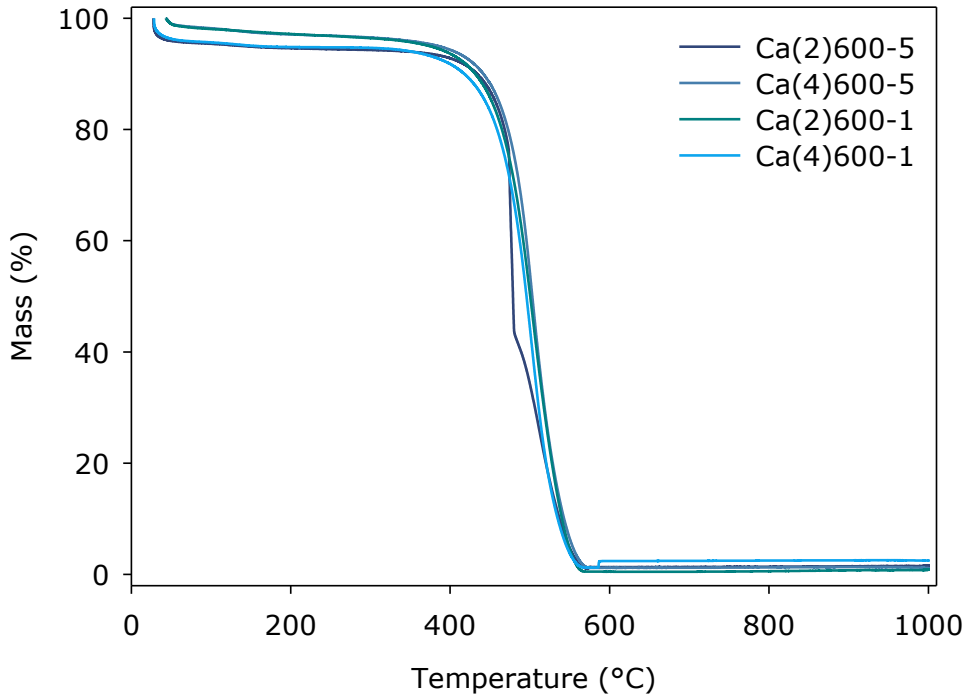

Figure 5.4. TGA plots of samples activated at 600 °C

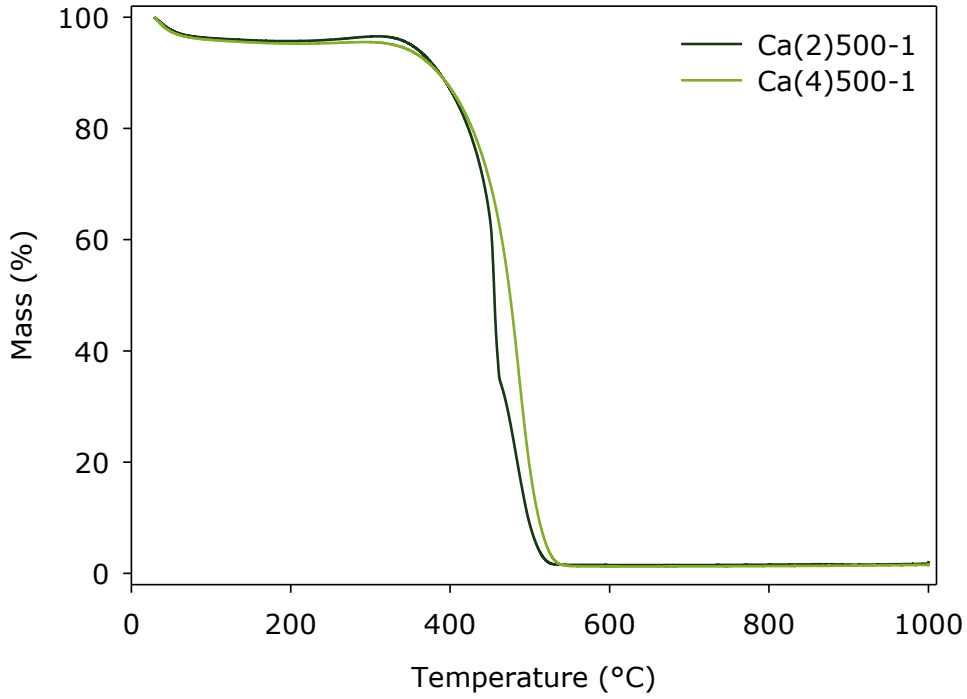

Figure 5.5. TGA plots of samples activated at 500 °C

Across all sample sets, neither activation time or amount of activating agent have any significant effect on thermal stability. This indicates that activation with $Ca(OH)_2$ results in structural development that is mostly dependent on temperature.

The majority of the samples show very low residual mass < 2.5 %, indicating very low or negligible levels of impurities. Ca(4)1000-1 exhibits a residual mass of 7.8 %. This small amount of impurity can be assumed to be calcium compounds formed during activation that were not removed during the washing process. Sample Ca(4)1000-1 also exhibits a small mass loss at 306 °C (Fig. 5.2, repeat measurement shown in Fig. 5.A1). As Ca(4)1000-1 has elemental composition similar to Ca(2)1000-1, this feature can be assumed to be related to the nature of the carbon structure generated at 1000 °C. Activation with $Ca(OH)_2$ under such harsh conditions may produce a small amount of highly amorphous carbon with no short-range order and therefore, low thermal stability.

5. 4. 4. Powder X-Ray Diffraction

Powder x-ray diffraction (PXRD) was used to assess the purity, structure and graphitisation of all the activated samples. The diffraction patterns are shown below in Figures 5.6 – 5.9. The particular areas of interest in the PXRD patterns are peaks at 2θ ≈ 22° and 44°, which correspond respectively to diffraction of the (002) and (100) planes of stacked graphite. The very low angle region of the pattern (< 15°) was featureless in regard to the sample analysis, so is not reported here.

The PXRD patterns for samples activated at 1000 °C are shown in Fig. 5.6. There are no sharp peaks, consistent with the absence of inorganic impurities as observed from the TGA plots. A noticeable peak of reasonable intensity at 2θ ≈ 22° for both samples indicates some degree of regularity and graphene stacking. R values of 1.9 for both samples indicate an average stacking of almost 2 graphene layers distributed throughout the structures. These defined graphitic peaks are in line with the high thermal stability of these samples observed through TGA. This can be attributed to the increased development of graphitic domains during activation above 750 °C.

The PXRD patterns for samples activated at 800 °C are shown in Fig. 5.7. A lack of sharp peaks confirms the low impurity level

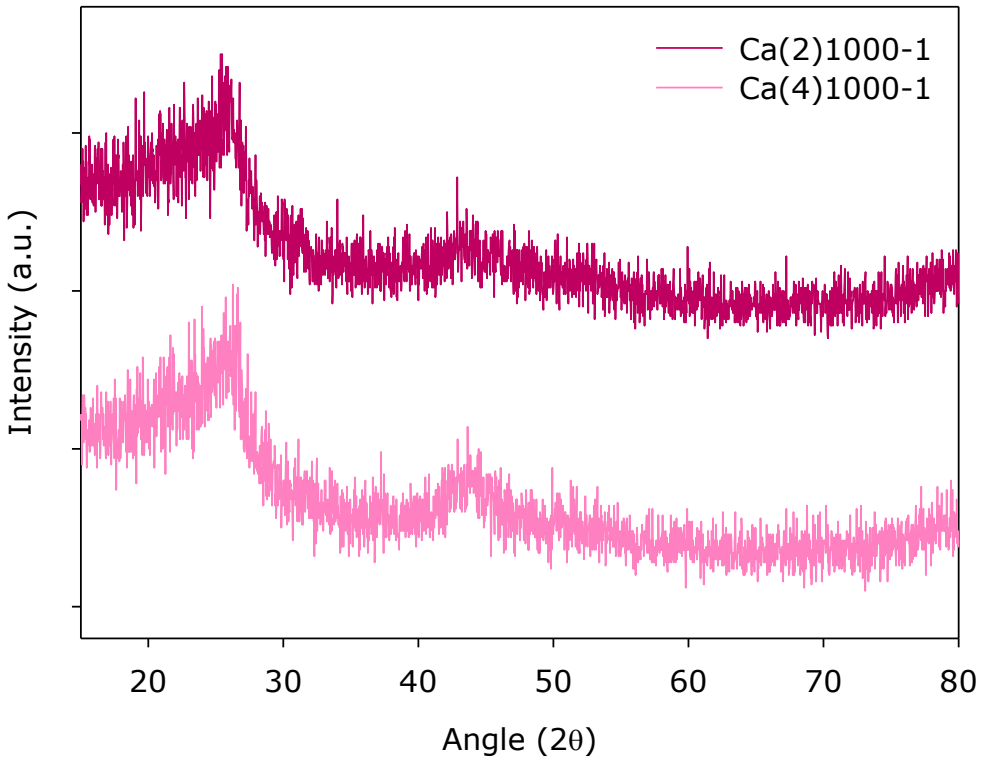

Figure 5.6. PXRD patterns of samples activated at 1000 °C

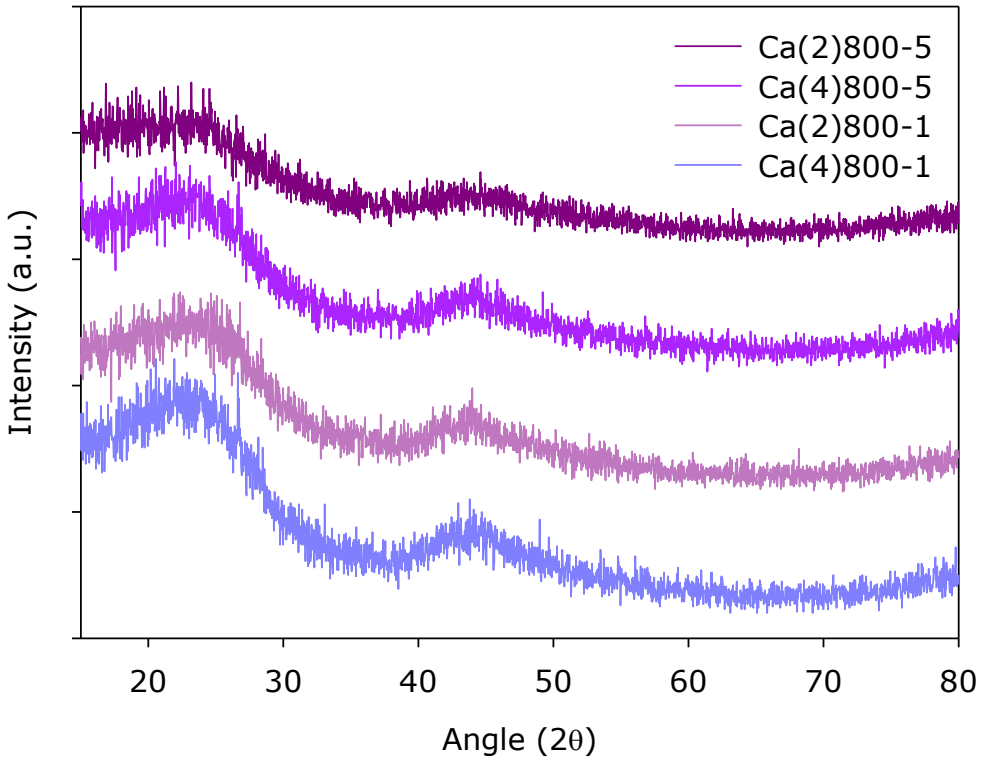

Figure 5.7. PXRD patterns of samples activated at 800 °C

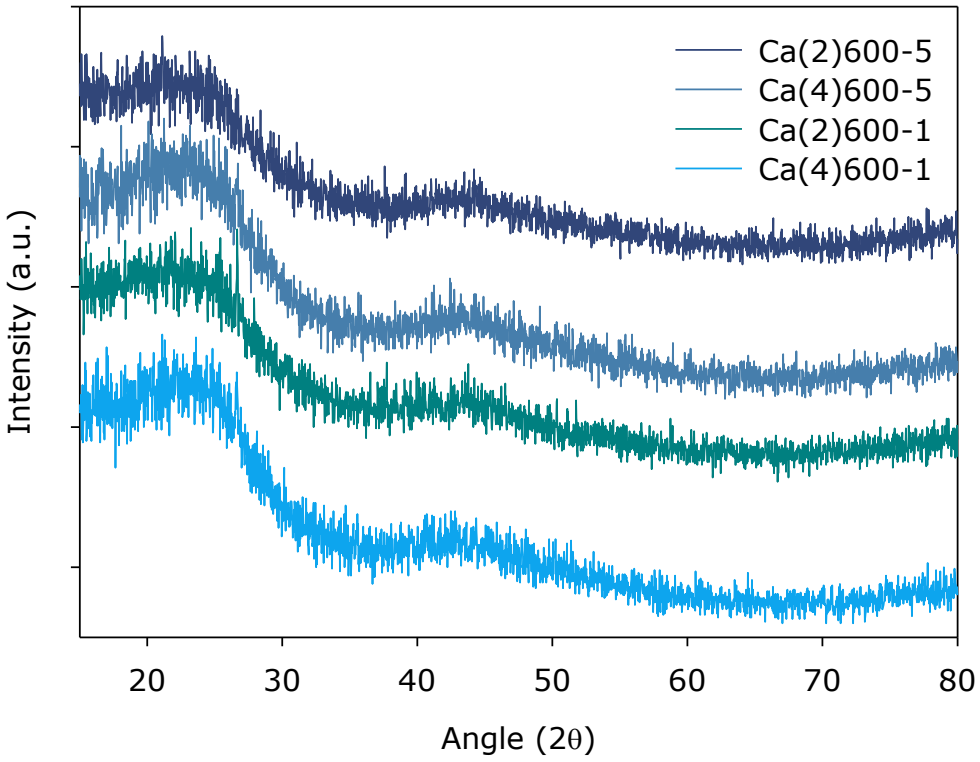

Figure 5.8. PXRD patterns of samples activated at 600 °C

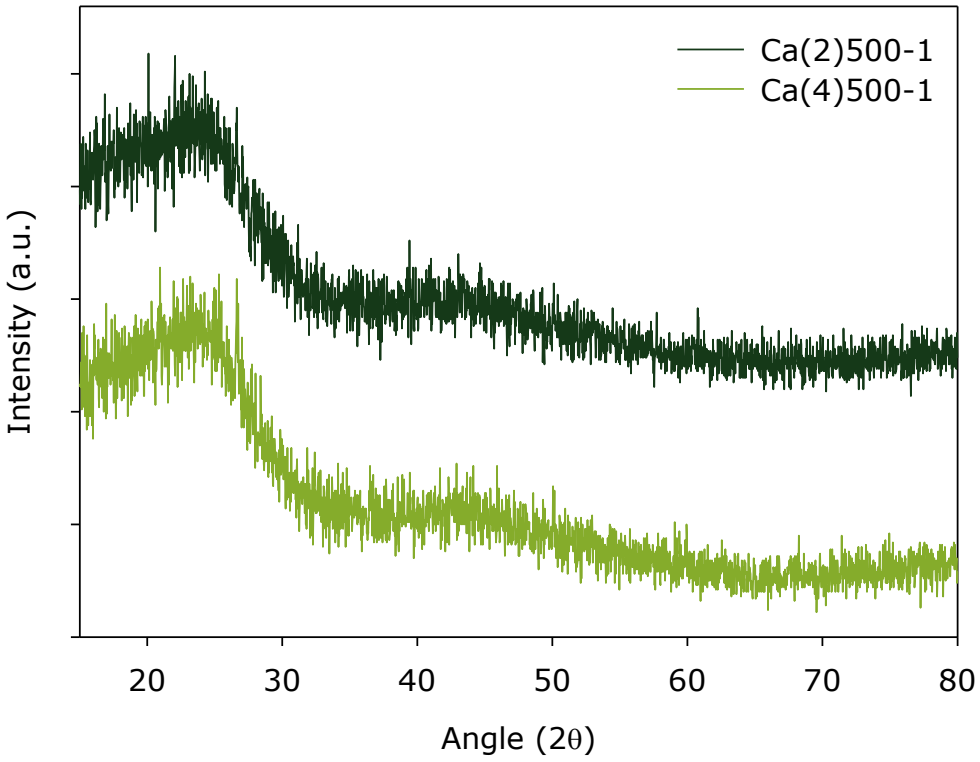

Figure 5.9. PXRD patterns of samples activated at 500 °C

indicated by the TGA plots. Noticeable peaks are present at 2θ ≈ 22°, but they are generally broader and of lower intensity than the equivalent peaks seen for samples activated at 1000 °C. This indicates a higher level of amorphous character and lower levels of graphene stacking compared with samples of the previous set. Indeed, R values of 1.4 (Ca(2)800-5), 1.4 (Ca(4)800-5), 1.5 (Ca(2)800-1) and 1.6 (Ca(4)800-1) confirm a higher level of irregularity. Despite this difference in regularity, samples activated at both 1000 and 800 °C exhibit similar thermal stabilities, as observed through TGA analysis (Fig. 5.2 and 5.3). This may be explained by the graphitic planes slipping out of alignment in samples activated at 800 °C. Graphitic domains remain present, but regularity is decreased, resulting in a more turbostratic structure.

The PXRD patterns of samples activated at 600 °C are shown in Fig. 5.8. The diffraction patterns are similar to those observed for samples activated at 800 °C; broad peaks of low intensity at both 2θ ≈ 22° and 44° indicate an irregular structure with some degree of graphite-like stacking. R values of 1.4 (Ca(2)600-5), 1.5 (Ca(4)600-5), 1.4 (Ca(2)600-1) and 1.5 (Ca(4)600-1) are similar for equivalent samples activated at 800 °C. As before, the lack of sharp peaks coincides with the very low residual mass observed through TGA.

The PXRD patterns of samples activated at 500 °C are shown in Fig. 5.9. The lack of sharp peaks confirms a low impurity level. Broad peaks of relatively low intensity at 2θ ≈ 22° and almost indiscernible peaks at 2θ ≈ 44° indicate an amorphous structure with some level of graphite-like stacking. R values of 1.6 for both samples indicate similar structures to samples activated at both 600 and 800 °C.

Overall, activation with $Ca(OH)_2$ creates reasonably amorphous structures with some degree of regular, graphitic-like stacking and low or negligible levels of impurities. Activation temperature up to 800 °C has little significant effect on the observed PXRD patterns, although activation at 1000 °C results in a higher degree of regularity.

5. 4. 5. Nitrogen Sorption Isotherms

The N_2 sorption isotherms recorded at -196 °C are shown below in Figures 5.10 – 5.13. Isotherms for all samples activated at either 1000, 800 or 600 °C exhibit similar shapes, so samples are assumed to be of similar porosity. The isotherms show mainly type IV(a) characteristics with some type II character; samples do not reach saturation by $P/P_0 = 1$. The isotherms can be classified as mainly type IV(a) due to an initial uptake at very low relative pressure, indicating some degree of microporosity, followed by a first knee concave to the x axis, followed by a second, broad knee convex to the x axis. This indicates monolayer and multilayer adsorption taking place on mesopore walls. In this system (N_2 adsorption at 77 K) the presence of an H3 hysteresis indicates capillary condensation taking place in pores of width > 40 Å and the presence of macropores that are not entirely filled with condensed adsorbate.

Overall, the isotherms for these samples indicate structures that are mainly mesoporous, with small, but varying proportions of both micro and macroporosity. The samples show low overall N_2 uptake, suggesting that surface areas are low, although the presence of meso and macropores may result in a large pore volume.

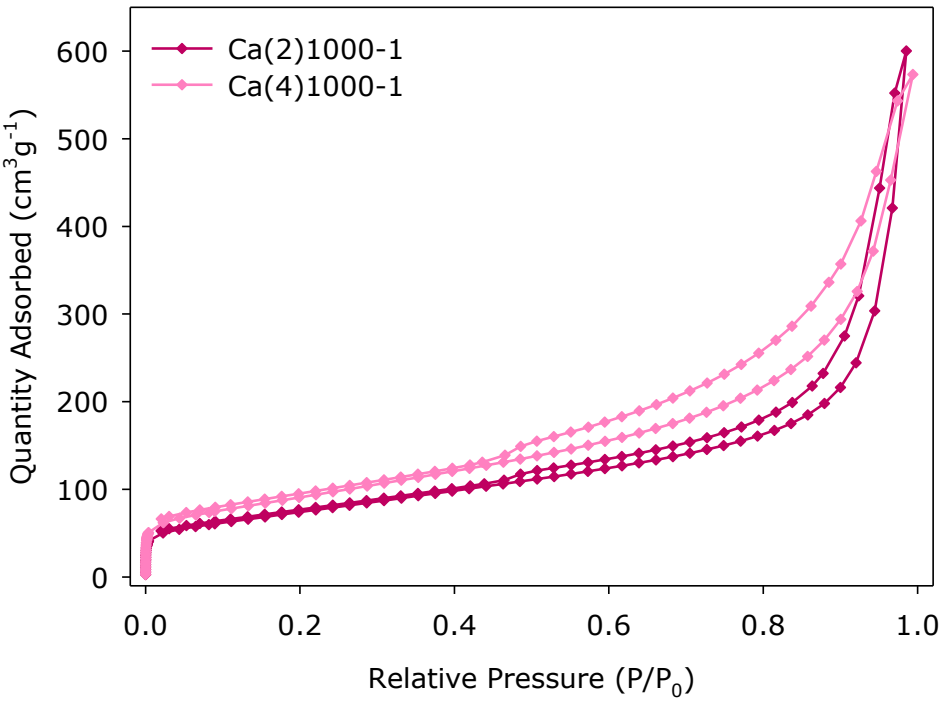

Figure 5.10. Sorption isotherms for samples activated at 1000 °C

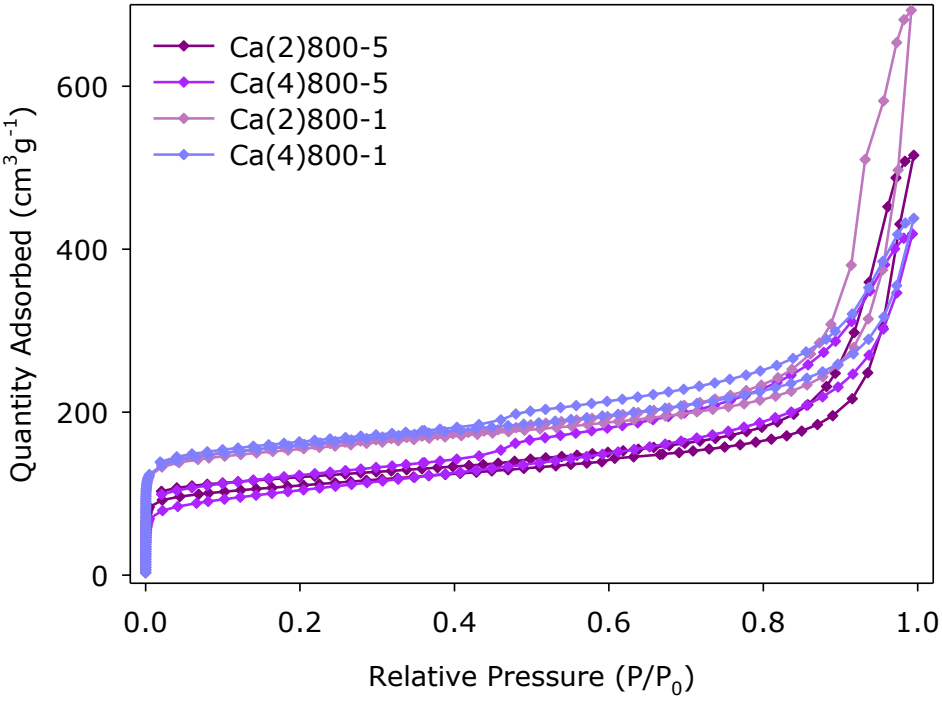

Figure 5.11. Sorption isotherms for samples activated at 800 °C

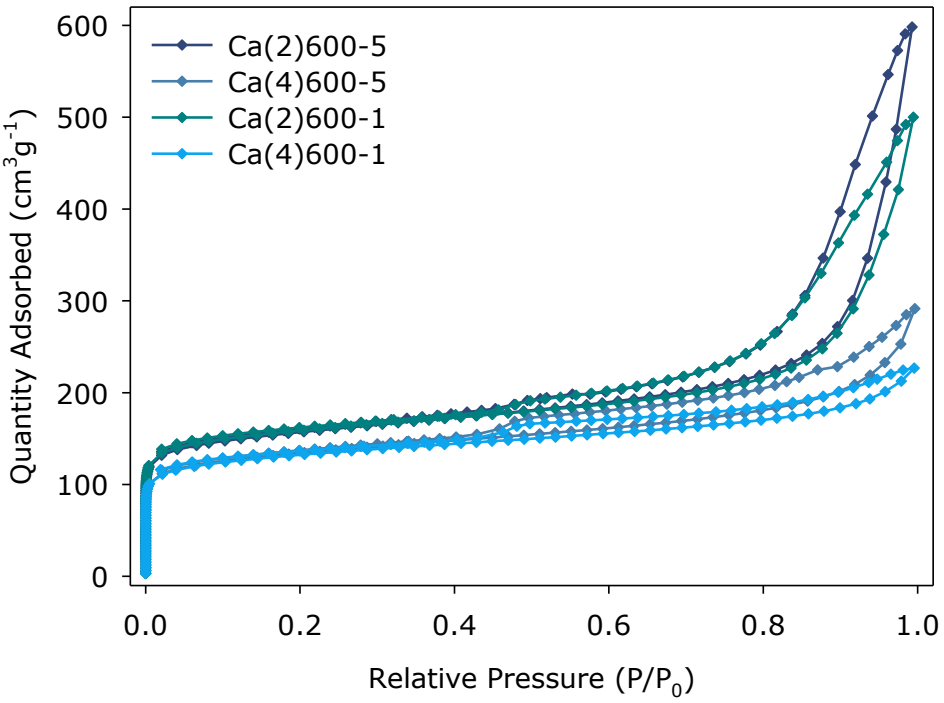

Figure 5.12. Sorption isotherms for samples activated at 600 °C

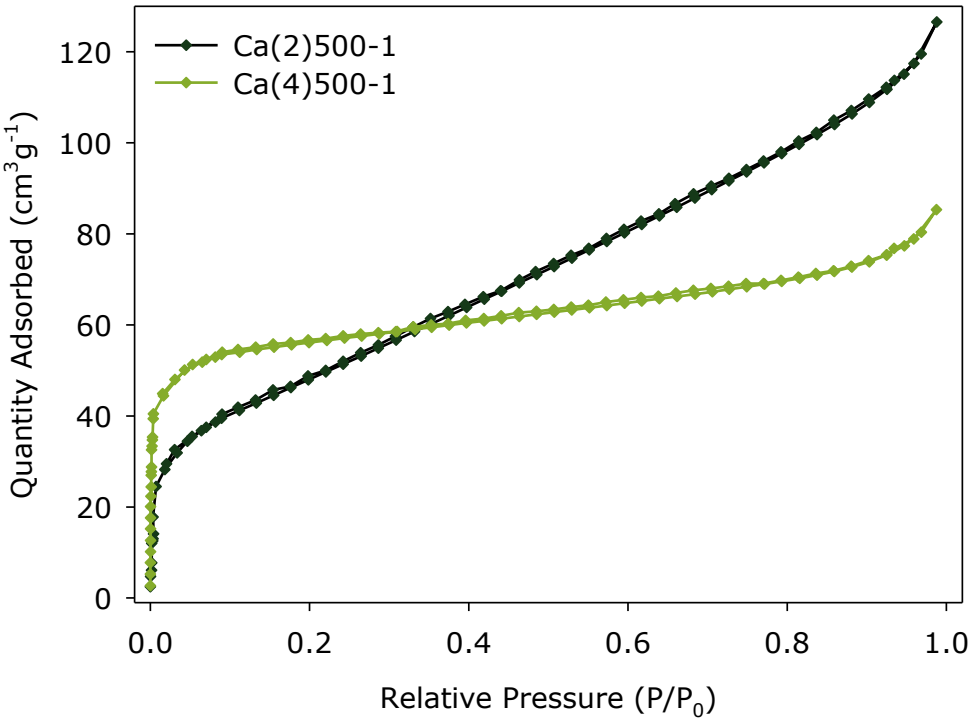

Figure 5.13. Sorption isotherms for samples activated at 500 °C

Samples activated at 600 °C (Fig. 5.12) show some degree of type I characteristics, indicating a greater presence of micropores. These samples, along with Ca(2)800-1 and Ca(4)800-1 exhibit a higher uptake of N_2 at very low relative pressure (all absorb > 100 cm^3 g^{-1} before the occurrence of the first knee) than samples activated under harsher conditions (those activated at 1000 °C as well as Ca(2)800-5 and Ca(4)800-5). The samples activated under harsher conditions would therefore be expected to possess a greater proportion of mesoporosity than those activated under gentler conditions.

Samples activated at 500 °C (Fig. 5.13) exhibit very low N_2 uptake and therefore they can be assumed to possess very low surface area and pore volume. The appearance of both type I and type II characteristics indicates mainly macro/non-porous materials with the presence of a very small proportion of micropores; overall, a very under-developed pore structure.

It is suggested from the N_2 sorption isotherms that activation of hydrochar with $Ca(OH)_2$ produces mainly mesoporous carbons with poorly developed porosity.

4. 6. Textural Properties; Surface Area and Pore Volume

The surface area and pore volume data, calculated from the N_2 sorption isotherms, are displayed below in Tables 5.3 and 5.4. Samples activated at both 500 and 1000 °C show the lowest surface areas of the set of between 173 and 313 $m^2\ g^{-1}$. Samples activated at 500 °C also show the lowest pore volume of the sample set, of 0.20 and 0.13 $cm^3\ g^{-1}$ for Ca(2)500-1 and Ca(4)500-1 respectively. It is clear that activation with $Ca(OH)_2$ at 500 °C results in poor pore development; few reactions occurring between the activating agent and the carbon skeleton results in little evolution of gases such as CO_2 and therefore only a small amount of pore creation. This low level of porosity was assumed from analysis of the N_2 sorption isotherms (Fig. 5.13) and as a result, associated micropore data was unable to be recorded for Ca(2)500-1.

Although having low surface area, samples activated at 1000 °C exhibit among the highest pore volumes, of 0.93 and 0.97 $cm^3\ g^{-1}$ for Ca(2)1000-1 and Ca(4)1000-1 respectively. This suggests mainly mesoporous structures, in line with analysis of the N_2 sorption isotherms (Fig. 5.10). Micropore data was too low to be recorded for both samples, further supporting the suggestion of highly mesoporous structures. It is clear that activation with Ca(OH)2 at 1000 °C leads to excessive, 'run-

Table 5.3. Surface area of all samples, calculated by BET theory. [a]Proportion of surface area arising from micropores, as a value and as a % of total surface area

Sample	Surface Area ($m^2\ g^{-1}$)	[a]Micropore Surface Area ($m^2\ g^{-1}$)
Ca(2)1000-1	255	N/A
Ca(4)1000-1	313	N/A
Ca(2)800-5	386	221 – 57%
Ca(4)800-5	363	116 – 32%
Ca(2)800-1	545	364 – 67%
Ca(4)800-1	562	362 – 64%
Ca(2)600-5	552	372 – 67%
Ca(4)600-5	472	317 – 67%
Ca(2)600-1	559	398 – 71%
Ca(4)600-1	465	330 – 71%
Ca(2)500-1	173	N/A
Ca(4)500-1	215	160 – 74%

away' reactions; a high volume of evolved gas creates very large pore channels and causes the collapse of smaller voids into larger pores.

Samples activated for 1 hr at 800 °C exhibit among the highest surface area and pore volume of the sample set, with

Table 5.4. Pore volume of all samples. [a]Proportion of pore volume arising from micropores, as a value and as a % of total pore volume

Sample	Pore Volume ($cm^3\ g^{-1}$)	[a]Micropore Volume ($cm^3\ g^{-1}$)
Ca(2)1000-1	0.93	N/A
Ca(4)1000-1	0.87	N/A
Ca(2)800-5	0.80	0.1 – 13%
Ca(4)800-5	0.65	0.05 – 8%
Ca(2)800-1	1.07	0.16 – 15%
Ca(4)800-1	0.68	0.16 – 24%
Ca(2)600-5	0.93	0.16 – 17%
Ca(4)600-5	0.45	0.14 – 31%
Ca(2)600-1	0.77	0.18 – 23%
Ca(4)600-1	0.35	0.15 – 43%
Ca(2)500-1	0.20	N/A
Ca(4)500-1	0.13	0.06 – 46%

surface areas of 545 and 562 $m^2\ g^{-1}$ and pore volumes of 1.07 and 0.68 $cm^3\ g^{-1}$ for Ca(2)800-1 and Ca(4)800-1 respectively. The two samples show reasonable micropore surface area of 67 and 64 %, however very low micropore volume of only 15 and 24 % for Ca(2)800-1 and Ca(4)800-1 respectively. This is in

line with analysis of the N_2 sorption isotherms (Fig. 5.11), suggesting the presence of both micro and mesopores.

Samples activated for 5 hrs at 800 °C show significantly lower surface areas than the equivalent samples activated for 1 hr, along with a reduction of microporosity (386 m^2 g^{-1}, 57 % and 363 m^2 g^{-1}, 32 % for Ca(2)800-5 and Ca(4)800-5 respectively). The reduction in pore volume is less significant, although micropore volume for samples activated for 5 hrs is very low; 13 and 8 % for Ca(2)800-5 and Ca(4)800-5 respectively. As with samples activated at 1000 °C, the textural data suggests that activation with $Ca(OH)_2$ under harsh conditions of 800 °C for 5 hours causes excessive and uncontrolled reactions with the carbon skeleton, resulting in high evolution of gases and therefore a highly mesoporous structure, with the possibility of the presence of some macropores.

Samples activated at 600 °C exhibit among the highest surface areas of the sample set, ranging between 465 and 559 m^2 g^{-1} with reasonable proportions of micropore surface area ranging between 67 and 71 %. The two samples activated at 600 °C with a char:$Ca(OH)_2$ ratio of 1:2 also exhibit high pore volume (0.77 and 0.93 cm^3 g^{-1} for Ca(2)600-1 and Ca(2)600-5 respectively), however low micropore volume of 23 and 17 % for Ca(2)600-1 and Ca(2)600-5 respectively. The equivalent

samples activated with a char:$Ca(OH)_2$ ratio of 1:4 exhibit a significantly lower pore volume (0.35 and 0.45 cm^3 g^{-1} for Ca(4)600-1 and Ca(4)600-5 respectively) although the reduction of micropore volume is less significant. It is clear that activation with $Ca(OH)_2$ at 600 °C develops mainly mesoporous carbons.

Overall, some of the samples have a considerable degree of microporosity that contributes to the total surface area, however the majority of pore volume arises from mesopores. This confirms analysis of the N_2 sorption isotherms of mainly mesoporous structures with varying degrees of microporosity.

5. 4. 7. Textural Properties; Pore Size Distributions

Pore size distributions (PSDs) and pore maxima values for all samples were calculated using non-local density functional theory and are displayed below in Figures 5.14 – 5.21 and Table 5.5. Figures show pore width of up to both 40 and 1000 Å to provide analysis of the micro, meso and macropore regions. As predicted from isotherm, surface area and pore volume analysis, the samples all show mainly mesoporous structures with varying degrees of both micro and macroporosity. The PSDs for samples activated at 1000 °C are shown in Figures 5.14 and 5.15. In both cases, the majority of the pore volume arises from large mesopores and small macropores, ranging between ~ 200 and 700 Å. Mesopore maxima are located at 400 and 272 Å for Ca(2)1000-1 and Ca(4)1000-1 respectively. Both samples show macropore maxima at 503, 685 and 862 Å. Within the micropore region, both samples show maxima at 5.9 and 11.8 Å, an indication of the collapse of smaller pores into larger pores.

The PSDs for samples activated at 800 °C are shown in Figures 5.16 and 5.17. Again, the majority of pore volume arises from pores of width ~ 200 to 700 Å. All 4 samples show pore maxima at 273 and 504 Å. Ca(2)800-1 and Ca(4)800-1 show pore maxima

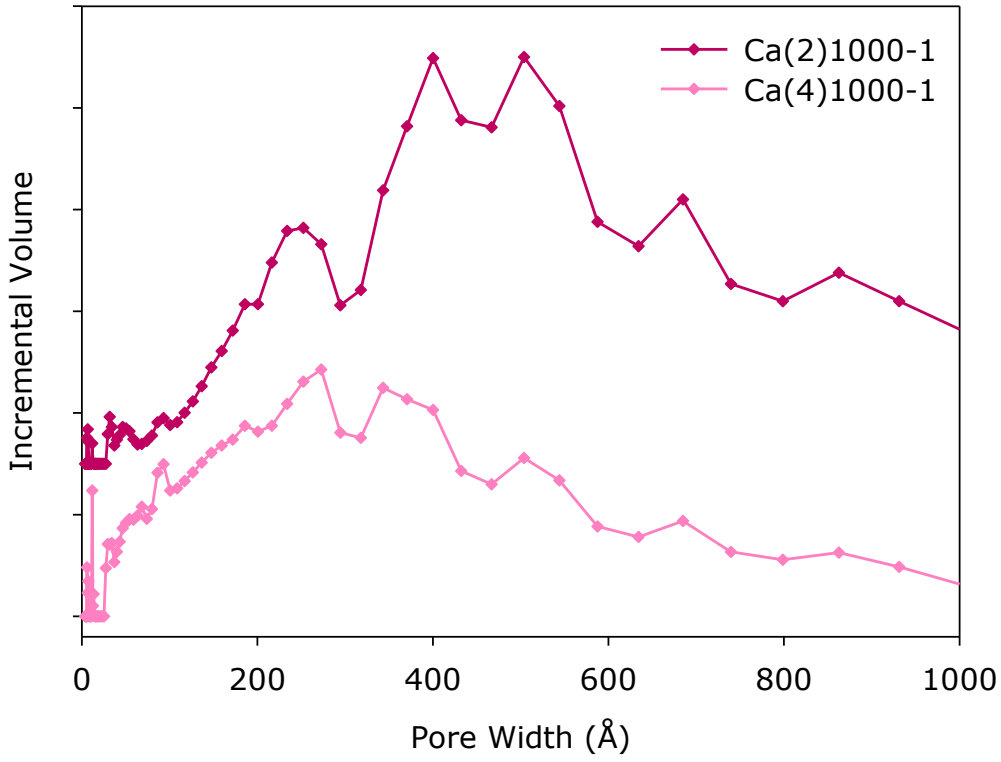

Figure 5.14. PSD up to 1000 Å of samples activated at 1000 °C

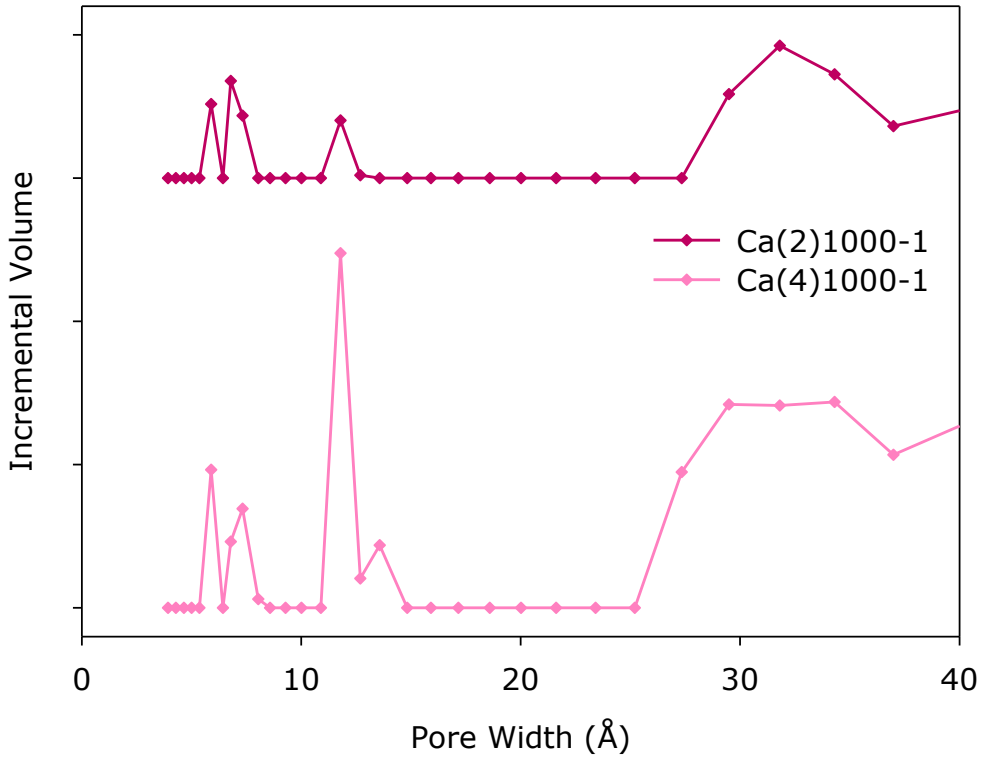

Figure 5.15. PSD up to 40 Å of samples activated at 1000 °C

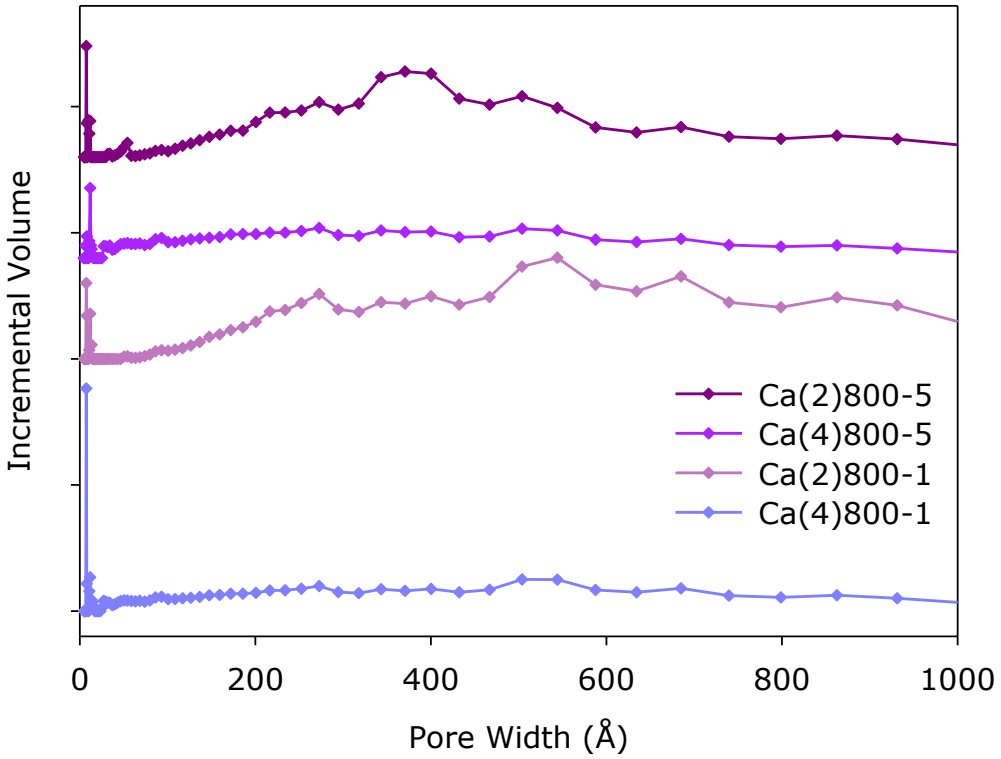

Figure 5.16. PSD up to 1000 Å of samples activated at 800 °C

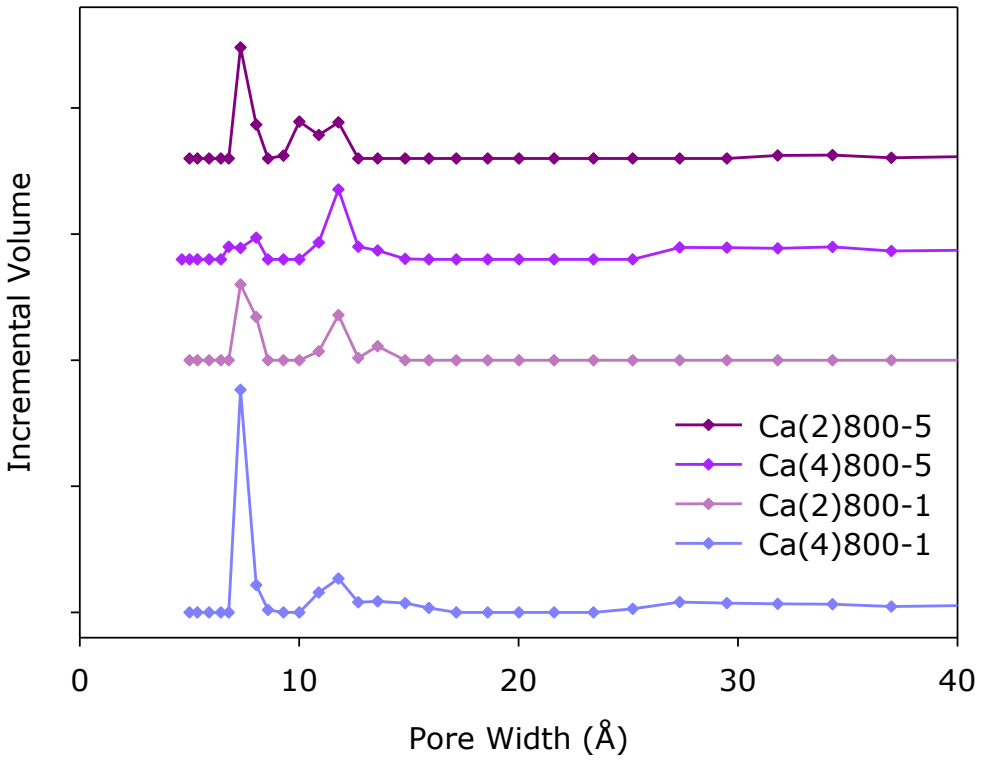

Figure 5.17. PSD up to 40 Å of samples activated at 800 °C

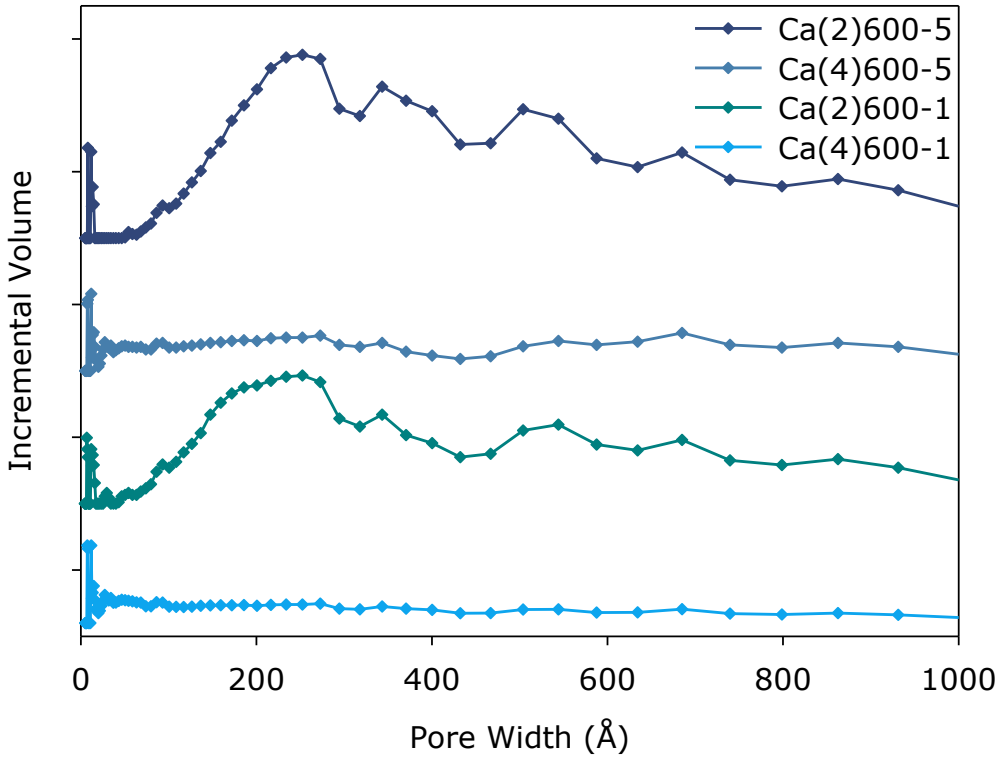

Figure 5.18. PSD up to 1000 Å of samples activated at 600 °C

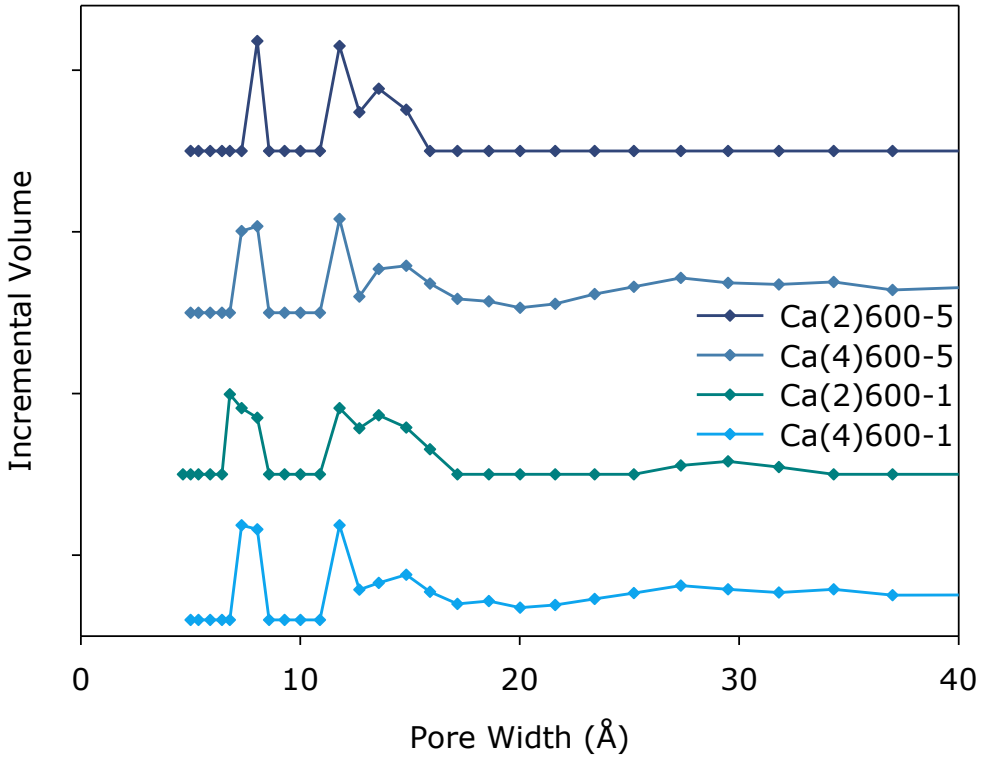

Figure 5.19. PSD up to 40 Å of samples activated at 600 °C

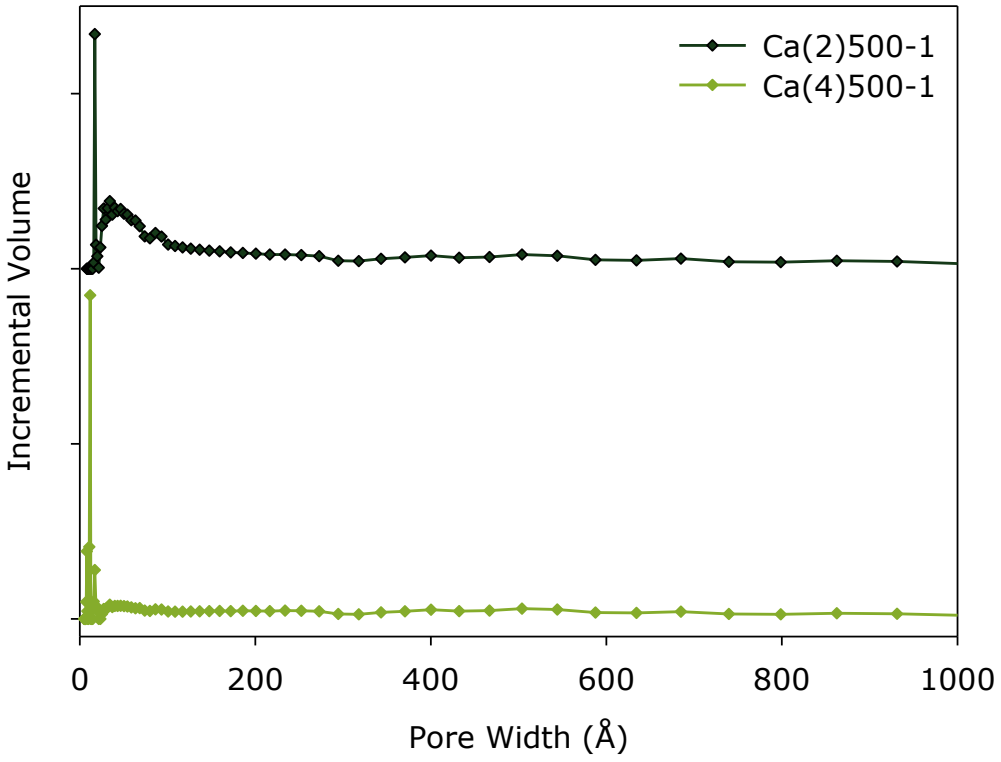

Figure 5.20. PSD up to 1000 Å of samples activated at 500 °C

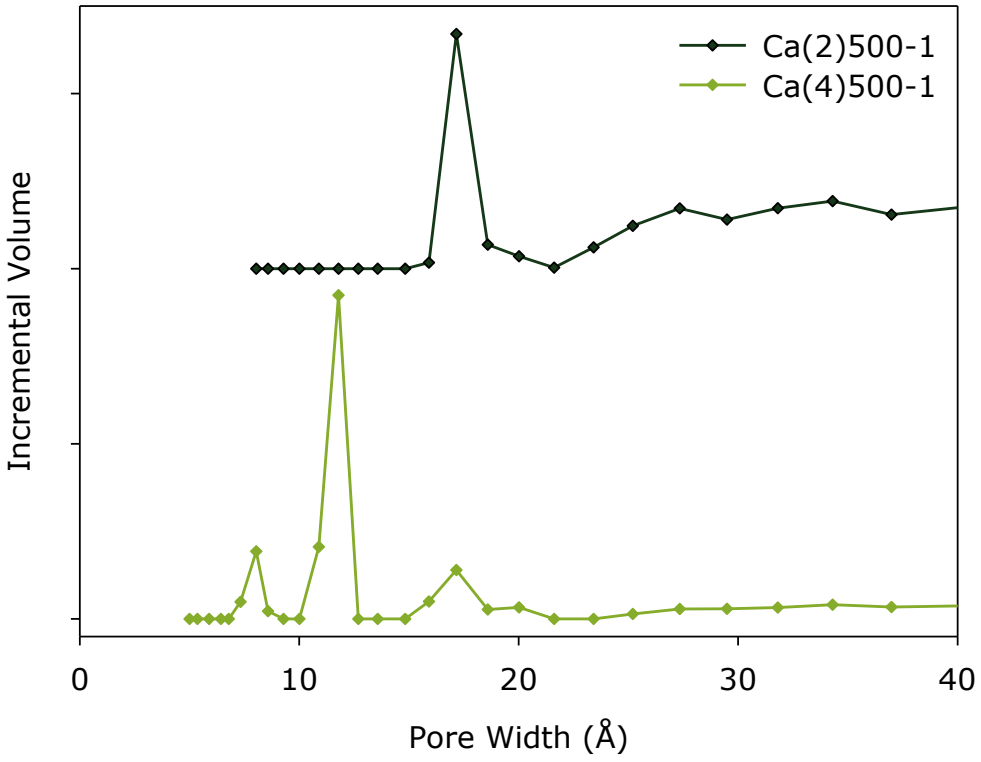

Figure 5.21. PSD up to 40 Å of samples activated at 500 °C

Table 5.5. PSD maxima of activated samples, obtained from NLDFT analysis

Sample	Pore Maxima (Å)		
	< 20 Å	**20 – 500 Å**	**> 500 Å**
Ca(2)1000-1	5.9/6.8/11.8	252/400	503/685/868
Ca(4)1000-1	5.9/7.3/11.8/13.6	272/343	503/685/868
Ca(2)800-5	7.3/10.0/11.8	217/273/370	504/685
Ca(4)800-5	6.8/8.0/11.8	273	504
Ca(2)800-1	7.3/11.8	273/400	504/544/692
Ca(4)800-1	7.3/11.8	273	504/544/685
Ca(2)600-5	8.0/11.8/13.6	253/343	504/685/862
Ca(4)600-5	7.3/8.0/11.8/13.6	273	504/685/862
Ca(2)600-1	6.8/8.0/11.8/13.6	253/343	544/685/862
Ca(4)600-1	7.3/8.0/11.8/14.8	273/343	504/544/685
Ca(2)500-1	17.2	253/400	504/685/862
Ca(4)500-1	8.0/11.8/17.2	253/400	504/685/862

at 544 Å, which suggests the collapse of pores of width 273 Å. Within the micropore region, all samples show significant pore volume at 7.3 Å (with the exception of Ca(4)800-5) and 11.8 Å.

The PSDs for samples activated at 600 °C are shown in Figures 5.18 and 5.19. Again, most of the pore volume arises from pores of width ~ 200 to 700 Å, with significant pore volume seen at 343, 544, 685 and 862 Å. As before, the large pore volume at 343 and 685 Å is evidence of pore collapse. Within the micropore region, all samples show pore maxima at 8.0 and 11.8 Å. All samples with the exception of Ca(4)600-1 also show pore maxima at 13.6 A.

The PSDs for samples activated at 500 °C are shown in Figures 5.20 and 5.21. As seen in Table 5.4 these two samples possess very low pore volume. Both samples share small pore maxima at 253, 400, 504, 685 and 862 Å, with the presence of pore volume at 253 and 504 Å indicating pore collapse. The samples show very little pore volume in the micropore region, with only Ca(4)500-1 possessing any pores of width < 17.2 Å.

Overall, the lack of micropore volume, especially in the 6 – 8 Å region, suggest that CO_2 uptake capacity at ≤ 1 bar would be poor, although the presence of larger meso and small macropores may result in improved performance at higher CO_2 pressures.

5. 4. 8. CO_2 Uptake Analysis

The CO_2 uptake capabilities of the carbon samples were analysed gravimetrically at 25 °C, over a pressure range of 0 – 40 bar. The adsorption isotherms up to 1 bar and 40 bar are shown below in Figures 5.22 – 5.29. The molar uptakes for the samples at a range of pressures is displayed in Table 5.6. It is important to analyse CO_2 uptake capabilities at very low pressure of 0.15 bar, to simulate typical conditions of a post-combustion flue gas stream. Analysis at 1 bar gives further information about low pressure uptake, while analysis at 20 and 40 bar provides uptake information at medium and high pressure respectively.

CO_2 uptake is low across all pressures, which is to be expected due to the low surface areas and in some cases, low pore volumes of the sample set. Samples activated at 500 °C exhibited the lowest CO_2 uptake capacity. This can be attributed to Ca(2)500-1 and Ca(4)500-1 possessing the two lowest surface areas (173 and 215 $m^2\ g^{-1}$ respectively) and pore volumes (0.20 and 0.13 $cm^3\ g^{-1}$ respectively) of the sample set.

Samples activated at 1000 °C also show low CO_2 uptake across all pressures, although they perform better at higher pressures (≥ 20 bar) than the samples activated at 500 °C.

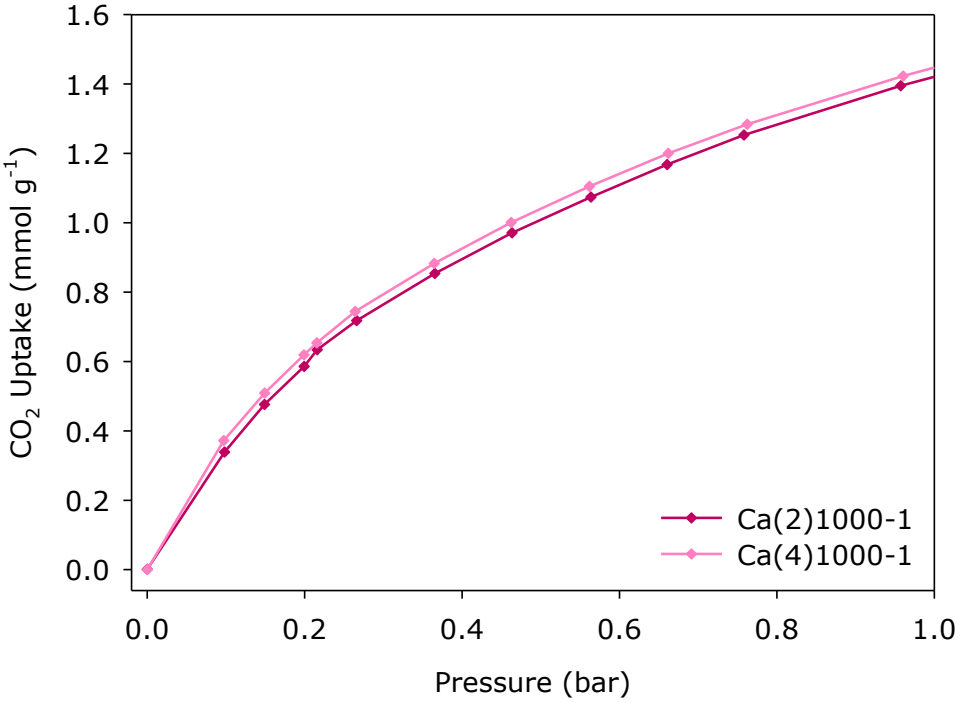

Figure 5.22. CO_2 uptake up to 1 bar for samples activated at 1000 °C

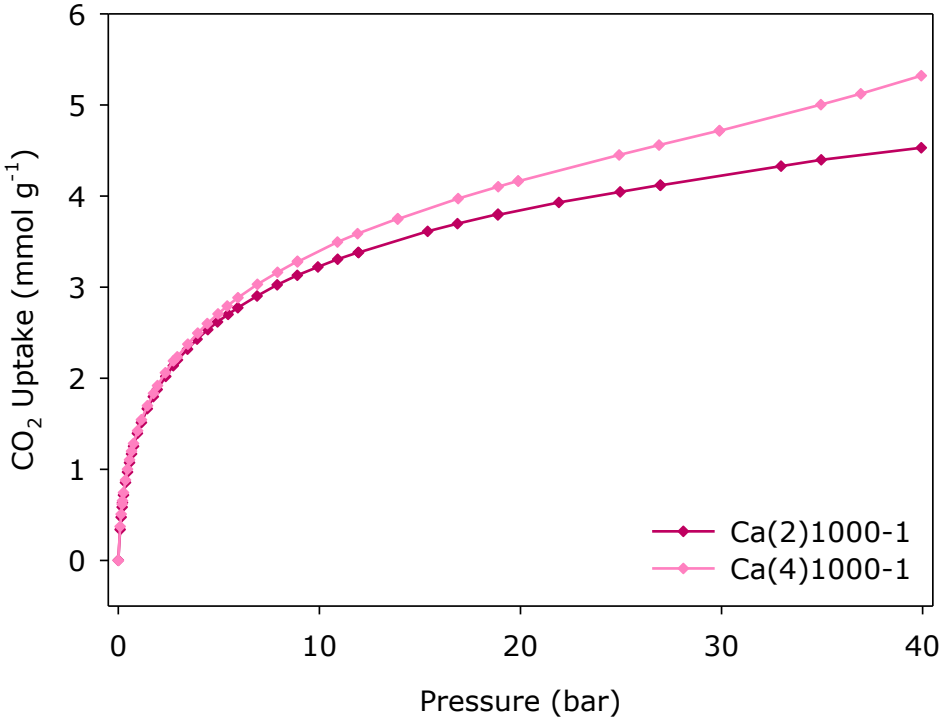

Figure 5.23. CO_2 uptake up to 40 bar for samples activated at 1000 °C

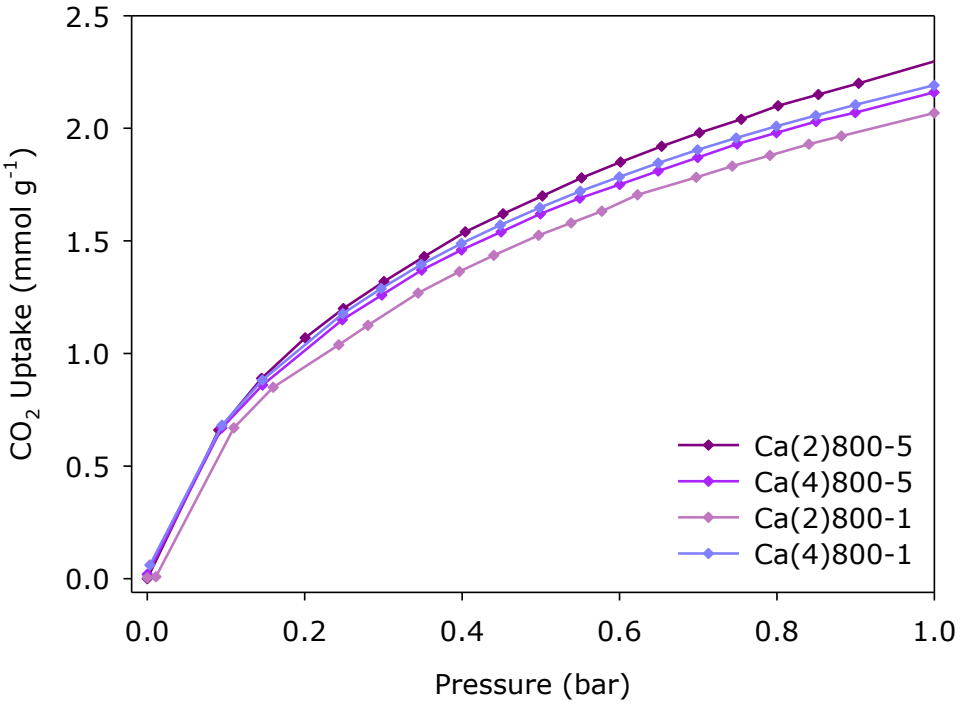

Figure 5.24. CO_2 uptake up to 1 bar for samples activated at 800 °C

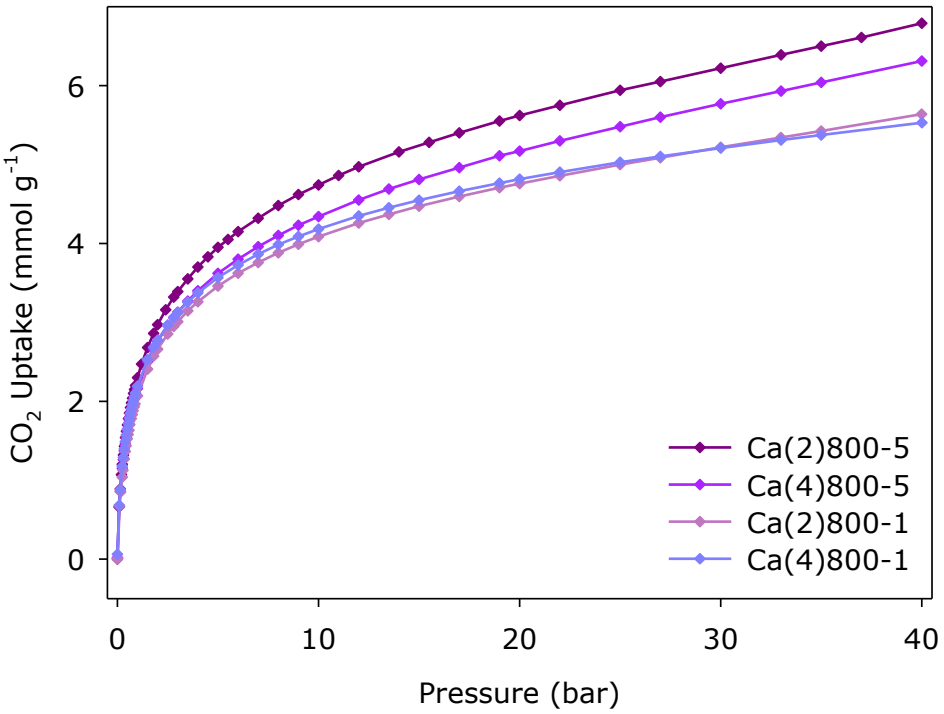

Figure 5.25. CO_2 uptake up to 40 bar for samples activated at 800 °C

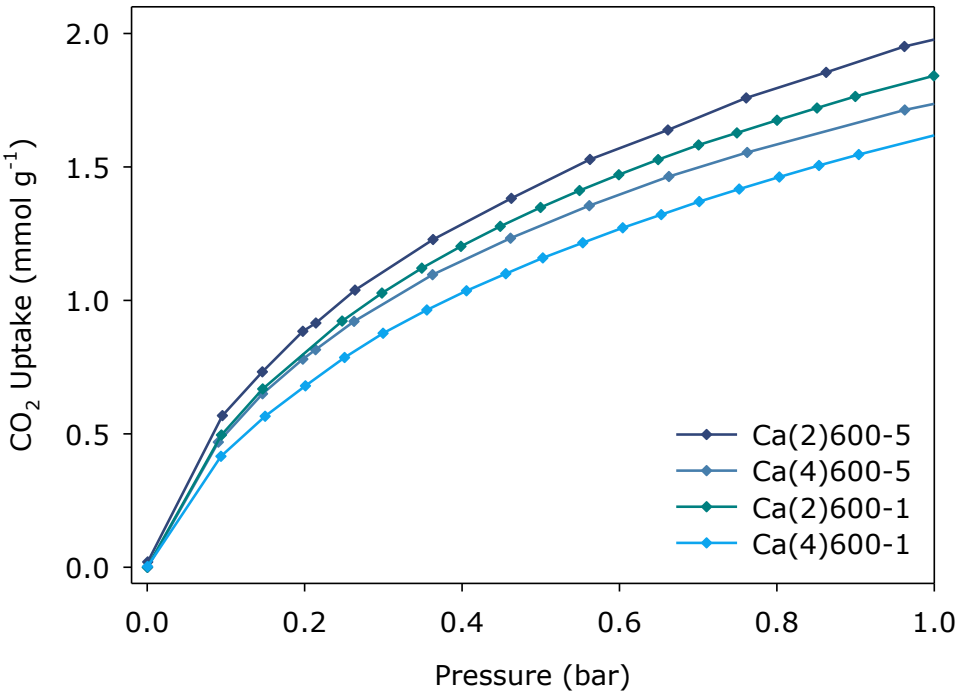

Figure 5.26. CO_2 uptake up to 1 bar for samples activated at 600 °C

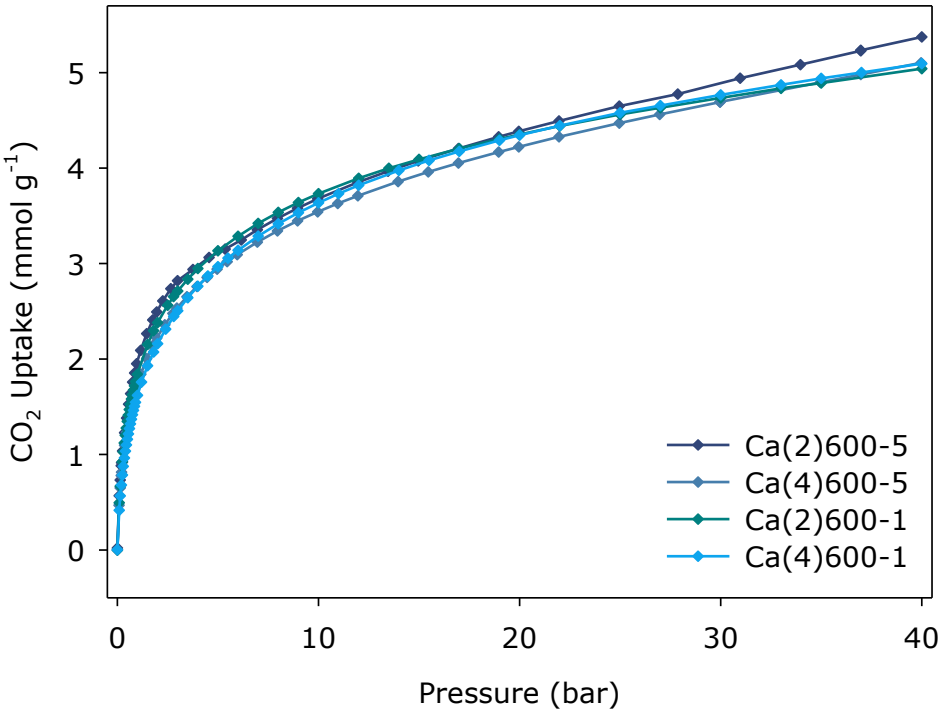

Figure 5.27. CO_2 uptake up to 40 bar for samples activated at 600 °C

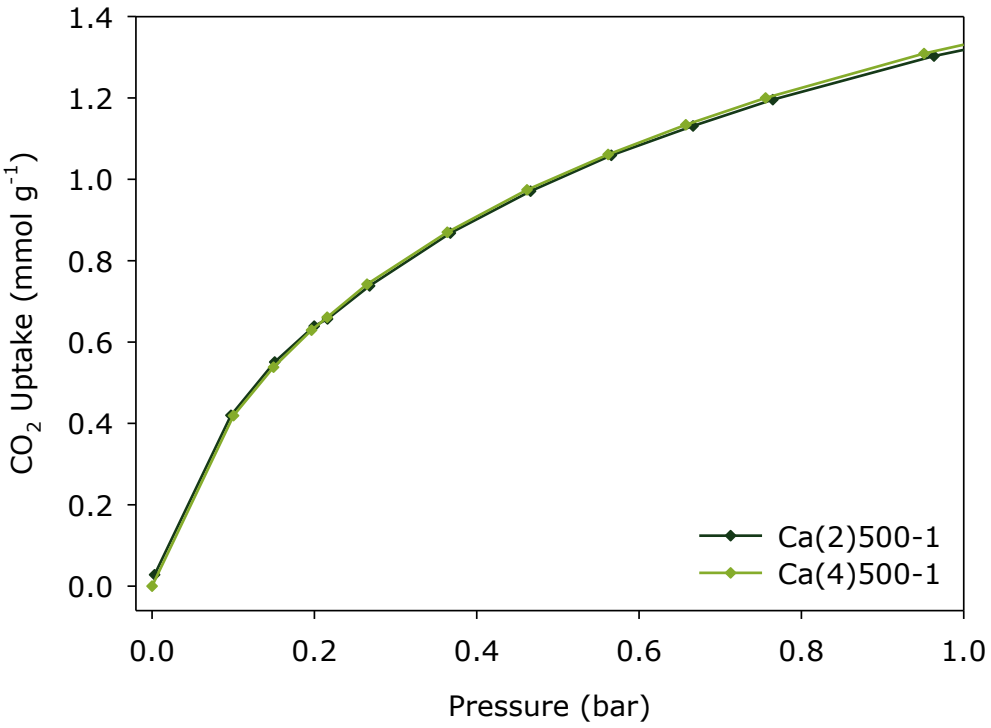

Figure 5.28. CO_2 uptake up to 1 bar for samples activated at 500 °C

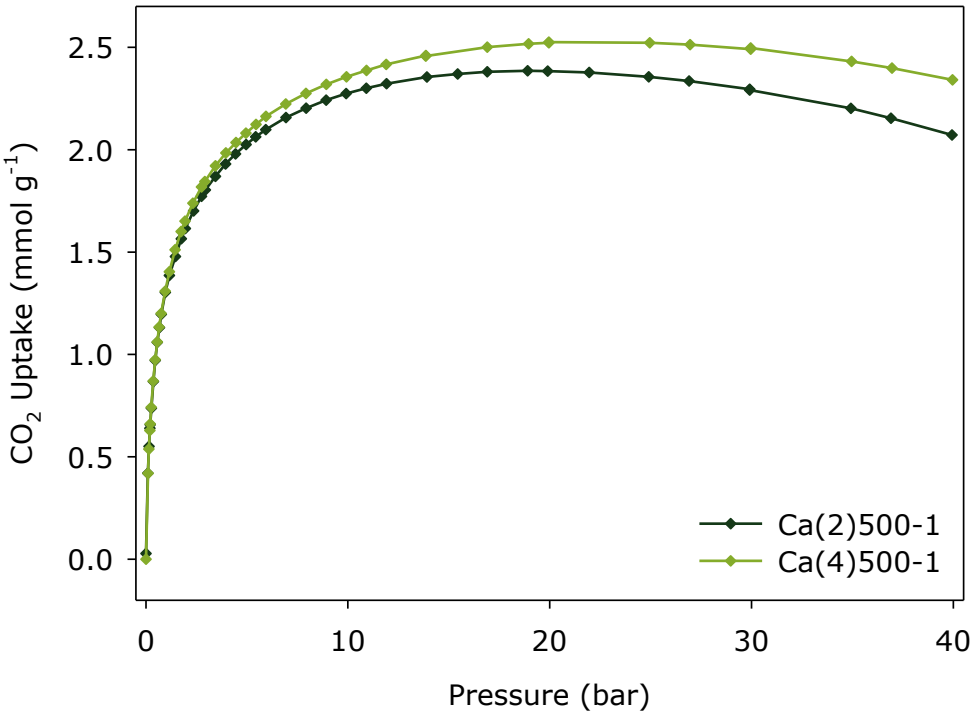

Figure 5.29. CO_2 uptake up to 40 bar for samples activated at 500 °C

Table 5.6. CO_2 uptake at 25 °C over a range of pressures of all samples

Sample	CO_2 Uptake (mmol g^{-1})			
	0.15 bar	**1 bar**	**20 bar**	**40 bar**
Ca(2)1000-1	0.5	1.4	3.8	4.5
Ca(4)1000-1	0.5	1.4	4.2	5.3
Ca(2)800-5	0.9	2.3	5.6	6.8
Ca(4)800-5	0.9	2.2	5.2	6.3
Ca(2)800-1	0.8	2.1	4.8	5.6
Ca(4)800-1	0.9	2.2	4.8	5.5
Ca(2)600-5	0.7	2.0	4.4	5.4
Ca(4)600-5	0.7	1.7	4.2	5.1
Ca(2)600-1	0.7	1.8	4.4	5.0
Ca(4)600-1	0.6	1.6	4.4	5.1
Ca(2)500-1	0.6	1.3	2.4	2.1
Ca(4)500-1	0.5	1.3	2.5	2.3

Ca(2)1000-1 and Ca(4)1000-1 possess low surface areas (255 and 313 m^2 g^{-1} respectively), but among the highest pore volumes (0.93 and 0.87 cm^3 g^{-1} respectively). The proportion of microporosity was unable to be recorded for these samples, suggesting it was too low to be accurately measured. PSDs (Fig. 5.14) confirm that the structures are dominated by large mesopores and macropores in the range 200 – 800 Å. This pore

structure accounts for low CO_2 uptake at low pressures (≤ 1 bar), but improved performance at higher pressures (≥ 20 bar).

Samples activated at 800 °C show the best CO_2 uptake of the sample set, higher than that of samples activated at 600 °C. Samples activated at 800 °C exhibit higher CO_2 uptake than equivalent samples activated at 600 °C in all cases. Samples in the 800 series have lower surface areas than equivalent samples in the 600 series in all cases, except for when using activation conditions of (4)-1 (char:$Ca(OH)_2$ ratio of 1:4, duration of 1 hr), as seen in Table 5.3. However, samples in the 800 series have larger pore volumes than equivalent samples in the 600 series in all cases, except for when using activation conditions of (2)-5 (char:$Ca(OH)_2$ ratio of 1:2, duration of 5 hrs), as seen in Table 5.4. In general, this results in samples in the 800 series having more meso/macroporous structures than equivalent samples in the 600 series. This is also indicated by the microporosity calculations and the PSDs (Tables 5.3 and 5.4, Fig.'s 5.16 – 5.19). This explains the improved adsorbance of samples activated at 800 °C at higher pressures of ≥ 20 bar.

In order to account for the uptake capacity of samples activated at 800 °C at lower pressures (≤ 1 bar), it is necessary to analyse the micropore region. For samples in the 800 series, microporosity is distributed across a pore maxima range of 6.8

– 11.8 Å, while for samples in the 600 series, the distribution is broader, extending 6.8 – 14.8 Å (Fig.'s 5.17 and 5.19). Therefore, the 800 series has a higher proportion of smaller micropores, which may be the reason for higher CO_2 uptake at low pressures ≤ 1 bar.

Overall, low CO_2 uptake exhibited across all pressures can be attributed to the low levels of porosity of the sample set. Low proportions of microporosity result in low CO_2 uptake at pressures of ≤ 1 bar. High uptake at pressures ≥ 20 bar is not possible due to low surface area and overall porosity, resulting in a low number of adsorption sites. The best conditions for CO_2 uptake when activating with $Ca(OH)_2$ is a temperature of 800 °C for a duration of 5 hrs.

5. 4. 9. Selectivity Measurements

To further assess the effect of using $Ca(OH)_2$ as activating agent, the selectivity of the carbon samples for CO_2 over N_2 was measured. A typical flue gas stream from a coal or gas burning power station is composed of approximately 85% N_2 and 15% CO_2 at atmospheric pressure. Low concentrations of other components may be found, including steam, acids and metal contaminants.[39,40] For this reason, the Ideal Adsorbed Solution Theory (IAST) method of calculating selectivity was used, which estimates the relative uptake of two gases in a binary mixture. The equilibrium selectivity factor at 1 bar was also measured. The results of both selectivity calculations are shown below in Table 5.7. The low pressure CO_2 and N_2 adsorption isotherms are displayed in Appendix Figures 5.A2 to 5.A13.

The IAST selectivity factor ranges between 10 – 35. Samples which exhibited among the highest CO_2 uptake capacities, possess among the lowest selectivity factors, with Ca(2)800-5 having an IAST selectivity of 10. Conversely, samples with the smallest CO_2 uptake capacities exhibited the highest IAST selectivity factors; Ca(4)500-1, Ca(2)1000-1 and Ca(4)1000-1 have selectivities of 29, 30 and 35 respectively, all excellent values for porous carbons.[36]

Table 5.7. Selectivity of CO_2 over N_2. [a]Under flue gas conditions (85%N_2/15%CO_2) at 1 bar and 25°C, calculated from the IAST equation. [b]At 1 bar and 25 °C

Sample	IAST Selectivity Factor[a]	Equilibrium Selectivity Factor[b]
Ca(2)1000-1	30	14
Ca(4)1000-1	35	14
Ca(2)800-5	10	4
Ca(4)800-5	14	6
Ca(2)800-1	18	7
Ca(4)800-1	20	8
Ca(2)600-5	12	5
Ca(4)600-5	20	8
Ca(2)600-1	24	11
Ca(4)600-1	15	7
Ca(2)500-1	22	8
Ca(4)500-1	29	10

Equilibrium selectivity factors for porous carbons at 1 bar are commonly within the range of ~ 5 – 11.[6,41,42] In this study, the equilibrium selectivity ranges between 4 – 14. Again, selectivity generally decreases as CO_2 uptake capacity increases. Samples

activated at 500 °C have low surface areas and pore volumes, while samples activated at 1000 °C have low surface areas and low proportions of microporosity. These factors result in low levels of adsorption sites for low pressure (≤ 1 bar) uptake. As competition for adsorption sites is high, CO_2 is selectively adsorbed over N_2 due to stronger electrostatic forces between the carbon surface and the quadrupole moment of the CO_2 molecules. Therefore, selectivity for these samples is higher.

For samples activated at both 600 and 800 °C, surface area, pore volume and proportion of microporosity is generally higher, resulting in less competition for adsorption sites under low pressure (≤ 1 bar) conditions. Therefore, selectivity factors for these samples are lower.

5. 5. Conclusions

An investigation was carried out into the activating ability of $Ca(OH)_2$, as a less corrosive alternative to commonly used KOH. A series of porous carbons was prepared via activation of eucalyptus hydrochar with $Ca(OH)_2$ under a range of activation conditions.

Experimental yields were within the range of comparable materials produced through KOH activation of hydrochar. Therefore, when considering $Ca(OH)_2$ as a less corrosive alternative to KOH, there is no decrease in sample yield.

SEM imaging revealed that regardless of activation conditions, the carbon samples were comprised of irregular particles with rough, amorphous surfaces. $Ca(OH)_2$ is a gentler activating agent than KOH, resulting in areas of carbon where the structure of the parent char has been retained.

The presence of regular, char-like structures is also indicated by PXRD analysis. PXRD patterns showed that activation with $Ca(OH)_2$ produces reasonably porous carbons that still retain some degree of regular, graphitic-like structures.

N_2 sorption isotherms showed that samples possessed type IV(a) isotherms; mainly mesoporous structures with varying

degrees of both micro and macroporosity. H3 hystereses indicated the presence of some large macropores.

Analysis of textural properties (surface area, pore volume and PSDs) showed that surface area is generally low for porous carbons, ranging between 173 – 562 m^2 g^{-1} confirming underdeveloped pore structures. Pore volume and proportion of microporosity varies, confirming the varying degrees of micro and macroporosity throughout the sample set. There is no clear trend in porosity development when altering activation conditions, although activating with a char:$Ca(OH)_2$ ratio of 1:2 results in larger proportions of meso and macroporosity than when using a ratio of 1:4.

CO_2 uptake is representative of low pore development and was generally low across all pressures. Highest uptake was observed for samples with the most developed pore structures, regardless of pore size. Ca(2)800-5 showed the highest uptake of 2.3 mmol g^{-1} at 1 bar and 25 °C.

Selectivity varied and was also representative of low pore development. Selectivity for CO_2 over N_2 under both flue gas conditions and equilibrium at 1 bar was highest for samples with the lowest surface areas (those activated at 500 or 1000 °C).

Limited adsorption sites for low pressure uptake increases competition, which favours the more polar CO_2 molecules.

Overall, activating hydrochar with $Ca(OH)_2$ as a less corrosive alternative to KOH produces carbons with low levels of pore development. Pore structures are mainly mesoporous, with varying degrees of both micro and macroporosity. Results are unpredictable, with activating agent ratio having only slight effect on results and activation duration having little noticeable influence. Resulting pore structure is only significantly affected by activation temperature and does not follow a clear trend. Low levels of pore development result in poor CO_2 uptake performance across a range of pressures.

5. 6. Future Work

The aim of this study was to compare the performance of $Ca(OH)_2$ with the commonly used KOH as an activating agent. For this reason, samples were activated under conditions that are often used with KOH to achieve the best results.

It may be the case that $Ca(OH)_2$ performs better under conditions not studied in this investigation. Therefore, activating hydrochar under alternative conditions may reveal optimum conditions for $Ca(OH)_2$ activation. Using a higher ratio of activating agent and temperatures not used in this study, for example char:$Ca(OH)_2$ ratio of 1:6 and temperatures of 700 and 900 °C, may encourage more extensive pore development and therefore higher gas uptake capacities.

5. 7. References

1 E. Fitzer, K.-H. Kochling, H. P. Boehm and H. Marsh, *Pure Appl. Chem.*, 1995, **67**, 473–506.

2 M. Sevilla and R. Mokaya, *Energy Environ. Sci.*, 2014, **7**, 1250–1280.

3 C. R. Correa and A. Kruse, *Materials (Basel).*, 2018, **11**, 1568.

4 J. Wang and S. Kaskel, *J. Mater. Chem.*, 2012, **22**, 23710–23725.

5 M. A. Lillo-Rodenas, J. Juan-Juan, D. Cazorla-Amor and A. Linares-Solano, *Carbon N. Y.*, 2004, **42**, 1371–1375.

6 M. Sevilla and A. B. Fuertes, *J. Colloid Interface Sci.*, 2012, **366**, 147–154.

7 S. Deng, H. Wei, T. Chen, B. Wang, J. Huang and G. Yu, *Chem. Eng. J.*, 2014, **253**, 46–54.

8 E. Masika and R. Mokaya, *Prog. Nat. Sci.*, 2013, **23**, 308–316.

9 A. Ganesan and M. M. Shaijumon, *Microporous Mesoporous Mater.*, 2016, **220**, 21–27.

10 Y. Kim, B. Lee, H. Suezaki, T. Chino, Y. Abe, T. Yanagiura, K. Chul and M. Endo, *Carbon N. Y.*, 2006, **44**, 1592–1595.

11 Z. Ma, Z. Zhang, Y. Qu, F. Lai, Q. Li, X. Wu, Q. Wu, Q. Li, H. Wang and Y. Huang, *Microporous Mesoporous Mater.*, 2019, **281**, 50–56.

12 H. Tamai, U. Nobuaki and H. Yasuda, *Mater. Chem. Phys.*, 2009, **114**, 10–13.

13 C. Liang, Z. Li and S. Dai, *Angew. Chemie - Int. Ed.*, 2008, **47**, 3696–3717.

14 J. Galán, A. Rodríguez, J. M. Gómez, S. J. Allen and G. M. Walker, *Chem. Eng. J.*, 2013, **219**, 62–68.

15 G. Yang, L. Tang, G. Zeng, Y. Cai, J. Tang, Y. Pang, Y. Zhou, Y. Liu, J. Wang, S. Zhang and W. Xiong, *Chem. Eng. J.*, 2015, **259**, 854–864.

16 A. Ahmadpour and D. D. Do, *Carbon N. Y.*, 1996, **34**, 471–479.

17 M. Molina-Sabio and F. Rodriguez-Reinoso, *Colloids Surfaces A Physicochem. Eng. Asp.*, 2004, **241**, 15–25.

18 M. Jagtoyen and F. Derbyshire, *Carbon N. Y.*, 1998, **36**, 1085–1097.

19 M. Sevilla, A. B. Fuertes and R. Mokaya, *Energy Environ. Sci.*, 2011, **4**, 1400.

20 M. Yuan, Y. Kim and C. Q. Jia, *Can. J. Chem. Eng.*, 2012, **90**, 1472–1478.

21 M. A. Lillo-Rodenas, D. Cazorla-Amoros and A. Linares-Solano, *Carbon N. Y.*, 2003, **41**, 267–275.

22 H. Teng and L. Hsu, *Ind. Eng. Chem. Res.*, 1999, **38**, 2947–2953.

23 M. Sevilla, G. A. Ferrero and A. B. Fuertes, *Carbon N. Y.*, 2017, **114**, 50–58.

24 J. Deng, T. Xiong, F. Xu, M. Li, C. Han, Y. Gong, H. Wang and Y. Wang, *Green Chem.*, 2015, **17**, 4053–4060.

25 M. Sevilla and A. B. Fuertes, *ChemSusChem*, 2016, **9**, 1–10.

26 A. Volperts, A. Plavniece, G. Dobele, A. Zhurinsh, I. Kruusenberg, K. Kaare, J. Locs, L. Tamasauskaite-Tamasiunaite, E. Norkus and I. Kruusenberg, *Renew. Energy*, 2019, **141**, 40–45.

27 G. Dobele, T. Dizhbite, M. V Gil, A. Volperts and T. A. Centeno, *Biomass and Bioenergy*, 2012, **46**, 145–154.

28 Y. V Tamarkina, L. A. Maslova, T. V Khabarova and V. A. Kucherenko, *Russ. J. Appl. Chem.*, 2008, **81**, 1167–1170.

29 M. Danish, R. Hashim, M. N. M. Ibrahim, M. Rafatullah, T. Ahmad and O. Sulaiman, *BioResources*, 2011, **6**, 3019–3033.

30 P. González-García, *Renew. Sustain. Energy Rev.*, 2018, **82**, 1393–1414.

31 M. Yang, L. Guo, G. Hu, X. Hu, L. Xu, J. Chen, W. Dai and M. Fan, *Environ. Sci. Technol.*, 2015, **49**, 7063–7070.

32 W. Sangchoom and R. Mokaya, *ACS Sustain. Chem. Eng.*, 2015, **3**, 1658–1667.

33 H. M. Coromina, D. A. Walsh and R. Mokaya, *J. Mater. Chem. A*, 2016, **4**, 280–289.

34 M. Sevilla and A. B. Fuertes, *Carbon N. Y.*, 2009, **47**, 2281–2289.

35 M. Sevilla and A. B. Fuertes, *Chem. A Eur. J.*, 2009, **15**, 4195–4203.

36 N. Balahmar, A. S. Al-jumialy and R. Mokaya, *J. Mater. Chem. A*, 2017, **5**, 12330–12339.

37 E. Hirst, A. Taylor and R. Mokaya, *J. Mater. Chem. A*, 2018, **6**, 12393–12403.

38 E. Haffner-Staton, N. Balahmar and R. Mokaya, *J. Mater. Chem. A*, 2016, **4**, 13324–13335.

39 R. Zhao, S. Deng, S. Wang, L. Zhao, Y. Zhang, B. Liu, H. Li and Z. Yu, *Appl. Therm. Eng.*, 2018, **128**, 818–829.

40 D. Bahamon, A. Díaz-Márquez, P. Gamallo and L. F.

Vega, *Chem. Eng. J.*, 2018, **342**, 458–473.

41 B. Adeniran, E. Masika and R. Mokaya, *J. Mater. Chem. A*, 2014, **2**, 14696.

42 M. Sevilla, C. Falco, M. Titirici and A. B. Fuertes, *RSC Adv.*, 2012, **2**, 12792–12797.

5. 8. Appendix

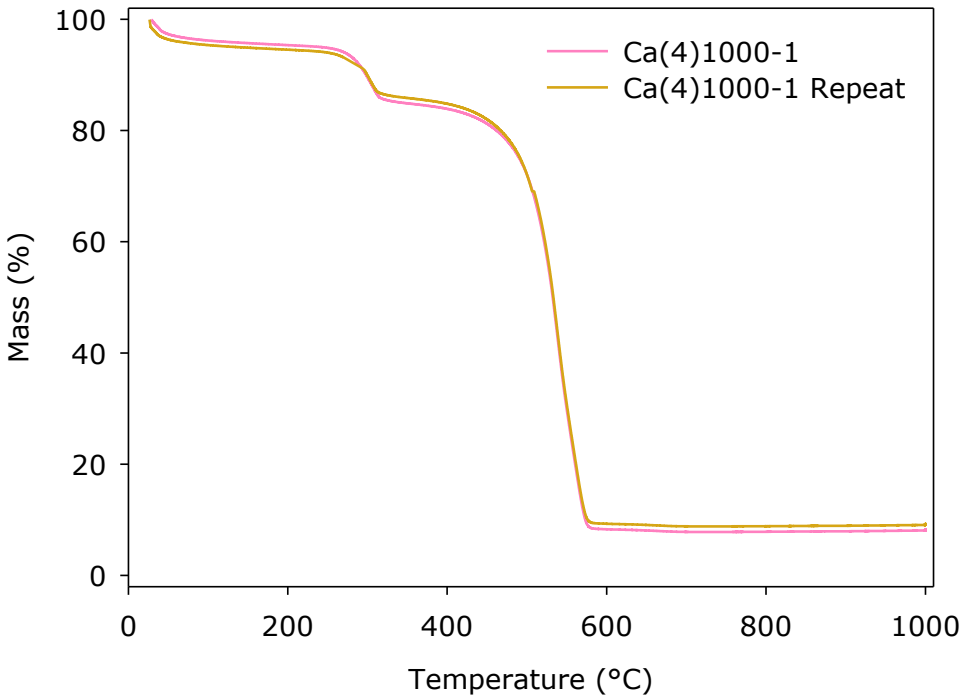

Figure 5.A1. Repeat TGA measurement of Ca(4)1000-1

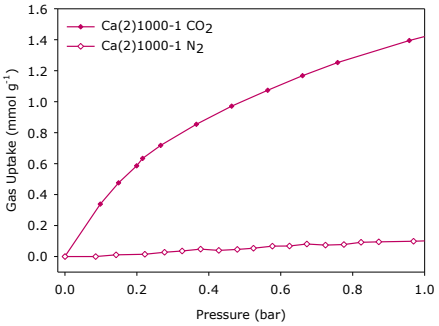

Figure 5.A2. CO_2 and N_2 uptake up to 1 bar at 25 °C of Ca(2)1000-1

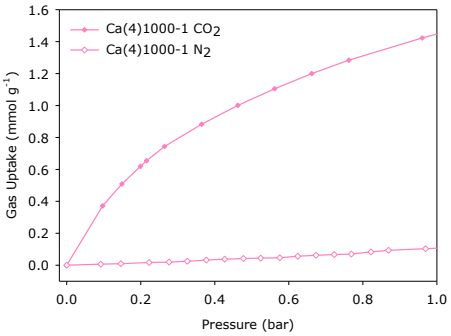

Figure 5.A3. CO_2 and N_2 uptake up to 1 bar at 25 °C of Ca(4)1000-1

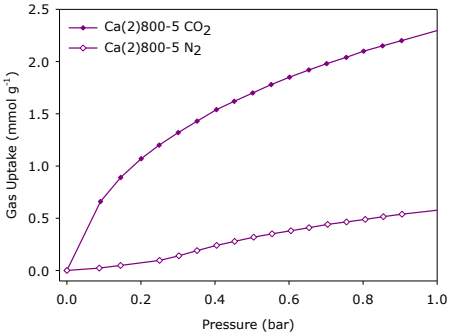

Figure 5.A4. CO_2 and N_2 uptake up to 1 bar at 25 °C of Ca(2)800-5

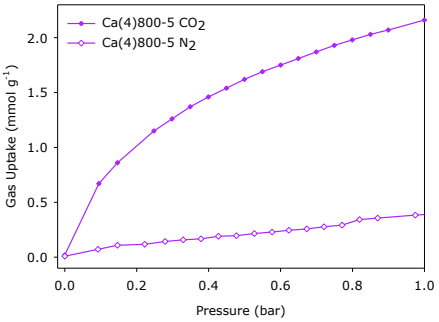

Figure 5.A5. CO_2 and N_2 uptake up to 1 bar at 25 °C of Ca(4)800-5

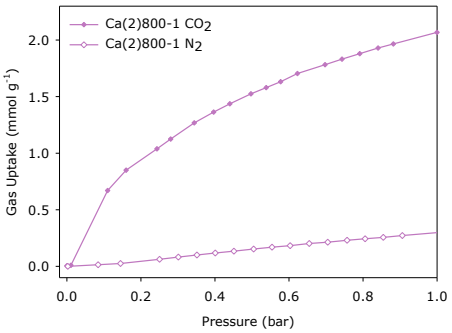

Figure 5.A6. CO_2 and N_2 uptake up to 1 bar at 25 °C of Ca(2)800-1

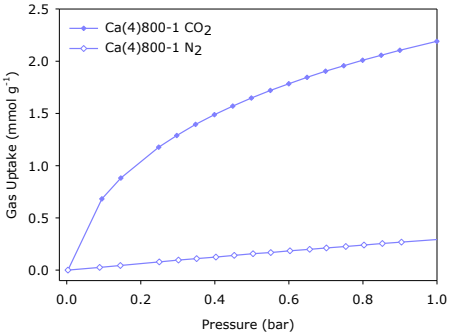

Figure 5.A7. CO_2 and N_2 uptake up to 1 bar at 25 °C of Ca(4)800-1

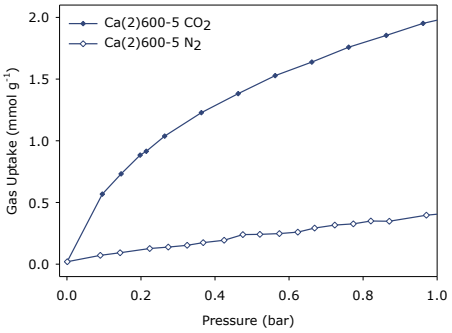

Figure 5.A8. CO_2 and N_2 uptake up to 1 bar at 25 °C of Ca(2)600-5

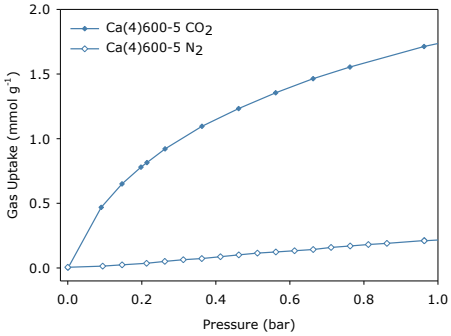

Figure 5.A9. CO_2 and N_2 uptake up to 1 bar at 25 °C of Ca(4)600-5

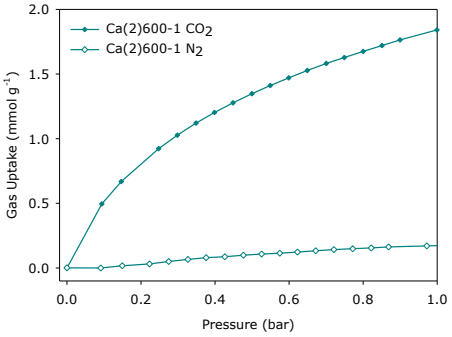

Figure 5.A10. CO_2 and N_2 uptake up to 1 bar at 25 °C of Ca(2)600-1

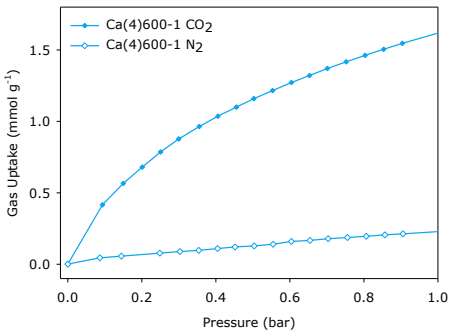

Figure 5.A11. CO_2 and N_2 uptake up to 1 bar at 25 °C of Ca(4)600-1

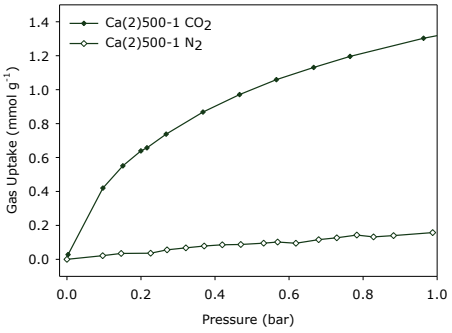

Figure 5.A12. CO_2 and N_2 uptake up to 1 bar at 25 °C of Ca(2)500-1

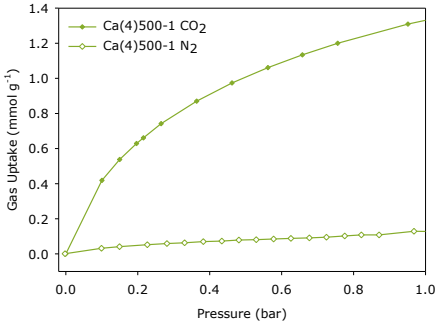

Figure 5.A13. CO_2 and N_2 uptake up to 1 bar at 25 °C of Ca(4)500-1

Chapter 6 – Investigating the Effects of Harsh Activation Conditions

6. 1. Abstract

The study reported in this chapter is an investigation into the effects of extreme activation conditions, including activation temperatures up to 1200 °C and activation duration up to 10 hrs. A further investigation was conducted into how potential negative effects of such conditions can be mitigated, such as a broad pore size distribution and low carbon yield. To tackle these issues, a carbon rich starting material, potassium hydrogen phthalate (KHP), previously shown to retain microporosity well, was chosen. A number of samples were activated directly from KHP alone, while others were activated alongside an additional carbon source. The carbon source used was either an airchar derived from spruce wood that in previous studies has been shown to retain microporosity well, or a traditional hydrochar derived from eucalyptus wood.

Extreme activating conditions up to 1200 °C and for up to 10 hrs produced a series of carbons with high surface area and pore volume, with a mixed proportion of both meso and microporosity, resulting in good CO_2 uptake across a range of pressures. The addition of a char during the activation process

was shown to produce high yielding, highly microporous carbons that exhibit good CO_2 uptake up to 1.2 mmol g^{-1} under flue gas conditions (0.15 bar). The char type added affected the textural properties of the carbons; adding hydrochar produced less developed, mesoporous carbons when compared with the addition of airchar.

6. 2. Introduction

In the synthesis of porous carbons, activation conditions such as activation temperature, time and activating agent, play a crucial role in the pore formation process. As a result, activated carbons are highly tailorable; activation conditions can be varied to produce a carbon with specific porosity and textural properties. As reported in many studies,[1–6] the general observed trend shows that as activation temperature, time and the ratio of activating agent is increased, more extensive activation occurs. Harsher activation conditions intensify reactions between a chemical activating agent and the carbon skeleton, increasing surface area, pore volume and broadening the pore size distribution (PSD) as wider pore channels are created and smaller pores collapse into larger pores.[1–6] As mentioned in previous chapters, in regard to low pressure CO_2 uptake ≤ 1 bar, a narrow PSD centred in the small micropore region (~ 6 – 8 Å) combined with a generous surface area and pore volume results in a greater uptake.[1,6–10] For this reason, many studies report results obtained under moderate conditions; activation temperature of ~ 800 °C, activation time of ~ 1 – 2 hrs and an activating agent to carbon ratio of ~ 2.[1,3,4,8,10–13] These can be regarded as 'standard conditions'.

The use of harsher and more extreme conditions is little reported in the literature, although it is important to understand the effect that such conditions have in order to acknowledge the full potential of the activated carbon field. Based on previous studies, the likely effects of harsh activation conditions are substantial surface areas and pore volumes, with little or no microporosity. Such structures, with large surface area and pore volume and therefore fast diffusion kinetics, can be used for applications such as electrode and supercapacitor materials,[14–16] gas storage and separation,[17–19] catalyst supports,[20–22] biomedical engineering[23–25] and pollutant removal.[26–28]

Extreme activation conditions may result in a decrease of porosity, as pore structures weaken and collapse due to prolonged etching of the carbon skeleton. This is likely to be accompanied by a severe reduction in carbon yield, as continued reactions of a chemical agent with the carbon skeleton result in the increased release of carbon in the form of CO_2 and CO.[1,6,11,29,30] The energy requirements of a synthesis method involving such activation conditions is another important consideration. The study reported here was an investigation into the effects of extreme activation conditions and how measures can be taken to mitigate the potential

negative effects, such as high mesoporosity and low carbon yield.

Firstly, a carbon rich starting material, potassium hydrogen phthalate (KHP) was chosen as it has been shown in previous studies to reliably produce activated carbons with high surface area and pore volume, while retaining a good proportion of microporosity.[31] KHP is an organic metal salt with a carbon content of 47 % and a C/K molar ratio of 7.8.

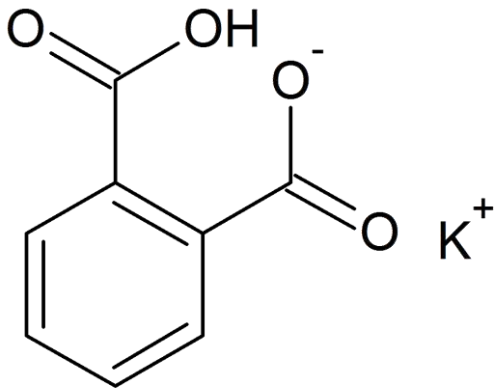

Figure 6.1. Potassium Hydrogen Phthalate (KHP)

This C/K ratio is high compared with conventional activation of hydrochar with KOH in a char:KOH weight ratio of 1:2, which is equivalent to a C/K molar ratio of 1.4. Due to the presence of both K and O, KHP is 'self-activating', therefore simplifying the activation process. KHP is also safe and non-reactive compared with KOH. Upon activation under standard conditions, KHP produces porous carbons with a carbon yield of ~ 17 %, similar

to that of hydrochar activated with KOH in a weight ratio of 1:2 under analogous conditions.[32]

KHP has been shown to produce activated carbons with high CO_2 uptake ability in previous studies. In 2014, Adeniran *et al*.[31] synthesised a family of microporous carbons through direct activation of KHP. The carbons produced had high surface area and pore volume of up to 2104 $m^2\ g^{-1}$ and 1.11 $cm^3\ g^{-1}$ respectively, with high corresponding proportions of microporosity of 86 and 74 % respectively, for a carbon sample activated at 900 °C for 2 hrs. This sample showed excellent CO_2 uptake at 20 bar and 25 °C of 12.7 mmol g^{-1}. Another sample, activated at 700 °C for 2 hrs exhibited a smaller surface area and pore volume of 795 $m^2\ g^{-1}$ and 0.44 $cm^3\ g^{-1}$ respectively, but larger corresponding proportions of microporosity (96 and 77 % respectively). This sample showed excellent CO_2 uptake at 25 °C and very low pressure of 0.15 bar of 1.7 mmol g^{-1}.[31] In 2016, Adeniran *et al*.[33] again directly activated KHP to produce similar results. An activation temperature of 700 °C and duration of 1 hr produced a carbon with surface area and pore volume up to 932 $m^2\ g^{-1}$ and 0.44 $cm^3\ g^{-1}$ respectively, with corresponding microporosity of 97 and 86 % respectively. The carbon performed well at very low pressure of 0.15 bar and 25 °C, showing a CO_2 uptake capacity of 1.6 mmol g^{-1}.[33]

Secondly, to improve the carbon yield of porous carbons self-activated from KHP at high temperatures, an additional carbon source was mixed with KHP before activation. The aim of the additional carbon source is to increase resulting yield, without compromising the self-activating process of KHP. The additional carbon source was either airchar or hydrochar. Airchar, as previously described in Chapter 4 of this thesis, is derived from biomass that has undergone a novel carbonisation method; flash air-carbonisation. As well as being carbon rich (~ 78 %), previous studies have shown airchar to be relatively resistant to KOH activation, a well-developed porosity forms, with high surface area and pore volume, but crucially a large proportion of microporosity is retained.[34,35] Hydrochar is derived from biomass which has undergone the traditional hydrothermal carbonisation method.[29,36]

The aims of this study were threefold. Firstly, the effects of harsh activation conditions (high temperatures up to 1200 °C and long activation durations up to 10 hrs) in the production of porous carbons were investigated; how these factors affect the porosity development and CO_2 uptake capacity of resulting carbons. An organic metal salt known to reliably produce microporous carbons that are ideal for CO_2 uptake was chosen as the starting material. Secondly, the effects of adding a

second, carbon rich starting material on the carbon yield of the resulting carbons was investigated. Two types of biochar were chosen as the additional carbon source; airchar and hydrochar. Thirdly, a comparison of the effects of char type on resulting porous carbons when activated alongside KHP was investigated.

6. 3. Material Synthesis

Samples prepared with no additional carbon source

Potassium Hydrogen Phthalate (KHP) was directly activated. KHP (~ 2.5 g) (99 %, Sigma Aldrich) was heated in a horizontal alumina furnace at a ramp rate of 10 °C min^{-1} to the required temperature (800, 1000 or 1200 °C) under a flow of nitrogen (100 mL min^{-1}). The samples were held at the target temperature for either 0.5, 1, 5 or 10 hrs, before being allowed to cool to room temperature, all under nitrogen flow. Samples were washed in deionised water (400 mL) for 2 hrs, before being collected by vacuum filtration and dried in air at 100 °C for 24 hrs. The final samples were denoted KHPx-y, where x represents the activation temperature and y represents the activation time.

Samples prepared with an additional carbon source

KHP (1 g) (Sigma Aldrich) was ground with char (either airchar or hydrochar) in a C/K weight ratio 3 – 6. The mixture was heated in a horizontal alumina furnace at a ramp rate of 10 °C min^{-1} to the required temperature (900 or 1000 °C) under a flow of nitrogen (100 mL min^{-1}). The samples were held at the target temperature for 2 hrs, before being allowed to cool to room temperature, all under nitrogen flow. Samples were

washed in deionised water (400 mL) for 2 hrs, before being collected by vacuum filtration and dried in air at 100 °C for 24 hrs. The final samples were denoted x-KHP(y)z, where x represents the char type (AC for airchar or HC for hydrochar), y represents the C/K ratio and z represents the activation temperature.

Airchar was collected from the outer layer of a charred beam of spruce wood, collected following the Carbon Neutral Laboratory (CNL) fire at the University of Nottingham in September 2014.

Preparation of hydrochar

An aqueous suspension of eucalyptus sawdust (3.2 g) in deionised water (10 mL) was placed in a stainless steel autoclave and heated at a ramp rate of 5 °C min^{-1} to 250 °C. The suspension was held at this temperature for 2 hrs before being allowed to cool to room temperature. The resulting hydrochar was collected by vacuum filtration and washed thoroughly with deionised water before being dried in air at 100 °C for 48 hrs. The yield of this process was 55 %.

Various methods were used to characterise and analyse the samples. Elemental analysis was carried out using a CE-440 Elemental Analyzer, Exeter Analytical, INC. Samples were combusted in oxygen at 975 °C.

Scanning electron microscopy was conducted using a Zeiss Evo 10 SEM machine with a tungsten filament, operating with a 20 kV accelerating voltage.

Thermal gravimetric analysis was carried out using a TA Instruments Analytical TGAQ500 machine. Samples were heated at a ramp rate of 10 °C min^{-1} to 1000 °C in a flow of air.

Powder x-ray diffraction analysis was carried out using a PANalytical X'Pet Pro diffractometer using CuKα radiation (λ = 1.5418 Å), operating at 40 kV and 40 mA. A step size of 0.026° and a step time of 30.6 s was used.

Analysis of textural properties was carried out by nitrogen sorption at -196 °C. An initial degassing stage was conducted using a Micromeritics SmartVac Prep degasser wherein samples were held under vacuum at 230 °C for 16 hours. The following analysis was carried out using a Micromeritics 3Flex. Surface areas were calculated using BET theory, from adsorption data within the linear isotherm plot (relative pressure (P/P_0) of 0.04 – 0.09). Total pore volumes were calculated from the nitrogen uptake close to saturation pressure ($P/P_0 \approx 0.99$). Micropore surface areas and pore volumes were calculated using t-plot analysis. Pore size distributions were determined by applying

non-local density functional theory (NLDFT) to the nitrogen adsorption isotherms.

Gas uptakes were measured using a Hiden Isochema XEMIS machine. After an initial degassing stage, where samples were held under vacuum at 230 °C for 3 hours, analysis was carried out with CO_2 as the adsorbing gas, at 25 °C and at pressures from 0 – 40 bar.

6. 4. Results and Discussion

6. 4. 1. Elemental Analysis and Carbon Yield

The carbon, hydrogen and oxygen content, as well as the C/O ratio of all samples are shown below in Tables 6.1 and 6.2. Nitrogen content is not reported, as in all cases the amounts were negligible. In most cases, the presence of hydrogen was also negligible. The carbon and hydrogen content of the organic component of the materials were measured and the remaining content assumed to be oxygen. The carbon yields for all samples are shown below in Tables 6.3 and 6.4. The elemental analysis results of airchar and hydrochar are displayed in Table 6.2.

The carbon, hydrogen and oxygen content, along with the C/O ratio of samples prepared from KHP alone are shown in Table 6.1. Overall, this sample set shows exceptionally high carbon content and C/O ratios.[12,29,35,37] At an activation temperature of both 1200 and 1000 °C, carbon content and C/O ratio increase with activation time. KHP1000-10 is the only sample at these temperatures to show any presence of hydrogen. At 800 °C, carbon content is still high although generally lower than analogous samples activated at higher temperatures. C/O ratios are significantly lower. At all three activation temperatures,

Table 6.1. Elemental analysis results of samples produced from KHP. C and H content was calculated though elemental microanalysis. The remaining content was assumed to be O. The atomic C/O ratio was calculated from these values

Sample	C%	H%	O%	C/O
KHP1200-10	96.8	N/A	3.2	40.4
KHP1200-5	95.5	N/A	4.5	28.4
KHP1200-1	93.7	N/A	6.3	20.0
KHP1200-0.5	92.7	N/A	7.3	16.8
KHP1000-10	98.1	0.4	1.5	90.9
KHP1000-5	95.7	N/A	4.3	29.6
KHP1000-1	94.9	N/A	5.1	24.7
KHP1000-0.5	89.3	N/A	10.7	11.1
KHP800-10	75.7	0.3	24.0	4.2
KHP800-5	86.0	N/A	14.0	8.1
KHP800-1	84.4	0.4	15.2	7.4
KHP800-0.5	90.3	0.5	9.2	13.0

there is no clear trend of activation time on elemental composition. At 800 °C there is a greater presence of hydrogen. At higher activation temperatures and longer durations, more extensive reactions of K-compounds with the carbon skeleton (see Chapter 1, section 1. 5. 3.) results in the loss of CO and CO_2, reducing the carbon content and to a greater extent, the

Table 6.2. Elemental analysis results of samples produced from KHP, airchar and hydrochar. C and H content was calculated though elemental microanalysis. The remaining content was assumed to be O. The atomic C/O ratio was calculated from these values

Sample	C%	H%	O%	C/O
AC-KHP(6)1000	87.0	N/A	13.0	9.0
AC-KHP(5)1000	82.3	N/A	17.7	6.2
AC-KHP(4)1000	85.6	N/A	14.4	7.9
AC-KHP(3)1000	92.7	N/A	7.3	16.8
AC-KHP(6)900	85.5	N/A	14.5	7.8
AC-KHP(5)900	85.5	0.3	14.2	8.0
AC-KHP(4)900	78.6	0.5	20.9	5.0
AC-KHP(3)900	82.5	N/A	17.5	6.3
HC-KHP(4)1000	89.1	0.5	10.4	11.4
HC-KHP(3)900	85.6	0.4	14.0	8.1
Airchar	77.7	3.1	19.2	5.4
Hydrochar	59.4	5.2	35.4	2.2

oxygen content. Increased release of H_2O further drives down the oxygen content. The carbon, hydrogen and oxygen content, along with the C/O ratios of samples prepared from KHP with an additional carbon source of either airchar or hydrochar are shown in Table 6.2. There are no clear trends in elemental composition with varying C/K ratio. Generally, this sample set shows lower carbon content and C/O ratios than the previous

Table 6.3. Carbon yield of samples produced from KHP. Averages calculated from the yield of each sample produced

Sample	Carbon Yield (%)
KHP1200-10	4.6
KHP1200-5	9.1
KHP1200-1	12.0
KHP1200-0.5	12.0
KHP1000-10	12.5
KHP1000-5	12.0
KHP1000-1	11.1
KHP1000-0.5	10.4
KHP800-10	15.2
KHP800-5	10.4
KHP800-1	17.3
KHP800-0.5	19.8

set, however this may be due to the selection of shorter activation time and lower activation temperatures than many samples investigated in the previous set. These factors result in limited reactions of the carbon skeleton, therefore reducing the volume of CO and CO_2 released during activation. However, in concordance with the previous data set, hydrogen content is low or negligible for most samples. The release of H_2 and H_2O during activation occurs under gentler conditions than the

Table 6.4. Carbon yield of samples produced from KHP, airchar and hydrochar

Sample	Carbon Yield (%)
AC-KHP(6)1000	32.2
AC-KHP(5)1000	25.5
AC-KHP(4)1000	22.3
AC-KHP(3)1000	15.8
AC-KHP(6)900	30.8
AC-KHP(5)900	24.8
AC-KHP(4)900	22.8
AC-KHP(3)900	12.4
HC-KHP(4)1000	17.8
HC-KHP(3)900	12.8

release of carbon compounds, so hydrogen is not a significant component of these materials. Hydrochar has a higher proportion of oxygen than air char (Table 6.2) resulting in a low C/O ratio. However, on activation, samples produced with hydrochar have a higher C/O ratio than analogous samples produced with airchar. The higher oxygen content of the hydrochar may make it more reactive, leading to more extensive reactions. As more CO_2 is released during activation, relative C/O ratio increases. The carbon yields of samples prepared from KHP alone are shown in Table 6.3. Ranging

between 4.6 and 19.8 %, the yields are low compared with previous porous carbon studies.[35,37,38] At an activation temperature of 1200 °C, carbon yield increases with activation time, however at 1000 °C this trend is reversed. At 800 °C, there is no clear trend.

The carbon yields of samples prepared from KHP with an additional carbon source of either airchar or hydrochar are shown in Table 6.4. Ranging between 12.4 and 32.2 %, the carbon yields are significantly higher than those seen for the previous sample set. Even when only KHP1000-1 and KHP800-1 (the two samples activated under conditions most closely resembling this sample set) are taken into account, their average yield of 14.2% is much lower than the average yield of both the AC-KHP(x)1000 samples (24.0 %) and the AC-KHP(x)900 samples (22.7 %).

At both 900 and 1000 °C, carbon yield increases as the proportion of K decreases. This can be attributed to limited reactions with the carbon skeleton taking place during activation, resulting in less carbon being lost through the formation of CO and CO_2.

It is clear that adding an additional source of carbon, thereby decreasing the proportion of K during activation leads to a

significant increase in the carbon yield of porous carbons and a more efficient synthesis method. Again, char type has no significant effect on carbon yield.

6. 4. 2. Scanning Electron Microscopy

Images collected by scanning electron microscopy (SEM) representative of both sample sets are shown below in Figures 6.2 and 6.3. SEM images of activated carbons derived from KHP alone (Fig. 6.2) show similar morphologies, comprising of irregularly shaped particles with sharp corners and a high degree of surface roughness, characteristic of activated carbons.[12,37,39] Areas of regular, micron-scale openings indicate some laminar structure and access to the internal hierarchical pore network. As the activation temperature increases from 800 to 1000 °C, the particles are smaller and more fragmented, with a seemingly higher degree of layering. It is clear that exposure to higher temperatures during activation results in more extensive fragmentation of the carbon particles.

SEM images of activated carbons derived from KHP with an additional source are shown in Figure 6.3. Figure 6.3 [E] shows an SEM image of airchar. Retention of the pre-carbonisation structure of the wood is clear, characterised by cellular monolith-like formations. Upon activation (Fig. 6.3 [A] and [B]), retention of the parent char is clear. Fragments of monolith-like particles are clear, alongside irregularly shaped particles with sharp corners and surface roughness, similar to the particle structure seen in samples activated via KHP alone. Fig. 6.3 [B]

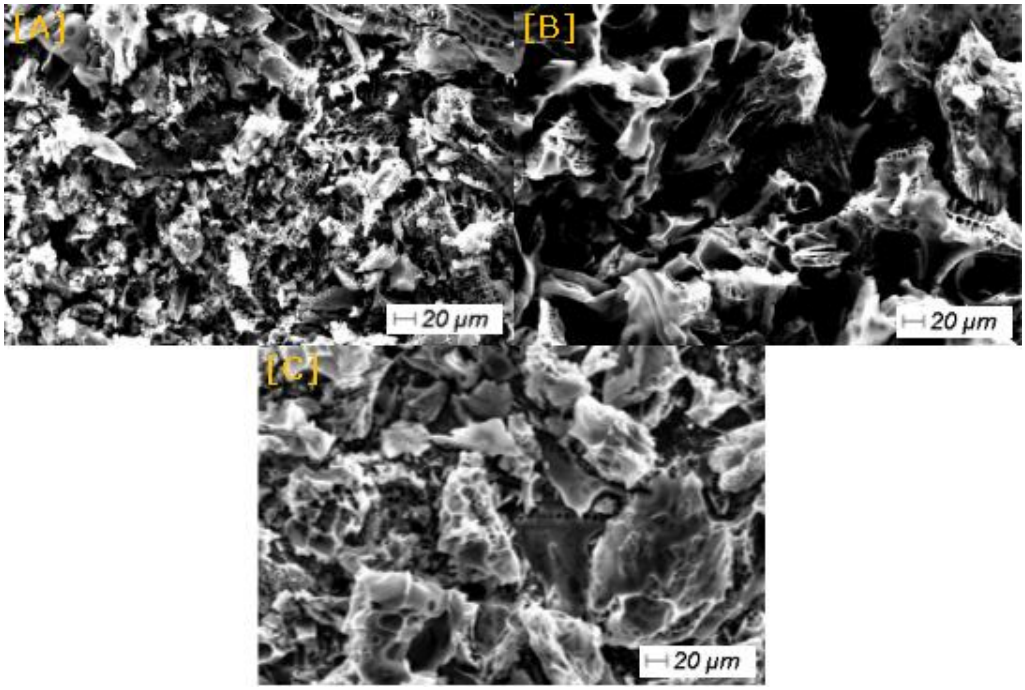

Figure 6.2. SEM images of [A] KHP1200-1, [B] KHP1000-1 and [C] KHP800-1

shows how activation of the char has taken place, with the development of regular, micron-scale openings forming on the cellular char structures. It is clear that activation of KHP alongside airchar results in a porous carbon with mixed morphology; a combination of woody, char-derived particles and irregular, KHP-derived particles.

Figure 6.3 (C) show a hydrochar particle activated with KHP. The inner particle retains the cellular-like woody structure of the parent hydrochar (Fig. 6.3 (F)), while the particle surface is amorphous and uneven. This difference between the inside and

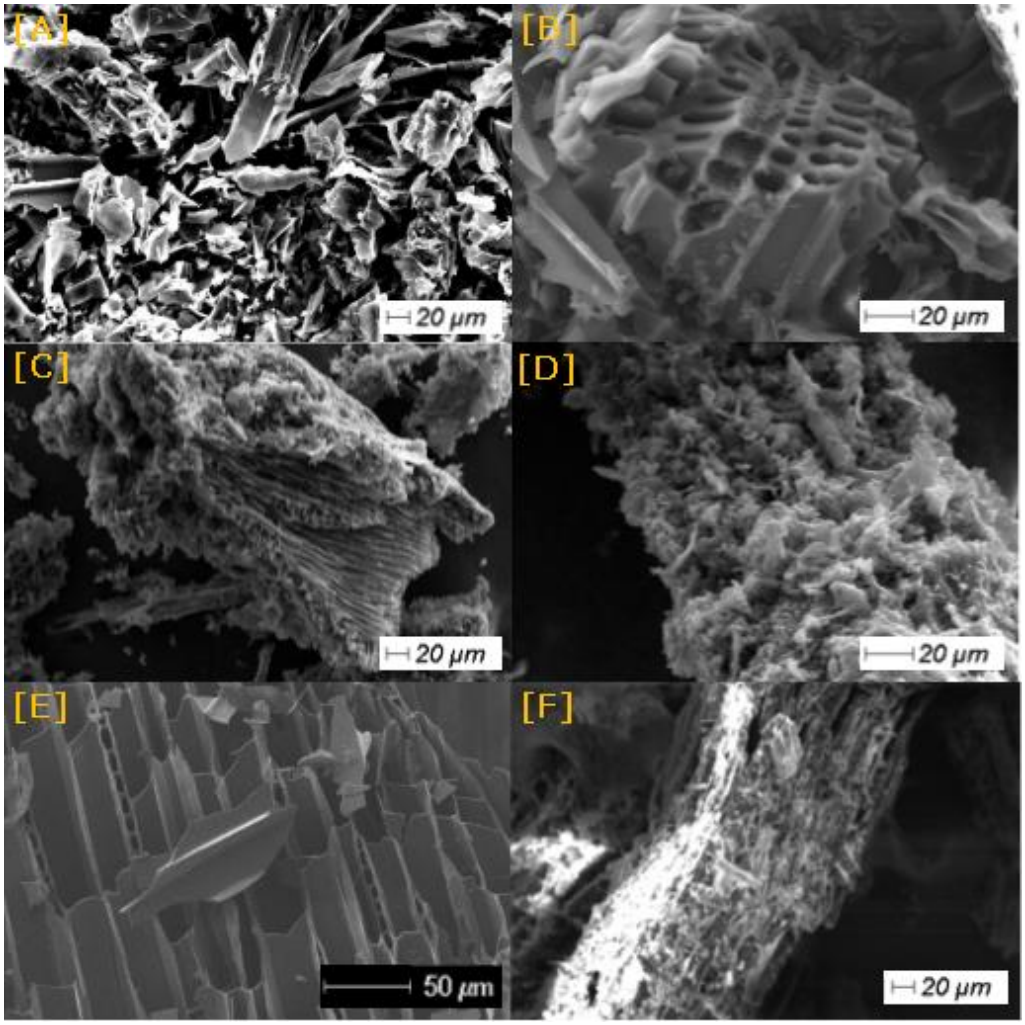

Figure 6.3. SEM images of [A] and [B] AC-KHP(4)1000, [C] and [D] SD-KHP(4)1000, [E] CNL1 airchar and [F] eucalyptus sawdust hydrochar

the outside surface of the particle indicates a poor activating ability of KHP on hydrochar.

6. 4. 3. Thermal Gravimetric Analysis

Thermal gravimetric analysis (TGA) was conducted to assess the structure, purity and thermal stability of all the activated carbon samples. The TGA plots for all activated samples are shown below in Figures 6.4 – 6.9. Some samples show a small mass loss at ~ 100 °C. This can be attributed to moisture loss and can be assumed to be associated with the length of time the sample spent exposed to the atmosphere, as opposed to any structural differences. All of the samples show a single sharp burn off curve within the approximate range 500 – 700 °C. The shape and range of the burn-off curve is indicative of single phase, amorphous carbon[40]. The high thermal stability seen across all samples can be attributed to the formation of some graphitic domains at activation temperatures above ~ 750 °C.[34]

The majority of the samples had low residual mass, < 6 %, with the exception of KHP800-10, which can be assumed to be an anomaly. Firstly, this shows that the activation of KHP is highly efficient and secondly, the addition of extra carbon has no effect on impurity level therefore any residual mass must be inorganic residues.

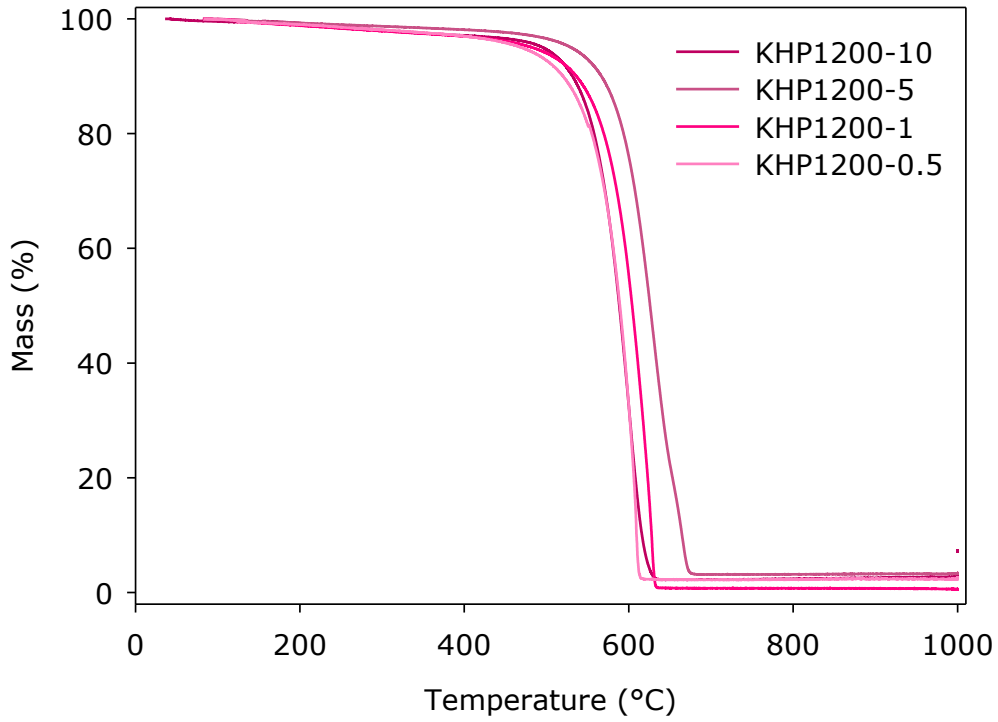

Figure 6.4. TGA plots of samples prepared from KHP at 1200 °C

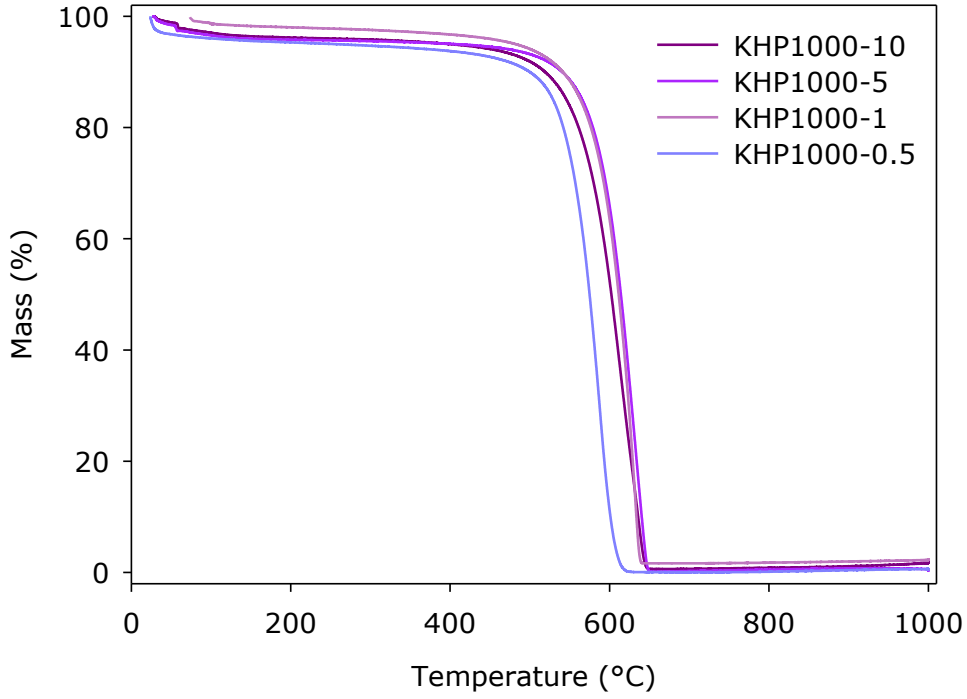

Figure 6.5. TGA plots of samples prepared from KHP at 1000 °C

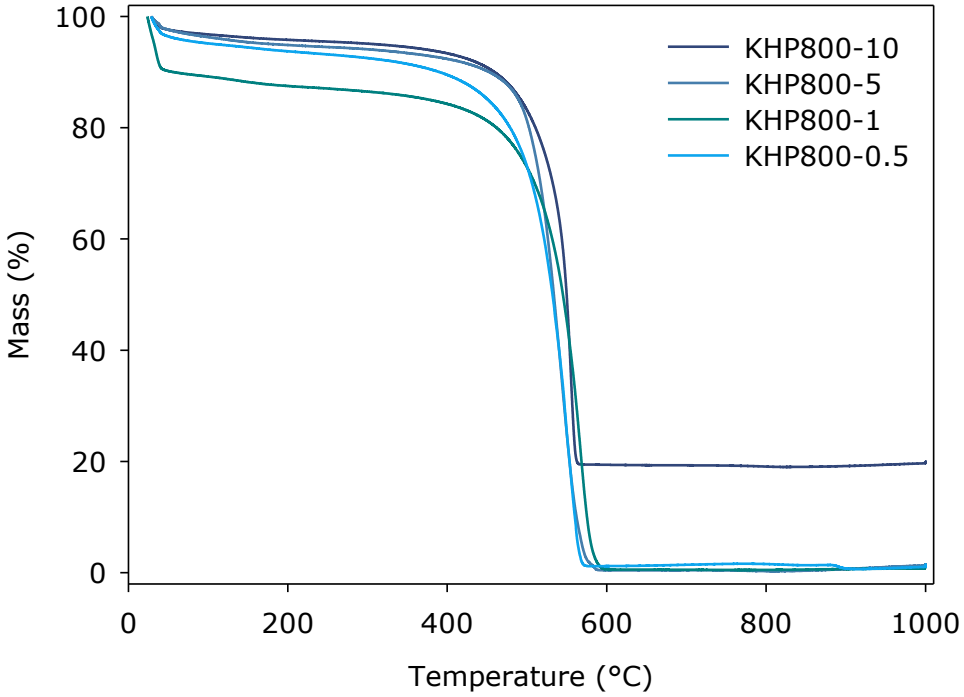

Figure 6.6. TGA plots of samples prepared from KHP at 800 °C

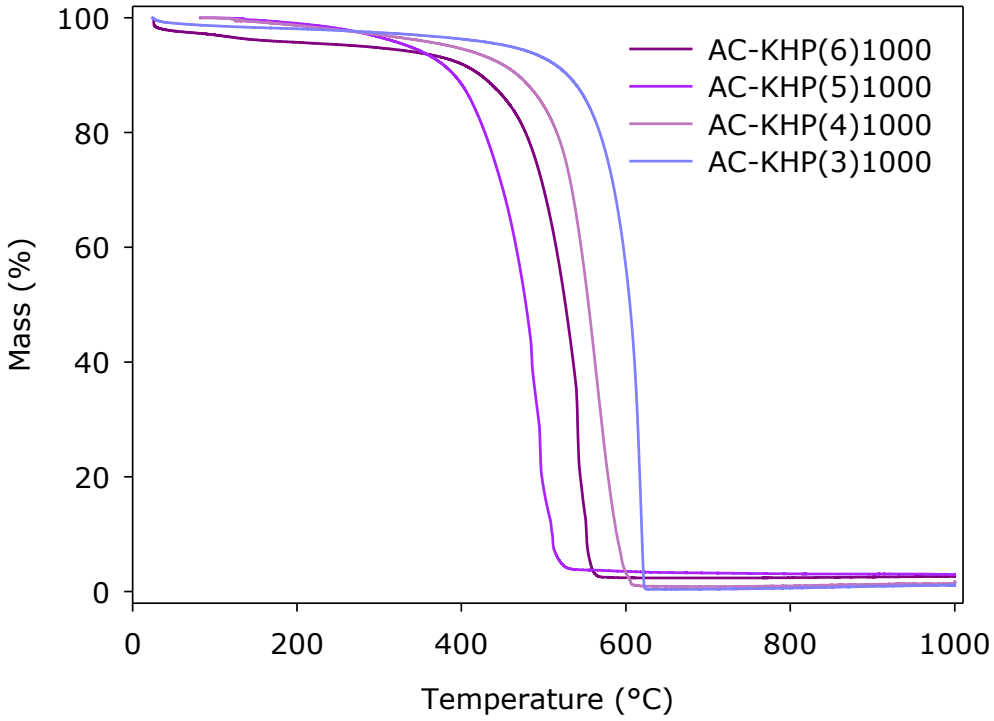

Figure 6.7. TGA plots of samples prepared from airchar and KHP at 1000 °C

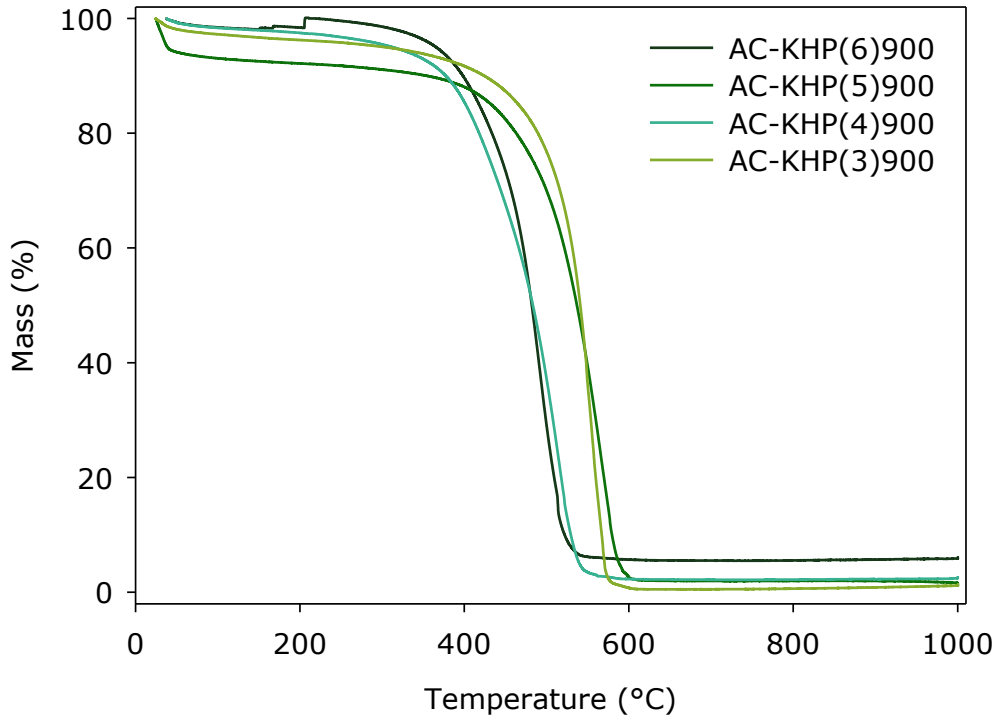

Figure 6.8. TGA plots of samples prepared from airchar and KHP at 900 °C

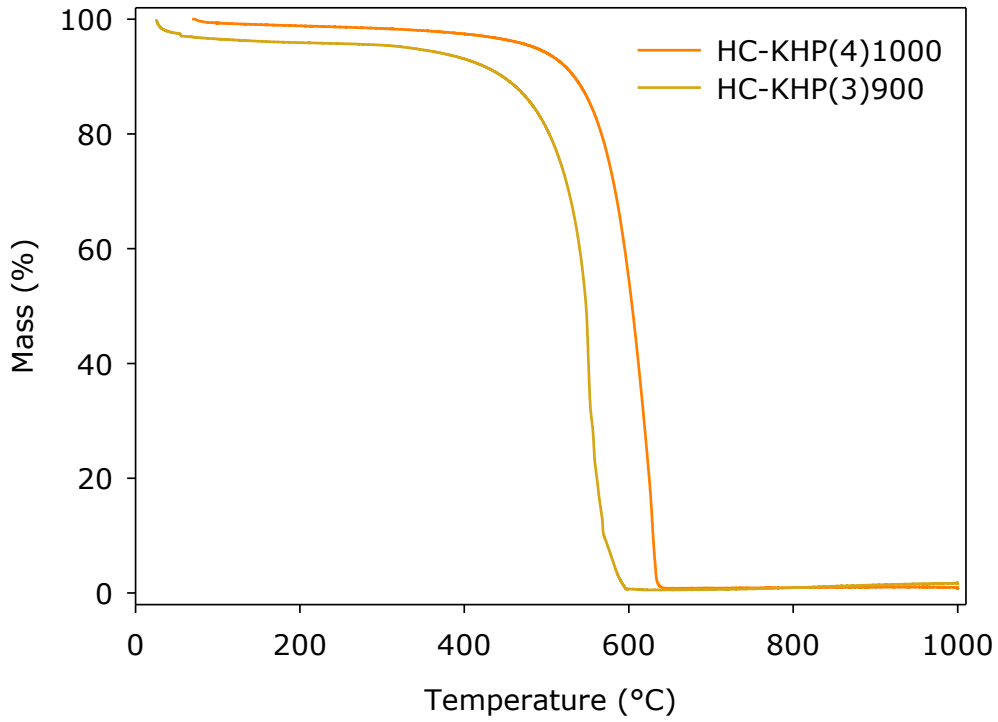

Figure 6.9. TGA plots of samples prepared from hydrochar and KHP

KHP800-1 represents 'standard activation conditions'. As seen in Figure 6.6, it has a similar level of thermal stability as KHP800-0.5. Thermal stability increases with increasing activation duration, indicating that sustained activation allows the development of more graphitic domains.

The KHP1200 and KHP1000 sample sets both show similar trends in thermal stability (Fig. 6.4 and 6.5). In both sets, the sample activated for 0.5 hrs exhibits the lowest thermal stability; short activation time allows for little graphitic development. The samples activated for 10 hrs (KHP1200-10 and KHP1000-10) also show low thermal stabilities. This may be an indication of over-activation; sustained activation reactions occurring at extremely high temperatures cause smaller pores to collapse into larger pores, reducing any structural ordering and graphitisation. It is clear that at very high temperatures of 1000 and 1200 °C, a moderate activation time of 1 – 5 hrs favours the formation of thermally stable graphitic domains.

The average burn-off temperature decreases from 622 to 617 to 553 °C from the KHP1200 sample set to the KHP1000 and KHP800 sets, respectively.

There is more variation in thermal stability in the sample sets with additional carbon, although the AC-KHP1000 and AC-KHP900 sample sets both generally follow the rough trend that thermal stability increases as proportion of K increases. This can be attributed to a higher proportion of activation and pore development.

When looking at the samples activated with hydrochar as the additional carbon source (Fig. 6.9), HC-KHP(4)1000 has a lower proportion of K, but is activated at a higher temperature than HC-KHP(3)900. This shows that a higher temperature is more important than a higher proportion of activating reactions in creating porous carbons with high thermal stability. Both HC-KHP(4)1000 and HC-KHP(3)900 have similar plots to the equivalent samples which use spruce airchar as the additional carbon source. This shows the carbon source does not have a considerable effect on thermal stability, phase or impurity level of the resulting activated carbons.

Overall, the method used in this study produces highly pure activated carbons with high thermal stability. Although a moderate activation time and a higher proportion of K does increase the resulting thermal stability, the biggest factor is a high temperature creating graphitic domains. Harsher activation temperatures generally result in higher thermal

stabilities. The addition of an extra carbon source has no effect on purity or thermal stability of resulting porous carbons.

6. 4. 4. Powder X-Ray Diffraction

Powder x-ray diffraction (PXRD) was used to assess the purity, structure and graphitisation of all the carbon samples. The diffraction patterns are shown below in Figures 6.10 – 6.15. The particular areas of interest of the PXRD patterns are peaks at 2θ ≈ 22° and 44°, as these correspond to diffraction of the (002) and (100) planes of stacked graphite, respectively. The very low angle region of the pattern (< 15°) was featureless in regard to the sample analysis, so is not reported here.

The PXRD patterns for samples activated with no additional carbon source are shown in Figures 6.10, 6.11 and 6.12. In most cases, there is no discernible peak at 2θ ≈ 22°; any increase in intensity may be obscured by the noise of the baseline. Peaks at 2θ ≈ 44° are weak in intensity and broad. All samples show highly irregular, amorphous carbon structures with few, if any, graphitic domains.[34] The highest R value of 1.12 is recorded for KHP1200-5, which corresponds to its high thermal stability seen in the TGA plots (Fig. 6.4). The R value can be assumed to equal

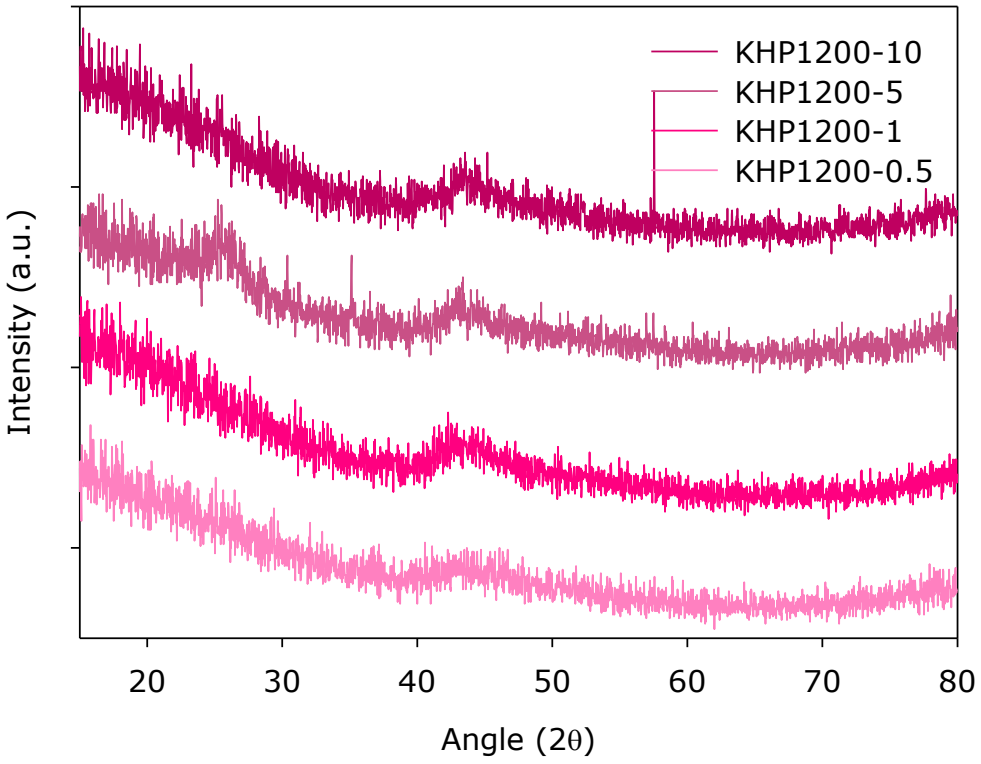

Figure 6.10. PXRD patterns of samples prepared from KHP at 1200 °C

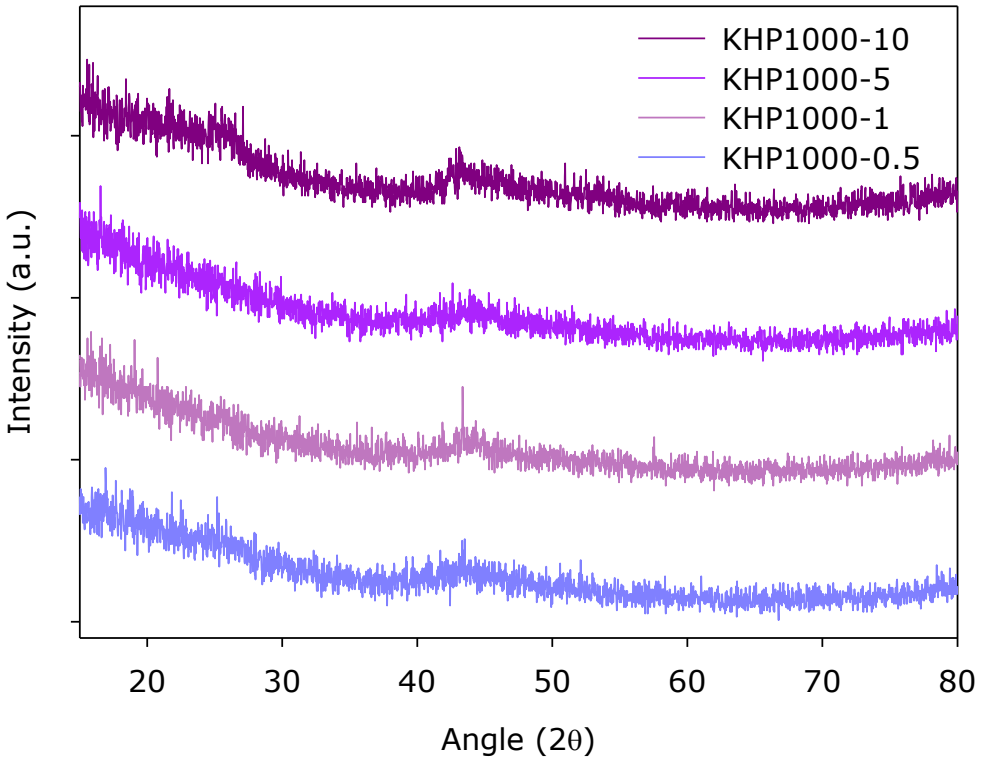

Figure 6.11. PXRD patterns of samples prepared from KHP at 1000 °C

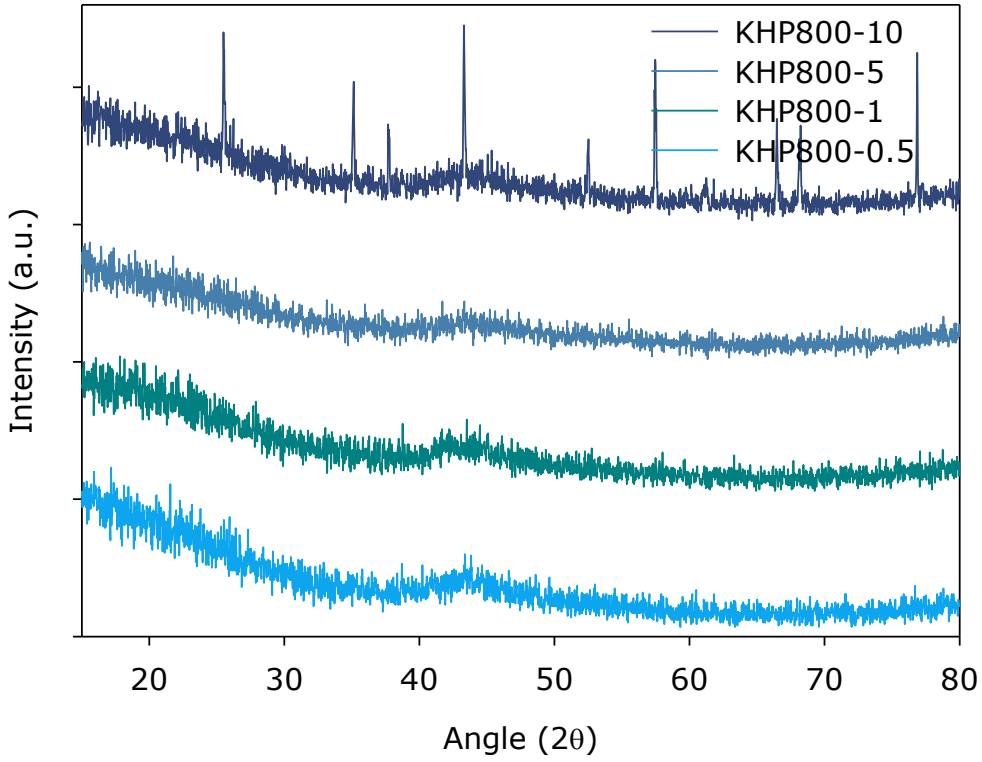

Figure 6.12. PXRD patterns of samples prepared from KHP at 800 °C

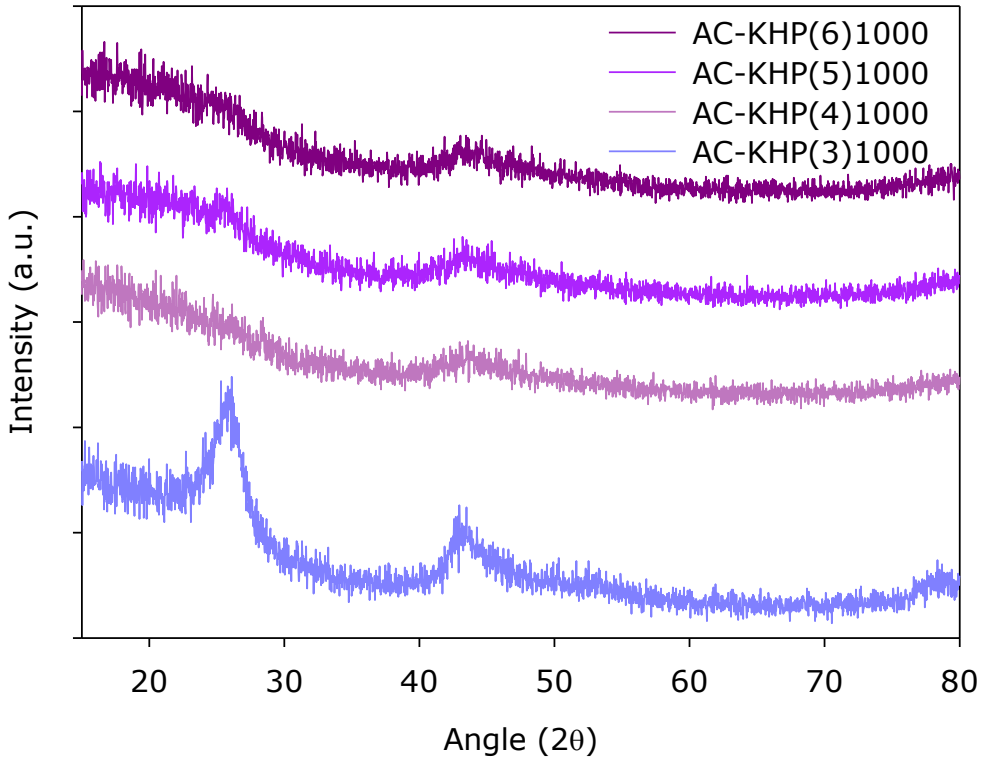

Figure 6.13. PXRD patterns of samples prepared from airchar and KHP at 1000 °C

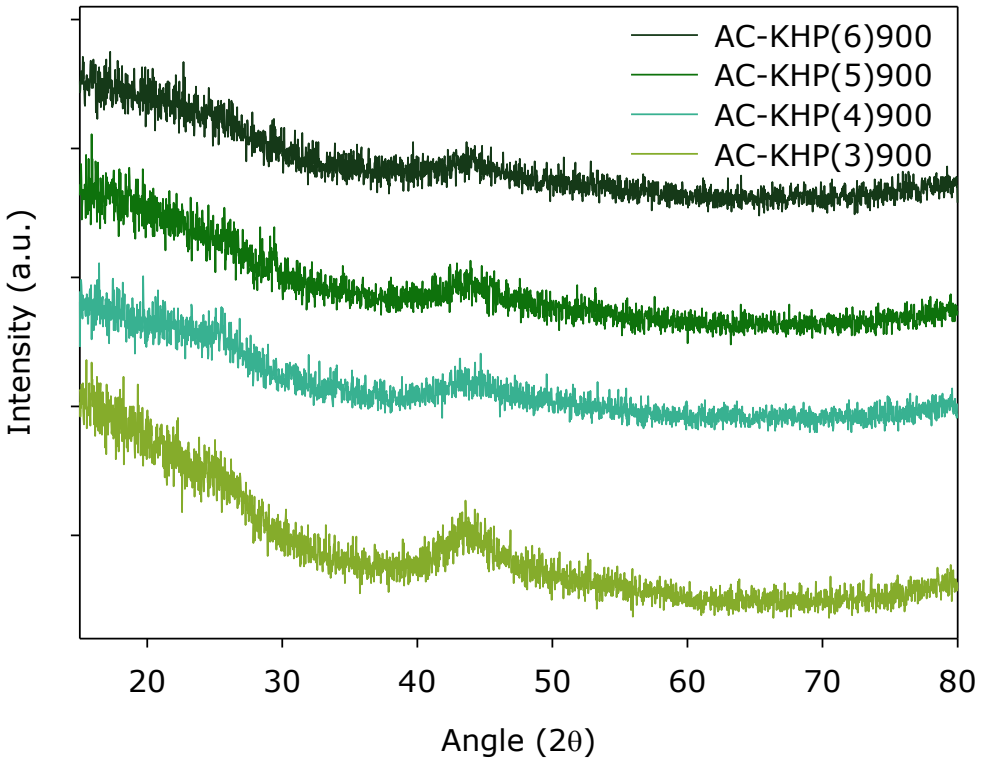

Figure 6.14. PXRD patterns of samples prepared from airchar and KHP at 900 °C

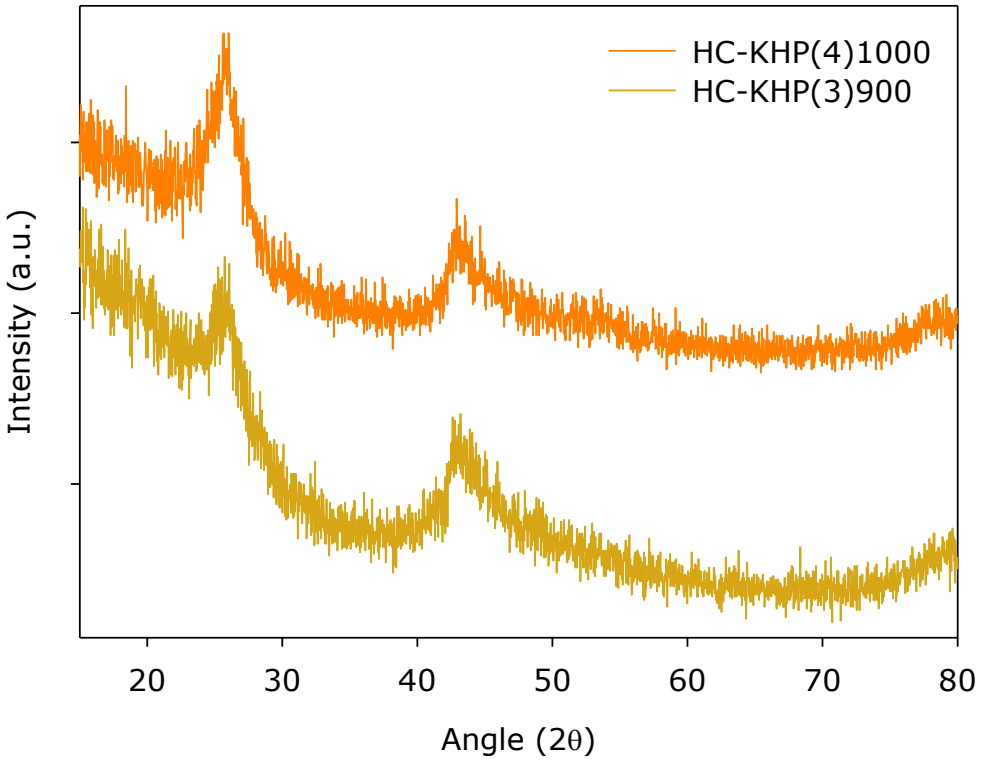

Figure 6.15. PXRD patterns of samples prepared from hydrochar and KHP

1 for the rest of the samples in these sample sets, indicating that all graphene sheets are singularly distributed.[41]

The only considerable indications of impurities are in the PXRD pattern for sample KHP800-10. Sharp peaks with high intensity relative to the baseline can be assumed to be due to potassium compounds formed during the activation process. This corresponds with the high residual mass at 1000 °C seen for the sample in the TGA plots (Fig. 6.6).

The PXRD patterns for samples activated with an additional carbon source are shown in Figures 6.13, 6.14 and 6.15. In most cases there is no discernible peak at $2\theta \approx 22°$; any increase in intensity may be obscured by the noise of the baseline. Peaks at $2\theta \approx 44°$ are weak in intensity and broad. As before, all samples show irregular, amorphous carbon structures. The R value for the majority of the samples in these sample sets can be assumed to equal 1, indicating that all graphene sheets are singularly distributed.[41] R values of 2.1, 1.4 and 1.4 were recorded for samples AC-KHP(3)1000, HC-KHP(4)1000 and HC-KHP(3)900 respectively. These samples possess a greater level or regularity and are more graphitic in structure. This corresponds with the high thermal stability shown by these samples in the TGA plots (Fig. 6.7 and 6.9).

There are no sharp, intense peaks in any of the PXRD patterns for these sample sets, confirming the high level of purity recorded through TGA.

Overall, all of the samples produce PXRD patterns characteristic of amorphous, turbostratic carbons, with a high level of irregularity and few graphitic domains. The majority of samples are highly pure, with singularly distributed graphene sheets. The PXRD patterns reveal no clear effect of changes to activation time, temperature or K proportion on the overall structure of the synthesised porous carbons. Adding spruce airchar as an additional carbon source also appeared to have little effect on overall structure. However, in the case of hydrochar as an additional carbon source, activation resulted in a more graphitic structure. As discussed in Chapter 4 of this thesis, hydrochar is less resistant to KOH activation than airchar. It may be the case that in this study, the additional hydrochar is more susceptible to graphitisation reactions when exposed to the harsher conditions, especially temperature, explored here.

6. 4. 5. Nitrogen Sorption Isotherms

The N_2 sorption isotherms, recorded at -196 °C are shown below in Figures 6.16 – 6.21. The isotherms for samples activated with no additional carbon source are shown in Figures 6.16, 6.17 and 6.18. The samples activated at 800 °C (Fig. 6.18) all show type I isotherms; sharp N_2 uptake at low relative pressure followed by a plateau indicating highly microporous samples. This is in line with previous studies reporting activation of KHP at moderate temperatures.[31,33] The isotherm knee broadens as activation time increases from 0.5 – 10 hrs, indicating a broadening of the pore size distribution (PSD) within the micropore range with prolonged activation. This is due to the development of broader pore channels and smaller pores collapsing into larger ones with sustained activation.

As activation temperature increases to 1000 and 1200 °C (Fig. 6.17 and 6.16) there is a clear evolution of the N_2 sorption isotherms. The isotherms remain type I, but as the temperature increases, knees become broader, the quantity of N_2 absorbed increases, hysteresis appear and in some cases, saturation is not reached until high relative pressure. It is clear that as activation temperatures become harsher, pore development extends into the mesopore region, broadening the PSD and

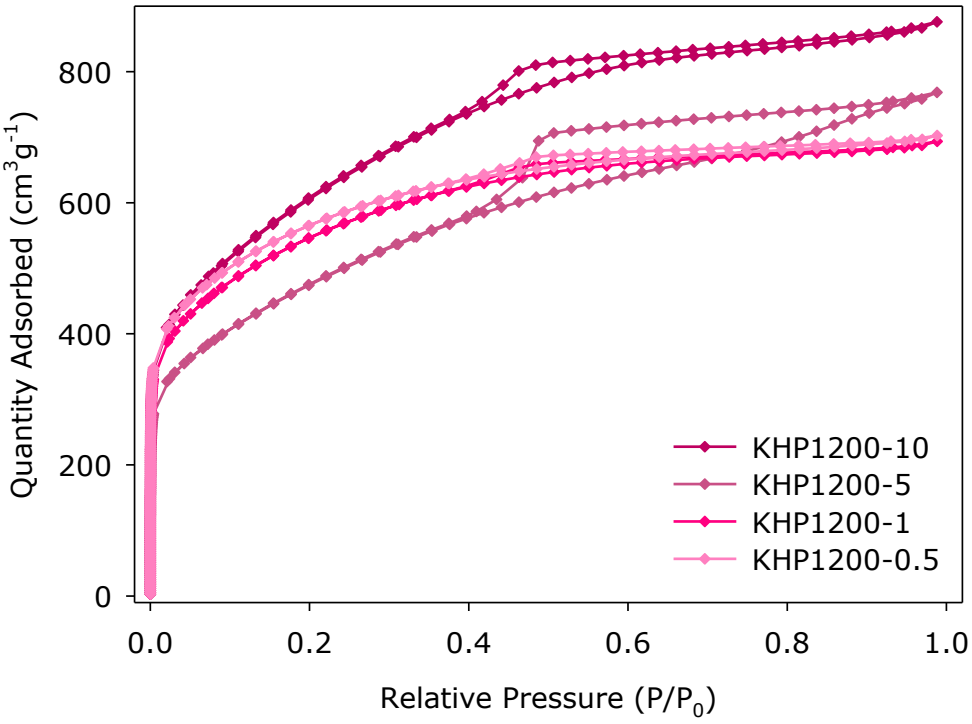

Figure 6.16. Sorption isotherms for samples prepared from KHP at 1200 °C

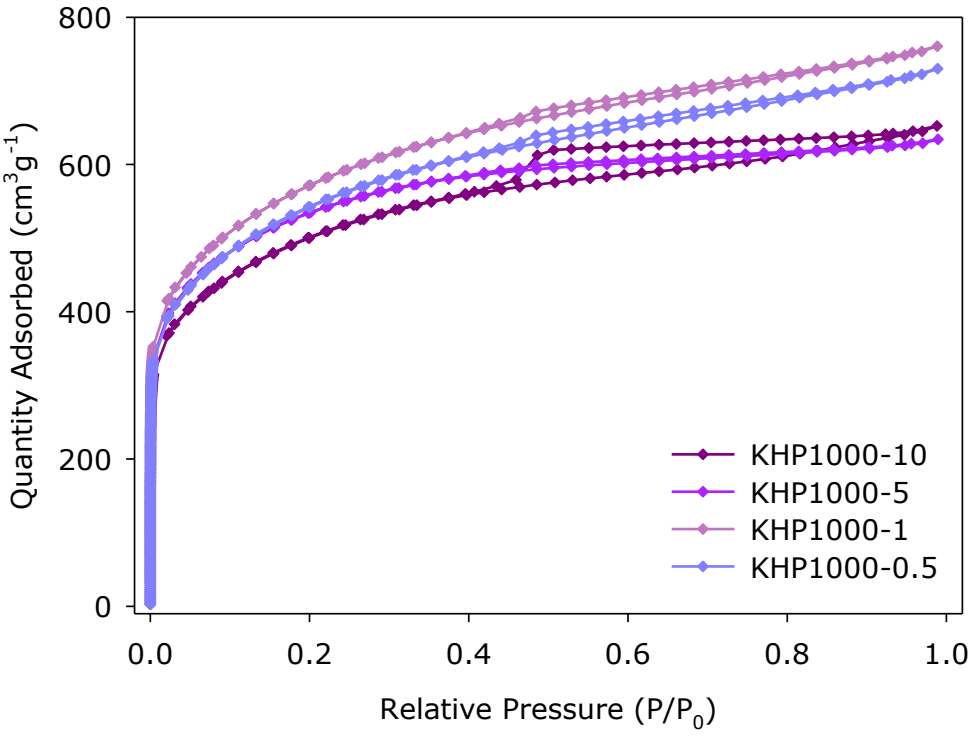

Figure 6.17. Sorption isotherms for samples prepared from KHP at 1000 °C

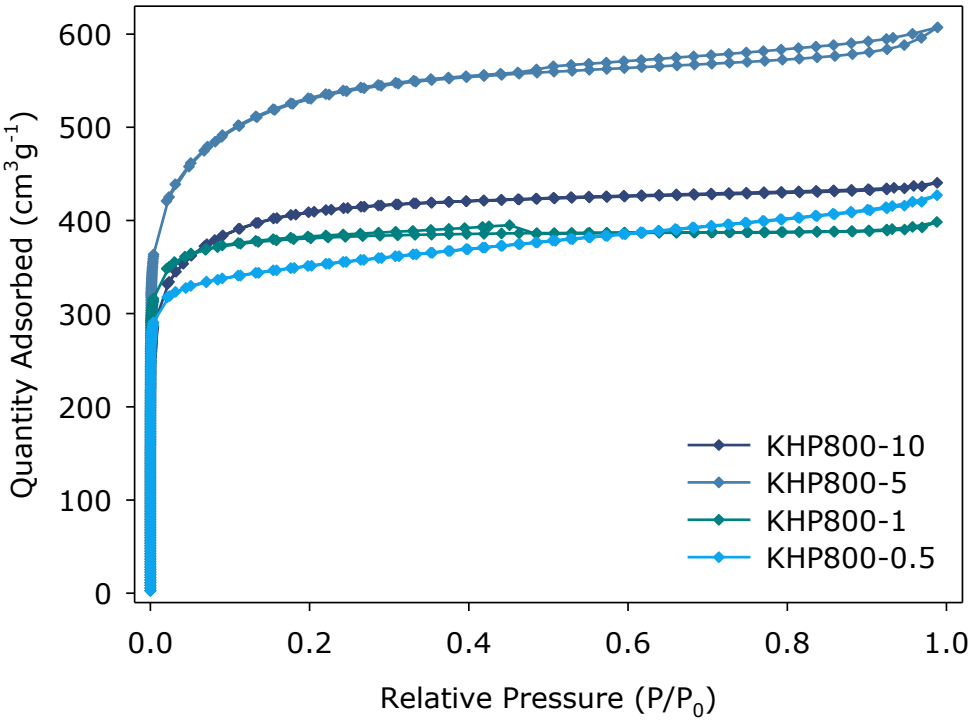

Figure 6.18. Sorption isotherms for samples prepared from KHP at 800 °C

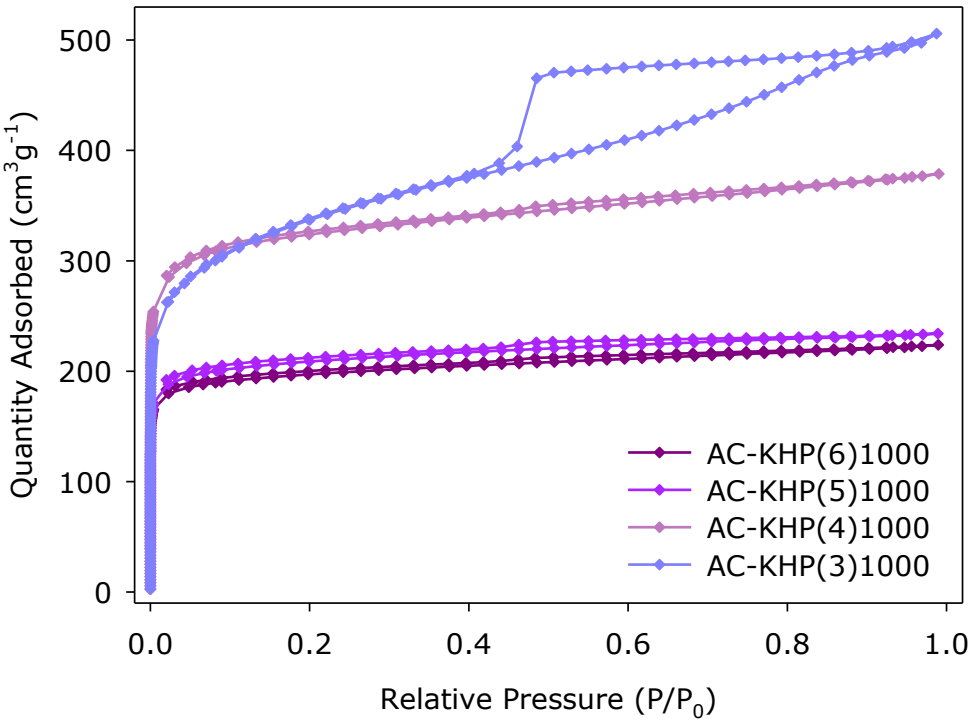

Figure 6.19. Sorption isotherms for samples prepared from airchar and KHP at 1000 °C

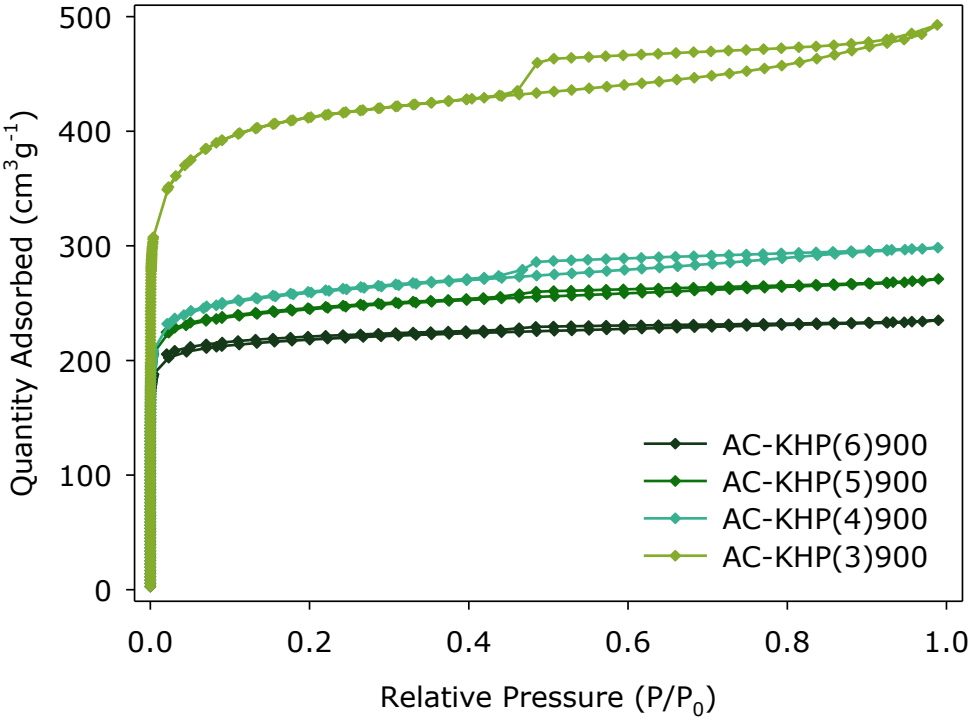

Figure 6.20. Sorption isotherms for samples prepared from airchar and KHP at 900 °C

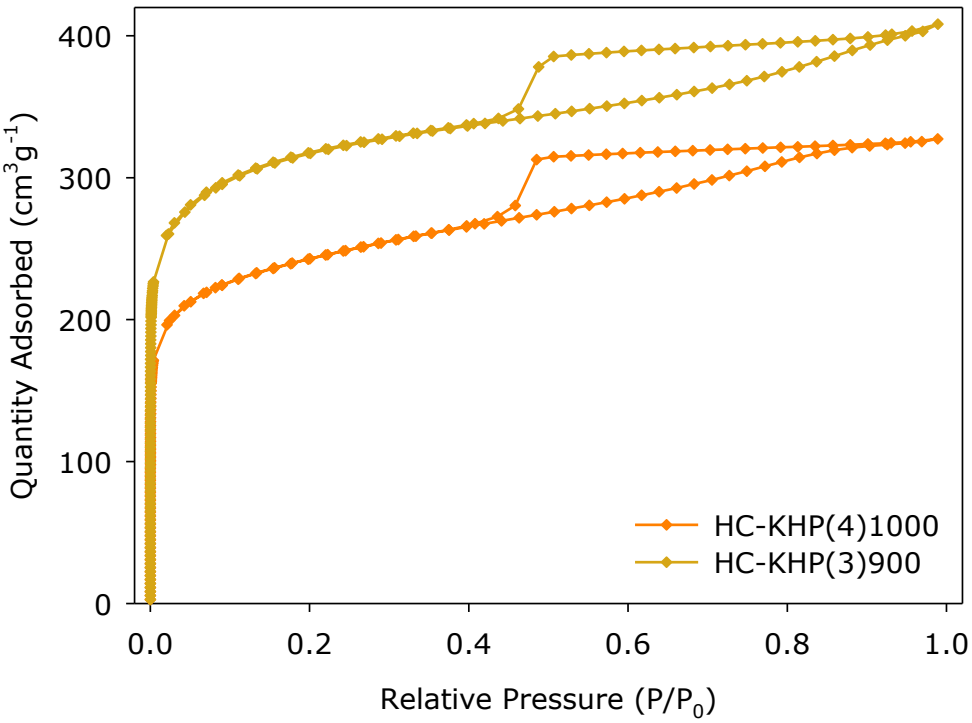

Figure 6.21. Sorption isotherms for samples prepared from hydrochar and KHP

material surface area and pore volume can be assumed to increase. KHP1000-10, KHP1200-5 and KHP1200-10 show a type H4 hysteresis loop, indicating capillary condensation occurring in mesopores within a sample that contains a high proportion of microporosity. The hysteresis loops close at $P/P_0 \approx 0.4$, characteristic of N_2 sorption.

The N_2 sorption isotherms for samples activated with an additional carbon source are shown in Figures 6.19, 6.20 and 6.21. All of the samples show a type I isotherm, indicating highly microporous samples with a narrow PSD centred below 20 Å. In all three sample sets, quantity of N_2 absorbed increases as the proportion of K increases. AC-KHP(3)900, AC-KHP(3)1000 and AC-KHP(4)1000 all show considerably higher N_2 absorption than the other samples in their respective sample sets. This indicates that a higher degree of activation leads to a more developed porosity with higher surface area and volume. The majority of the samples show a very sharp knee at low relative volume indicating samples with a narrow distribution of small micropores. Increasing activation temperature from 900 to 1000 °C does not seem to have any considerable effect on isotherm shape.

The only samples from these sets that deviate from the type I shape are AC-KHP(3)1000, AC-KHP(3)900, AC-KHP(4)900, HC-

KHP(4)1000 and HC-KHP(3)900. These samples also show a slightly broader knee indicating a broadening of the PSD. They also all show a type H4 hysteresis loop, indicating capillary condensation occurring in mesopores. As with the previous samples, hysteresis loops close at $P/P_0 \approx 0.4$, characteristic of N_2 sorption. Saturation is reached at higher relative pressure than other samples in these sets.

In all cases, the carbons produced exhibit N_2 sorption isotherms characteristic of highly microporous materials with narrow PSDs centred in the small micropore region. Harsher activation temperatures (≥ 1000 °C), as well as prolonged activation (≥ 5 hrs) broadens the PSD, creating mesopores and increasing overall porosity to the point where it may become detrimental, leading to pore collapse. Samples activated with an additional carbon source exhibited less developed porosity, indicated by lower N_2 uptake. When airchar was used as the additional carbon source, samples retain a high degree of microporosity indicated by type I isotherms. When hydrochar was used as the additional carbon source, there is clearer development of mesoporosity, in line with results from Chapter 4 that airchar is more resistant to activation than hydrochar.

6. 4. 6. Textural Properties; Surface Area and Pore Volume

The surface area and pore volume data, calculated from the N_2 sorption isotherms, are displayed below in Tables 6.5 – 6.8. The surface area and pore volume data for samples activated with no additional carbon source are displayed in Tables 6.5 and 6.7 respectively. The samples show very good surface area and pore volume of up to 2124 $m^2\ g^{-1}$ and 1.36 $cm^3\ g^{-1}$ respectively for KHP1200-10, similar to previous textural data reported for activated KHP.[31] The high surface area and pore volume is accompanied by a low proportion of microporosity of 8 and 6 % respectively. This data is in line with the corresponding isotherm (Fig. 6.16) which shows high N_2 uptake and a broad knee.

The lowest surface area for this group of 1321 $m^2\ g^{-1}$ is shown by KHP800-0.5, with a very high micropore proportion of 81 %. The lowest pore volume for this group of 0.66 $cm^3\ g^{-1}$ is shown by KHP800-1, with a very high micropore proportion of 85 %. The textural data for these two samples is again in line with the corresponding isotherms (Fig. 6.18); high N_2 uptake at very low relative pressure followed by a sharp knee indicates highly microporous materials, but an overall low N_2 uptake indicates a poorly developed porosity. This can be attributed to the lower activation temperature and short activation time.

Table 6.5. Surface area of samples prepared from KHP, calculated by BET theory. [a]Proportion of surface area arising from micropores, as a value and as a % of total surface area

Sample	Surface Area ($m^2\ g^{-1}$)	[a]Micropore Surface Area ($m^2\ g^{-1}$)
KHP1200-10	2124	174 – 8%
KHP1200-5	1669	188 – 11%
KHP1200-1	1964	573 – 29%
KHP1200-0.5	2051	742 – 36%
KHP1000-10	1823	727 – 40%
KHP1000-5	1964	904 – 46%
KHP1000-1	2080	786 – 38%
KHP1000-0.5	1972	722 – 37%
KHP800-10	1553	1154 – 74%
KHP800-5	1991	1335 – 67%
KHP800-1	1460	1329 – 91%
KHP800-0.5	1321	1064 – 81%

There are no clear trends that apply to the textural data of these samples. Generally, surface area and pore volume increase with activation temperature and time. Although surface area increases with activation temperature, microporosity decreases significantly. In terms of achieving a high surface area, whereas

Table 6.6. Surface area of samples prepared from KHP, airchar and hydrochar, calculated by BET theory. [a]Proportion of surface area arising from micropores, as a value and as a % of total surface area

Sample	Surface Area ($m^2\ g^{-1}$)	[a]Micropore Surface Area ($m^2\ g^{-1}$)
AC-KHP(6)1000	740	614 – 83%
AC-KHP(5)1000	786	646 – 82%
AC-KHP(4)1000	1224	979 – 80%
AC-KHP(3)1000	1237	623 – 50%
AC-KHP(6)900	825	724 – 88%
AC-KHP(5)900	923	783 – 85%
AC-KHP(4)900	979	798 – 82%
AC-KHP(3)900	1566	1234 – 79%
HC-KHP(4)1000	903	559 – 62%
HC-KHP(3)900	1190	816 – 69%

at 800 °C ('standard' temperature) a moderate activation time of 5 hrs is optimal, at the extreme temperature of 1200 °C a long activation time of 10 hrs is optimal. However at both temperatures, a very short activation time of 0.5 hrs results in the highest proportion of microporosity.

Table 6.7. Pore volume of samples prepared from KHP. [a]Proportion of pore volume arising from micropores, as a value and as a % of total pore volume

Sample	Pore Volume ($cm^3\ g^{-1}$)	[a]Micropore Volume ($cm^3\ g^{-1}$)
KHP1200-10	1.36	0.08 – 6%
KHP1200-5	1.19	0.09 – 8 %
KHP1200-1	1.08	0.24 – 22%
KHP1200-0.5	1.09	0.30 – 28%
KHP1000-10	1.01	0.29 – 29%
KHP1000-5	0.98	0.36 – 37%
KHP1000-1	1.18	0.31 – 26%
KHP1000-0.5	1.13	0.29 – 26%
KHP800-10	0.68	0.46 – 68%
KHP800-5	0.94	0.53 – 56%
KHP800-1	0.62	0.53 – 85%
KHP800-0.5	0.66	0.43 – 65%

The surface area and pore volume data for samples activated with an additional carbon source are displayed in Tables 6.6 and 6.8. The samples show good surface area and pore volume. The highest surface area of 1566 $m^2\ g^{-1}$ is exhibited by AC-KHP(3)900, with a corresponding proportion of microporosity of

Table 6.8. Pore volume of samples prepared from KHP, airchar and hydrochar. [a]Proportion of pore volume arising from micropores, as a value and as a % of total pore volume

Sample	Pore Volume ($cm^3\ g^{-1}$)	[a]Micropore Volume ($cm^3\ g^{-1}$)
AC-KHP(6)1000	0.35	0.25 – 71%
AC-KHP(5)1000	0.36	0.26 – 72%
AC-KHP(4)1000	0.59	0.39 – 66%
AC-KHP(3)1000	0.78	0.25 – 32%
AC-KHP(6)900	0.36	0.29 – 81%
AC-KHP(5)900	0.42	0.32 – 76%
AC-KHP(4)900	0.46	0.32 – 70%
AC-KHP(3)900	0.76	0.49 – 64%
HC-KHP(4)1000	0.51	0.23 – 45%
HC-KHP(3)900	0.63	0.33 – 52%

79 %. The largest pore volume of 0.78 $cm^3\ g^{-1}$ is exhibited by AC-KHP(3)1000, with a corresponding proportion of microporosity of 32 %. The lowest surface area and pore volume of 740 $m^2\ g^{-1}$ (corresponding microporosity of 83 %) and 0.35 $cm^3\ g^{-1}$ (corresponding microporosity of 71 %) respectively, were both exhibited by AC-KHP(6)1000. This data is in line with the isotherms displayed in Figures 6.19 and 6.20. It is clear that a higher proportion of carbon (and therefore a

lower proportion of K) during activation results in less developed porosity, but a greater proportion of microporosity. Generally, samples activated with an additional carbon source show poorer pore development than those activated from KHP alone, indicated by lower surface areas and pore volumes. However, they generally show higher proportions of microporosity, crucial for low pressure CO_2 uptake.[31,35,37]

The effect of temperature on samples activated with an additional carbon source is minimal; proportion of K is a more influential factor. However, the lower activation temperature of 900 °C generally results in slightly higher proportions of microporosity. As predicted from studying the N_2 sorption isotherms (Fig. 6.16 – 6.21), samples activated with airchar as the additional carbon source exhibit more developed porosity, with greater retention of microporosity, than equivalent samples activated with hydrochar, confirming the resistance of airchar to excessive activation.

6. 4. 7. Textural Properties; Pore Size Distributions

Pore size distributions (PSDs) and pore maxima values for all samples were calculated using non-local density functional theory and are displayed below in Figures 6.22 – 6.27 and Tables 6.9 and 6.10. The PSDs for samples activated without an additional carbon source are displayed in Figures 6.22 – 6.24. The samples show similar PSDs, dominated by micropores, with varying degrees of small mesoporosity. This is in line with isotherm and textural data. All samples show significant pore volume at 5.9 Å. All samples activated at either 1000 or 1200 °C also show significant pore volume at 11.8 Å. This can be assumed to be due to the collapse of small pores of width 5.9 Å into pores of 11.8 Å at the harsher activation temperatures. Pore volume of 11.8 Å for samples activated at 800 °C is minimal. As the activation temperature increases from 800 to 1200 °C, there is significant broadening of the PSDs into the small mesopore region. Samples activated at 800 °C (Fig. 6.24) show minimal mesoporosity. At 1000 and 1200 °C (Fig. 6.23 and 6.22) pore maxima at 21.6 and 27.3 Å appear. This occurs to a greater extent for samples activated at the harshest temperature of 1200 °C, which also sees significant pore volume at 34.3 Å. At 800 and 1000 °C, there is no significant change in PSD with increasing activation time. At

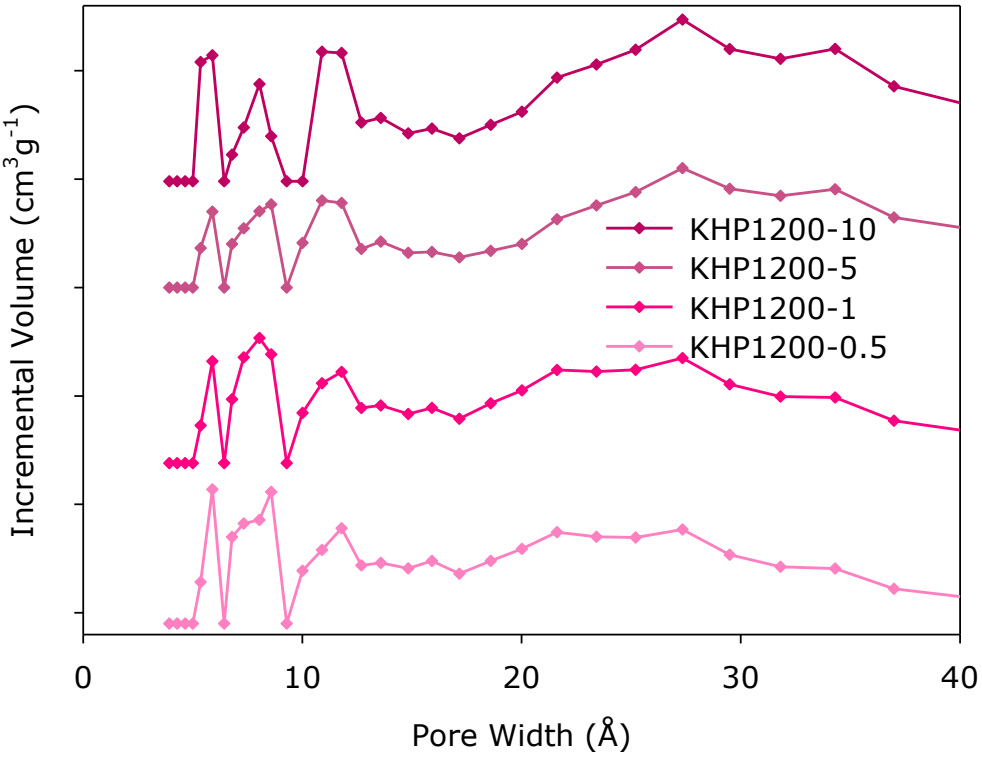

Figure 6.22. PSDs for samples prepared from KHP at 1200 °C

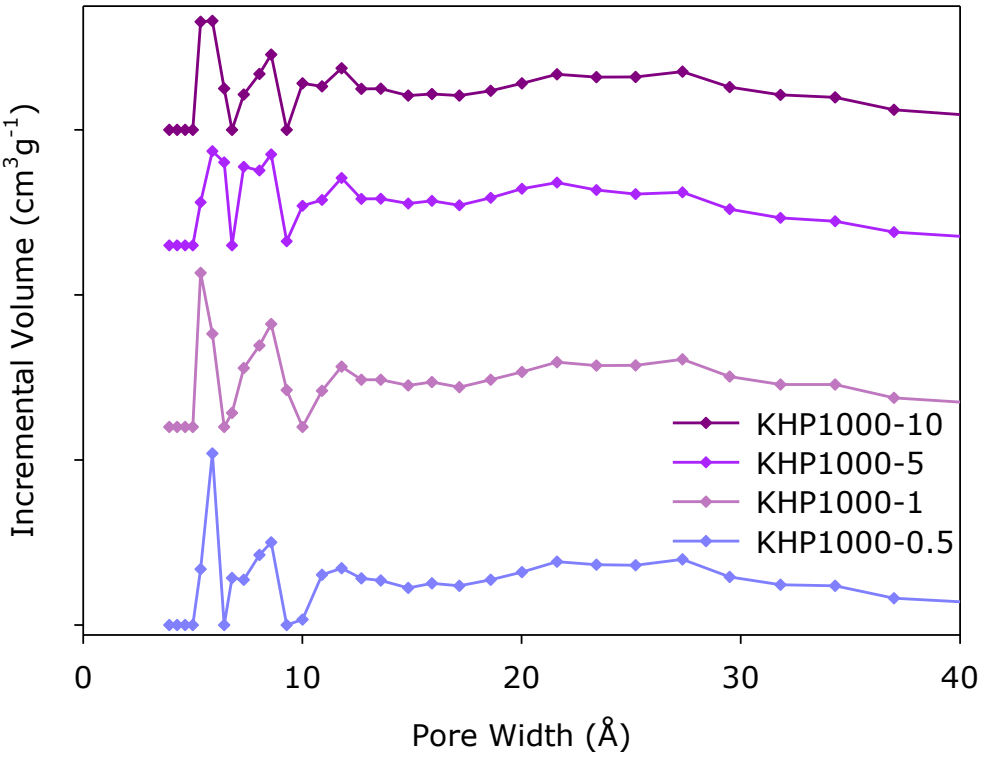

Figure 6.23. PSDs for samples prepared from KHP at 1000 °C

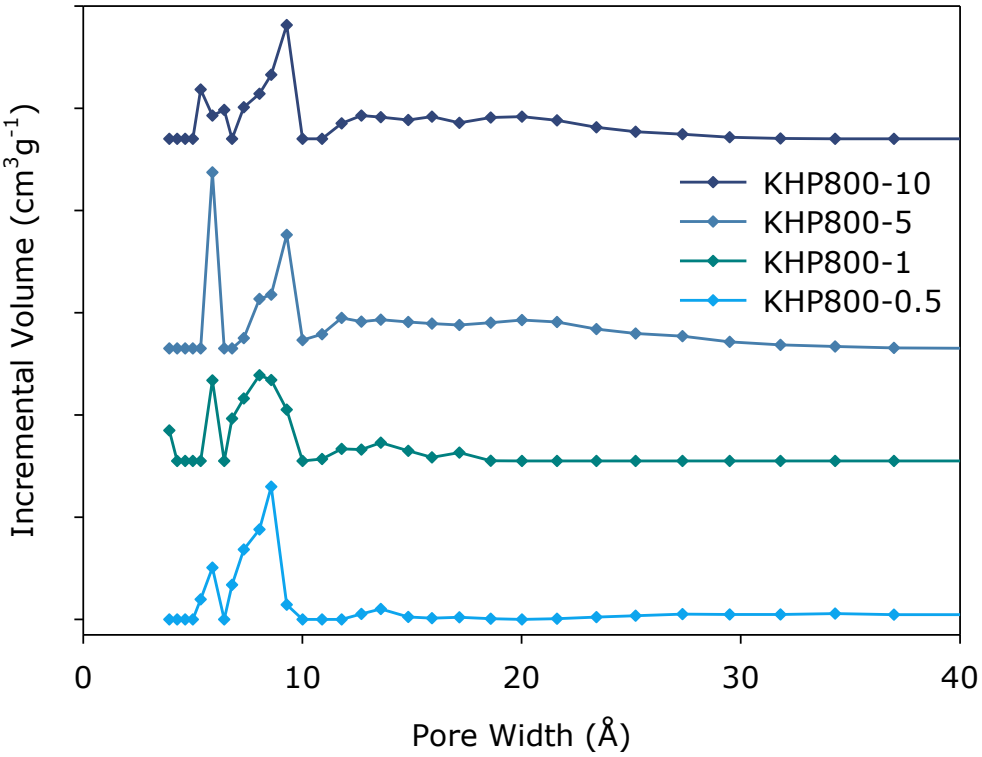

Figure 6.24. PSDs for samples prepared from KHP at 800 °C

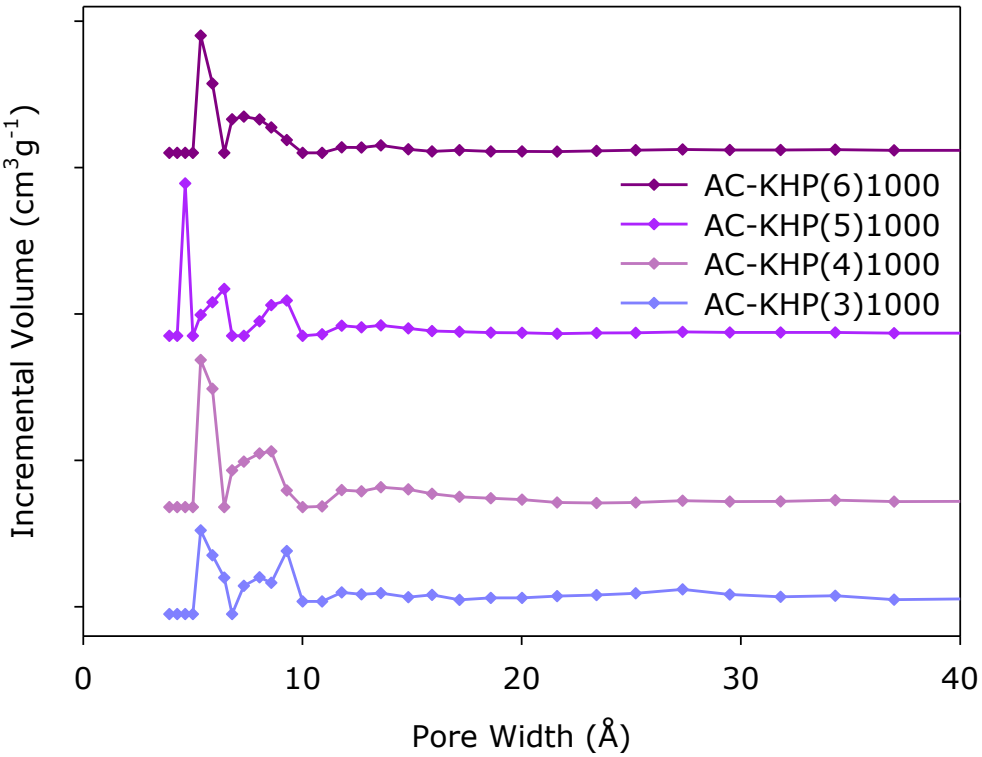

Figure 6,25. PSDs for samples prepared from airchar and KHP at 1000 °C

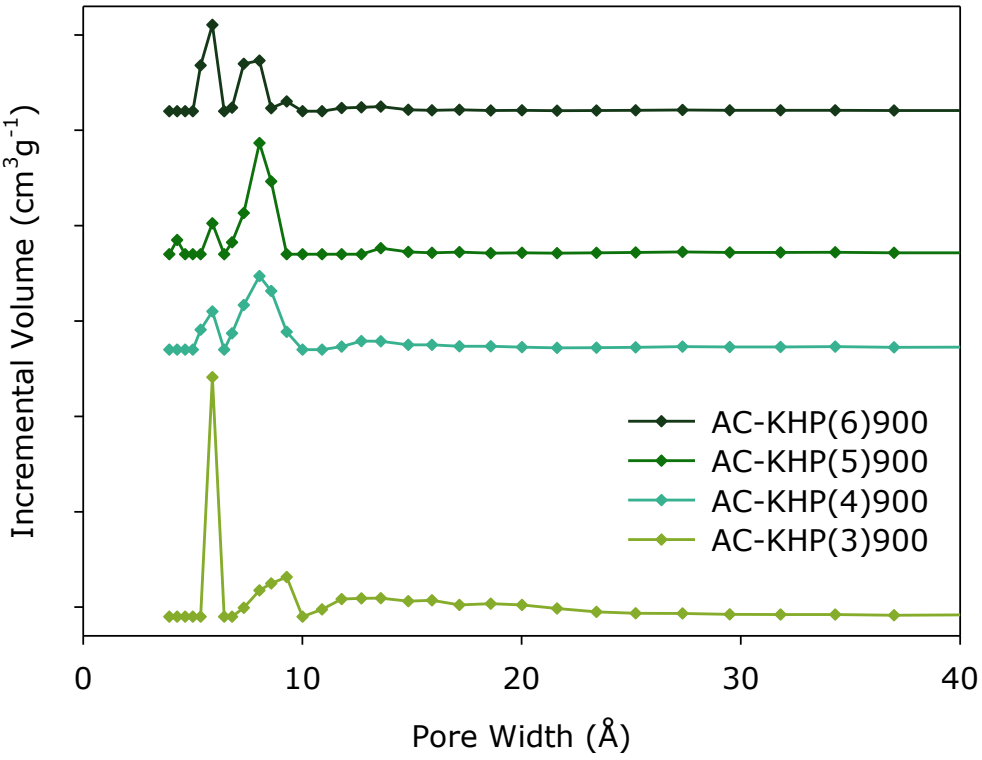

Figure 6.26. PSDs for samples prepared from airchar and KHP at 900 °C

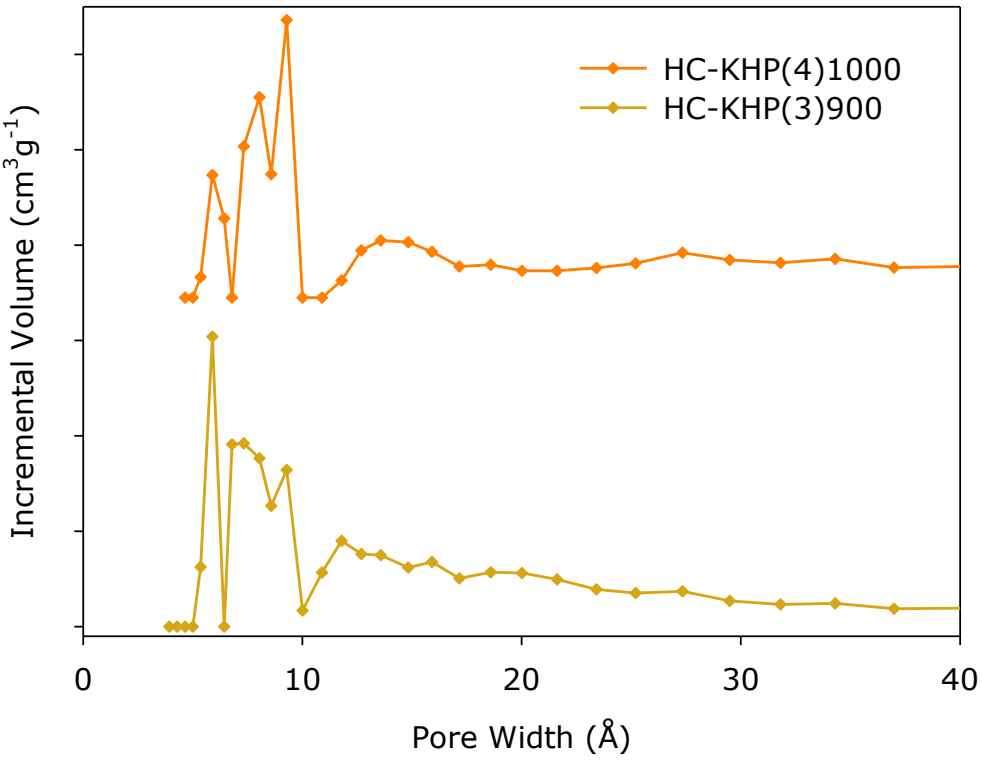

Figure 6.27. PSDs for samples prepared from hydrochar and KHP

Table 6.9. PSD maxima of samples prepared from KHP, obtained from NLDFT analysis

Sample	Pore Maxima (Å)	
	< 20 Å	**> 20 Å**
KHP1200-10	5.9/8.1/10.9/11.8	27.3/34.3
KHP1200-5	5.9/8.6/10.9/11.8	27.3/34.3
KHP1200-1	5.9/8.1/11.8	21.6/27.3
KHP1200-0.5	5.9/8.6/11.8	21.6/27.3
KHP1000-10	5.4/5.9/8.6/11.8	21.6/27.3
KHP1000-5	5.9/7.3/8.6/11.8	21.6/27.3
KHP1000-1	5.4/8.6/11.8	21.6/27.3
KHP1000-0.5	5.9/8.6/11.8	21.6/27.3
KHP800-10	5.4/9.3	20.0
KHP800-5	5.9/9.3	20.0
KHP800-1	5.9/8.6/17.2	N/A
KHP800-0.5	5.9/8.6	N/A

1200 °C, increasing activation time from 0.5 to 10 hrs causes noticeable increase in the proportion of mesoporosity, in line with the sorption isotherm data. However, it is clear that activation temperature has a greater effect on pore distribution than activation time.

Table 6.10. PSD maxima of samples prepared from KHP, airchar and hydrochar, obtained from NLDFT analysis

Sample	Pore Maxima (Å), < 20 Å
AC-KHP(6)1000	5.4/7.3/8.0
AC-KHP(5)1000	4.7/6.5/9.3
AC-KHP(4)1000	5.4/8.4
AC-KHP(3)1000	5.4/8.0/9.3
AC-KHP(6)900	5.9/7.4/8.0/9.3
AC-KHP(5)900	4.3/5.9/8.0
AC-KHP(4)900	5.9/8.0
AC-KHP(3)900	5.9/9.3
HC-KHP(4)1000	5.9/8.0/9.3/13.6
HC-KHP(3)900	5.9/7.4/9.3/11.8/15.9

The PSDs for samples activated with an additional carbon source are displayed in Figures 6.25, 6.26 and 6.27. The samples all show a similar PSD, dominated by small micropores < 10 Å, in line with isotherm data. Samples activated at 900 °C with airchar as the additional carbon source, all show significant pore volume at 5.9 Å, and another pore maxima between 8 – 9.3 Å. The equivalent samples activated at 1000 °C display smaller pore maxima, at 4.7 – 5.4 Å and at 6.5 – 9.3 Å. This

suggests that activation at the lower temperature creates slightly smaller pores. Both samples activated with hydrochar as the additional carbon source show 3 peak maxima < 10 Å, at 5.9 Å, 7.4 – 8.0 Å and 9.3 Å. This distribution is similar to the airchar-added samples. However, both HC-KHP(4)1000 and HC-KHP(3)900 show a broadening of the PSD into the large micro- and small mesopore region, with pore volumes extending up to ~ 30 Å. This corresponds with the type H4 hysteresis loops seen on the sorption isotherms (Fig. 6.21) and the low proportion of microporosity recorded in the textural data. This is evidence of the less resistant nature of hydrochar to activation than airchar.

Overall, samples activated with additional carbon exhibit a narrower PSD than those activated without. In particular, samples activated with airchar as the carbon source exhibit a very controlled porosity centred in the small micropore region < 10 Å. The development of a controlled porosity may be a result of two factors: the resistant nature of airchar and the lower K:C ratio of the samples activated with additional char.

6. 4. 8. CO_2 Uptake Analysis

The CO_2 uptake capabilities of the carbon samples were analysed gravimetrically at 25 °C over a pressure range of 0 – 40 bar. The adsorption isotherms up to 1 bar and 40 bar are shown below in Figures 6.28 – 6.39. The molar uptakes for the samples at a range of pressures is displayed in Tables 6.11 – 6.12. It is important to analyse CO_2 uptake capabilities at very low pressure of 0.15 bar to simulate typical conditions of a post-combustion flue gas stream. Analysis at 1 bar gives further information about low pressure uptake, while analysis at 20 and 40 bar provides uptake information at medium and high pressure respectively.

The CO_2 uptake isotherms for samples prepared from KHP alone are displayed in Figures 6.28 – 6.33, with quantitative data recorded in Table 6.11. CO_2 uptake at 0.15 bar ranges between 0.5 and 1.3 mmol g^{-1}, which is among the highest uptakes at this pressure recorded in previous studies.[12,31,35,37] The lowest uptake of 0.5 mmol g^{-1} was exhibited by KHP1200-5, in line with the sample's textural data. KHP1200-5 possesses a large pore volume in the large micropore/small mesopore region (Fig. 6.22), with an average pore size of 27.3 Å and among the lowest proportion of microporosity of this sample set. This pore structure is

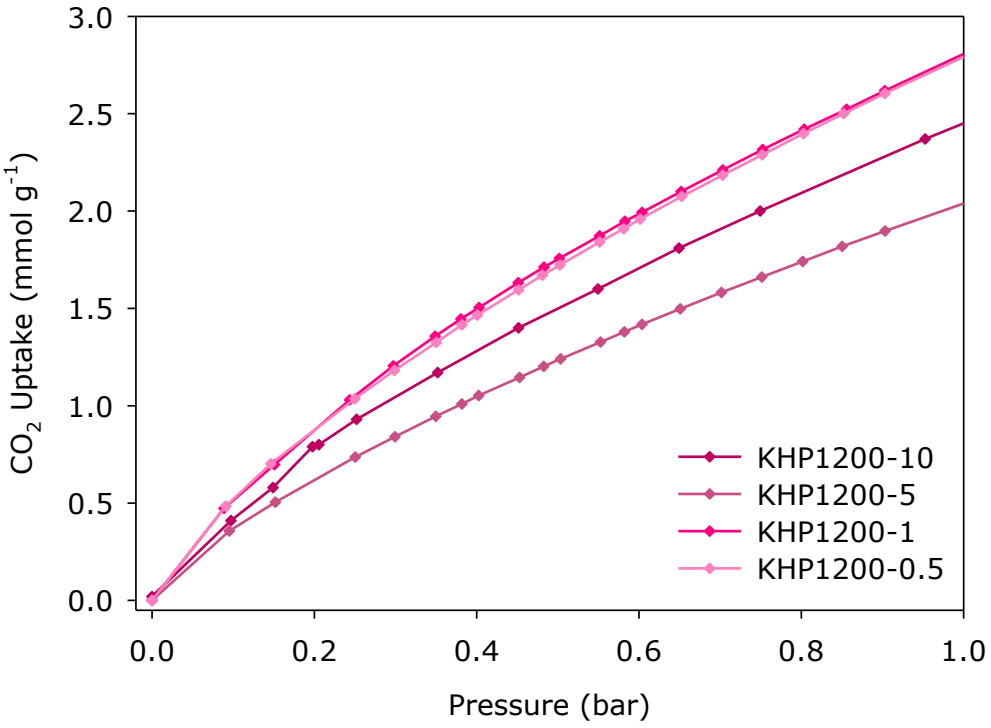

Figure 6.28. CO_2 uptake up to 1 bar for samples prepared from KHP at 1200 °C

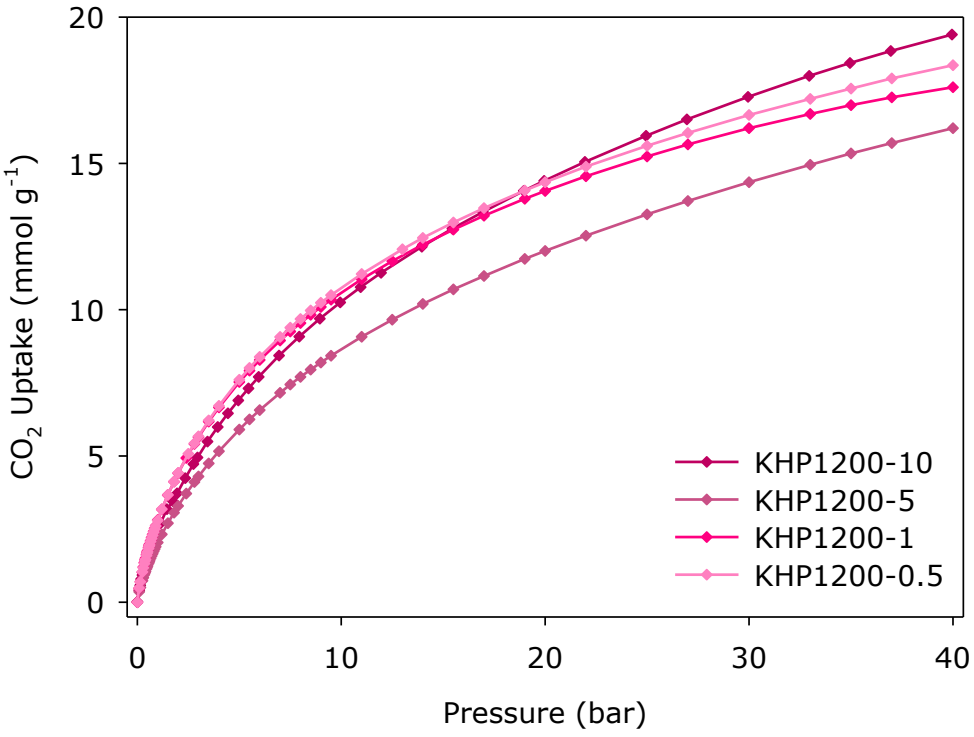

Figure 6.29. CO_2 uptake up to 40 bar for samples prepared from KHP at 1200 °C

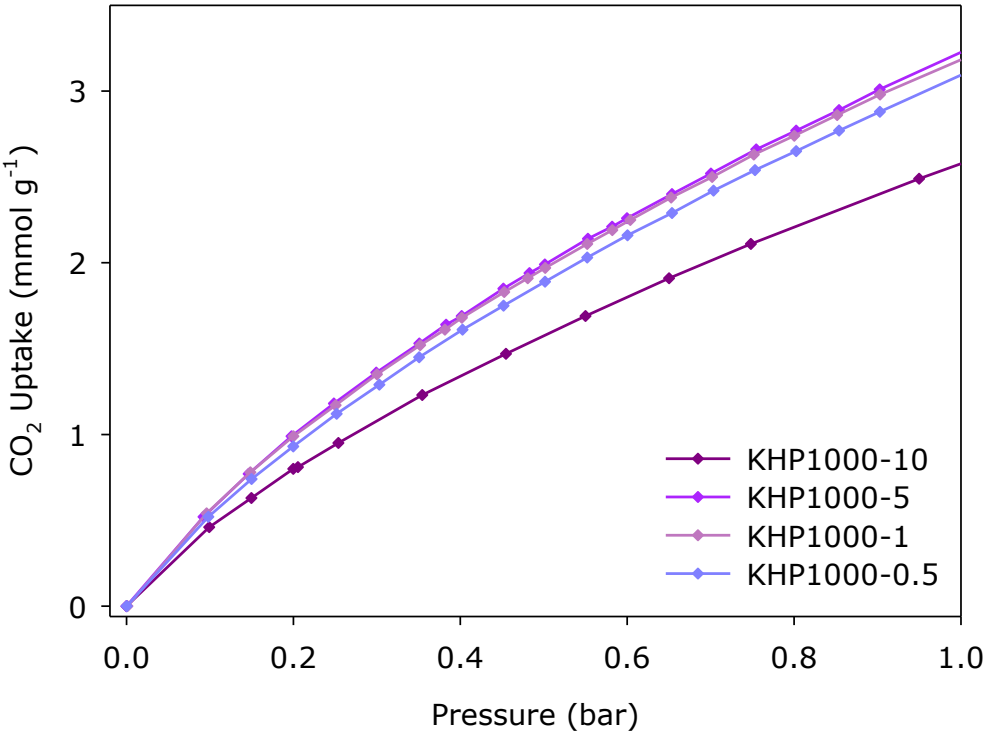

Figure 6.30. CO_2 uptake up to 1 bar for samples prepared from KHP at 1000 °C

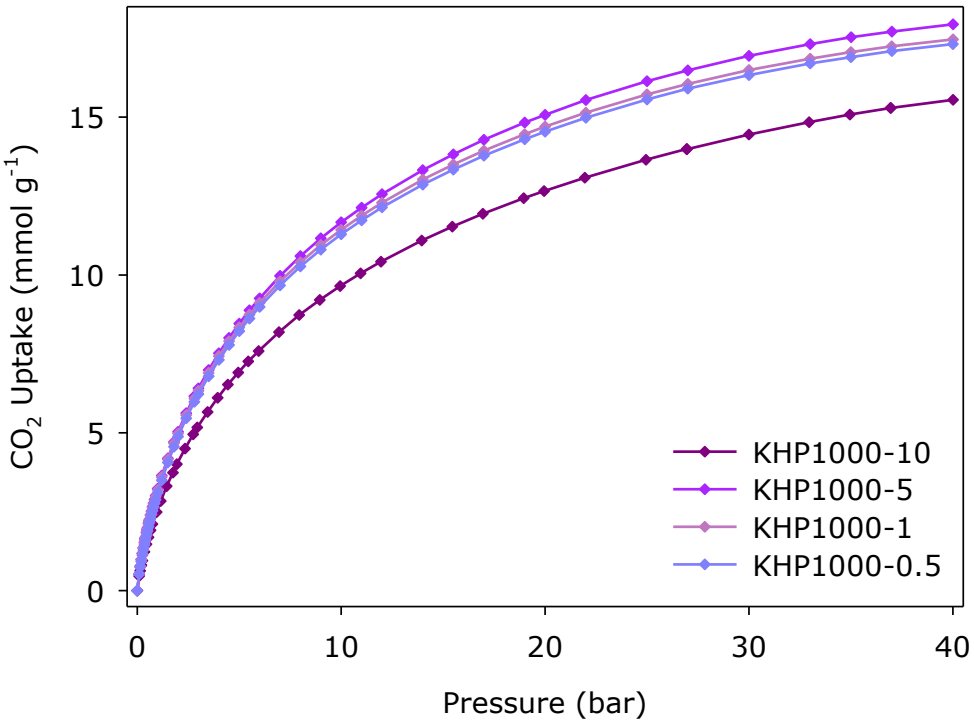

Figure 6.31. CO_2 uptake up to 40 bar for samples prepared from KHP at 1000 °C

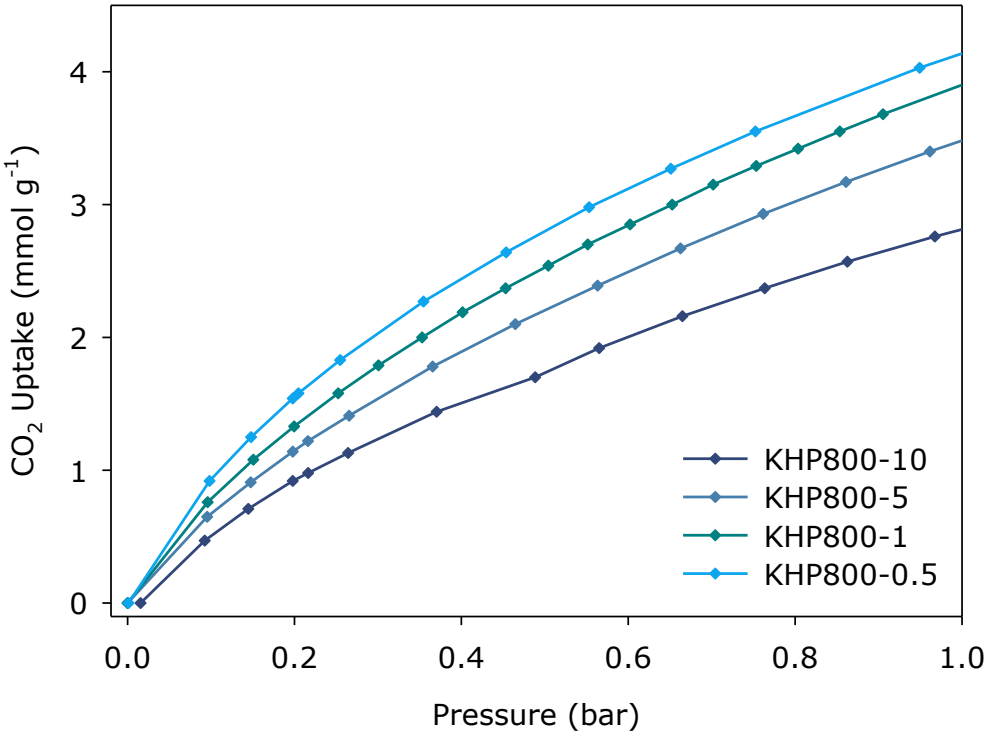

Figure 6.32. CO_2 uptake up to 1 bar for samples prepared from KHP at 800 °C

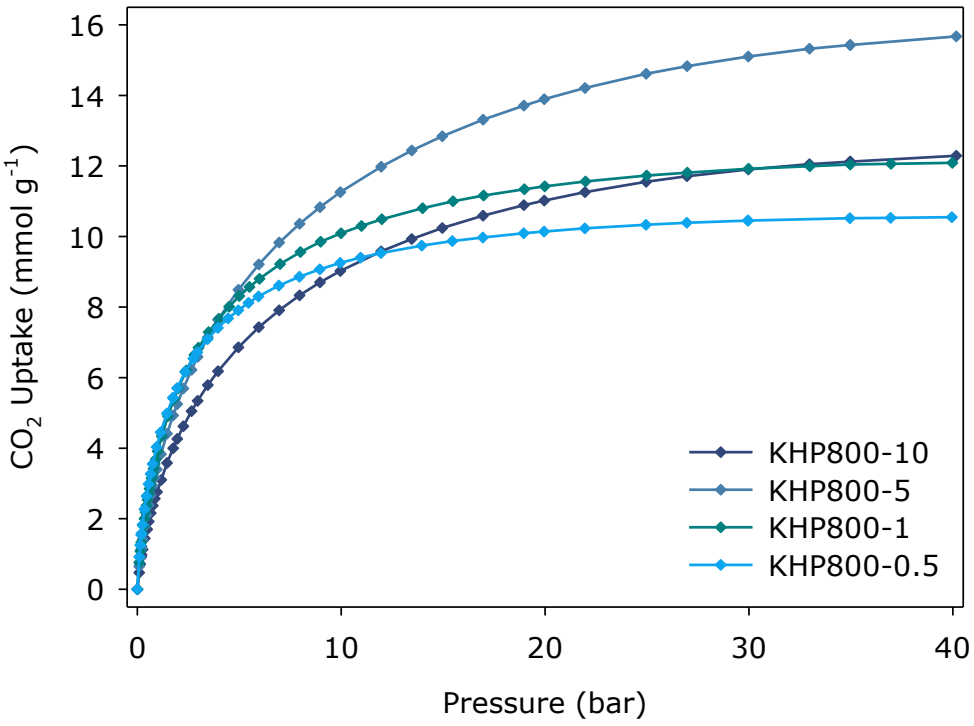

Figure 6.33. CO_2 uptake up to 40 bar for samples prepared from KHP at 800 °C

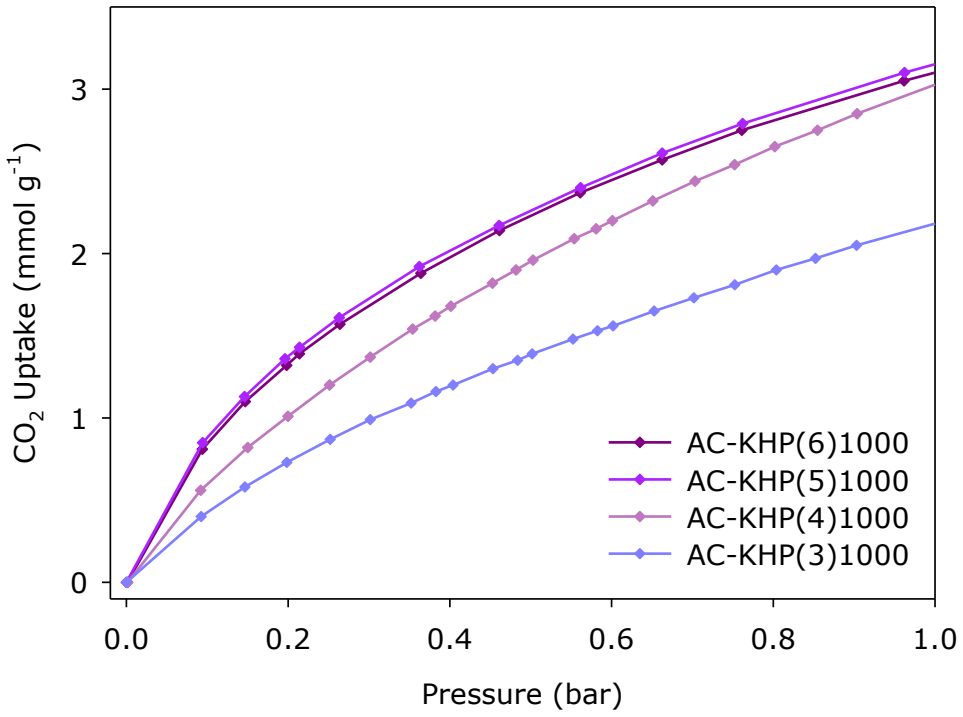

Figure 6.34. CO_2 uptake up to 1 bar for samples prepared from airchar and KHP at 1000 °C

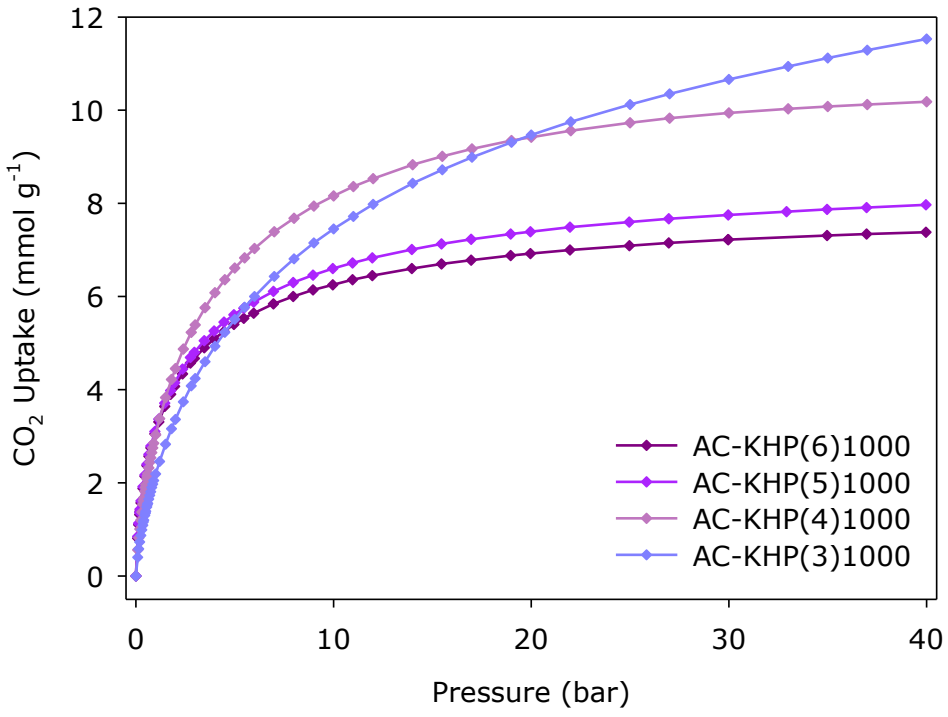

Figure 6.35. CO_2 uptake up to 40 bar for samples prepared from airchar and KHP at 1000 °C

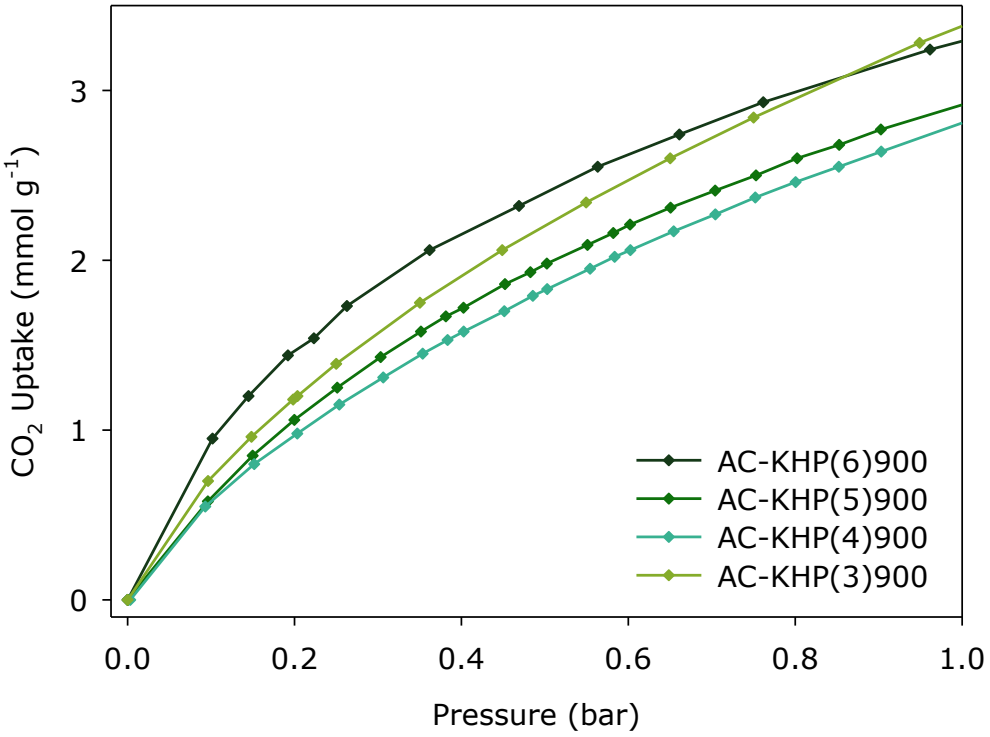

Figure 6.36. CO_2 uptake up to 1 bar for samples prepared from airchar and KHP at 900 °C

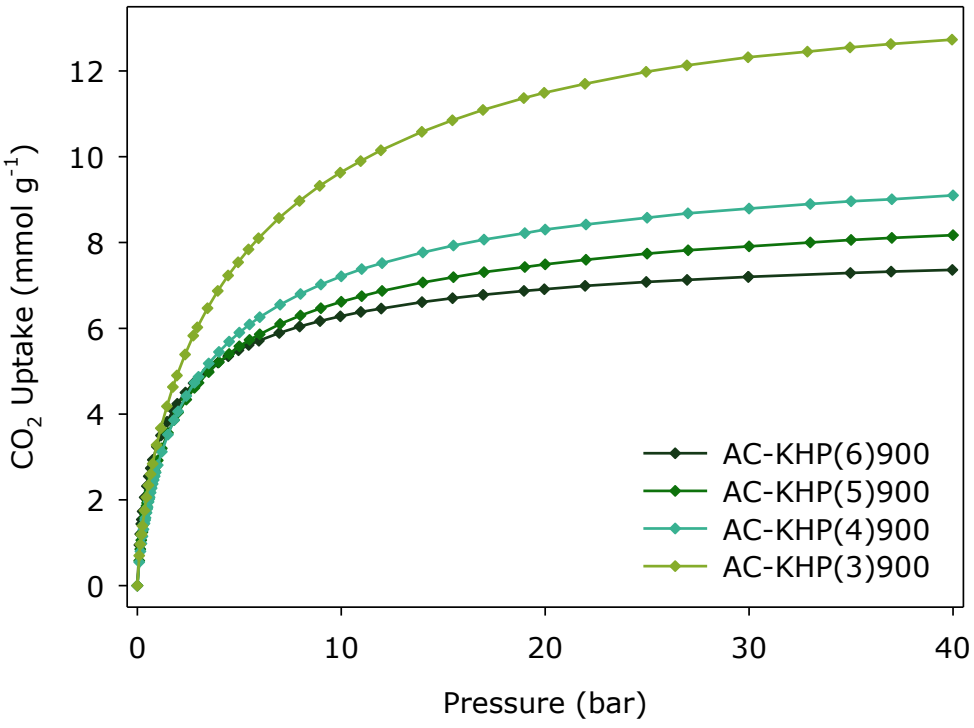

Figure 6.37. CO_2 uptake up to 40 bar for samples prepared from airchar and KHP at 900 °C

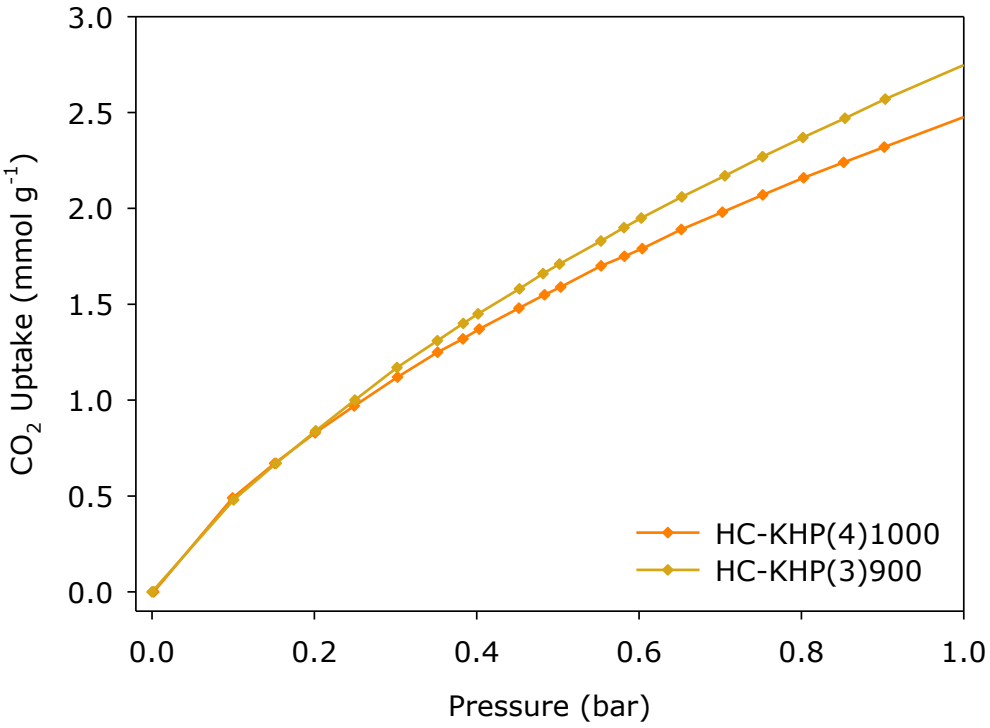

Figure 6.38. CO_2 uptake up to 1 bar for samples prepared from hydrochar and KHP

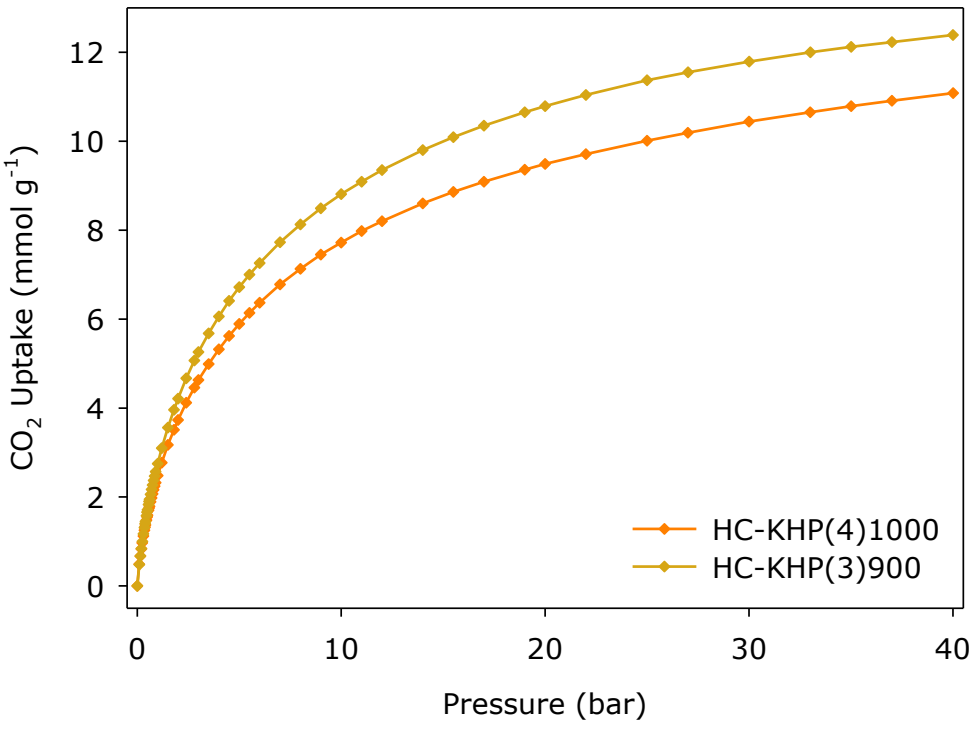

Figure 6.39. CO_2 uptake up to 40 bar for samples prepared from hydrochar and KHP

Table 6.11. CO_2 uptake at 25 °C over a range of pressures of samples produced from KHP

Sample	CO_2 Uptake (mmol g^{-1})			
	0.15 bar	**1 bar**	**20 bar**	**40 bar**
KHP1200-10	0.6	2.5	14.4	19.4
KHP1200-5	0.5	2.0	12.0	16.2
KHP1200-1	0.8	2.8	14.1	17.6
KHP1200-0.5	0.7	2.8	14.3	18.3
KHP1000-10	0.7	2.6	12.7	15.6
KHP1000-5	0.8	3.2	15.1	17.9
KHP1000-1	0.8	3.2	14.7	17.5
KHP1000-0.5	0.7	3.1	14.5	17.3
KHP800-10	0.7	2.8	11.0	12.2
KHP800-5	0.9	3.5	13.9	15.6
KHP800-1	1.1	3.9	11.4	12.1
KHP800-0.5	1.3	4.1	10.1	10.5

characteristic of low uptake at low pressures.[31,35,37] The highest CO_2 uptake at 0.15 bar of 1.3 mmol g^{-1} was exhibited by KHP800-0.5, despite having the smallest surface area of this sample set (1321 m^2 g^{-1}, Table 6.5). KHP800-0.5 possesses a highly microporous structure with negligible porosity > 10 Å and

Table 6.12. CO_2 uptake at 25 °C over a range of pressures of samples produced from KHP, airchar and hydrochar

Sample	CO_2 Uptake (mmol g^{-1})			
	0.15 bar	**1 bar**	**20 bar**	**40 bar**
AC-KHP(6)1000	1.1	3.1	6.9	7.4
AC-KHP(5)1000	1.1	3.2	7.4	8.0
AC-KHP(4)1000	0.8	3.0	9.4	10.2
AC-KHP(3)1000	0.6	2.2	9.5	11.5
AC-KHP(6)900	1.2	3.3	6.9	7.4
AC-KHP(5)900	0.9	2.9	7.5	8.2
AC-KHP(4)900	0.8	2.8	8.3	9.1
AC-KHP(3)900	1.0	3.4	11.5	12.7
HC-KHP(4)1000	0.7	2.5	9.5	11.1
HC-KHP(3)900	0.7	2.7	10.8	12.4

an average pore size of 8.6 Å (Fig. 6.24), ideal for CO_2 uptake.[1,31]

At 1 bar, the CO_2 uptake for samples activated with no additional carbon source ranged from 2.0 to 4.1 mmol g^{-1}. As with uptake at 0.15 bar, the highest and lowest uptakes were exhibited by KHP1200-5 and KHP800-0.5 respectively. At 20 bar, CO_2 uptake ranges from 10.1 to 15.1 mmol g^{-1}. Here, KHP800-0.5 exhibits the lowest uptake of the sample set of 10.1

mmol g^{-1} due to its small surface area. The highest uptake of 15.1 mmol g^{-1} is exhibited by KHP1000-5. The performance of KHP1000-5 at 20 bar can be explained by its broad porosity. KHP1000-5 possesses a PSD primarily below 10 Å, but contains a significant volume of large micropores > 10 Å and small mesopores in the range 20 – 40 Å (Fig. 6.23). The surface area, pore volume (1964 m^2 g^{-1} and 0.98 cm^3 g^{-1} respectively, Tables 6.5 and 6.7) and microporosity data sit in the middle of the sample set range, and the corresponding isotherm is type I with a broad knee (Fig. 6.17).

At 40 bar, the CO_2 uptake for samples activated without an additional carbon source ranges from 10.5 to 19.4 mmol g^{-1}. The lowest uptake of 10.5 mmol g^{-1} is again exhibited by KHP800-5. The largest uptake of 19.4 mmol g^{-1} is given by KHP1200-10. This sample was activated under the harshest conditions and as a result possesses the largest surface area and pore volume of the sample set (2124 m^2 g^{-1} and 1.36 cm^3 g^{-1} respectively, Tables 6.5 and 6.7), with a very low proportion of microporosity. This broad porosity with high surface area favours high pressure CO_2 uptake.

Overall, activation temperature has a larger and clearer effect of CO_2 uptake capacity than activation time. At 0.15 bar, the average uptake for samples activated at 1200, 1000 and 800

°C is 0.7, 0.8 and 1.0 mmol g^{-1} respectively, increasing to 2.5, 3.0 and 3.6 mmol g^{-1} respectively at 1 bar. The higher the activation time, the broader the PSD, often extending into the small mesopore region. This is due to increased activation reactions taking place at higher temperatures, leading to the development of new, wider pore channels, and the collapse of small pores into larger ones. This increased porosity is determined by a large surface area and pore volume, a structure that does not perform well at low pressures of ≤ 1 bar. At 20 bar the trend changes, with the average CO2 uptake for samples activated at 1200, 1000 and 800 °C increasing to 13.7, 14.3 and 11.6 mmol g^{-1} respectively, reversing to 17.9, 17.1 and 12.6 mmol g^{-1} respectively at 40 bar. Therefore, it is clear that at a mid-pressure of 20 bar, samples activated at 1000 °C, with mid-range surface area, pore volume and microporosity perform best. At high pressure of 40 bar, samples activated at 1200 °C, with high surface area and pore volume, but low proportion of microporosity perform best.

According to the CO_2 adsorption isotherm (Figs. 6.29, 6.31 and 6.33) samples activated at 800 °C reach CO_2 saturation by 40 bar. Sample activated at higher temperatures, especially those activated at 1200 °C do not reach saturation by 40 bar pressure.

The CO_2 uptake isotherms for samples prepared from KHP with an additional carbon source of airchar or hydrochar are displayed in Figures 6.34 – 6.39, with quantitative data recorded in Table 6.12. At very low pressure of 0.15 bar, CO_2 uptake ranges between 0.6 – 1.2 mmol g^{-1}. The lowest uptake of 0.6 mmol g^{-1} is exhibited by AC-KHP(3)1000 which has among the highest surface area and the highest pore volume of this sample set (1237 m^2 g^{-1} and 0.78 cm^3 g^{-1} respectively, Tables 6.6 and 6.8). It displays a large hysteresis in the N_2 sorption isotherm (Fig. 6.19) indicating the presence of mesoporosity and has the lowest proportion of microporosity of this sample set, which can be considered the cause of poor performance at low pressure. The highest CO_2 uptake at 0.15 bar of 1.2 mmol g^{-1} is exhibited by AC-KHP(6)900. AC-KHP(6)900 possesses among the lowest surface area and pore volume of this sample set (825 m^2 g^{-1} and 0.36 cm^3 g^{-1} respectively, Tables 6.6 and 6.8), but the highest proportion of microporosity, resulting in excellent performance at very low pressure.

At pressure of 1 bar, CO_2 uptake ranges between 2.2 – 3.4 mmol g^{-1}. The lowest uptake of 2.2 mmol g^{-1} is again exhibited by AC-KHP(3)1000. This can be attributed to its low proportion of microporosity. The highest uptake of 3.4 mmol g^{-1} is

exhibited by AC-KHP(3)900. AC-KHP(3)900 has the highest surface area and among the highest pore volume of this sample set (1566 m^2 g^{-1} and 0.76 cm^3 g^{-1} respectively, Tables 6.6 and 6.8). PSD data (Fig. 6.26) shows a large proportion of small micropores of 5.9 Å diameter, while the N_2 sorption isotherm (Fig. 6.20) contains a hysteresis indicating an additional presence of mesopores. Good performance of this sample at low pressure can be attributed to the combination of high surface area and a large presence of small micropores.

At 20 bar, CO_2 uptake ranges between 6.9 – 11.5 mmol g^{-1}. The lowest uptake of 6.9 mmol g^{-1} is given by both AC-KHP(6)1000 and AC-KHP(6)900, the two samples activated with the lowest proportion of K. Similar to AC-KHP(6)900, AC-KHP(6)1000 has the lowest surface area and pore volume of this sample set (740 m^2 g^{-1} and 0.35 cm^3 g^{-1} respectively, Tables 6.6 and 6.8) and a good proportion of micropores. At 20 bar, CO_2 uptake ability becomes more dependent on surface area and pore volume, and less on proportion of microporosity. The highest CO_2 uptake at 20 bar of 11.5 mmol g^{-1} is again exhibited by AC-KHP(3)900. At this pressure, it is assumed to be the large surface area and pore volume of AC-KHP(3)900 responsible for the high uptake.

At 40 bar, CO_2 uptake ranges between 7.4 – 12.7 mmol g^{-1}. As seen at 20 bar, the lowest uptake of 7.4 mmol g^{-1} is given by

both AC-KHP(6)1000 and AC-KHP(6)900, due to their low surface area and pore volume. Again, as seen at 20 bar, the highest uptake at 40 bar is given by AC-KHP(3)900, due to its large surface area and pore volume.

The difference in activation temperature within this sample set does not have any significant effect on ultimate CO_2 uptake, although the two temperatures investigated (900 and 1000 °C) are similar. On average, samples activated at 900 °C performed equally, or slightly better than the analogous samples activated at 1000 °C. The minimal effect of temperature was predicted through study of the samples' textural properties; those activated at 900 °C exhibited a slightly increased proportion of microporosity combined with good surface areas when compared with analogous samples activated at 1000 °C.

The C/K ratio during activation has a much more significant effect on ultimate CO_2 uptake. Taking an average of analogous samples activated at the two temperatures, at low pressures ≤ 1 bar, CO_2 uptake decreases with decreasing C/K ratio, where moderate activation leading to a microporous structure is favourable. At higher pressures of 20 and 40 bar, CO_2 uptake increases with decreasing C/K ratio. Extensive activation leading to high surface areas and pore volumes is favourable for high pressure uptake.

AC-KHP(3)900 exhibits high CO_2 uptake across all pressure ranges. A high surface area and pore volume, with a relatively high proportion of microporosity make it ideal for CO_2 uptake across a range of pressure applications. AC-KHP(3)1000 also has a high surface area and pore volume, but has a low proportion of microporosity. This results in low uptake ≤ 1 bar and reasonable uptake ≥ 20 bar. It is clear that a larger K/C ratio results in a more developed porosity, but the addition of airchar retains a high proportion of microporosity. Samples activated with added hydrochar perform below the average performance of airchar-added samples at low pressures (≤ 1 bar), but perform above the average at pressures ≥ 20 bar. The presence of hydrochar promotes the development of a more mesoporous porosity, which performs better at higher pressures. Samples prepared with no additional carbon source perform better across all pressure ranges.

6. 5. Conclusions

An investigation was conducted into the effects of extreme activation conditions, including activation temperatures up to 1200 °C and activation duration up to 10 hrs. A family of porous carbons were produced from an organic metal salt, potassium hydrogen phthalate (KHP), activated under a range of conditions. KHP800-1, activated under 'standard conditions' exhibited a highly microporous and amorphous structure with relatively low thermal stability. C/O ratio was low (7.4) although carbon yield was high (17.3 %). The sample possessed surface area and pore volume of 1460 m^2 g^{-1} and 0.62 cm^3 g^{-1} respectively (corresponding microporosity of 91 and 85 % respectively), with a narrow PSD centred below 10 Å. These factors resulted in a carbon that performed well in terms of CO_2 uptake at low pressures (1.1 and 3.9 mmol g^{-1} at 0.15 and 1 bar, respectively), becoming saturated by 20 bar.

To investigate the effects of harsher activation conditions, samples were prepared from KHP at temperatures up to 1200 °C and for durations of up to 10 hrs. The data shows that an increased activation temperature has a more substantial effect than increased activation duration.

Longer activations at higher temperatures results in extensive reactions of K-compounds with the carbon skeleton, increasing the evolution of CO_2 and CO. This increases C/O ratio but decreases overall carbon yield. The observed decrease in carbon yield is generally mild, except in the case of KHP1200-10 and KHP120-5 where there is a drastic decrease in yield to only 4.6 and 9.1 % respectively. An increased activation temperature and time allows the generous formation of graphitic domains, increasing thermal stability in most samples. However, thermal stability is lower than expected for KHP1200-10 and KHP1000-10; extensive activation may lead to pore structure collapse, disrupting graphitic domains.

KHP was chosen as a starting material due to its reliability at producing microporous carbons. Indeed, all N_2 sorption isotherms of this sample set are strongly type I, with KHP1200-1 and KHP1200-0.5 still retaining a good degree of microporosity. Increasing activation temperature from 800 to 1000 °C results in a significant increase in surface area, although the increase from 1000 °C to 1200 °C is not as substantial. Samples activated at 1000 °C retain 37 – 46 % microporous surface area, compared with samples activated at 1200 °C, which exhibit as low as 8 % microporosity. Samples activated at both 1000 and 1200 °C show a substantial increase

in pore volume compared with analogous samples activated at 800 °C. As with surface area, microporous volume is retained to some extent at 1000 °C (26 – 37 %), but a big reduction at 1200 °C indicates highly mesoporous samples. This is confirmed by the PSDs.

Overall, all samples activated at 1000 and 1200 °C have high surface area and pore volume, with some degree of microporosity. Such conditions efficiently produce carbons with mixed proportions of meso and microporosity, resulting in good CO_2 uptake across all pressure ranges, as well as potential use in applications requiring mesoporous carbons. However, the most extreme conditions (1000-10, 1200-5 and 1200-10) begin to be detrimental to pore development, leading to pore collapse and very low carbon yields.

A further investigation was conducted into how a large reduction of carbon yield can be avoided. A series of samples were activated alongside an additional carbon source of either spruce wood-derived airchar that has been previously shown to retain microporosity effectively, or a traditional eucalyptus wood-derived hydrochar. This series of samples contained a lower C/O ratio but significantly higher carbon yield than samples activated with no added carbon source. The samples are still highly porous; all N_2 sorption isotherms are strongly

type I, although the presence of hysteresis indicates some mesoporosity in samples activated at a C/K ratio of 3. The higher proportion of K in these samples results in more extensive reactions with the carbon skeleton, broadening the PSD into the mesopore region. However, microporosity data shows that the level of mesoporosity is small and overall, the sample series shows significantly higher levels of microporosity than samples activated with no additional carbon.

Compared with the first sample series, carbon-added samples generally have lower surface area and pore volumes. This, along with the larger proportion of microporosity can be attributed to the lower proportion of K when additional carbon is used.

Due to the high levels of microporosity and lower surface area, these samples perform well in terms of CO_2 uptake at low pressures of 0.15 and 1 bar, but are less efficient at higher pressures. The high proportion of microporosity results in these carbons performing better at 0.15 bar (flue gas conditions) than those samples activated with no additional carbon source.

Overall, using additional carbon during activation produces high yielding, highly microporous carbons that are excellent adsorbents for very low pressure CO_2.

This investigation also studied the effect of char type (airchar or hydrochar) when used as an additional carbon source. Adding hydrochar produced a higher C/O ratio and similar carbon yield compared with adding airchar. PXRD patterns indicated that the use of hydrochar created much more ordered and graphitic carbons than airchar. Thermal stability is unaffected. Greater hysteresis exhibited by hydrochar-added samples indicates a greater presence of mesopores, which is confirmed by the PSDs. This was expected as airchar has previously been shown to be better at retaining microporosity, and the higher oxygen content of hydrochar may make it more reactive towards activation. As a result of the more ordered, mesoporous structure, hydrochar-added samples show lower surface area, pore volumes and microporosity than the analogous samples activated with airchar.

HC-KHP(3)900 exhibited lower CO_2 uptake capacity than AC-KHP(3)900 across as pressure ranges. HC-KHP(4)1000 performed worse at lower pressures, but better at higher pressures than AC-KHP(4)1000.

Overall, the addition of hydrochar produces a less developed, more mesoporous structure than carbons produced with the addition of airchar.

6. 6. Future Work

A further investigation into the activation of KHP at 1200 °C, for a duration of up to 10 hrs with an additional carbon source, would determine whether the low carbon yield of such conditions could be overcome.

Samples activated without an additional carbon source which have high surface area and pore volume and a large proportion of mesoporosity, may be suitable for applications such as methane storage, pollutant removal or drug delivery. Further studies could investigate their potential in alternative fields.

Repeating the study with an alternative organic metal salt, such as potassium phthalimide, would provide more information about the effects of harsh activation conditions on a self-activating material. Activating this with a char would allow further analysis of the benefits of an additional carbon source.

6. 7. References

1 M. Sevilla and R. Mokaya, *Energy Environ. Sci.*, 2014, **7**, 1250–1280.

2 C. R. Correa and A. Kruse, *Materials (Basel).*, 2018, **11**, 1568.

3 M. A. Lillo-Rodenas, J. Juan-Juan, D. Cazorla-Amor and A. Linares-Solano, *Carbon N. Y.*, 2004, **42**, 1371–1375.

4 J. Wang and S. Kaskel, *J. Mater. Chem.*, 2012, **22**, 23710–23725.

5 M. Sevilla and A. B. Fuertes, *Energy Environ. Sci.*, 2011, **4**, 1765–1771.

6 M. Sevilla and A. B. Fuertes, *J. Colloid Interface Sci.*, 2012, **366**, 147–154.

7 E. Jang, S. W. Choi and K. B. Lee, *Fuel*, 2019, **248**, 85–92.

8 S. Deng, H. Wei, T. Chen, B. Wang, J. Huang and G. Yu, *Chem. Eng. J.*, 2014, **253**, 46–54.

9 S. Lee and S. Park, *J. Colloid Interface Sci.*, 2013, **389**, 230–235.

10 Z. Liu, Z. Du, H. Song, C. Wang, F. Subhan, W. Xing and Z. Yan, *J. Colloid Interface Sci.*, 2014, **416**, 124–132.

11 M. Sevilla, G. A. Ferrero and A. B. Fuertes, *Carbon N. Y.*,

2017, **114**, 50–58.

12 H. M. Coromina, D. A. Walsh and R. Mokaya, *J. Mater. Chem. A*, 2016, **4**, 280–289.

13 G. Singh, K. S. Lakhi, K. Ramadass, C. I. Sathish and A. Vinu, *ACS Sustain. Chem. Eng.*, 2019, **7**, 7412–7420.

14 Y. Kim, B. Lee, H. Suezaki, T. Chino, Y. Abe, T. Yanagiura, K. Chul and M. Endo, *Carbon N. Y.*, 2006, **44**, 1592–1595.

15 Z. Ma, Z. Zhang, Y. Qu, F. Lai, Q. Li, X. Wu, Q. Wu, Q. Li, H. Wang and Y. Huang, *Microporous Mesoporous Mater.*, 2019, **281**, 50–56.

16 S. Joseph, D. M. Kempaiah, M. R. Benzigar, H. Ilbeygi, G. Singh, S. Naidu Talapaneni, D. Park and A. Vinu, *Microporous Mesoporous Mater.*, 2019, **280**, 337–346.

17 X. Liu, L. Zhou, J. Li, Y. Sun, W. Su and Y. Zhou, *Carbon N. Y.*, 2006, **44**, 1386–1392.

18 B. Yuan, X. Wu, Y. Chen, J. Huang, H. Luo and S. Deng, *Environ. Sci. Technol.*, 2013, **47**, 5474–5480.

19 H. Zhou, S. Zhu, I. Honma and K. Seki, *Chem. Phys. Lett.*, 2004, **396**, 252–255.

20 H. Tamai, U. Nobuaki and H. Yasuda, *Mater. Chem. Phys.*, 2009, **114**, 10–13.

21 C. Liang, Z. Li and S. Dai, *Angew. Chemie - Int. Ed.*, 2008, **47**, 3696–3717.

22 X. He, Y. Zhang, C. Zhu, H. Huang, H. Hu, Y. Liu and Z. Kang, *New J. Chem.*, 2015, **39**, 8667–8672.

23 R. V Ramanujan, S. Purushotham and M. H. Chia, *Mater. Sci. Eng. C*, 2007, **27**, 659–664.

24 Q. Zhao, Y. Lin, N. Han, X. Li, H. Geng, X. Wang, Y. Cui and S. Wang, *Drug Deliv.*, 2017, **24**, 94–107.

25 J. Zhu, L. Liao, X. Bian, J. Kong, P. Yang and B. Liu, *Small*, 2012, **8**, 2715–2720.

26 Y. Zheng, H. Niu, D. He, S. Wang, Y. Cai and S. Zhang, *Microporous Mesoporous Mater.*, 2019, **276**, 251–259.

27 J. Galán, A. Rodríguez, J. M. Gómez, S. J. Allen and G. M. Walker, *Chem. Eng. J.*, 2013, **219**, 62–68.

28 G. Yang, L. Tang, G. Zeng, Y. Cai, J. Tang, Y. Pang, Y. Zhou, Y. Liu, J. Wang, S. Zhang and W. Xiong, *Chem. Eng. J.*, 2015, **259**, 854–864.

29 M. Sevilla, A. B. Fuertes and R. Mokaya, *Energy Environ. Sci.*, 2011, **4**, 1400.

30 M. Sevilla and A. B. Fuertes, *J. Mater. Chem. A*, 2013, **1**, 13738–13741.

31 B. Adeniran, E. Masika and R. Mokaya, *J. Mater. Chem.*

A, 2014, **2**, 14696.

32 W. Sangchoom and R. Mokaya, *ACS Sustain. Chem. Eng.*, 2015, **3**, 1658–1667.

33 B. Adeniran and R. Mokaya, *Chem. Mater.*, 2016, **28**, 994–1001.

34 E. Haffner-Staton, N. Balahmar and R. Mokaya, *J. Mater. Chem. A*, 2016, **4**, 13324–13335.

35 E. Hirst, A. Taylor and R. Mokaya, *J. Mater. Chem. A*, 2018, **6**, 12393–12403.

36 M. Sevilla and A. B. Fuertes, *Carbon N. Y.*, 2009, **47**, 2281–2289.

37 N. Balahmar, A. S. Al-jumialy and R. Mokaya, *J. Mater. Chem. A*, 2017, **5**, 12330–12339.

38 B. Adeniran and R. Mokaya, *Nano Energy*, 2015, **16**, 173–185.

39 M. Sevilla, P. Valle-vigón and A. B. Fuertes, *Adv. Funct. Mater.*, 2011, **21**, 2781–2787.

40 E. Masika and R. Mokaya, *Prog. Nat. Sci.*, 2013, **23**, 308–316.

41 B. Adeniran and R. Mokaya, *J. Mater. Chem. A*, 2015, **3**, 5148–5161.

Chapter 7 – Overall Conclusions

This Thesis detailed an investigation into the tailoring of activated carbons in order to improve their CO_2 uptake capacity. The investigation comprised of 4 studies which focussed on different aspects of porous carbon synthesis. The studies investigated metal doping, a novel carbonisation technique, an alternative activating agent and the use of harsh activating conditions.

Chapter 3 described a study of the effects of metal doping of activated carbons, with the aim of increasing heterogeneity of the surface and therefore uptake of quadrupolar CO_2. A metal salt, potassium hydrogen phthalate was activated at either 800 or 900 °C to produce microporous, high surface area carbons. The carbons were subsequently doped with either K, Li, Na or Ba in nitrate salt form. Surface and elemental analysis revealed that metal ions were distributed evenly across the carbon surface, accompanied by a high oxygen presence which is absent in undoped equivalents. Metal doping reduces the accessibility of the pore structure in all cases, with the effect increasing as metal ion size decreases. This may be due to smaller metal ions may sitting within the pores, reducing pore size and therefore access to the internal pore structure. Additionally, the hygroscopic effect from a greater presence of

smaller ions may result in greater contraction of the carbon structure, reducing the number of pores large enough to be measured by N_2 adsorption. Despite the reduction in accessible pores, the reduction in CO_2 adsorption of the doped samples was not as reduced as would be expected, indicating that the presence of metal ions increased CO_2 uptake ability.

Chapter 4 details a study of a novel carbonisation method, air-carbonisation. Air-carbonisation of spruce biomass was conducted and the results compared to equivalent biomass carbonised by the traditional hydrothermal carbonisation method. Air-carbonisation was shown to produce a char, 'airchar' that was more porous and resistant to KOH activation than the hydrothermally produced hydrochar. Upon KOH activation, airchar resulted in high surface area carbons that retained a greater microporosity, resulting in CO_2 uptakes of up to 4.5 mmol g^{-1} at 1 bar and 25 °C. Further investigation was carried out to determine whether wood composition had an impact on the resulting char. It was found that although the wood type did effect char formation, there were no differences upon activation.

Chapter 5 details an investigation into the use of $Ca(OH)_2$ as an alternative activating agent to commonly used, highly corrosive KOH. A series of samples was produced though $Ca(OH)_2$

activation of biomass. The pore structures produced were found to be mainly mesoporous, with varying degrees of both micro and macroporosity. However, overall pore development was low, with surface area and pore volume reaching a maximum of 562 m^2 g^{-1} and 1.07 cm^3 g^{-1} respectively. This resulted in low CO_2 uptake, reaching a maximum of 2.3 mmol g^{-1} at 25 °C and 1 bar. Despite the benefits of using a less corrosive activating agent, the use of $Ca(OH)_2$ to produce microporous carbons with high surface area may not be viable due to the unpredictable results it provides.

Chapter 6 details an investigation into the effects of harsh activation conditions. Potassium hydrogen phthalate was thermally treated at temperatures of up to 1200 °C and for durations of up to 10 hrs. The result was a series of high surface area carbons with pore volume comprised of a mixed proportion of both meso and microporosity. The addition of a char during the activation process was shown to produce high yielding, highly microporous carbons that exhibit good CO_2 uptake up to 3.4 mmol g^{-1} at 25 °C and 1 bar. The char type affected the textural properties of the carbons; adding hydrochar produced less developed, mesoporous carbons when compared with the addition of airchar.

Overall, the research conducted and presented in this thesis added a number of key findings to the field of adsorbent activated carbon materials. KHP is a relatively little used starting material in the synthesis of such carbons and the research presented here provides more data about its suitability for such a purpose. A novel carbonisation method (air-carbonisation) has been analysed in detail and shown to be a beneficial preparation method. The data regarding the effect of air-carbonisation presented here can therefore be used as a foundation for future investigations into the carbonisation method. There is very little research presented in the literature surrounding the use of $Ca(OH)_2$ as a chemical activating agent in the synthesis of activated carbons. The findings of the investigation detailed in Chapter 5 therefore provide evidence of how $Ca(OH)_2$ can be used as a chemical activating agent, the results it has shown to produce and potential applications. There is also very little research presented in the literature surrounding the use of harsh temperatures up to 1200 °C in the preparation of activated carbons. The results presented in Chapter 6 of this thesis can therefore be used as a basis for further investigations into the use and benefits of high temperature activation.

Future work should centre on building on the evidence base presented in this thesis. Alternative methods of doping metals onto the carbon surface should be investigated, as well as the effects of doping other Group 1 and 2 metals. Air-carbonisation should be trialled with a wider range of biomass sources possessing varying lignin and cellulose content. This would enable better understanding of the physical process of air-carbonisation. $Ca(OH)_2$ should be used as a chemical activating agent with a range of starting materials, to see how this affects the structure of resulting porous carbons. Analysis of this process using TGA coupled with mass spectrometry would allow for better understanding of the chemical reactions taking place during activation.